UNIVERSITY OF SOUTHAMPTON

A Thesis

Submitted for the Degree of

Doctor of Philosophy

DOUBLE-FREQUENCY STATOR CORE VIBRATION IN LARGE TWO-POLE TURBOGENERATORS

by

Ariadne Ann Tampion

August 1990

CONTENTS

UNIVERSITY OF SOUTHAMPTON

ABSTRACT

FACULTY OF ENGINEERING AND APPLIED SCIENCE

ELECTRICAL ENGINEERING

Doctor of Philosophy

DOUBLE-FREQUENCY STATOR CORE VIBRATION IN LARGE TWO-POLE TURBOGENERATORS

by Ariadne Ann Tampion

This Thesis describes the development of a model to represent the variation with load and excitation of double-frequency stator core vibration in large two-pole turbogenerators. The model has a dual purpose, serving first to investigate causes of this effect; secondly to provide predictions suitable for an on-line monitoring scheme.

Electromagnetic forces at the stator bore are represented as tooth-tip forces formed from the integral of Maxwell stress over a slot pitch. Conversion to core-back vibration is by means of transfer coefficients derived from structural finite-element analyses of isolated core models.

A simple model, in which the rotor and stator are considered infinitely permeable with sinusoidally distributed sheets of surface current, is used to demonstrate the primary cause of the variation of core vibration: a load-dependent circumferential stress distribution combining with the radial distribution at phase displacements dependent on excitation.

This model is insufficient for prediction purposes, hence a more powerful model is developed to take into account slotting and magnetic saturation by means of regions of finite permeability, anisotropic in the slotted zones. The windings are represented by Fourier series of current sheets. This model shows the importance of magnetic saturation; also that the variation of vibration with active load is dependent on rotor slotting.

Comparison of predicted vibration levels with test measurements from three machines shows that the absolute level of core-back vibration is pricipally dependent on the support structure. Two of the effects in evidence are examined in a qualitative study.

For John,

Who makes all things seem possible

ACKNOWLEDGEMENTS

This project was funded by the CEGB/SERC cofunding panel.

I would like to thank my Supervisor, Dr Richard Stoll, for his help and encouragement throughout the work; also for his wise and sparing criticism of the first draft of the Thesis. Thanks are also due to Dr Jan Sykulski for his frequent input of ideas; and for so cheerfully allowing me to carry out the lengthy, noisy task of producing my graphs on the printer in his office.

The progress detailed here would never have been achieved without the support of our contacts within industry, who gave freely and willingly of their time to provide us with ideas, suggestions, and, most importantly, raw data.

John Sutton, now of National Power, remained our CEGB contact throughout. His constant support was invaluable, and it was he who obtained the extensive Fawley measurements which proved so useful. His colleagues Stephen Page and, later, Khalid Kamash supplied much-needed mechanical expertise to the work. Stephen Page deserves special thanks for the day he spent helping me interpret the ANSYS documentation, and directing me to the works of Timoshenko.

Contacts within turbogenerator manufacturers supplied essential data relating to machine geometry, plus all-important vibration measurements against which to validate the model. Most sincere thanks are therefore due to Dr Robert Whitelaw of GEC Alsthom Turbine Generators and Dr Michael Ralph of NEI Parsons.

Thanks are also due to Emeritus Professor Percy

Hammond, for the helpful comments he made when examining my Transfer Report. And mention must be made of Professor Kurt Schwarz, who took a keen interest in the progress of this work, and instilled in me the importance of precision in one's terminology: never again will I refer to "no-load" when I mean open circuit. Important, too, were the moral support and inspiration provided by numerous friends and colleagues; the constant friendship of Peter Kyberd, with whom I shared an office, being a particular source of strength.

Thank-you to Eric Catchpole for the beautiful diagrams he prepared on his AUTOCAD system. And finally thank-you to my parents, Dr Doreen Tampion and Dr William Tampion, for loan of a word-processor on which to produce a fair copy of the Thesis, and their unswerving belief that the result would be good.

SYMBOLS AND ABBREVIATIONS

Note: In general, the customary symbols for quantities have been used. Due to the cross-disciplinary nature of this work, the result has been some duplication of symbols. The author believes that this strategy yields a more readily comprehensible text than would be the case if each symbol were unique. Meaning is always made clear in context.

Electrical and Magnetic Quantities

- A — Magnetic vector potential
- B — Magnetic flux density
- e.m.f. — Electromotive force
- E — e.m.f. phasor quantities
  - E_f Excitation e.m.f.
  - E_g Air-gap e.m.f.
- F — m.m.f. phasor quantities
  - F_a Armature (stator) m.m.f.
  - F_f Excitation m.m.f.
  - F_r Resultant [radial] m.m.f
- f — Cyclic frequency
- H — Magnetic field intensity
- I — Conductor current
- K — Surface current density
- k_g — Carter coefficient
- m.m.f. — Magnetomotive force
- m — Harmonics of rotor current distribution
- n — Harmonics of stator current distribution
- P — Active power
- Q — Reactive power
- q* — Density of surface magnetic polarity
- R — Resistance
- V — Voltage
  - V_T Terminal Voltage
  - V_{ph} Phase Voltage
- X — Reactance

α Stator load angle

β Angle between E_g and V_T

δ Rotor load angle

λ Torque angle

μ_o Prermeability of free space

μ_x Relative permeability (subscript denoting relevant material)

Φ Magnetic flux

ϕ Power factor angle

ω Angular frequency

Mechanical Quantities

$d_{x,y}$ Double-frequency core-back displacement amplitude (x denotes direction of displacement; y direction of bore force distribution responsible)

E Young's modulus

F_x Force (in direction x)

I Second moment of area

$k_{x,y}$ Transfer coefficient of double-frequency stator bore force to core-back displacement (subscripts as for $d_{x,y}$)

n Order of natural mode

T_e Electrical Torque

ρ Density

σ Stress

ψ Time-phase angle between F_r and F_θ

Geometrical Quantities

c Ratio of coil pitch to pole pitch

K_c Chording factor

K_d Distribution factor

K_w Winding factor

L [active] Length (depending on application)

l_g Air-gap length

n_t Number of turns per [rotor] coil

n_p Number of parallel paths in [stator] winding

Q_x Number of slots per pole [per phase] (subscript

refers to rotor or stator)

R_x	Radius (of whatever is denoted by x)
r	Radius, in general functions of radius
δ	Iron space factor
Δ	Slot pitch
Θ	Space angle
τ	Half slot width

Principal Subscripts

r	Radial
Θ	Circumferential
n	Normal
t	Tangential
R	Rotor
S	Stator
oc	Open circuit

General

t	time
v	velocity

'Data' is a plural noun, but its general use as a singular noun in construction is acknowledged by Longman's Concise English Dictionary.

Appropriate symbols are defined at point of use for:

(i) arbitrary constants and functions;

(ii) quantities used in one derivation only;

(iii) functions defined for the purpose of simplifying the appearance of equations.

CHAPTER ONE
INTRODUCTION

1.1 Objective

The main objective of this work is to gain understanding of the mechanisms of double-frequency stator core vibration in cylindrical rotor two-pole synchronous machines. It has long been known that the core vibration of large turbogeneratore varies with load and power factor, but no rigorous analysis has been performed to determine why and how. The secondary objective is the development of a mathematical model to simulate core vibration on load, given geometrical and material data relating to any given machine.

The need for this work has arisen out of recent serious consideration given to installation of condition monitoring equipment on operational turbogenerators in power stations. Although often far from benign, causing wear to the stator itself and the risk of fatigue failure to support structures and auxiliary plant, the double-frequency core vibration is a natural part of the machine's operation. It is therefore important that it be distinguished from vibration variations due to potentially catastrophic damage to the rotor. Understanding the effect is preferable to simple mapping at various loads, as such knowledge could then be used as an aid to devising future monitoring strategies, and could also be of relevance to the designer of new machines.

Development of an actual monitoring program does not form part of this work. Stator core vibration is one of many effects which would need to be included in such a program. No framework yet exists for a proposed general program, and therefore no guidelines for fitting specific modules within it. However, this application is born in mind with respect to the development of the model. Hence an analytical approach is taken as opposed to finite-element

analysis, which would not be appropriate to a small sub-routine of a program for a micro-computer. If a sufficiently flexible analytical model is devised, a wide range of parameters may be investigated for their contribution to the effect, thereby facilitating eventual adoption of the simplest model which adequately represents the observed behaviour.

1.2 Condition Monitoring of Turbogenerators

Condition monitoring is defined by Tavner and Penman[1] as "the continuous evaluation of the health of plant and equipment throughout its serviceable life". According to Ham[2], there are four distinct benefits to be obtained from condition monitoring. These are: (i) better planning of scheduled overhaul work by monitoring the progress of anticipated deteriorations; (ii) forewarning of the need for unscheduled overhaul work by monitoring the progress of unexpected deteriorations, thus enabling this work to be co-ordinated with existing commitments; (iii) minimisation of damage due to unpredictable and potentially catastrophic failures by detecting them at their onset; (iv) maximisation of the continuous operating efficiency of the plant.

Condition monitoring is becoming increasingly popular at the present time due to lower levels of plant manning combined with a profusion of relatively cheap electronics for fault detection and interpretation[3]. Like any other concept which gathers momentum rapidly, it is becoming very fashionable[3]. However, monitoring does incur costs, both in terms of equipment and manpower, so a cost-benefit analysis is essential prior to the installation of any monitoring equipment. In general terms, the total cost of the monitoring system should be less than the total costs incurred in the event of failure of the plant.

Another important consideration is whether monitoring techniques exist which are able to identify deterioration and the onset of known failure mechanisms within the plant to be monitored. If they do not, monitoring is unlikely to succeed[3]. The amount of warning that the monitoring system is able to give is important too[4]. If this is insufficient for any avoiding action to be taken, the monitoring system is really useless. Conversely, a system which can give weeks or months of warning may be worthwhile employed even on an item of plant of relatively low strategic importance. In any event, automatic monitoring should never be seen as a complete substitute for periodic inspection by a skilled operator[3].

Large turbogenerators are strong candidates for condition monitoring due to their high capital cost, and the cost of lost generation in the event of an outage. Electrical plant has traditionally had a high reliability. This is not so much an inherent feature as a result of conservative design[4]. However, in recent decades, turbogenerators have been pushed closer to their design limits in an attempt to couple them with larger steam turbines, the efficiency of which increases with increased size. This is because a machine cannot be made indefinitely large. The need for a 50Hz output frequency restricts the maximum speed to 3000rpm for a two-pole machine. This rotational speed itself puts constraints on the diameter of the rotor. The length may be increased, but only whilst the rotor does not bow unacceptably under its own weight. These are the inherent limitations on physical size.

Output may still be increased for a machine of given size by increasing its electric and magnetic loadings (total amperes per metre of stator bore periphery and peak of fundamental air-gap flux density distribution respectively). The magnetic loading is limited ultimately by saturation; the electric loading by the capabilities of the cooling

system. With designs pushed closer to operational limits, the risk of failure becomes greater.

Transducers are currently available which are suitable for the measurement of electrical, magnetic, thermal and mechanical quantities in a large electrical machine. The key to incorporating them into a useful monitoring system is the processing of the signals. Tavner[3] discusses the importance of primary local processing at a monitoring "pod" attached to the machine, to avoid an over-complex system which relies too heavily on a remote computer. Ham[2] describes comprehensive monitoring systems in which large quantities of data are accumulated over periods of time and presented as computer graphics displays which give an easily read overview of plant operation.

1.3 Vibration Monitoring

Vibration is one of the quantities monitored within a complete turbogenerator monitoring scheme. Vibration measurements are usually made at the bearing pedestals. Their greatest use is in identifying shaft problems and rotor surface cracking[4]. Although the development of electrical problems, such as an inter-turn short circuit, within a generator often alters vibration levels, such problems cannot be identified unambiguously in this way, so air-gap search coils may also be used. Every machine has its own characteristic vibration "signature". Sophisticated methods of interpreting vibration signatures are being developed[5], but their wide application will depend primarily on economic factors.

The present state of diagnostic testing on primary generating plant in the UK is described in a paper by D.L. Thomas[6]. Only a low level of monitoring is usual, in the form of the Turbine Supervisory Equipment (TSE), which

measures overall levels of all quantities. The purpose of such monitoring is to warn the operator if levels exceed prescribed limits, so that further investigation of the problem may be carried out.

More detailed vibration measurements, in the form of amplitude, phase and frequency data, are collected only intermittently. Data is collected under three circumstances. In the first case, this is when a machine is returned to service after an overhaul. As alignments are never quite the same as they were previously, the vibration signature will be slightly different, and a record needs to be made for future comparison. Secondly, test measurements are made on-load, to ensure that a history of the machine's in-service behaviour is available for problem diagnosis. Thirdly, the vibration signature during run-down is recorded. This provides more information than the on-load data, as it contains the response to a range of exciting frequencies.

This strategy was adopted after problems caused by transverse cracks in rotors had been experienced. These problems were then eliminated by alterations to the design of the rotors. However, the monitoring strategy had proved useful in the diagnosis of other problems, so it was retained, with consideration being given to its future expansion. It had also established that fault diagnosis is considerably easier if a detailed vibration history of the machine has been built up over its operating life. A natural method of extending the scheme would be to collect data continuously. This gives the advantage of improved quality and reliability of data, and raises the possibility of correlating vibration data with plant operating parameters. For these reasons, the potential of on-line monitoring equipment for turbogenerators is being seriously investigated.

1.4 Double-frequency Vibration of the Stator Core

One of the components of an electrical machine's vibration signature is the vibration of its stator core at double the power frequency. The origin of this phenomenon is the magnetic interaction between rotor and stator.

When the machine is on open circuit, and the rotor is excited, the stator core forms part of the magnetic circuit for the rotor flux. Magnetic poles are therefore induced on the surface of the stator bore: a north pole facing the rotor south pole, and vice versa. These unlike poles then attract, and the stator is distorted. In a two-pole machine this effect is known as stator ovalising, as the distorted stator core takes on an oval shape. As the rotor rotates, the distortion of the stator rotates with it. This is illustrated by Figure 1.1 for a 50Hz machine. The effect at a point on the core back is of a vibration twice the rotational frequency of the rotor, as both poles attract the stator iron.

When the machine is on load, this effect persists. In addition, there is an interaction between the currents of the rotor and stator. This interaction also produces a four-pole force distribution, which is phase displaced in space and time from the first effect. The resultant ovalising amplitude depends on the respective magnitudes and phase displacements of both effects.

The precise manner in which the level of ovalising vibration varies with load is not well understood. The assumption that higher currents lead to higher forces and therefore higher vibration levels has been proved incorrect by observations which show that a decrease of the order of 30-40% between open circuit and full rated load at a lagging power factor is universal on large two-pole electrical machines. There is also a harmonic content to the stator

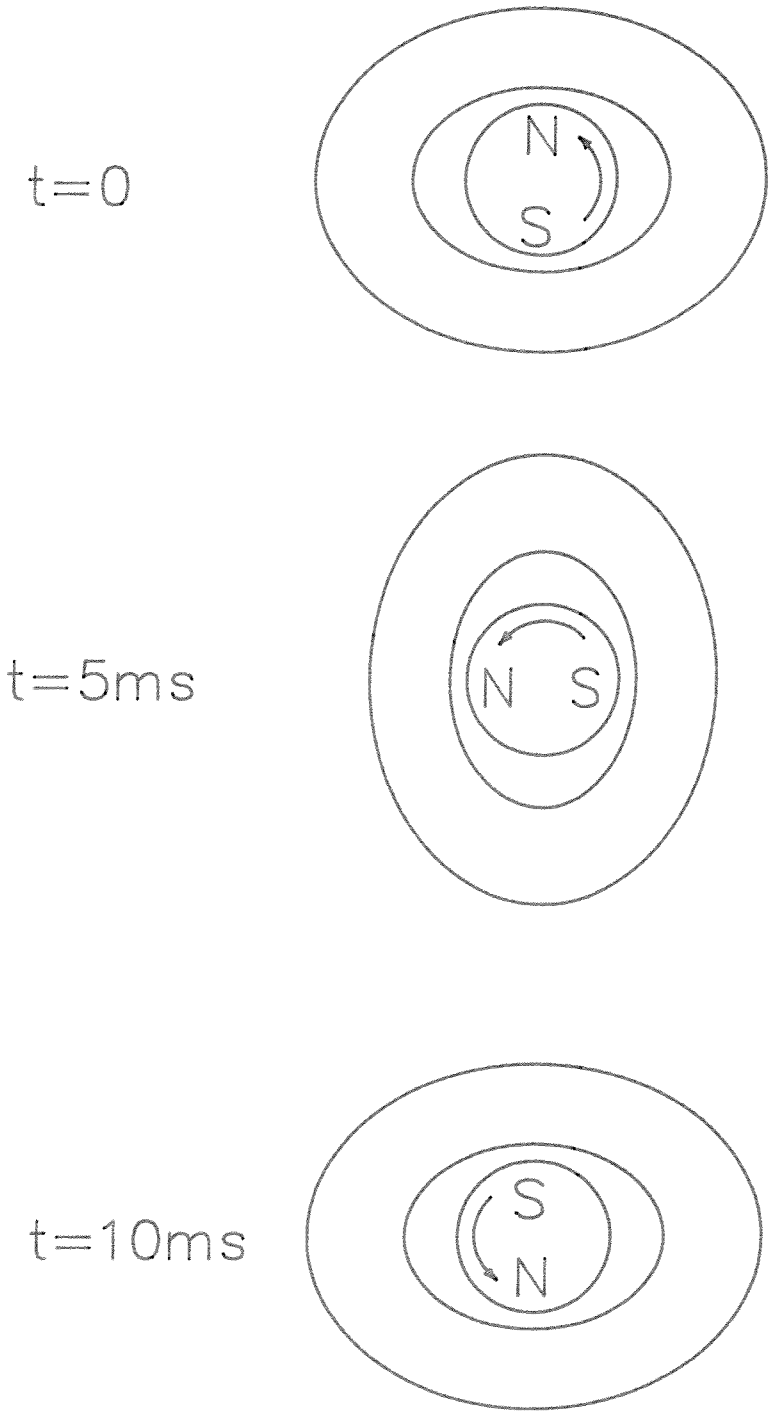

Figure 1.1 Stator core ovalising in a two-pole electrical machine

core vibration which may be detectable in the vibration signature of a machine.

If on-line vibration monitoring schemes are to be applied to large turbogenerators, it is important that this natural vibration of the stator core should not be mistaken for shaft damage. An understanding of its variation with load is therefore essential if the widespread adoption of such monitoring technology is to succeed.

1.5 Content of the Thesis

This Thesis starts with a review of published work concerning stator core vibration. This encompasses a description of its secondary effects, and design strategies geared to its mitigation, as well as attempts to explain and model it.

There follows a chapter in which the background theory to this work is introduced. The principle of operation of electrical machines in general is discussed briefly, before a more detailed description of the operation of the synchronous generator. It is then shown how Fourier analysis may be employed to represent a machine winding as a current sheet. Electromagnetic field theory is used to derive the magnetic flux density in the air gap from the source currents in the winding. Finally, forces in a magnetic field are discussed, and the expressions for normal and tangential Maxwell stress derived.

The fourth chapter starts with the development of a very simple model to represent forces within an electrical machine. It has infinitely permeable iron, and sinusoidally distributed current sheets for windings. The importance of the higher current sheet harmonics is introduced in a general discussion, in which it is shown that combinations

of these contribute to a double-frequency force. The conversion of Maxwell stress distribution at the stator bore to point forces on tooth tips is justified and performed. The operation of computer programs to implement both a very simple model and a more advanced one incorporating higher harmonics is described. Some results for the variation of tooth force with time taking load data from a real generator are produced, but it is then shown that it is not valid to do this: a simplified model requires simplified input data to be self-consistent.

In the fifth chapter attempts are made to construct a mechanical model of the stator core which can convert tooth forces to core-back vibration levels. The finite-element package ANSYS is used for this purpose. At first, a simple annulus is used to represent the stator core in tests to show how the relative time-phases of four-pole distributions of radial and circumferential forces can produce reinforcement or cancellation of the ovalising distortions due to each individual set of forces. Then a search is made for a more detailed model of the stator core. In the one eventually developed, the toothed structure is accurately represented whilst the windings and slot wedges are included in a simplified form. Modal analysis is employed to provide confidence in the models by ascertaining that their natural frequencies are close to those expected from an actual stator. Finally, linear transfer coefficients are extracted by which to convert the calculated tooth forces to core-back vibration levels.

The sixth chapter starts with the development of a self-consistent simple model. This model demands that load condition and terminal voltage be kept true to life, whilst excitation current and load angle are assigned compatible but fictitious values. This scheme coupled with an infinitely permeable model is found to be insufficient, so a model with regions of finite permeability is developed. The

slotted regions of both the rotor and the stator are represented as regions of anisotropic permeability. After a series of sensitivity studies on this model, the calculations of consistent rotor current and load angle are grafted onto the front end of the program. Iterative routines are adopted to determine the permeability of the slotted regions to represent saturation on load. This method of modelling saturation is tested by its ability to predict load angle; and it is further shown that the process incorporates by default the modelling of field leakage.

In the seventh chapter, the predictions of the model are compared with vibration measurements taken on operational turbogenerators. In conjunction with this, the specific effects of the current sheet higher harmonics and the effects of mechanical coupling between the stator and its support structure are discussed. In order to use the model to predict a wide range of load conditions for which data does not exist, routines are developed to estimate the rotor current. This is because a knowledge of the actual excitation current is necessary for the purpose of allocating permeability values to the regions of the finite permeability model. Finally a comprehensive set of load conditions is modelled. The trends shown are discussed; also the nature and level of possible errors in the overall calculation.

Three generators are used in this work. They were selected as ones for which vibration data already exists. The difficulties and expense of taking such measurements made it impractical to commission any specially. One of the machines is the 500MW Ferrybridge type generator, manufactured by NEI Parsons. This generator was used extensively in the early work, due to the early availability of constructional and electrical data supplied by the manufacturers. This was further helped by the extensive series of load tests performed on a machine of this design

at Fawley power station. The two other machines were made by GEC Alsthom Turbine Generators. They were used more extensively later on in the work because numerical vibration data became available by the middle of the project. One is a 500MW generator installed at West Burton power station. The vibration data for this machine appeared fairly extensive, but was actually taken at intervals over a long time period, starting immediately after overhaul, so that the time-variations due to the machine settling down onto its supports masked variations due to load. The second is a 350MW generator, which proved especially useful in the validation of the model. Not only were the measurements all taken over a short period of time, but at variable MVAR for one value of MW, and at variable MW for one value of MVAR, thereby facilitating neat graphical representation of results. Data for all three machines is given in Appendix A.

Two computers were used: one for the structural analyses and one for the electromagnetic force models. The structural analyses were performed on a VAX mini-computer. The electromagnetic model was realised on the IBM 3090 mainframe at Southampton University. The software developed in the course of this work is listed in Appendix B.

CHAPTER TWO

PREVIOUS WORK ON STATOR CORE VIBRATION

2.1 Historical Perspective

In the 1930's, progress in electrical machines technology led to the development of two-pole turbine generators with ratings of about 20MVA. These machines were of sufficient size for the inherent double-frequency vibration of the stator core to become a nuisance, in terms of noise and mechanical transmission of the vibrations to surrounding structure and plant.

Engineers of the time recognised that as MVA ratings increased, this problem would become more severe. Work was done in the USA in the 1940's and 1950's to investigate ways of mitigating the effects of the vibration[7-10]. The principal strategies were to isolate the vibrating parts as much as possible and design to avoid resonances.

Although simple mathematical analyses were performed on the vibrational behaviour of the core structure, the origin of the exciting force was taken to be the radial magnetic pull between the poles of the rotor and stator, and thus proportional to the square of the radial air-gap flux density. This effect was implicitly assumed to be independent of other effects at work within the machine.

In the 1960's and 1970's, work was done at C.A. Parsons and Company Ltd, in England[11-15]. By this time machine ratings had exceeded 500MVA. The first papers made a closer study of the effects of the vibration, including longitudinal vibration and the vibration of the end windings. In the course of their study, the authors took measurements of the ovalising amplitude, including some with the machine on three-phase short circuit. They observed that the amplitude was greater than it should be according

to a B_r^2 law. This was the first indication that this simple model might be incomplete.

Later papers from Parsons described attempts to incorporate other double-frequency forces besides that originating from the radial air-gap flux into a model which could accurately describe the vibrational behaviour of a stator core under load conditions. First, a "quadrature axis force" was postulated, which proved insufficient for this task, predicting only a 5% decrease in vibration for a 500MW generator between open circuit and full rated load. Later, two distinct physical sources of additional double-frequency force were identified, and the model developed to represent them came closer to simulating the observed behaviour, although still diverged significantly from measurement at some higher loads.

2.2 Mechanical Behaviour of the Stator Core

In order to design machines and mountings so that the effects of vibration are minimised, it is necessary to study the mechanical behaviour of the stator core.

It is not possible to eliminate the cause of the vibration. Its magnitude could be decreased by reducing the air-gap magnetic flux density and increasing the rigidity of the core, but such measures would be only partially satisfactory and would result in a considerable increase in the cost of the machine[7,9]. However, in some cases the use of increased core depth has been considered a success[8]. In general, it is best to attach the core to the support structure by means of flexible supports which minimise the transmission of vibration and noise; also to design the core and frame to avoid resonant conditions[9].

The stiffness of the stator core is important in that

it affects both the static distortion and the resonant frequency of the structure. The core is composed of stacked laminations bolted together under pressure between heavy end-plates. It is thus of comparable stiffness to a solid steel cylindrical tube when resisting distortion[7]. Tests in which a stack of punchings were loaded radially with a hydraulic jack showed it to be not only very stiff but quite elastic up to loads considerably in excess of those expected from the magnetic forces[8]. In accompanying tests the same authors[8] determined that the resonant frequency of a stator core is always higher than the normal operating frequency, but that in large cores it is close enough for there to be significant dynamic magnification. This result is also mentioned by Richardson[11]. The contact area between laminations is also important[11]. If these are punched out of sheets of steel of uneven thickness, poor contact at the outer edges will reduce the effective core radius, with a resultant decrease in stiffness. It has also been shown[16] that the presence of the stator winding increases damping generally, and suppresses tooth resonances which are evident in a stator core with empty slots.

Small machines may be made smaller, and with reduced core losses for a given rating, by manufacturing them out of high-permeability grain-oriented steel[9]. In larger machines, however, vibration considerations outweigh the advantages. Not only does the reduced size of core have a reduced stiffness, but the higher magnetic loading possible increases the forces present. The effect is further exacerbated by the fact that such steels have a lower Young's modulus than ordinary steel[11,12], both increasing the static distortion and lowering the resonant frequency, so increasing the dynamic magnifier. Thus electrical design must be subjugated to the needs of mechanical design in these instances.

The stiffness of the frame also needs to be considered.

Although it is low enough in comparison to that of the core to be left out of calculations of core deformation[8], the stiffness does affect the resonant frequencies of the structure. It is important to design a frame to avoid resonant conditions, as the effects of an excellent suspension system could be largely nullified if a resonance is excited in the support structure. Baudry, Heller and Curtis investigated this problem using plastic scale models[9]. These had the advantage of a scaled-down Young's modulus, so that the deflections of the scale models were large enough to be measured accurately, which would not have been the case had they been made of steel. The trend towards machines of larger diameter has produced perforce frames of lower stiffness. In acceptance of this fact, and to reduce overall weight, "soft type" stator frames are becoming more common[17]. Such frames are deliberately designed so that their natural frequencies are well below those of the electromagnetic forces at normal operating speed. It is important that the dynamic behaviour of soft type frames be well understood to avoid problems during run-up and run-down.

In order to design effective resilient mountings for the stator core it is necessary to consider the levels of both radial and tangential deformation caused by an ovalising force. For a thin ring, the maximum tangential deflection is half the maximum radial deflection[7,8]. In a thick ring, which is a better model of a stator core, the tangential deflection is half the radial deflection on the neutral axis only: towards the inner diameter it is greater; towards the outer diameter it is less.

This result has been used for the development of the vertical spring mounting[10]. This form of mounting was designed to be used between the two frames of a double-frame structure, consisting of metal plates between the frames, tangential to each. The original need for a double frame

arose when the size of electrical machines started to exceed shipping limitations. But it also has advantages in terms of suspension. The inner frame may be clamped tightly to the stator core such that the two may be considered integrally as one thick ring. At a radius four-thirds the radius of the neutral axis, the tangential displacement passes through a minimum before increasing again.

The neutral axis of a section coincides with its centroid[18]. The centroid is found by dividing the first moment of area by the total area[19]. The polar first moment of area of a ring about an axis through its centre is $2\pi(R_o^3-R_i^3)/3$ where R_o is the outer radius; R_i the inner radius. Its total area is $\pi(R_o^2-R_i^2)$. For example, considering the West Burton generator, R_o=1.27m and R_i=0.64135m, giving a neutral axis at 0.99m. Four-thirds of the neutral axis is therefore 1.32m. If extensions to the inner frame are made so that spring plates are attached at exactly this radius, the tangential forces transmitted to the supports will be a minimum. The spring plates are effectively flexible radially and rigid tangentially. Results in terms of suppressed vibration have been proved superior to those obtained using traditional longitudinal spring bar mountings.

2.3 Secondary Effects of Stator Core Vibration

2.3.1 Longitudinal Vibration

The radial forces, besides exciting ovalising vibration, also excite longitudinal transverse vibration[11]. Variation of radial vibration amplitude along the length of the core was investigated by Penniman and Taylor[8]. They took their measurements on the outside of the core and found the level to be a maximum at the centre and a minimum at each end, which makes sense upon

consideration of the fact that the ends are clamped to substantial circular end plates.

Richardson[11] took measurements of the slot opening width as a function of time to determine the ovalising amplitude on the inside of the core, and found that it increases towards the ends. This is evidence that the core is also vibrating in a longitudinal mode. Further evidence is available in the form of polishing of the slots[12], which was most noticeable over a large band at the centre of the stator and small bands at each end.

Tests conducted at C.A. Parsons on a prototype generator unfortunate enough to display a longitudinal resonance at normal operating speed (3000rpm) identified the mode as flexural, consisting of a simple beam component superimposed on a torsional component[11]. It was noted earlier that the radial stiffness of stacked laminations is comparable to a cyindrical tube of solid steel[7,8]. However, longitudinally this is not the case, as the layers of resin are now considered in series with the steel. An effective Young's modulus was found to be 1.5×10^5psi as opposed to 30×10^6psi for solid steel[11]. Recent work by Garvey of GEC Alsthom Large Machines Ltd[20] includes an extensive investigation into the moduli of stacks of laminations at different clamping pressures. He found that the Young's modulus of the laminated structure in compression perpendicular to the plane of the laminations is always less than 3% of the modulus of solid steel. It increases slightly with increased clamping pressure and is lower for varnished laminations. A similar pattern was observed with respect to the shear modulus. He went on to show that this decreased shear modulus reduces by a factor of almost four the natural frequency of a variant of the simple ovalising mode of a laminated cylinder in which the centre ovalises along an axis at 90° to the two ends. This particular mode would experience significant forcing from a

skewed rotor, and is therefore unlikely to be excited in a turbogenerator, but demonstrates in general that combinations of radial and flexural beam modes become more important when a structure is built from laminations.

These results reinforce the conclusion noted in Section 2.2: that electrical design of large generators may have to be subjugated to mechanical design, and that mechanical considerations need to be brought into the design process at an early stage.

2.3.2 Vibration of End Windings

The end windings of a large generator constitute a significant mass, and so their vibrational behaviour is of considerable interest. There will be forces in the end windings due to the currents of individual conductors acting upon one another; also vibration excited by the motion of the stator core. Richardson and Hawley[12] are not sure whether it is correct to study these effects together or as separate items. It is in this one paper that they describe extensive measurements carried out on the end windings of a 200MW and a 500MW generator. The measurements were made under both open- and short-circuit conditions, over a range of speeds. The behaviour of the end windings was very similar under both conditions and on both machines. The natural response of the end windings in both cases occurred at about 2000rpm. This means that although this critical speed must be passed through during run-up, the vibration level at normal operating speed is low. One implication of this result is that it is probably not worthwhile trying to reduce the vibration of the end windings by stiffening them. To do so would raise the resonant frequency and so could have the reverse effect.

2.3.3 Damage to Component Parts due to Vibration

In Reference 11, Richardson outlines a number of identifiable mechanisms of damage or wear which are either completely attributable to or exacerbated by stator core vibration.

Simple insulation failures are rare. Usually a failure follows progressive deterioration and is triggered by a fault. Unfortunately the fault current tends to destroy evidence, but a picture can be put together from known mechanisms of wear. Besides wear to conductor insulation, problems include wedge wear, conductor bar bouncing, and the migration of insulating tape from conductor to slot wall. Vibration damages the insulation both of the main conductor tube and of individual conductor strands. Damage to the main tube insulation takes the form of pitting to the surface, giving an appearance very similar to that of corona damage. Wear to conductor strand insulation is not uniform along the length of the core, and shows nodes and anti-nodes which indicate that the strands are being excited to vibrate at higher harmonic modes.

The stator slot wedges require periodic tightening, due to wear attributable to double-frequency vibration. The cyclic alterations in slot opening width are likely to be the immediate mechanism. In a double-layer winding, the two conductors in a slot will exert forces on one another and on the core. These "bar bouncing" forces serve both to disturb the conductors, causing wear, and contribute to the overall forces on the core[11,12,15].

The phenomenon of tape migration, where the stator conductor bars are insulated with mica tapes, has long been known and attributed to thermal effects. Copper has a higher coefficient of expansion than the steel of the core, and on start-up the conductors get hot first, before the

heat is transmitted to the core. Thus the conductors expand in their slots and the insulation is squeezed tightly against the slot wall. When the machine is taken off load the effect reverses. The copper cools first and shrinks, leaving some insulation behind. If this were the sole cause of the effect, wear due to tape migration would be of equal severity for top and bottom layer conductors; perhaps worse for those on the bottom layer. In reality, it is significantly worse for top layer conductors. The top layer conductors are more affected by the opening and closing of the slots due to ovalising vibration. This vibration aids the migration of tape and is present during the heating cycle with current flowing, but not during the cooling cycle if the excitation has been removed. There is thus a reduced tendency for the insulation to return to its original position.

In addition to wear to stator components, the transmission of vibration to the support structure will cause wear here, with the danger of fatigue failure to parts of this structure.

2.4 Modelling Stator Core Vibration

2.4.1 Early Ideas

In early work on stator core vibration, the prime consideration was design to alleviate the undesirable effects of the vibration. The physical causes were not investigated. It was believed that the radial ovalising forces were due to the radial flux in the machine, and independent of other effects. Mathematically, the vibration amplitude was considered to be proportional to the magnitude of the radial air-gap flux density squared, and equations to predict the subsequent deformation of the core were developed to a high degree of sophistication[21].

It was not until specific measurements of ovalising amplitude with a machine on steady three-phase short circuit were made[11,12], that the inadequacy of the B_r^2 law became noticeable. In particular, 500MW generators on test[12] showed vibration levels on short circuit that were 40% of the levels on open circuit. Considering the radial air-gap flux density alone, this vibration should only have been about 6% of the open circuit level.

Another indication that the B_r^2 law was incomplete came with observations of vibrational behaviour with variation in power factor[13]. Qualitative observation of the variation in noise level of generators on load led to more specific tests. In one, a 500MW generator, operating at rated output and unity power factor, underwent a load change to the rated power factor of 0.85 lag, with the active load maintained constant. In effect, the rotor current had been considerably increased, which in theory should lead to an increase in vibration and noise. In fact there was a marked reduction in noise level. The fact that the torque had remained constant eliminated any possibility that the stator core had merely "bedded" into its casing. The authors of Reference 13 followed up their results by examining archive records of noise recorded on generators. The results were inconclusive, for although the loads had been recorded, the power factors had not.

But it had been overwhelmingly proven that the level of stator core vibration is not proportional to the square of the radial air-gap flux density. In order to make sensible predictions, it was necessary to develop a more sophisticated model.

2.4.2 The Quadrature Axis Force

Richardson and Hawley[13] postulated a force on the quadrature axis in addition to the force due to the radial

air-gap flux density in the direct axis, and suggested that overall vibration levels might depend as much on the phase relationship between the two as on their magnitudes. These authors state that the quadrature axis force is proportional to the product of rotor and stator currents divided by air-gap length. They make a simple calculation to predict vibration levels on three-phase short circuit which gives a result of the right order of magnitude.

They then go on to consider the impact that this force might have on the progress of design advances in large turbogenerators. In particular, two approaches which are intended to increase machine output by increasing specific electric loading are the development of water-cooled rotors and the development of superconducting machines. In both cases the vibration due to the quadrature axis force may make such advances impractical. The other parameter important in the quadrature axis force is the air-gap length. Reducing the air gap has three distinct well-known undesirable effects on rotor surface losses[13]. Consideration of the fact that reduction of airgap length will also result in an increase in quadrature axis force and therefore a possibly pronounced effect on machine vibration, means that design strategies tending towards smaller air gaps must be pursued with extreme care.

Problems concerning mechanical wear due to machine vibration as catalogued in Reference 11 will be much the same whether the exciting force is in the direct or quadrature axis. However, problems caused by local variations in ovalising force could be exacerbated if the direct and quadrature axis forces both vary locally in different ways. Richardson and Hawley[13] describe the effect of hysteretic heating. They noticed that at one particular location where they had positioned a thermocouple on the core, a significant temperature rise was recorded unconnected with any load change. They attributed this to

local variations in ovalising force which caused high local stresses in some laminations. The resilience of the varnish film between laminations increases with temperature, so, as the local strain energy generates heat, the varnish film will suddenly shear, generating more heat in the process. This will happen some time after the initial heating due to the local strain in the laminations. This effect had not been recorded before but could become of increasing importance as specific ratings of generators are increased.

2.4.3 Attempts at Verification of the Quadrature Axis Force

Hawley, Hindmarsh and Crawford[14] developed a mathematical model to describe the variations of stator core vibration with load and power factor. The rotor and stator are assumed to have smooth surfaces, on which lie sinusoidally distributed current sheets. Laplacian fields are assumed in the air gap and in the two iron members. A simple electromagnetic analysis produces expressions for the radial and circumferential components of flux density: B_r and B_θ. These are then inserted into the equation for radial force:

$$F_r = (B_r^2 - B_\theta^2)/2\mu_o \qquad (2.1)$$

It is worthy of note that the authors did not consider the corresponding circumferential magnetic force to be of relevance in this situation.

Results obtained from vibration measurements taken on a 5MW generator in the laboratory and a 500MW generator on site were then compared with the results of the force calculations from the model. The model did not fare well from the comparisons. For the 5MW generator, the B_θ^2 component is small compared to the B_r^2 component, and the predicted variations in vibration with load are the same from the model as from a B_r^2 law, showing a small increase instead of the measured decrease of 10% between open circuit

and full load. For the 500MW generator, the model shows a trend in the right direction. A B_r^2 law predicts an increase of about 10% in vibration amplitude between open circuit and full load. The model predicts a decrease of about 5%. Measurements show a decrease of 40%. This indicates that there may be some truth in the model, but it is by no means the whole truth.

Further tests on the 5MW generator investigated over- and under-excited running. Both the B_r^2 law and the model predict a slight increase in vibration for over-excited running (lagging power factor), and a corresponding decrease for under-excited running. Measurement shows just the reverse. These results show that the vibration level is dependent on power factor and that once again this particular model gives an incomplete picture.

The same authors go on to consider qualitatively other effects which may influence the amount of core ovalising. These are: (i) unequal forces on opposite sides of teeth at the edges of phase bands; (ii) local variations in the load torque which in fact act against its average direction; (iii) the fact that the actual force on each tooth tip is the vector sum of the radial ovalising force and the circumferential load force, which becomes proportionally greater with increased load. The authors consider that the second item may be the most significant.

2.4.4 Identification of Further Ovalising Forces at the Stator Bore

A much more recent paper by Marlow[15], also of Parsons, includes a synopsis of a more detailed analysis of the ovalising vibration of a turbogenerator stator core. Two further ovalising forces are identified positively in addition to that due to the air-gap flux density. The first is the "bar bounce" force arising from the interaction of

the stator current with the cross-slot leakage flux. It acts radially, with a steady component and a double-frequency component similar to that caused by the radial air-gap flux density. The second is the tangential (circumferential) force on the stator teeth arising from the interaction of the air-gap flux and the cross-slot leakage flux. It has a steady component, which is the machine torque, and a four-pole rotating component.

These three forces are then summed vectorially to give the resultant. A graph of ovalising amplitude against increasing load (unscaled) is used to compare calculation with measurement. The model as used shows a 20% decrease between lowest and highest loads whilst the measurements show about 30%. The variation is erratic at low loads, and this is attributed to variations in power factor; however the author makes it clear that a variation with load is being demonstrated.

CHAPTER THREE

ELECTRICAL MACHINES AND ELECTROMAGNETISM

3.1 Introduction: The Alignment Principle

The alignment principle is the most pictorial method of demonstrating the basic mode of operation of all electrical machines. Any rotating electrical machine may be looked upon as two concentric magnets. In the simplest case of a two-pole machine, the rotor has a north and a south pole on its outer surface; the stator on its inner surface. There is an attractive force between unlike poles of rotor and stator and a repulsive force between like poles, which together try to bring the magnets into alignment so that the north pole of the rotor faces the south pole of the stator and vice versa. The magnitude of this force depends on the misalignment angle λ, as shown in Figure 3.1. In a rotating machine, the force will manifest itself as a torque; thus λ is known as the torque angle.

It follows that for the machine to produce constant torque, λ must be kept constant. This implies that the poles of the rotor and stator must rotate synchronously. Differences between different types of electrical machine stem from the different ways in which the poles are produced, and the different ways in which their misalignment is maintained.

Each type of machine may furthermore act either as a motor or a generator, depending on whether energy input to the system is via the rotor or the stator. If the rotor is pulled around by the motion of the poles of the stator, the machine is a motor. If the rotor is driven by external shaft power and acts to pull the stator poles around with it, the machine is a generator.

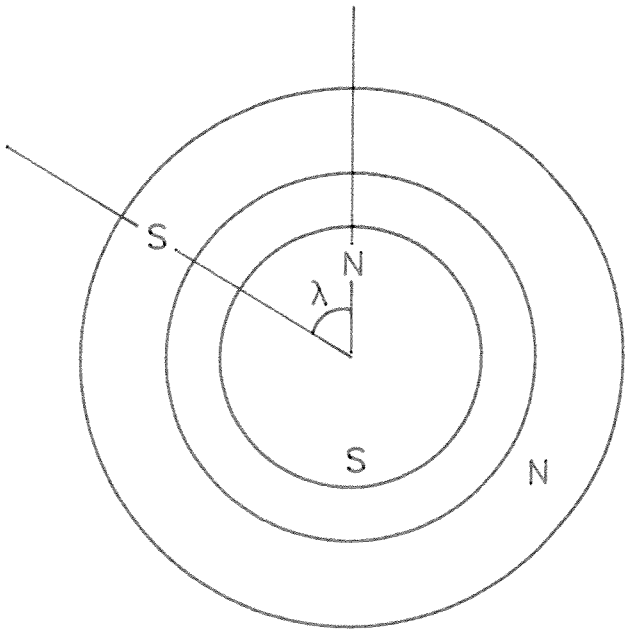

Figure 3.1 Misaligned concentric magnet representation of an electrical machine

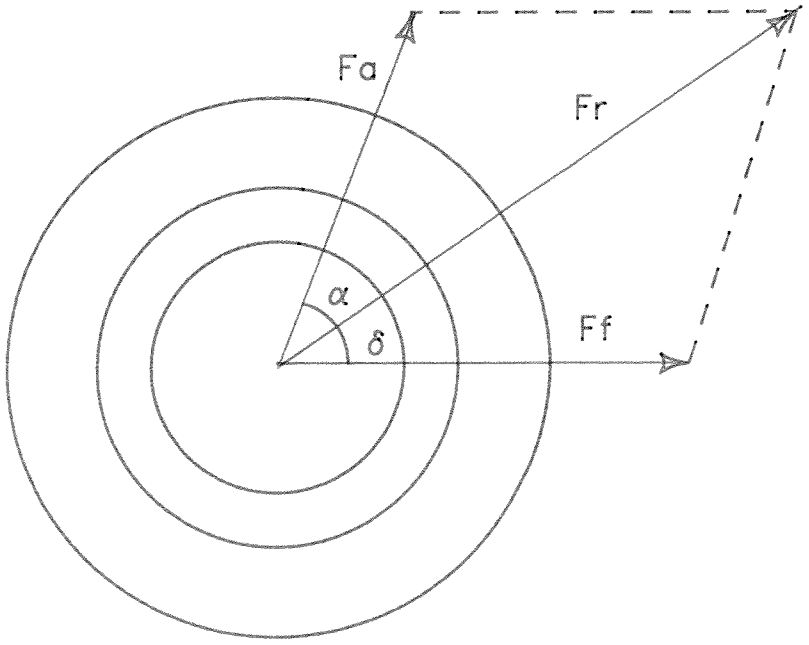

Figure 3.3 Rotor and stator load angles

3.2 The Synchronous Generator

A turbogenerator is a variety of synchronous machine. The rotor is driven by a steam turbine, and is almost invariably two-pole in 50Hz power systems to maximise the rotational speed, as explained in Section 1.2. Its winding is fed with direct current. Therefore its poles are fixed in position upon its surface. The rotor winding slots generally cover about two-thirds of the surface; the expanses of unslotted steel between go and return conductors are known as the pole faces.

To maintain a constant misalignment between rotor and stator poles, the stator poles rotate synchronously with the mechanical rotation of the rotor. This is the origin of the name "synchronous" machine. The stator poles are not physically located in space but are the result of current flowing in the stator winding on load. Their axes are located at the points where the net stator current flow reverses direction. This means that the frequency of the generated current is dependent only on the speed of the rotor, and not on load, making the use of synchronous generators especially advantageous in a national generation network, where frequency must be kept within fine limits.

When the generator is on open circuit, the stator poles are only those induced in the stator iron by the rotor, as shown in Section 1.4, so there is no misalignment angle λ. However an e.m.f. is induced in each coil of the stator winding due to the change in magnetic flux which links it as the rotor rotates, in accordance with Faraday's Law:

$$\text{e.m.f.} = -\frac{d\Phi}{dt} \qquad (3.1)$$

Alternatively a single conductor may be considered, in which case the flux-cutting rule must be used. When a conductor moves relative to a magnetic field in a direction perpendicular to the field, it can be thought of as

"cutting" the magnetic flux. An e.m.f. is induced across the conductor in accordance with the rule:

$$e.m.f. = BLv \tag{3.2}$$

where B is the flux density, L the component of length of the conductor perpendicular to the field and v the component of its velocity perpendicular to the field. In the case of the stator conductor it is of course the field which moves.

The magnetic flux arises from the magnetic field of the rotor, which, being an electromagnet, can be thought of as setting up a magnetomotive force. The radial component of magnetic field H in the air gap varies with position around the rotor, being at a maximum, but of opposite direction, at each pole centre and therefore zero equidistant between poles. Its distribution can be inferred from Ampère's law and Figure 3.2. Ampère's law states:

$$\oint H.dl = I \tag{3.3}$$

and means that if the magnetic field intensity at points in space is integrated around a closed loop the result gives the total m.m.f., which is equal to the current enclosed by the loop.

To demonstrate how the m.m.f. distribution within an electrical machine may be derived from Ampère's law, it is convenient to use a simplified model of the machine in which the air-gap length is assumed small compared to the rotor radius. Then the radial component of magnetic field intensity in the air gap, H_r, may be assumed independent of radius and therefore a function of angle only. Thus the m.m.f. across the air gap is given by $H_r l_g$, where l_g is the air-gap length, at any position Θ. This approximation is not a good one for a large turbogenerator, in which the air gap tends to be of significant dimension compared to the rotor radius and variation of H_r must be taken into account. However, the simple model is still good for illustrative purposes.

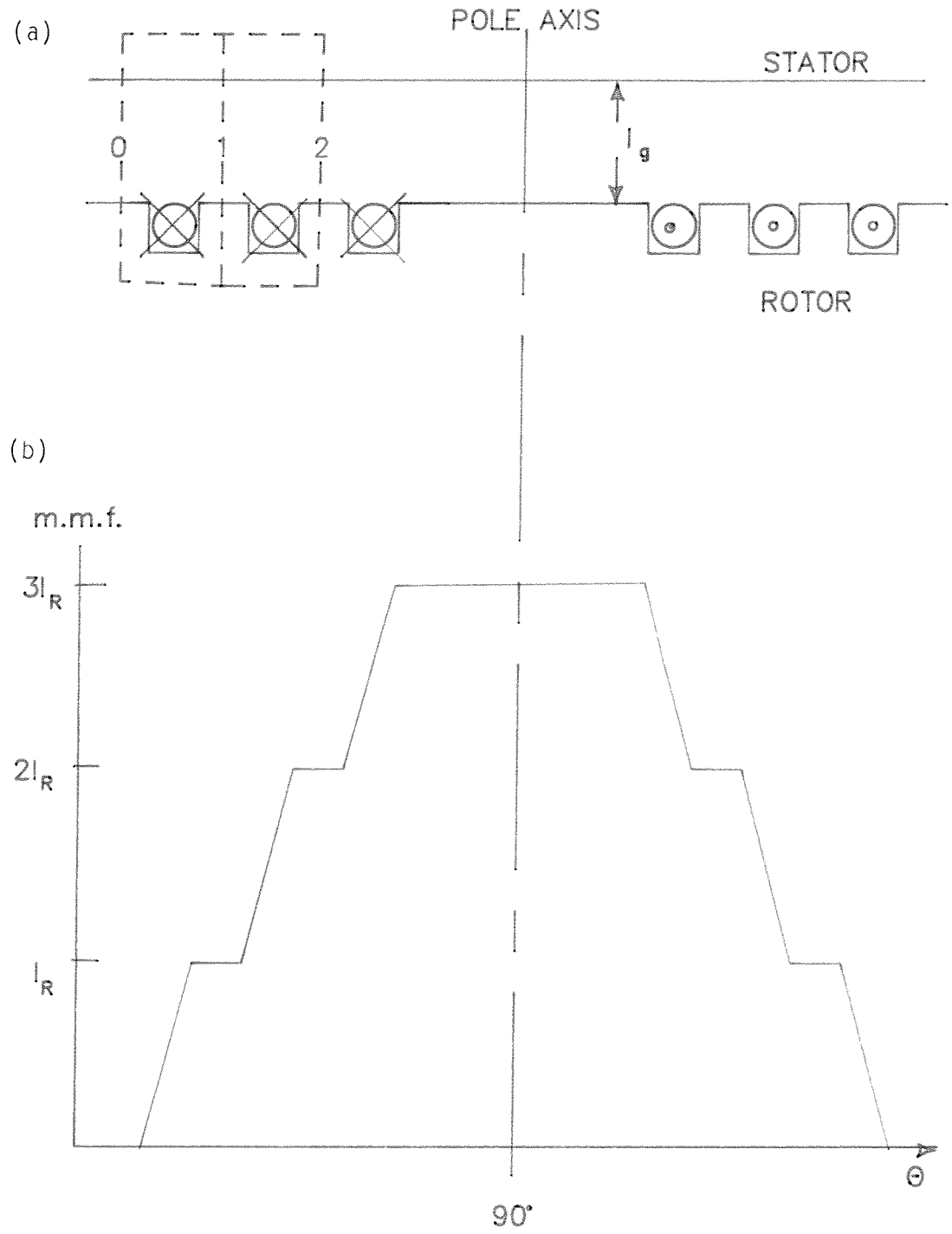

Figure 3.2 Distribution of rotor m.m.f. in the air gap

Figure 3.2(a) illustrates how the air-gap m.m.f. due to the rotor winding may be determined by this method. For simplicity, the stator winding is not shown. The figure shows a developed view of one rotor pole pitch. The dashed line enclosing the first conductor on the left-hand-side is taken as the integration loop for Ampère's law. It is useful to think of this line as describing a magnetic tube in which the flux is constant. The magnetic flux density (B) and the magnetic field intensity (H) are related by the following expression:

$$B = \mu_o \mu_r H \qquad (3.4)$$

in which μ_o is the permeability of free space and μ_r the relative permeability of the material. If μ_r is assumed very high in the iron, then H there is very low, so, to a good approximation, all the m.m.f. is in the air gap.

Position 0 in the air gap is equidistant between the pole axes. Therefore H_r is zero at this point, and so is the m.m.f. Hence all the m.m.f. around the loop is concentrated at position 1 in the air gap. If the rotor conductors carry a current I_R, the m.m.f. at position 1 is equal to I_R. Similarly, the m.m.f. at position 2 is equal to $2I_R$. Figure 3.2(b) shows the variation of air-gap m.m.f. around the pole pitch.

The waveform of Figure 3.2(b) is approximiately sinusoidal in shape. Therefore the distribution of m.m.f. around the air gap could be approximated by the function $F_f = \hat{F}_f \sin \Theta$. For a rotor of circular cross-section, the distance from rotor surface to stator bore, that is, the air-gap length, is constant. Thus the magnetic field intensity and the flux density (from equations (3.3) and (3.4)) follow the same sinusoidal distribution.

When the rotor rotates, the sinusoidal flux density distribution rotates with it. If the rotation is in the

direction of increasing Θ, the flux density at the stator surface varies with time as $\hat{B}\sin(\Theta-\omega t)$. This is equivalent to the stator conductors moving at angular speed ω through a stationary field $\hat{B}\sin\Theta$. Then the flux cutting rule, equation (3.2), is applicable. The active length of the stator conductors is L, and their velocity is ωR_s, where R_s is the stator bore radius, so the instantaneous e.m.f. induced in a single stator conductor is $\hat{B}\sin\Theta.L\omega R_s$. In a two-pole machine $\omega=2\pi f$ where f is the supply frequency, so the peak induced e.m.f. may be given by $2\pi f R_s L\hat{B}$. Like the m.m.f., it is sinusoidal in variation. The advantage of sinusoids is that their waveshape is unchanged by the process of differentiation.

The stator of a turbogenerator typically has 48 or 54 evenly spaced slots, each of which contains two conductors to form a double-layer winding. If two conductors on opposite sides of the stator are connected in series, the peak induced e.m.f. is twice that for one conductor. The stator conductors form a three-phase winding. This involves connecting in series a number of adjacent conductor bars to form a phase band. There is then a corresponding phase band on the opposite side of the winding incorporating the return conductors. It is not possible to calculate the total induced e.m.f. of a phase band by multiplying the peak e.m.f. of each by the number of conductors, as these peaks will not occur at the same instant in time, but will be phase displaced. Thus the total phase e.m.f. is reduced by a factor K_d, known as the distribution factor, which is the ratio of the phasor sum of the induced e.m.f.'s to their arithmetic sum.

Furthermore, the stator coils usually do not span a complete pole pitch. The reason is to save on the weight and cost of end-winding copper, and to suppress some higher harmonics of e.m.f. generated because, as is evident from Figure 3.2(b), the m.m.f. waveform is not a perfect

sinusoid. The result is that the e.m.f.'s of the two sides of one coil have to be summed vectorially, reducing the total phase e.m.f. by a further factor, K_c, the chording factor. The product of K_c and K_d is known as the winding factor, K_w. Therefore, if there are z conductors in series per phase, the r.m.s. phase voltage is given by:

$$V_{ph} = \sqrt{2}\pi f z R_s L K_w \hat{B} \qquad (3.5)$$

When the machine is on load, current flows in the stator winding and the stator poles are misaligned with respect to the rotor poles. The m.m.f. associated with the stator, which is now also an electromagnet, is known as the armature reaction, F_a. It is approximately sinusoidally distributed in the air gap, but phase-displaced from that of the rotor. The two m.m.f.'s combine to form a resultant. It is this resultant air-gap m.m.f., F_r, which induces the stator e.m.f. Therefore it is more usual, when considering an active alignment angle inside the machine, to take the rotor load angle δ, which is the angle between the line of action of the peak of the rotor m.m.f., F_f, and that of the resultant, F_r. The stator load angle α may also be defined[22], but seems to be rarely used. They are related to the torque angle λ by $\delta+\alpha=\lambda$. The situation is depicted in Figure 3.3.

If the machine outline of Figure 3.3 is ignored, the remainder represents an m.m.f. phasor diagram. It is evident that the armature reaction F_a can be resolved into two components, corresponding to two sinusoidally distributed m.m.f. distributions. One, equal to $F_a \cos \lambda$, is in phase with the rotor m.m.f. F_f, which means there is no misalignment and no contribution to the torque. The other component, $F_a \sin \lambda$, which is at 90° to the rotor m.m.f., is solely responsible for the torque. If the resultant m.m.f. is also resolved, its sine component is equal to that of the armature reaction, whilst its cosine

component is the sum of the rotor m.m.f. and the cosine component of armature reaction.

As stated earlier, it is the resultant m.m.f. which induces the stator e.m.f. Although the rotor is usually thought of as the "field" winding, both the rotor and the stator contribute to the magnetising effort. In Figure 3.3, the cosine component of armature reaction is added to the rotor m.m.f. to give the total magnetising m.m.f. The rotor therefore is providing insufficient m.m.f. to maintain the required level of resultant m.m.f. and flux, and hence terminal voltage. The machine is underexcited. If the rotor were instead providing too much m.m.f., the cosine component of armature reaction would have to be subtractive. The machine would be overexcited.

If the machine is connected to an "infinite busbar", defined as a source of balanced three-phase voltage of constant magnitude and frequency which can deliver or absorb active and reactive power without limit, and is underexcited, the stator winding acts as an inductor, and draws lagging MVARs. If the machine is a generator, and therefore considered to be a source of power, both active and reactive, it is said to be operating on leading power factor. Similarly, an overexcited synchronous generator is said to be operating on lagging power factor. Thus the power factor of a synchronous generator connected to an infinite busbar can be controlled by the excitation current fed to the rotor.

Any large grid system is, to a reasonable approximation, an infinite busbar. The MVAR load on it varies greatly during the day. Industrial electric motors and domestic equipment are predominantly inductive in nature and require lagging MVARs to be generated. At night, demand for power is low, and the network is dominated by its many hundreds of miles of highly capacitive transmission lines

and underground cables, which absorb large amounts of leading MVAR. The controllability of the synchronous generator's MVAR output is therefore extremely advantageous in a generation network.

3.3 The Equivalent Circuit of the Synchronous Generator

A model of the synchronous generator can be developed in which each phase of the output is considered to be an alternating voltage source in series with an impedance. Such a model is not as good for the purposes of understanding the operation of the machine as one based on the interplay between two magnets. However, it is extremely useful if the machine is to be represented in the process of a circuit calculation. The effects of magnetisation and leakage from a magnetic circuit are classified and quantified as simple circuit elements. The equivalent circuit is also the starting point for the construction of the voltage phasor diagram.

The equivalent circuit of one phase of the synchronous generator is shown in Figure 3.4. The voltage source E_f is known as the field e.m.f. It corresponds to the phase voltage which would be induced in the stator winding if the excitation current fed to the rotor at the load in question were maintained on open circuit. The armature reaction is represented by a series reactance X_a. If the machine is overexcited, E_f is greater than V_{ph}, and some of E_f is dropped across X_a. If the machine is underexcited, reactive current flow is from the terminals to the equivalent source, and thus the voltage drop across X_a is additive to the source voltage. This represents the way in which the armature reaction contributes to the overall magnetisation, as described in Section 3.2. Leakage of flux from the magnetic circuit of the armature field is represented as a further reactance X_l. The two are generally lumped together

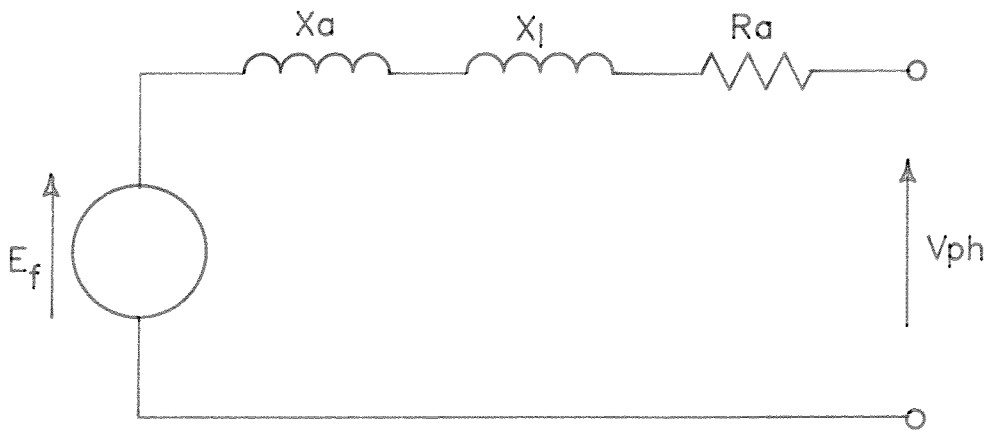

Figure 3.4 Equivalent circuit of the synchronous generator

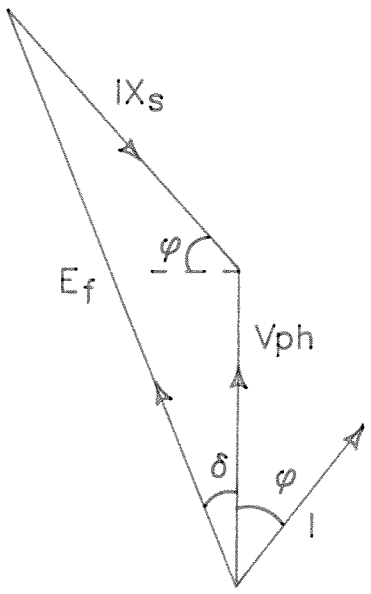

Figure 3.5 Voltage phasor diagram of the synchronous generator

as the synchronous reactance X_s. The resistive component R_a represents the resistance of the stator winding. In a large turbogenerator this is very small in comparison to the synchronous reactance, and may be ignored without introducing significant error into calculations. Thus each phase of the synchronous generator may be represented in a circuit as an a.c. voltage source E_f in series with a reactance X_s.

The voltage phasor diagram may be constructed in accordance with Kirchoff's law by ensuring that the voltage phasors for each part of the equivalent circuit sum to form a closed polygon. It is usual to take V_{ph} as reference and represent it as a vertical line. The current I is not strictly a part of the diagram but is usually included to show the power factor angle ϕ. The voltage drop across the synchronous reactance is then at 90° to the current phasor. The triangle is closed by the field e.m.f. phasor, and the load angle δ is revealed. Figure 3.5 shows the situation for an overexcited machine.

The voltage phasor diagram may be related to the m.m.f. phasor diagram by considering that F_r corresponds to V_{ph}, F_f to E_f and F_a to IX_s. In the same time-frame the m.m.f. phasor diagram is 90° out of phase with the voltage phasor diagram. The F_r phasor is a horizontal line directed towards the left-hand side of the page. In the absence of saturation, the two triangles are similar. However, saturation on load causes X_s to decrease, hence the two angles δ are not the same for m.m.f. and e.m.f. The flux density triangle may also be drawn. As it is the flux which induces the e.m.f. (equation (3.1), Faraday's law), the flux density and e.m.f. triangles are always similar.

3.4 Current Sheet Representation of Windings

3.4.1 Introduction: Fourier Analysis

In Section 3.2 it was noted that the distribution of m.m.f. around the air gap is approximately sinusoidal. This would only be absolutely so if the current were distributed sinusoidally. This is obviously not a practical arrangement; real windings consist of discrete conductors in separate slots, each carrying a uniform current. However, both windings lie around a circular surface, so the distribution of current in them is by nature periodic. As such, it may be represented by a Fourier series, a sum of sine and cosine terms of frequencies an integral multiple of the fundamental.

Fourier analysis is a useful tool for handling functions which are difficult to represent algebraically. For a function to be so represented over an indefinite range it must be periodic, although non-periodic functions may also be represented over a restricted range, if this is defined as the period. Fourier analysis works as a mathematical wave analyser, using the fact that the product of two sinusoids has a mean of zero, unless they are of identical frequency. Thus if any function is equivalent to a sum of sinusoidal terms of differing frequencies, multiplying it by a sinusoid of any given frequency and taking the average of the function over a period will produce a result related to the amplitude of the component of the selected frequency within the original function. Phase differences between sinusoids of different frequency are taken into account by resolving each into sine and cosine terms.

In algebraic form, this is to say that any function $F(\Theta)$ may be represented by a Fourier series such that:

$$F(\Theta) = a_0 + \sum_n a_n \cos n\Theta + \sum_n b_n \sin n\Theta \qquad (3.6)$$

where a_0 is the mean of the function, and a_n and b_n are obtained from:

$$a_n = \frac{1}{\pi} \int_0^{2\pi} F(\Theta) \cos n\Theta \, d\Theta \qquad (3.7)$$

and:

$$b_n = \frac{1}{\pi} \int_0^{2\pi} F(\Theta) \sin n\Theta \, d\Theta \qquad (3.8)$$

The function may then be approximated in a controlled way by truncating the series at any value of n. In this example, if the current distribution function is truncated following n=1, the result is a sinusoidal distribution. A better approximation may be obtained by using more terms.

A further simplification to the representation of the windings may be obtained by considering the currents to have no depth. The result is a current sheet. The magnitudes of the slot currents are represented within the amplitudes of the terms of the series, but for the purpose of field calculations the current sheet is seen as a boundary condition only. As a first approximation, the current sheet is sinusoidally distributed. In the limit it consists of ribbons of current on the surface of the rotor or stator, each ribbon representing the amount of current flowing in the corresponding slot.

3.4.2 The Rotor Winding

As described in Section 3.2, the rotor of a turbogenerator carries a two-pole d.c. winding. This winding covers only about two-thirds of the surface, leaving two solid pole faces. Figure 3.6 shows the cross-section of such a rotor. A group of concentric coil sides span an angle of 2δ. The slot pitch within the wound section is Δ; the slot width 2τ. The actual coils are af', be' and so on, but for the purposes of analysis it is easier to suppose

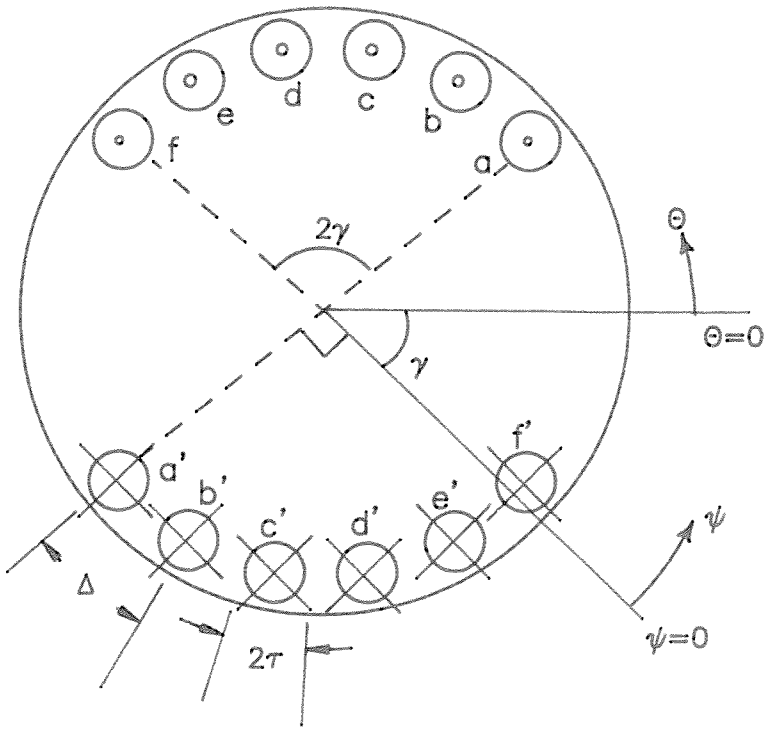

Figure 3.6 The rotor winding

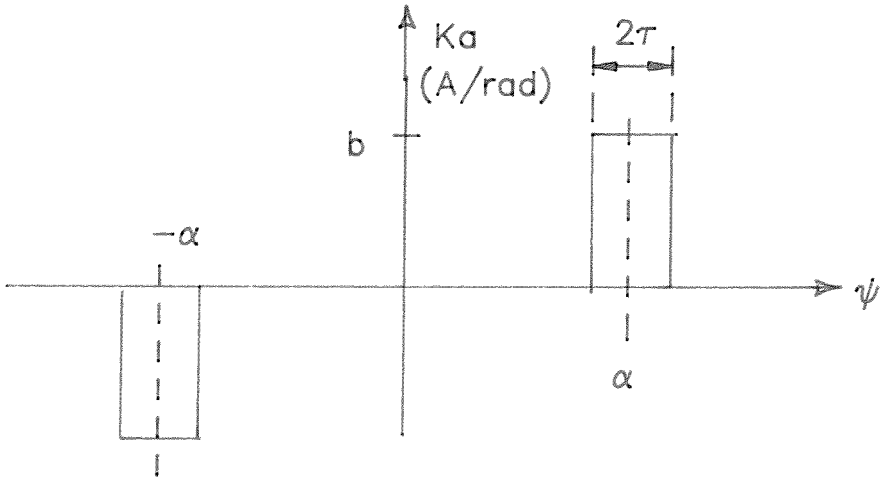

Figure 3.7 Current distribution in a single coil

that the coils are equally pitched: aa',bb' etc.

As all coils are alike, it is possible to derive a Fourier series for one coil, and deduce that for all the other coils the expression is similar, but phase displaced from the first. The expression for the entire current sheet is then the sum of the expressions for the individual coils. Figure 3.7 shows the current distribution in the coil aa', given a general pitch 2α, although in this case $2\alpha=\pi$. It is evident that the mean current distribution is zero, and that the function is an odd one, so that only sine terms exist. The current distribution function K_a in coil aa' may then be represented by the following Fourier series:

$$K_a(\psi) = \sum_m \hat{K}_m \sin m\psi \qquad (3.9)$$

where:

$$\hat{K}_m = \frac{1}{\pi}\int_{-\pi}^{\pi} K_a \sin m\psi \, d\psi \qquad (3.10)$$

The function K_a is equal to b over the width of the slot on one side of the coil, -b on the other side and zero elsewhere; thus this can be substituted explicitly into (3.10):

$$\hat{K}_m = \frac{1}{\pi}\int_{-\alpha-\tau}^{-\alpha+\tau} (-b) \sin m\psi \, d\psi + \frac{1}{\pi}\int_{\alpha-\tau}^{\alpha+\tau} b \sin m\psi \, d\psi \qquad (3.11)$$

The resulting expression can be simplified by means of a trigonometric identity to give:

$$\hat{K}_m = \frac{4b}{m\pi} \sin m\alpha \sin m\tau \qquad (3.12)$$

The area $2\tau b$ is the coil current in amps, $n_t I_R$, where I_R is the rotor current and n_t the number of turns per coil. Thus $\hat{K}_m$ can be related directly to I_R. Furthermore, the coils are fully pitched, so $\alpha=\frac{1}{2}\pi$. This means that the expression is non-zero for odd values of m only, as the sine of an integral multiple of π is zero. For odd m:

$$\sin \tfrac{1}{2}m\pi = (-1)^{\frac{1}{2}(m-1)} \qquad (3.13)$$

Hence:

$$\hat{K}_m = \frac{2n_t I_R}{m\pi\tau} (-1)^{\frac{1}{2}(m-1)} \sin m\tau \qquad (3.14)$$

The Fourier series for coil bb', which is displaced from coil aa' by the slot pitch Δ, is then given by:

$$K_b = \sum_m \hat{K}_m \sin m(\psi-\Delta) \qquad (3.15)$$

For a complete rotor winding, with Q coils, the current distribution function is K_R, where the subscript R denotes a rotor quantity. If the terms Δ, τ and Q are given the same subscript, the resulting expression for K_R is:

$$K_R = \frac{2n_t I_R}{\pi\tau_R} \sum_{q=0}^{Q_R-1} \sum_m \frac{1}{m} (-1)^{\frac{1}{2}(m-1)} \sin m\tau_R \sin m(\psi-q\Delta_R) \qquad (3.16)$$

An equivalent expression can be derived for the summation of the finite series:

$$\sum_{q=0}^{Q_R-1} \sin m(\psi-q\Delta) = \frac{\sin \frac{1}{2}Q_R m\Delta_R}{\sin \frac{1}{2}m\Delta_R} \sin m(\psi-\tfrac{1}{2}(Q_R-1)\Delta_R) \qquad (3.17)$$

It is evident from Figure 3.6 that $2\delta=(Q-1)\Delta$. The axis of coil aa' was quite logically used to derive the current distribution function of that coil in isolation. However, for the function relating to the entire winding it is more reasonable to use the pole axis as reference. This involves substituting $\Theta=\psi-\delta$. Thus the expression for the rotor current sheet is:

$$K_R = \sum_m \hat{K}_{Rm} \sin m\Theta \qquad (3.18)$$

If the current density is to be given in amps per metre, having been derived in amps per radian, the expression must be divided by the rotor radius R_R. Hence the individual peak harmonic current densities are given by:

$$\hat{K}_{Rm} = \frac{2n_t I_R}{m\pi\tau_R R_R} (-1)^{\frac{1}{2}(m-1)} \sin m\tau_R \frac{\sin \frac{1}{2}Q_R m\Delta_R}{\sin \frac{1}{2}m\Delta_R} \qquad (3.19)$$

To represent rotation of the rotor, Θ is replaced by $\Theta-\omega t$ in equation (3.18), and $m\Theta$ by $m(\Theta-\omega t)$.

3.4.3 The Stator Winding

An expression for the stator current sheet may also be built up from the current sheet expressions for individual coils. The starting point for the derivation is identical, and shown equally well by Figures 3.6 and 3.7. However, in Figure 3.6, the group of coil sides must be taken to represent a phase band when applied to a three-phase stator winding. Equation (3.12) is the point at which the derivations of the current sheet expressions for the two windings diverge. First, it is unusual for stator coils to be fully pitched, as discussed in Section 3.2. Thus α is not equal to $\frac{1}{2}\pi$. If c is the ratio of the coil pitch to the pole pitch, $\alpha=\frac{1}{2}\pi c$. Again, the area $2\tau b$ is the coil current in amps. However, whereas the rotor winding has coils made up of several individual turns, the stator of a large machine usually has single turn coils which may carry the terminal current in two or more parallel paths. So while the rotor slot current is a multiple of the terminal excitation current, the stator slot current can be less than or equal to the terminal value. The fact that the winding is, in fact, a double layer winding, is incorporated at a later stage in the derivation when more than one coil is considered. So in the case of a stator coil, $2\tau b=I_s/n_p$, where n_p is the number of parallel paths. I_s is actually an alternating current, but at this stage it is taken to be the peak of this current, the time variation also being accounted for later.

The expression for the amplitude of the nth harmonic component of the current sheet representing one coil of the stator winding is therefore as follows:

$$\hat{K}_{sn} = \frac{2I_s}{n\pi\tau_s n_p} \cdot \sin\tfrac{1}{2}n\pi c \cdot \sin n\tau_s \qquad (3.20)$$

The subscript S denotes stator quantities, and n is used for the nth harmonic order to distinguish stator harmonics from rotor harmonics, denoted by m. With the substitutions described incorporated, the expression for the harmonic current sheets of one phase band of the stator winding, including the return conductors, is similar to equation (3.19). Again, the origin is moved from the axis of the first coil to the axis of the phase band.

It is usual for a turbogenerator stator winding to have 60° phase bands, which means there is an identical group of Q_s coils of the same phase in the other pole, carrying an instantaneous current of opposite sign. Therefore, if a complete phase is to be represented, then sin nΘ must be replaced by sin nΘ-sin n(Θ±π) in the stator equivalent expression to equation (3.18). Another way of writing this angular dependence is sin nΘ(1-cos nπ). Thus for cos nπ=1, which is true for even harmonics, the expression is zero. For odd harmonics the harmonic current sheet amplitude is double that for one phase band.

The complete current sheet is made up of three phases. The 60° groups are separated by 60° in space, and the current in them is also separated by 60° in time, as it is an alternating current of peak I_s. Sin nΘ is now replaced by:

$$\sin n\Theta \cos \omega t + \sin n(\Theta-\pi/3) \cos (\omega t-\pi/3) + \sin n(\Theta-2\pi/3) \cos (\omega t-2\pi/3)$$

There are two important results of this. The first is that all harmonics which are a multiple of three are eliminated. The second is a distinction between harmonics for which n=6k+1 and those for which n=6k-1, k being any integer. For the first set, which includes the fundamental plus the 7th, 13th and so on, the distribution of the current sheet in space and time follows the pattern sin (nΘ-ωt), whilst for the second set (5th, 11th, etc) it follows the pattern

$\sin(n\Theta+\omega t)$. The physical manifestation of this distinction is in the direction of rotation of the harmonics. The 7th, 13th and so on rotate in the same direction as the fundamental stator m.m.f., and hence in the same direction as the mechanical rotation of the rotor. The other harmonics rotate in the opposite direction.

In operation, the peak of the fundamental stator current lags that of the rotor by the torque angle λ. Thus:

$$K_s = \sum_m \hat{K}_{sn} \sin(n\Theta \pm \omega t + \lambda) \qquad (3.21)$$

in which:

$$\hat{K}_{sn} = \frac{6\hat{I}_s}{\pi n_p R_s} \cdot \frac{\sin n\tau_s}{n\tau_s} \cdot \sin \tfrac{1}{2}n\pi c \cdot \frac{\sin \tfrac{1}{2}nQ_s\Delta s}{\sin \tfrac{1}{2}n\Delta s} \qquad (3.22)$$

In Section 3.2, the distribution factor K_d and the chording factor K_c were introduced in a qualitative fashion. They can be identified quantitatively from within equation (3.22). The nth harmonic distribution factor, K_{dn}, is given by:

$$K_{dn} = \frac{\sin \tfrac{1}{2}nQ_s\Delta s}{Q_s \sin \tfrac{1}{2}n\Delta s} \qquad (3.23)$$

Apart from Q_s in the denominator, it is included in the last factor on the right-hand side of equation (3.22). The nth harmonic chording factor is given by:

$$K_{cn} = \sin \tfrac{1}{2}n\pi c \qquad (3.24)$$

The term $\sin n\tau_s/n\tau_s$ appears due to the fact that the slot conductor surface closest to the air gap does not describe an arc of the surface, but a chord. It is often approximated to unity for low values of n. However, the calculations of Section 6.1 proved sufficiently sensitive to small errors in $\hat{K}_{s1}$ for its retention to be essential. For this reason it is helpful to incorporate it into the winding factor, for the purpose of calculating generated voltage (equation 3.5). Hence a simplified expression for $\hat{K}_{sn}$ is as

follows:

$$\hat{K}_{sn} = \frac{6Q_s I_s}{\pi n_p R_s} \cdot K_{wn} \qquad (3.25)$$

3.5 Flux Density and Vector Potential

A pair of current-carrying conductors exert on one another what is generally known as a magnetic force. In fact the origin of this force is electrostatic: it is due to the presence of negatively charged electrons and positive ions in each conductor. There is virtually no actual electrostatic force between the conductors as each has equal numbers of ions and electrons, and is therefore electrostatically neutral. However, when current flows, the electrons are set in motion, and so have a velocity relative to the ions and electrons of the other conductor. The rules of relativity become applicable, with the result that the electrostatic forces are no longer balanced. This manifests itself in the appearance of a magnetic field[24].

Relativistic forces between charges may be the origin of a magnetic field, but they do not provide the most readily applicable model for the purpose of machine calculations. It is more usual to represent the magnetic energy as being stored in a field, in space. This proves very useful in Faraday's law, equation (3.1), for determining the induced e.m.f. in a winding. A mechanism is therefore required to convert the mutual effect of the currents into a field distribution.

Any current flowing is considered to have associated with it an electrokinetic momentum, which exists in space around it and is in the same direction as the current. This quantity, usually designated A, is often known as the vector potential, due to the similarity of the equations describing

it to those involving an electrostatic potential. It is related to the magnetic flux density by the vector relationship **B** = curl **A**.

In a current sheet model of a turbogenerator, the current, therefore the vector potential, is in the axial direction only in all locations well removed from the end region. This simplifies the curl equations considerably. If a cylindrical (r,Θ,z) co-ordinate frame is used, as is sensible in a rotating electrical machine, **B** has only radial and circumferential components, given by:

$$B_r = \frac{1}{r}\frac{\partial A_z}{\partial \Theta} \quad \text{and} \quad B_\theta = -\frac{\partial A_z}{\partial r} \tag{3.26}$$

To obtain an expression for A_z in the air gap, it is necessary first to set up general expressions for A_z (for simplicity referred to as A) in the rotor body and stator core as well as in the air gap, with arbitrary coefficients, the values of which must be determined by consideration of boundary conditions. As both current distributions are sinusoidal, the circumferential distribution of A is also sinusoidal. As no field sources exist within the three regions, as opposed to on their boundaries, Laplace's equation applies[25], and variation of A with radius assumes a polynomial form. As the current distributions may be described by a Fourier series, so may the vector potential distribution. The three expressions for the nth harmonic of vector potential take the form:

Rotor: $A_{1n} = L_{1n} r^n \sin n\Theta$ (3.27a)

Air gap: $A_{2n} = (L_{2n} r^n + M_{2n} r^{-n}) \sin n\Theta$ (3.27b)

Stator: $A_{3n} = (L_{3n} r^n + M_{3n} r^{-n}) \sin n\Theta$ (3.27c)

where L and M are arbitrary coefficients.

There are two relevant boundary conditions to be considered. First, the radial component of flux density,

B_r, is always continuous across a boundary. If only axial A exists, this condition is effectively equivalent to continuity of A across the boundary. Secondly, the difference in the tangential component of magnetic field intensity, H_θ, between sides of a boundary, is equal to the surface current density on that boundary. If no current is present, H_θ is continuous. B_θ and H_θ are related according to equation (3.4).

The system of equations is further simplified if it is assumed that no flux leaks from the core back. This provides a third boundary condition of A=0 at the core back radius.

Expressions for B_r and B_θ can then be derived by differentiation of A. For the nth harmonic flux density these take the form:

$$B_{rn} = \hat{B}_{rRn} \cos n(\Theta-\omega t) + \hat{B}_{rsn} \cos (n\Theta\pm\omega t+\lambda) \qquad (3.28)$$

$$B_{\theta n} = \hat{B}_{\theta Rn} \sin n(\Theta-\omega t) + \hat{B}_{\theta sn} \sin (n\Theta\pm\omega t+\lambda) \qquad (3.29)$$

where $\hat{B}_{rRn}$, $\hat{B}_{rsn}$, $\hat{B}_{\theta Rn}$ and $\hat{B}_{\theta sn}$ are all functions of radius. If, as in this work, the flux density at only one radius (the stator bore) is of interest, then they may be considered constant.

3.6 Magnetic Force on a Current-Carrying Conductor: Electrical Torque Developed by a Machine

The force on a current-carrying conductor in a magnetic field may conveniently be calculated by combining the effects of all other currents in its vicinity into a resultant magnetic field **H**, corresponding to a magnetic flux density **B**. The force is then given by the vector equation:

$$\mathbf{F} = I\mathbf{l} \times \mathbf{B} \qquad (3.30)$$

in the case where a conductor of length l lies in a uniform flux density B[26].

This method may be applied to a current sheet model of an electrical machine to determine the torque developed. As the current is axial, only radial flux will produce a circumferential component of force. The respective torques on the rotor and stator current sheets are equal and opposite. They may be obtained from the current of the sheet of interest and the component of flux density due to the other current sheet. As both current and flux density are sinusoidally distributed, an integration is necessary. The force on the stator current sheet, therefore, is given by:

$$F_s = \int_0^{2\pi R} B_{rR} K_s L \, dx \qquad (3.31)$$

where L is the active length of the machine and x the distance around the stator bore.

To convert to a torque, it is necessary to multiply by the stator bore radius. It is also convenient to use a cylindrical co-ordinate system and integrate with respect to Θ, such that $x=R_s\Theta$. The integral to be evaluated is then:

$$T_e = R_s \int_0^{2\pi} \hat{B}_{rR} \cos(\Theta-\omega t).\hat{K}_s \sin(\Theta-\omega t+\lambda).LR_s \, d\Theta \qquad (3.32)$$

and gives:

$$T_e = \pi \hat{B}_{rR} \hat{K}_s R_s^2 L.\sin\lambda \qquad (3.33)$$

3.7 Magnetic Force on a General Iron Part: The Maxwell Stress System

In ferromagnetic materials, the most common of which is iron, the structure of the atoms is such that they behave as magnetic dipoles, and therefore experience a force from an applied magnetic field. The material becomes magnetised

as all the individual dipoles are forced to align themselves with the applied field. This process occurs in stages[27]. In an unmagnetised piece of iron, groups of atomic dipoles similarly aligned form domains. Under the influence of an applied field, domains orientated more closely in line with the axis of this field grow at the expense of others. Eventually only one domain exists, and the common axis of the atomic dipoles then swings to align itself exactly with the applied field. A magnetised piece of iron therefore has a field of its own, which opposes the field which produced it. The two fields will interact, and there will be a force upon the iron part.

Evaluation of this force is not as simple as evaluation of the force on electric current. It would not be practical to sum all the forces on individual atomic dipoles. Field theory provides the solution, for it is possible to consider the magnetic energy, and the magnetic forces, to be properties of a field in space. If a system is at rest, all the forces are in equilibrium. Their magnitudes may be determined without disturbing the system by means of a thought experiment in which a section of the field is removed. In order to maintain equilibrium, forces must then be applied to the boundaries equivalent to the forces applied by the lost field section before it was removed. By this means, the forces due to the field at the locations corresponding to the section boundaries may be evaluated. If this boundary is drawn so as to enclose totally an iron part, the force on the part may be obtained, without the need to consider the magnetic field within the iron.

An electric or magnetic field may be described by tubes of flux. This is a direct consequence of the inverse square law[28]. A tube of electric flux ends on a surface of electric charge; a tube of magnetic flux on a surface of magnetic pole strength. If the magnetic field is completely solenoidal, the tube has no end; it joins back upon itself.

By definition, the axis of a tube of flux follows the direction of the field. The total field energy contained within a cross-section of the tube is constant along the tube, so that in regions of intense field, the tube has a small diameter; in regions of weak field a much larger diameter. It follows that a section of tube is a convenient element of space to remove from the magnetic field in the thought experiment described above.

In this thought experiment it is useful to think of the tube section as being surrounded by a membrane, which has vanishingly small but finite depth, can be assigned conditions which replicate the effect of the lost tube on surrounding tubes and cancel the field of these other tubes inside itself. At each end, the membrane needs a surface polarity of strength q^*, where $q^*=B$ in accordance with Gauss's theorem, and B is the flux density which existed inside the original element of tube. On the sides of the tube, the membrane needs a surface current density K, where $K=H$ and H is the magnetic field intensity which existed originally.

The forces on the membrane may then be found, as they are equal to the forces on the equivalent surface polarity and surface current. The field intensity and flux density are H and B outside the membrane and zero inside, so the average values within the actual membrane wall are ½H and ½B. One definition of unit magnetic field is unit force upon unit polarity, from which the stress on the ends of the membrane is normal to the surface and of magnitude $\frac{1}{2}Hq^*$. The force on current is given by equation (3.30), adapted to the case of a surface current density K, so that Il becomes K. Again, this stress is normal to the surface, and its magnitude is ½BK. The directions of the forces are such that there is a tension along the tube of flux and a pressure upon the sides. The situation is summarised by Figure 3.8. As $q^*=B$ and $K=H$, the stress on both the sides

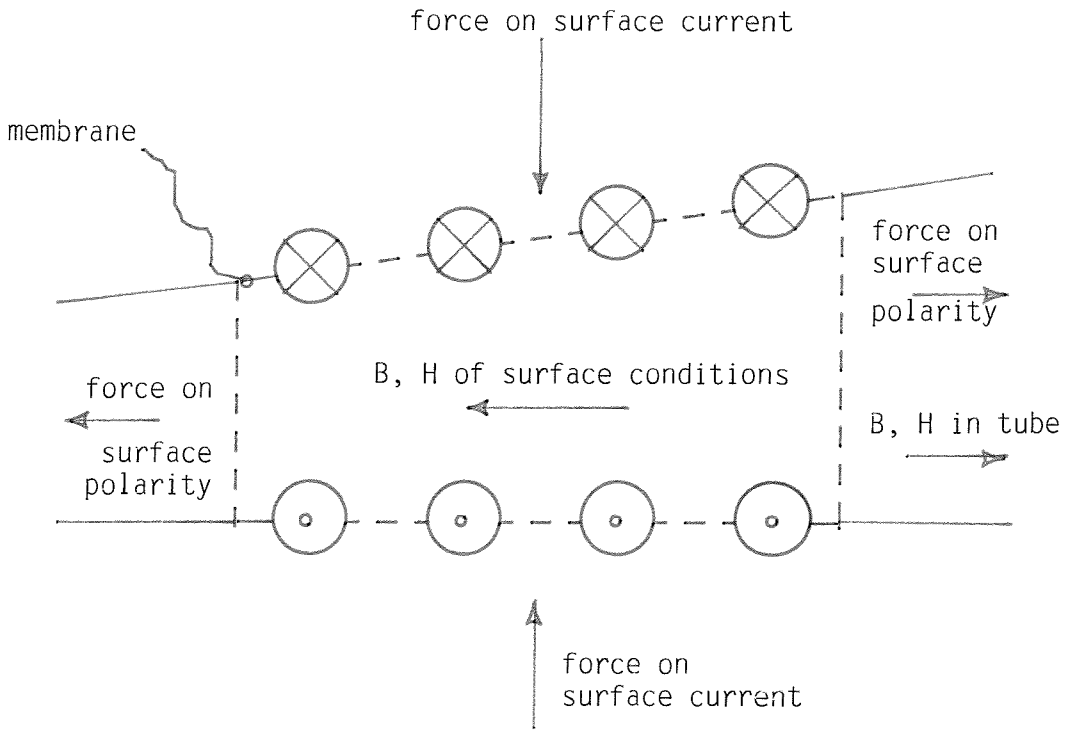

Figure 3.8 Forces on a membrane replacing a tube element of flux

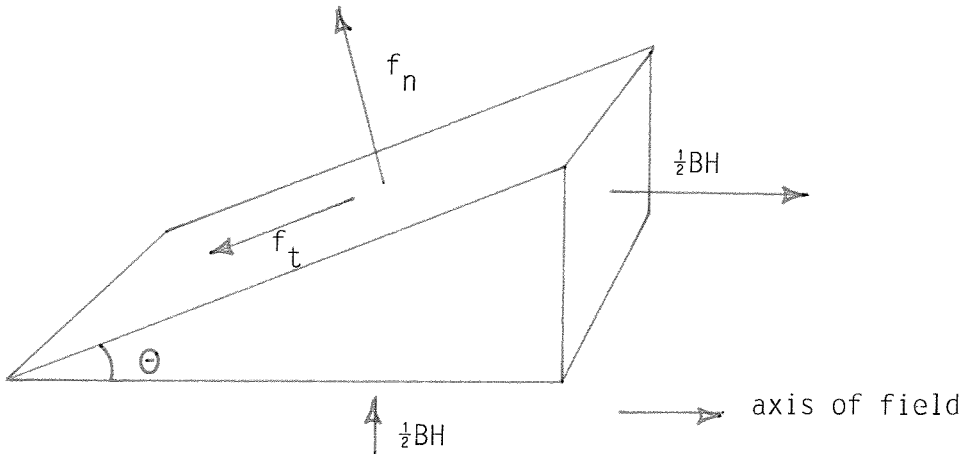

Figure 3.9 A wedge in equilibrium in a magnetic field

and the ends of the membrane, is ½BH. This is also the stress which would have been acting on the lost section of tube before it was removed.

The derivation of the stress on a section of a tube of flux was particularly straightforward because its axis follows that of the field. It is more useful to be able to determine the force on a surface at any orientation to the field axis. Such a force will in general have both normal and tangential components. Expressions for these components can be obtained by considering the equilibrium of a wedge inside a magnetic field[29]. This wedge is shown in Figure 3.9. It is of unit depth, and the hypotenuse of the cross-section is of unit length. Thus the normal and tangential components of the total force on the top are f_n and f_t. If the field axis is perpendicular to the side, as shown, the forces on the side and bottom will be normal to those planes only, and will equal ½BH sin Θ and ½BH cos Θ respectively.

Equating horizontal forces on the wedge gives:

$$\tfrac{1}{2}BH \sin\Theta = f_n \sin\Theta + f_t \cos\Theta \qquad (3.34)$$

and equating vertical forces gives:

$$\tfrac{1}{2}BH \cos\Theta = f_t \sin\Theta - f_n \cos\Theta \qquad (3.35)$$

If equation (3.34) is rearranged to give an expression for f_n in terms of f_t, and this is substituted into equation (3.35), the result is an expression in terms of f_t only. The same may be done for f_n, resulting in the following expressions:

$$f_t = BH \cos\Theta \sin\Theta = B_n H_t \qquad (3.36)$$

$$f_n = \tfrac{1}{2}BH(\sin^2\Theta - \cos^2\Theta) = \tfrac{1}{2}(B_n H_n - B_t H_t) \qquad (3.37)$$

where $B_n = B \sin\Theta$, $H_n = H \sin\Theta$, $B_t = B \cos\Theta$ and $H_t = H \cos\Theta$.

Finally, general expressions for components of force per unit area, or stress, σ, may be derived. In air, these

may be given entirely in terms of B, using the relationship $B=\mu_o H$. Inside iron the equations have no meaning anyway. These general expressions are known as the Maxwell stress equations, because they were first derived by James Clerk Maxwell[30].

When considering the magnetic stresses inside a rotating electrical machine, it is convenient to use a cylindrical co-ordinate system. Then the normal component of Maxwell stress becomes a radial component; the tangential component a circumferential one. The expressions for radial and circumferential Maxwell stress, σ_r and σ_θ, then become:

$$\sigma_r = (B_r^2 - B_\theta^2)/2\mu_o \qquad (3.38)$$

$$\sigma_\theta = B_r B_\theta/\mu_o \qquad (3.39)$$

The integral of the total Maxwell stress over a closed surface gives the total force on a body in a magnetic field. This is a well-demonstrated fact[29][31]. The beauty of the technique is that a geometrically awkward surface may be enveloped by a simple one, and the force on the irregular body calculated accurately.

CHAPTER FOUR

FORCE PATTERNS INSIDE AN ELECTRICAL MACHINE

4.1 Development of a Minimum Model

The simplest possible model of an electrical machine which may be developed for this application consists of infinitely permeable rotor and stator, each with a sinusoidally distributed current sheet on its surface. The model is two-dimensional, so takes no account of end effects. Restriction of the model to two dimensions is considered a reasonable approximation at all stages of modelling, due to the fact that the axial length of a two-pole turbogenerator is high in proportion to its diameter.

Rotor and stator current sheets are described respectively by:

$$K_R = \hat{K}_R \sin(\Theta-\omega t) \tag{4.1}$$

$$K_S = \hat{K}_S \sin(\Theta-\omega t+\lambda) \tag{4.2}$$

The total vector potential A in the air-gap is the sum of the individual vector potentials due to the rotor and stator excitation, and is in the axial direction only.

The vector potential due to the rotor is obtained by considering a current sheet to exist on the rotor surface only. The general equation for A in the air-gap is similar to equation (3.27b).

$$A_R = (L_R r+M_R r^{-1}) \sin(\Theta-\omega t) \tag{4.3}$$

The boundary conditions in this case occur at the stator surface, where:

$$H_{\theta S}-H_{\theta G} = 0 \tag{4.4}$$

and at the rotor surface where:

$$H_{\theta G}-H_{\theta R} = K_R \tag{4.5}$$

The derivation of H from A is given in Section 3.5. As rotor and stator have both been specified as infinitely permeable, $H_{\theta S}$ and $H_{\theta R}$ are zero. From these boundary conditions, explicit expressions for L_R and M_R can be derived.

$$L_R = \frac{\mu_o \hat{K}_R}{(R_S/R_R)^2-1} \tag{4.6}$$

$$M_R = L_R R_S^2 \tag{4.7}$$

Hence an explicit expression for the air-gap vector potential due to the rotor current sheet:

$$A_R = \frac{\mu_o \hat{K}_R}{(R_S/R_R)^2-1} \left(r + \frac{R_S^2}{r}\right) \sin(\Theta-\omega t) \tag{4.8}$$

The derivation of the expression for the air-gap vector potential due to the stator current sheet is similar, and gives:

$$A_S = \frac{\mu_o \hat{K}_S}{1-(R_R/R_S)^2} \left(r + \frac{R_R^2}{r}\right) \sin(\Theta-\omega t+\lambda) \tag{4.9}$$

The flux density is obtained via the curl equations (3.26) given in Section 3.5, and the general expressions for total radial and circumferential flux density are:

$$B_r = L_R\left(1+\frac{R_S^2}{r^2}\right) \cos(\Theta-\omega t) + L_S\left(1+\frac{R_R^2}{r^2}\right) \cos(\Theta-\omega t+\lambda) \tag{4.10}$$

$$B_\theta = L_R\left(\frac{R_S^2}{r^2}-1\right) \sin(\Theta-\omega t) + L_S\left(\frac{R_R^2}{r^2}-1\right) \sin(\Theta-\omega t+\lambda) \tag{4.11}$$

The purpose of this work is to study forces at the stator bore, so $r=R_S$ is substituted into equations (4.10) and (4.11) to give the components of flux density at this radius. The rotor term in B_θ disappears. This is a direct consequence of specifying infinite magnetic permeability: all the flux from the rotor enters the stator surface at right angles.

Taking the specific case of a fixed radius and fundamental current sheets only, the components of B can be expressed in a manner similar to equations (3.28) and (3.29):

$$B_r = \hat{B}_{rR} \cos(\Theta-\omega t) + \hat{B}_{rs} \cos(\Theta-\omega t+\lambda) \quad (4.12)$$

$$B_\theta = \hat{B}_{\theta s} \sin(\Theta-\omega t+\lambda) \quad (4.13)$$

The Maxwell stress distribution at the stator bore can then be calculated from equations (3.38) and (3.39) but it is useful first to rewrite (4.12) and (4.13) in the form:

$$B_r = (\hat{B}_{rR}+\hat{B}_{rs} \cos\lambda) \cos(\Theta-\omega t) - \hat{B}_{rs} \sin\lambda \sin(\Theta-\omega t) \quad (4.14)$$

$$B_\theta = \hat{B}_{\theta s} \sin\lambda \cos(\Theta-\omega t) + \hat{B}_{\theta s} \cos\lambda \sin(\Theta-\omega t) \quad (4.15)$$

Squaring or cross-multiplying these components produces an expression of the form:

$$f_1 \cos^2(\Theta-\omega t) + f_2 \sin^2(\Theta-\omega t) + f_3 \sin(\Theta-\omega t) \cos(\Theta-\omega t) \quad (4.16)$$

where f_1, f_2 and f_3 represent functions of $\hat{B}_{rR}$, $\hat{B}_{rs}$, $\hat{B}_{\theta s}$ and λ. This becomes more physically meaningful when the following simple trigonometric identities are considered:

$$\cos^2\Theta = \tfrac{1}{2}(1 + \cos 2\Theta) \quad (4.17)$$

$$\sin^2\Theta = \tfrac{1}{2}(1 - \cos 2\Theta) \quad (4.18)$$

$$\cos\Theta \sin\Theta = \tfrac{1}{2}\sin 2\Theta \quad (4.19)$$

It is now clear that each Maxwell stress equation in the simple, fundamental-only, case, is composed of two terms. The constant term in the circumferential stress expression is the origin of the machine torque. The constant term in the radial stress expression is the net radial magnetic pull acting to compress the stator annulus towards the rotor. Both double-frequency terms contribute towards the ovalising of the stator core.

Implementation of this model by a computer program

involves first expressing the flux density expressions in the manner of equations (4.14) and (4.15), separated into terms in cos $(\Theta-\omega t)$ and sin $(\Theta-\omega t)$. The sine and cosine coefficients are then converted into an overall magnitude by taking the square root of the sum of the squares. The phase angle of the expression is found using a four-quadrant inverse tangent subroutine. This is necessary because the Fortran ATAN function only returns values between $-\pi/2$ and $+\pi/2$. The result is a flux density expression of the following form for each of the components:

$$B = \hat{B} \cos (\Theta-\omega t-\alpha) \qquad (4.20)$$

Ultimately the stress expressions too are expressed in a similar manner. The reference angle for all such expressions is the axis of the rotor m.m.f. at time t=0. Manipulation of the flux expressions shows that the sine component of the radial stress is:

$$(\hat{B}_r^2 \sin 2\alpha_r - \hat{B}_\theta^2 \sin 2\alpha_\theta)/4\mu_o \qquad (4.21)$$

and the cosine component is:

$$(\hat{B}_r^2 \cos 2\alpha_r - \hat{B}_\theta^2 \cos 2\alpha_\theta)/4\mu_o \qquad (4.22)$$

Whilst for the circumferential stress the sine component is:

$$\hat{B}_r \hat{B}_\theta \sin (\alpha_r+\alpha_\theta)/2\mu_o \qquad (4.23)$$

and the cosine component:

$$\hat{B}_r \hat{B}_\theta \cos (\alpha_r+\alpha_\theta)/2\mu_o \qquad (4.24)$$

The final expressions are of the form:

$$\sigma = \hat{\sigma} \cos (2(\Theta-\omega t)-\beta) \qquad (4.25)$$

The angle β produced by the subroutine is a double-frequency angle, so if a spatial stress distribution around the stator bore is to be considered this angle must be divided by two.

The angle between the peaks of the two stress distributions is the difference between β_r and β_θ. This is also a double-frequency angle. Furthermore, both β_r and β_θ

are lag angles, so to determine the angle by which the circumferential stress wave lags the radial stress wave it is necessary to subtract β_r from β_θ.

4.2 Higher Current Sheet Harmonics

A refinement of the model described in the Section 4.1 can be devised by including the higher harmonics of the current sheets. This facilitates a more accurate representation of any individual machine, for the higher harmonics contain information relating to the slotting of the rotor and stator and to the chording and phase-banding of the stator.

If the model is further assumed to have finite permeability, the rotor term in the circumferential flux expression at the stator surface reappears in equation (4.13), giving the following expressions for the flux density components at the stator bore:

$$B_r = \sum_m \hat{B}_{rRm} \cos m(\Theta-\omega t) + \sum_n \hat{B}_{rSn} \cos (n\Theta\pm\omega t+\lambda) \qquad (4.26)$$

$$B_r = \sum_m \hat{B}_{\theta Rm} \sin m(\Theta-\omega t) + \sum_n \hat{B}_{\theta Sn} \sin (n\Theta\pm\omega t+\lambda) \qquad (4.27)$$

Expressions for the magnitudes of the higher harmonic current sheets were derived in Section 3.2, and the associated expressions for harmonics of vector potential and flux density will be derived in Section 4.3.

Only the double-frequency vibration is of interest in this work. It is important, however, not to neglect higher harmonics. The Maxwell stress expressions, with higher current sheet harmonics included, are products of series. The fundamental components of each series combine to form the double frequency stress as already shown; but so also do certain combinations of higher harmonics.

To demonstrate this effect it is most illustrative to examine, term by term, the products which arise on formation of B_r^2 and B_θ^2 (as in the radial Maxwell stress), and of $B_r B_\theta$ (as in the circumferential Maxwell stress).

(i) $(\sum_m \hat{B}_{rRm} \cos m(\Theta-\omega t))^2$

For any two rotor harmonics m_1 and m_2, the relevant term of this series may be written as:

$$\tfrac{1}{2}\hat{B}_{rRm1}\hat{B}_{rRm2} [\cos (m_1+m_2)(\Theta-\omega t) + \cos (m_1-m_2)(\Theta-\omega t)] \quad (4.28)$$

By inspection, a double-frequency component is produced by combination of fundamentals, but also by combination of every pair of higher harmonics for which $m_1-m_2=2$.

(ii) $(\sum_n \hat{B}_{rSn} \cos (n\Theta\pm\omega t+\lambda))^2$

The individual terms take a different form depending on whether the stator harmonics to be combined, n_1 and n_2, are of like or unlike rotation.

For harmonics of like rotation (including like harmonics) it becomes:

$$\tfrac{1}{2}\hat{B}_{rSn1}\hat{B}_{rSn2} [\cos \{(n_1+n_2)\Theta\pm2\omega t+2\lambda\} + \cos (n_1-n_2)\Theta] \quad (4.29)$$

whereas for harmonics of unlike rotation it becomes:

$$\tfrac{1}{2}\hat{B}_{rSn1}\hat{B}_{rSn2} [\cos \{(n_1+n_2)\Theta+2\lambda\} + \cos \{(n_1-n_2)\Theta\pm2\omega t\}] \quad (4.30)$$

The first expression only produces a double-frequency component for $n_1=n_2=1$. The second produces one from combinations of 5th and 7th harmonics, also 11th and 13th and so on. Both expressions contain a term which is frequency-independent. This term can be interpreted as a series of standing waves of radial stress around the stator bore, of harmonic order 6k (where k is any integer), which are an intrinsic consequence of a three-phase winding.

(iii) $2 \sum_{m} \hat{B}_{rRm} \cos m(\Theta-\omega t) \sum_{n} \hat{B}_{rSn} \cos (m\Theta \pm \omega t+\lambda)$

Each term of this product may be expressed as:

$$\hat{B}_{rRn}\hat{B}_{rSn} [\cos \{(m+n)\Theta-(m\mp1)\omega t+\lambda\} + \cos \{(n-m)\Theta+(m\pm1)\omega t+\lambda\}] \quad (4.31)$$

The first term within the expression produces a double-frequency component for n=m=1; the second term for n=1 and m=3. No other double-frequency components are produced by this series product.

The three series products arising from B_θ^2 are similar to those arising from B_r^2 and need no further discussion.

The four series products which make up the complete expression for circumferential Maxwell stress are different from those which make up the radial expression in two ways. First, they are all products of a sine series and a cosine series, as opposed to two sine series or two cosine series. Secondly, each term of each series is formed of the product of a radial flux density term and a circumferential flux density term. This means that each individual stress term is unique. In the radial stress expression this is not so. For instance, in (i), setting $m_1=j$ and $m_2=k$ gives the same result as $m_1=k$ and $m_2=j$.

The product of the rotor radial flux series and the rotor circumferential flux series produces a double-frequency component for $m_1-m_2=2$, in a similar fashion to (i) of the radial Maxwell stress. Likewise, the product of the stator radial and stator circumferential flux series produces a double-frequency component for each pair of harmonics of order 6k±1. As in (ii) of the radial expressions, there also exists a frequency-independent term. This produces a series of standing waves of circumferential stress of harmonic order 6k. This effect is better known than the corresponding radial one due to the problems it

causes with torque ripple in induction motors[32].

The remaining two products are the equivalent of (iii) in the radial stress expression. They produce double-frequency components from the combination of fundamentals and the combination of stator fundamental with rotor third harmonic flux density only.

The expressions discussed above give a good qualitative feel for the origins of double-frequency stress on the stator bore. However, it is not easy to deduce immediately the magnitudes of the individual effects, as they are in many cases phase displaced from one another in space by λ or 2λ. Furthermore, the relative magnitudes of the harmonic flux densities are heavily dependent on the geometry of the individual machine. Indeed, winding configurations are often designed to suppress a particular harmonic.

In a general analysis, therefore, it is of limited benefit to assess the relative advantages of various harmonic terms. It is more profitable to investigate the effect of higher harmonics empirically for each individual machine, using a computer model capable of handling them. This is done later on in the work. Meanwhile, a broad statement may be made to the effect that double-frequency stress levels produced by combinations of higher harmonic fluxes are likely to fall off sharply with increased order of the harmonics, as the harmonic current sheet expression (hence the flux density) includes a factor of $1/m$. The terms of the stress expression, therefore, include a factor of $1/m_1 m_2$.

4.3 Practical Implementation of a Model Including Harmonics

The minimum model of Section 4.1 started with sheets of current and resulted in sheets of stress. The analysis

proceded from one sinusoid to the next by expressing each in the standard form M cos $(\Theta-\omega t-\alpha)$. The constants M and α were obtained from an expression originally derived by hand, then implemented as explicit algebraic statements by the computer.

Once higher harmonics are taken into account, the simple sinusoids of the minimum model becomes series of sinusoids. The volume of trigonometric manipulation necessary to handle the analysis becomes very great, and it is advantageous to change to a numerical scheme.

The scheme adopted involves first setting up arrays to hold as elements the individual magnitudes of the harmonics of flux density. Four arrays are needed to cover rotor and stator, radial and circumferential flux density. As before, the magnitudes of flux density are obtained by consideration of the magnetic vector potential in the air-gap at a radius equal to the stator bore.

The expressions for harmonic components of A are more complicated than the fundamental expressions given in equations (4.8) and (4.9). Each harmonic of air-gap vector potential due to the rotor current sheet is described by:

$$A_{Rm} = \frac{\mu_o R_R^{1-m} \hat{K}_{Rm}}{m[(R_S/R_R)^{2m}-1]} \left(r^m + \frac{R_S^{2m}}{r^m}\right) \sin m(\Theta-\omega t) \qquad (4.32)$$

whilst that due to the stator current sheet is given by:

$$A_{Sn} = \frac{\mu_o R_S^{1-n} \hat{K}_{Sn}}{n[1-(R_R/R_S)^{2n}]} \left(r^n + \frac{R_R^{2n}}{r^n}\right) \sin (n\Theta\pm\omega t+\lambda) \qquad (4.33)$$

As in the fundamental case, application of the curl equations (3.26) produces expressions for the flux density. Considering the special case of flux density at the stator bore, the expressions for the pth harmonic are:

$$B_{rp} = 2L_{Rp}R_S^{p-1}p \cos p(\Theta-\omega t) + L_{Sp}[R_S^{p-1}+(R_R^{2p}/R_S^{p+1})]\, p \cos (p\Theta\pm\omega t+\lambda) \qquad (4.34)$$

$$B_{\theta p} = pL_{sp}[(R_R^{2p}/R_s^{p+1})-R_s^{p-1}] \sin(p\Theta \pm \omega t+\lambda) \qquad (4.35)$$

where the harmonic L coefficients are defined similarly to the fundamental ones in equations (3.27).

For any snapshot in time, $t=t_0$, the radial and circumferential flux densities at any point on the stator bore of the model can be calculated. Each harmonic flux density magnitude is recalled in turn, multiplied by the appropriate trigonometric function of space, the result being added to a cumulative total. Such point magnitudes of flux density in the model can then be converted directly to point stresses by application of equations (3.38) and (3.39).

The result of such a scheme is a series of point stresses at intervals around the stator bore for a particular snapshot in time. This form of output is not particularly useful for two reasons. First, it is difficult to interpret in relation to stator ovalising. Secondly, it has little physical meaning. Equations (3.38) and (3.39) may represent the stress distribution on a smooth stator carrying a surface current sheet. However, a real machine has separate conductors, each carrying uniform current, embedded in slots and separated by teeth. A model is only of use inasmuch as it produces results which relate to the system being modelled. Results intrinsic to the model are of academic interest only.

4.4 The Idea of a Tooth Force

The integral of Maxwell stress over a closed surface correctly describes the total force on a body contained within that surface, as noted in Section 3.7. The only strictly valid application to an electrical machine, therefore, occurs when the boundary is drawn to circumnavigate the air-gap completely. The only results

which may be obtained with total confidence are the machine torque and the net radial magnetic pull between rotor and stator.

As noted in Section 4.3, the distribution of Maxwell stress calculated from the simple model clearly cannot be expected to simulate the real distribution of stress at the stator bore, due to the inhomogenous nature of the stator bore surface and the lack of uniqueness associated with the stress. However, some sort of force distribution must be defined if core ovalising is to be investigated. Two factors combine to suggest which form this distribution should take. The first is the fact that when a current-carrying conductor is surrounded by magnetic material and placed in a magnetic field, most of the force which would have acted upon the conductor is transferred to the magnetic material[33]. This is the situation pertaining in an electrical machine, where most of the force acts upon the teeth. The second is a result of more recent work[34] which showed that the force on a tooth in an electrical machine is concentrated at its tip.

Thus the concept of a "tooth force" is derived. The tooth force is the integral of the Maxwell stress, be it radial or circumferential, over a slot pitch, centred on a tooth. The value of this integral is assigned to a point force acting at the centre of the tooth tip.*

There is also a practical advantage to such an arrangement. An important part of this work is the structural analysis of the stator core using the finite-element package ANSYS. This package may be fed force data only in terms of point forces or surface pressures. If it is given data in the form of a pressure, it converts this to point force. For greatest control of the problem to be analysed, which of course is never quite the same as the problem it is set up to depict, point forces clearly need to

* It must be stressed that the use of smooth air-gap surfaces in the model may lead to some degree of fundamental error in the evaluation of this tooth force. The level of this error has not been quantified but would merit further investigation.

be specified directly.

In the minimum model of Section 4.1 the tooth force, in common with all other features of this model, may be calculated by trigonometry. The peak of the tooth force occurs at the same time as the peak of the stress wave. The magnitude of this peak tooth force is given by:

$$F = R_s \int_{\frac{1}{2}\Delta s}^{\frac{1}{2}\Delta s} \hat{\sigma} \cos 2\Theta \, d\Theta \qquad (4.36)$$

or, more explicitly,

$$F = R_s \hat{\sigma} \sin \Delta s \qquad (4.37)$$

The numerical model described in Section 4.3 demands a rather more involved treatment. Including stator current sheet harmonics in the model corresponds to taking into account chording and phase-banding in the real stator winding. The force on each stator tooth will depend on where it lies within a phase band. Therefore it is not possible to define a single tooth force magnitude. Within a phase band each tooth will experience a different force, although the pattern repeats in subsequent phase bands. The force on each tooth will not only have a different harmonic content, but it will have a different double-frequency fundamental too, due to the combinations of harmonics discussed in Section 4.2.

The reference angle $\Theta=0$ is defined in Section 3.2 as the axis of a stator phase band. Teeth are then numbered in anti-clockwise order, starting from this reference. The location of tooth number 1 depends on whether the number of slots in a phase band is odd or even. When it is odd, $\Theta=0$ falls at a slot centre; when even at a tooth centre. In both cases it is the first complete tooth which receives the number 1.

Implementation of the scheme starts as before by

storage of the harmonic flux density magnitudes in an array. The remainder of the calculation is enclosed in a loop, the loop variable being the tooth number. Thus any particular tooth, or any series of adjacent teeth, may be examined. The tooth force, by definition, is fixed in space, and its variation in time is of interest. Whereas in Section 4.3 it was necessary to specify a snapshot in time in order to produce a one-dimensional data set, the new analysis generates time variations at a small and meaningfully defined set of snapshots in space.

The scheme produces two results of interest. The first is the variation of the force on a particular tooth with time. The second, and more important, result is the time fundamental of the double-frequency oscillating force on the tooth. It can be expressed in terms of an amplitude and a phase angle, and as such corresponds to the result of the minimum model, but in addition incorporates the effect of combinations of higher harmonics.

In both cases it is necessary to calculate the instantaneous tooth force at frequent intervals over one cycle, which is half a power cycle so covers values of ωt from $\omega t=0°$ to $\omega t=180°$. Taking ωt in increments of $1°$ produces a tooth force output in increments of $2°$, sufficient to give a smooth variation.

At each point in time, the flux density is required at several points across a slot pitch. Thus a two-dimensional array is set up to hold both radial and circumferential values obtained by summing the contributions of each separate harmonic as before. It is very important when calculating the point values of flux density to specify the correct location of the relevant tooth in space. The angles of the points must be offset by a number of slot pitches equal to the tooth number minus one. An extra half slot pitch must also be added where the number of coils in a

phase band is even.

The contents of the flux array are then used to calculate radial and circumferential instantaneous values of Maxwell stress at each of the points. The results are stored in a stress array of identical dimensions. These stress values are integrated numerically to produce the radial and circumferential components of tooth force at the relevant instant in time. Simpson's formula is used for the integration, which is essentially a simple quadratic approximation to the space stress function[35]. Each instantaneous tooth force is stored as an element of an array, there being a separate array for each component of force, in order that they may be named in a mnemonic fashion.

All that is necessary to show the variation of tooth force with time is to plot the values of instantaneous tooth force over one cycle. To determine the tooth force fundamental in terms of amplitude and phase angle it is necessary to perform a Fourier analysis on the time functions stored numerically in the tooth force arrays. Fourier analysis was discussed in Section 3.4.1. In the present analysis each instantaneous tooth force is multiplied by the corresponding point on a double-frequency sine or cosine wave. The resulting function is integrated numerically, again using Simpson's formula. Four coefficients result: sine and cosine for radial and circumferential tooth force.

The magnitude of each component of tooth force is found by taking the square root of the sum of the squares of the sine and cosine coefficients. The phase angle is found with the four quadrant inverse tangent subroutine described in Section 4.1. The phase angle for any tooth force will contain a component relating to the location of that tooth around the stator bore. The phase difference between radial

and circumferential tooth forces, however, relates directly to that calculated in the minimum model. The difference in this case is obtained by subtraction of the phase angle of the circumferential force from that of the radial force. Unlike the angles of the other model, the angles produced here are lead angles. This is due to the fact that the argument of the trigonometric functions is $\Theta-\omega t$, so that the entire sine series produced by Fourier analysis is preceded by a minus sign.

4.5 Initial Tooth Force Results

The first results were graphs of the variation of tooth force with time. They were produced on a Calcomp plotter which, together with its supporting software, is available for use with Southampton University's IBM 3090 computer. At this time, the only machine data available related to the 500MW Ferrybridge generator. The only completely specified load conditions given (i.e. including rotor current) were for open circuit and full rated load, when the generator operates at a power factor of 0.85 lag.

Figure 4.1 shows the time variation of force on tooth 1 when the machine is on open circuit. Rather more than a complete cycle is shown to give a better picture of the waveform. There is no circumferential force, as this is only produced by the interaction of rotor and stator currents. The radial force waveform has a flat top which corresponds to the passage of the rotor pole face over the tooth. This is when the magnetic pull on the stator iron is greatest.

The open circuit condition on tooth 1 was used as a test condition for tuning the numerical implementation of the model. The spacing of the points in time at 56μs (1° of the power cycle) was seen at once to be satisfactory from

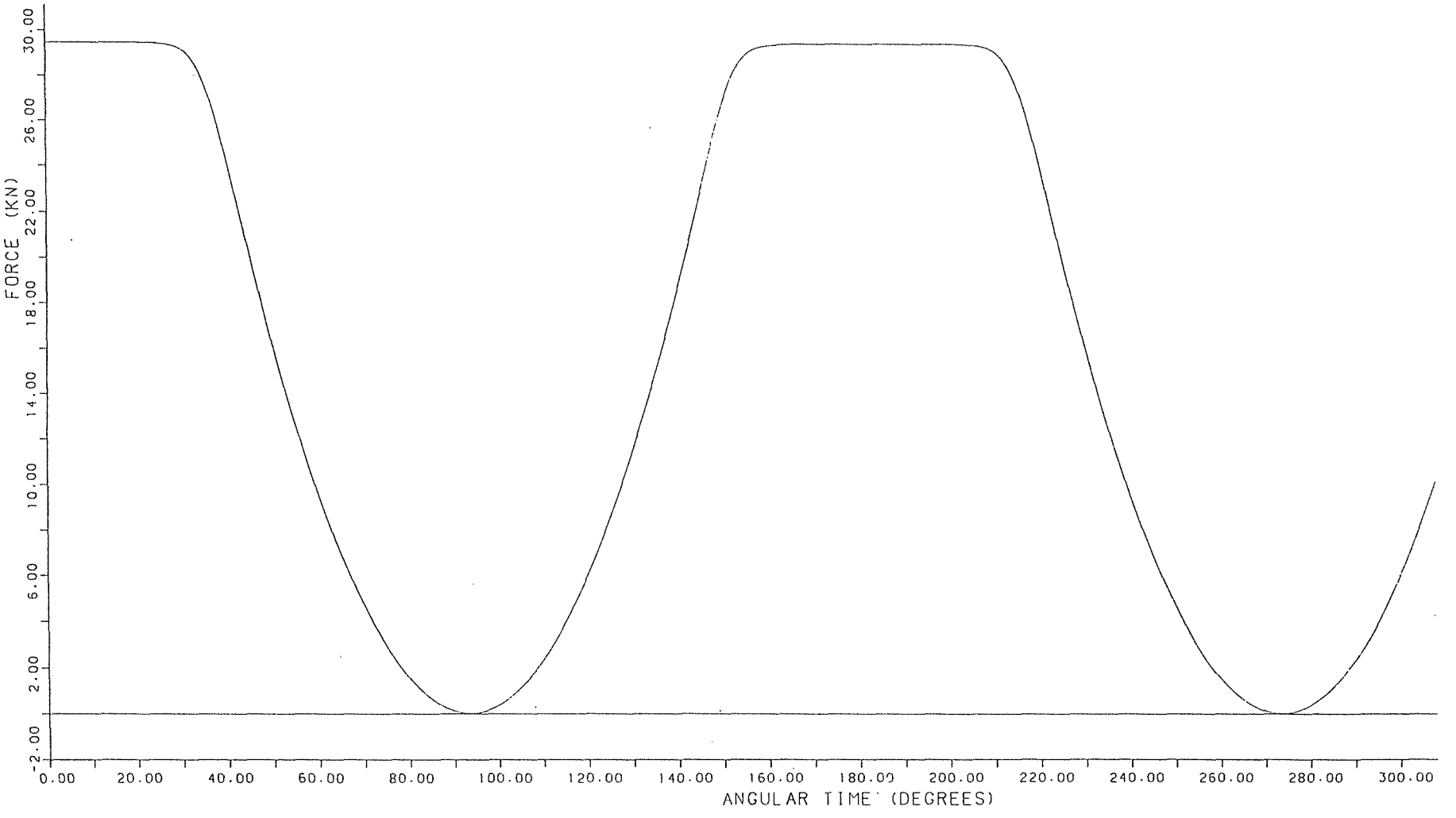

Figure 4.1 Time variation of force on tooth 1 of the Ferrybridge machine on open circuit

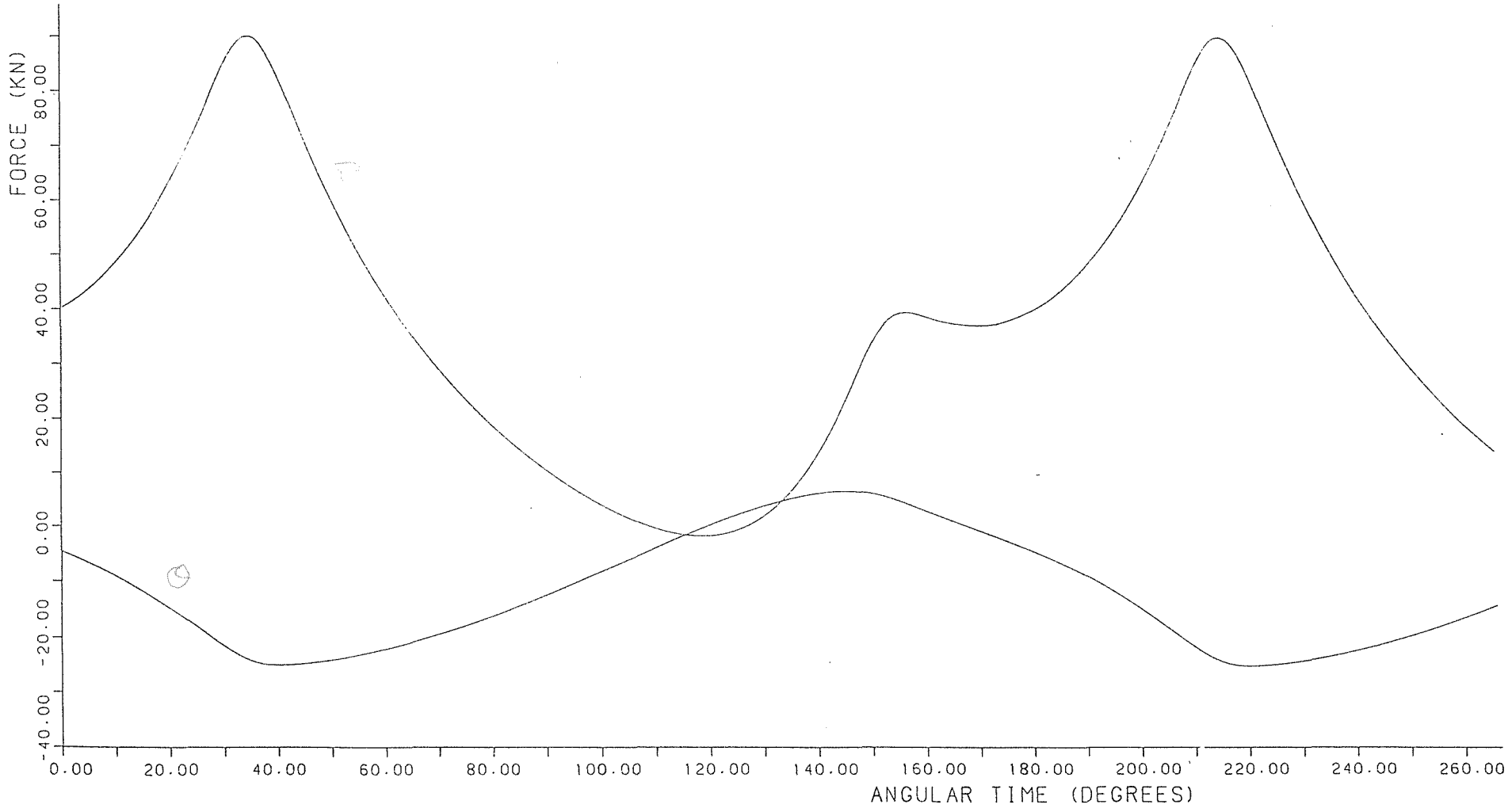

Figure 4.2 Time variation of force on tooth 1 of the Ferrybridge machine on full rated load

the smooth shape of the curve. The Simpson integration of stress over the slot pitch was tried using 5, 7 and 9 points. There was no apparent advantage to using 9, so 7 points were used in all future analyses. The final parameter to be tuned was the maximum number of higher harmonics in the current sheets. The graph shown uses rotor current sheet harmonics up to the 29th. Using fewer produces discernible ripple on the flat tops. This sets the size to be defined for the arrays of harmonic flux density magnitudes discussed in Section 4.3 and 4.4.

Figure 4.2 shows the time variation of force on tooth 1 when the machine is on full rated load. Input to the program consists of the two currents, from which the current sheet magnitudes are calculated, and the torque angle between the peaks of the respective current sheets. The two currents were available as data items. The torque angle had to be calculated from the m.m.f. phasor diagram described in conjunction with Figure 3.5. The calculation of the fundamental m.m.f. phasors F_f and F_a from the current sheets is quite straightforward. Figure 3.2 shows that the peak m.m.f. due to the rotor is equal to the sum of the coil-side currents in one pole. If the current is represented as a surface density of sinusoidal distribution, the integral of a quarter-cycle gives the peak m.m.f. Hence the peak fundamental m.m.f. due to the rotor is $\hat{K}_{R1}R_R$ and that of the stator is similarly $\hat{K}_{S1}R_S$.

The shape of the tooth force waveforms shows that the tooth force includes a considerable harmonic content when the machine is on high load. The signs of the mean values (positive for radial force; negative for circumferential) might appear to be wrong, but are actually correct due to the fact that the Maxwell stress system uses the opposite sign convention to the usual cylindrical co-ordinate frame. Only the double power freqency fundamental of the tooth force wave is of real interest in this work. It is also

likely that the higher harmonic forces are largely damped out by the mass of the stator iron.

Whilst Figure 4.2 is illustrative in a qualitative way, the calculation which produced it may not be a valid representation of the machine in question. The model used is a considerable simplification of the true situation, specifying as it does infinitely permeable iron. The values of current used as data are taken from real life, where they contain components to overcome leakage and magnetic saturation. Further checks are necessary to gauge the magnitude of this obvious incompatibility.

An important quantity is the terminal voltage. A fair assessment of the model may reasonably be made by investigating how closely it is satisfied. In Section 3.2, the r.m.s. phase voltage for a two-pole machine was shown to be:

$$V_{ph} = \sqrt{2}\pi f z L R_s K_w \hat{B}_r \qquad (3.5)$$

As the winding of the generator is connected in star, the terminal voltage is a factor of $\sqrt{3}$ higher. The only factor in equation (3.5) not known from data is the peak fundamental radial air-gap flux density, $\hat{B}_r$. The value to be used in this test is the one calculated by the model. This appears in an interim calculation, and it was a simple matter to print it out. The value obtained was 1.485T.

At once, this looks unrealistically high. Typical working flux densities in electrical machines are 1.8-2.0T peak for teeth[36]. The teeth take up approximately half the surface area of the stator bore and provide a path for most of the flux. By comparison, flux would enter a smooth stator at all points equally. Thus the peak air-gap flux density that might be expected in the model should be about half of this quoted value, i.e. about 1T.

The terminal voltage calculation procedes as follows:

$V_T = \sqrt{3} \times \sqrt{2} \times \pi \times 50 \times 18 \times 5.96 \times 0.654 \times 0.9154 \times 1.485$

$= 36.7kV$

The rated terminal voltage of the Ferrybridge generator is 22kV, so this value is clearly far too high. The conclusion to be drawn is that it is not sensible to develop a simple model and expect all data items drawn from the real system to produce consistent results. If a simple model is to be used, it is necessary to restrict the degrees of freedom of the model in a controlled way, such that whilst certain quantities may assume the values they take in the system to be modelled, other quantities must be assigned fictitious values in order that the model may be self-consistent. Such an approach is developed in Chapter Six.

CHAPTER FIVE

MECHANICAL BEHAVIOUR OF AN ISOLATED STATOR CORE

5.1 Introduction: The Isolated Core

The stator core of a large turbogenerator can by no means be considered to exist in isolation. It is attached to the outer casing via an inner frame, which is itself attached to a heavy reinforced concrete structure. The complete unit includes the turbine and is mounted on the foundations of a building which contains many other structures. The mechanical coupling amongst this multiplicity of structures is extremely complex. There are many opportunities both for damping and for the excitation of resonances. It is beyond the scope of this work to model the structural surroundings of the machine; although it is necessary to recognise that their effect on the amplitude of core-back double-frequency vibration may be considerable.

There are also independent good reasons for modelling the mechanical behaviour of the core in isolation. It is a relatively simple analysis, thus leaves more scope for thorough investigation of the effect of various parameters. It isolates the effect to be investigated, which is a great advantage as this work is principally the study of this one effect. The general validity of this approach is investigated in Chapter Seven, when the vibration results of the model are compared with test measurements on several machines.

5.2 The ANSYS Package

5.2.1 General Strengths and Limitations

ANSYS is a powerful finite-element package commercially available from Swanson Analysis Systems of the USA. It includes an extensive graphics capability in both pre- and post-processors. It has a large library of 1-, 2- and 3-dimensional elements to aid the modelling of a wide range of structures. It is capable of an assortment of different types of analysis: static, harmonic, transient, buckling, thermal and mode frequency. The analyses it performs are essentially unitless: the manual states that it will operate with "any self-consistent system of units". It is thus ideal for use with the SI unit system, which is self-consistent by design. Facilities for user-defined constant scaling factors are available to enable meaningful data to be produced in other systems of units.

The genuine limitations of ANSYS are few, but three distinct sources of difficulty within the package affected this work.

The first was the documentation. This is of necessity extensive for such a powerful package. It is structured for completeness, grouping similar commands together in lengthy sub-sections and including considerable in-depth theory of the implementation of each type of analysis. This leaves no easily accessible route to the relevant commands for the user interested only in a small subset of the package's capabilities and possessing only limited familiarity with the terminology of finite-element theory. Constant cross-referencing of manuals is necessary. Often only an on-line test can produce the information really sought.

The second difficulty concerned the wavefront of the analysis processor. The equations to be solved in the

course of a finite-element analysis are stored in matrix form. Connections between elements in the mesh appear as off-diagonal elements in the matrix. The wavefront is a measure of how far off the leading diagonal the furthest non-zero off-diagonal elements are to be found. As long as the wavefront is small enough, the size of the matrix itself may be indefinitely large. The number of dimensions to an element affects the wavefront; one-dimensional elements being most economical and three-dimensional elements most extravagant. In a harmonic analysis, each item of data is held as a real and an imaginary part, thus reducing the maximum available wavefront by a factor of two. In a mode frequency analysis, it is necessary to specify the number of master degrees of freedom in the structure. This directly determines the wavefront. However the single most important factor in determining the wavefront of a given problem is the numbering of the nodes within the mesh, which needs considerable skill and insight on the part of the operator.

The wavefront size available with ANSYS is a customer option. The greater the wavefront, the greater the cost of the package. It is usual for universities to have a particularly cheap "educational" version with a maximum wavefront capability of about 200. The Southampton package is an enhanced version of the standard educational package, having a wavefront of 500 (reduced to 250 for harmonic analyses). This proved completely adequate, but only when problem geometries were defined with great care.

The third difficulty stemmed from the lack of attention to front-end detail which unduly inconveniences the user with a circular or cylindrical problem in contrast to the user with a rectangular problem. Entry of problem geometry is allowed in either Cartesian or polar co-ordinates, with a useful discontinuity option for the polar user, who may chose whether the range of angle is from -180° to +180° or from 0° to 360°. However, load data entry (force, imposed

displacements and so on) is restricted to Cartesian co-ordinate form only. Furthermore, when complex loading is specified for a harmonic analysis, this must not only be in rectangular co-ordinates, but also in real and imaginary parts, instead of the often far more natural form of amplitude and phase angle. The output from a harmonic analysis can only be supplied in Cartesian co-ordinates, but there is an option which allows it to be printed out in amplitude and phase angle form.

The practical consequence of the third difficulty was the need to produce a fair quantity of auxiliary software to convert force data into a form acceptible to the ANSYS pre-processor, and to convert output into a form which could be readily interpreted. Fortunately the latter was mainly avoided due to the correspondence between rectangular and polar co-ordinate systems on the 0°, 90°, 180° and 270° planes of a circular cross-section; although for some later tests, in particular those concerned with fixing of the core, it became a tedious necessity.

5.2.2 Initial Operating Tests and Decisions

A series of initial operating tests was necessary for two reasons. Often a simple test resulted in a considerable saving in time over that which would have been required to locate the necessary information in the manuals. Indeed, certain commands appeared to be absent from the documentation altogether. The second, and more important, reason was to obtain an assessment of the complexity of problem which could be solved by the package. The results of such an assessment would then provide guidelines regarding how many features of the stator core could be included in the mechanical model: for instance, whether windings and slot wedges could be included, or, at the other extreme, whether a simple annulus would have to suffice.

The harmonic and modal analyses only are of interest here. The harmonic analysis is most important, because oscillating forces are to be considered. The role of the modal analysis is in assessing the mechanical validity of the models analysed by ANSYS. Such models of necessity give a highly simplified representation of the structure. In particular, the connectivities between elements cannot allow for slip when, for instance, a slot conductor is represented adjacent to the slot wall. The four-node mode resonant frequencies of stators have been found to lie between 160Hz and 200Hz for the largest machines; higher for smaller machines[9]. Given that a completely faithful model of the stator core cross-section is an impossibility, tailoring the simple model towards a resonant frequency which corresponds to that of the actual structure is a more effective means of producing global mechanical equivalence than modelling faithfully those features which are included specifically in the model.

In theory, a static analysis should be sufficient for the ovalising problem, as the mode shape does not change with time, simply rotates in space. Thus for any snapshot in time the difference between the major and minor radii is the peak-to-peak amplitude of vibration. The problems here are in interpretation of the output. This is straightforward for a simple forcing system, such as a radial force only. Then the major axis of the elliptical mode shape will correspond to the line of action of the peak force. However, when a system of forcing including both radial and circumferential distributions displaced in space and time is considered, there is some uncertainty as to the whereabouts of the major and minor axes, which may indeed fail to correspond to "measurement" points. Once the axes have been identified it is still necessary to convert the displacement results from rectangular to polar co-ordinates. Such an operation is completely feasible and would present no serious problems. It is an approach which might be taken

when using a package which possesses only a static capability. However, as ANSYS can handle complex loading in the dynamic mode, it makes little sense not to make full use of the facility, and produce immediately meaningful data output.

The element type selected from the ANSYS element library is described as a "Two Dimensional Isoparametric Solid". This element type has four nodes, each with two degrees of freedom. It may be assigned properties of Young's modulus, Poisson's ratio, density and coefficient of expansion with temperature, although only the first three are used in this work. Selecting the value of Key Option 3 equal to 2 specifies that the elements are considered to represent a cross-section of a structure which experiences no axial strain. This is the option closest to the situation to be modelled, and forms a useful working approximation.

An early and vital decision involved whether to model a complete core or a section of it, and, if so, whether this should take the form of a half-core, a quarter-core, or even a single tooth. The advantage of modelling a small section of the stator is that it may be depicted in much greater detail for a given problem wavefront. The disadvantage is that boundary conditions for the cut edges need to be specified. Such boundary conditions could only be unnatural, for they would have to specify some restriction on movement of the boundaries. When the core is under the influence of a rotating force pattern, all points internal and surface move in both radial and circumferential directions during the force cycle. This is so even in physical reality, for, even though the stator is attached to its inner and outer frames and associated support structure, the coupling does not prevent movement completely, although it may reduce it significantly. When the results are obtained from an analysis with unnatural boundary conditions

specified, it becomes necessary to distinguish in some way between results due to the effect being studied and those due to the nature of the boundary conditions. Thus a whole new area of uncertainty is introduced.

The decision was therefore made to model, as far as possible, complete core cross-sections. This way all internal boundary conditions could be avoided, and, with care, external boundary conditions could be minimised in their intrusiveness.

To investigate the need for, and in particular the minimisation of, external boundary conditions, a very simple annulus was devised. It is made of the material of the Ferrybridge stator core, but has an inner radius of 8m and an outer radius of 10m. It is two elements thick in the radial direction and possesses 60 circumferential elements, as shown in Figure 5.1.

In the first test, this annulus was fixed on the outer diameter at two points: the top and bottom by reference to its position on the screen. It was excited by two equal and opposite radial harmonic forces on the inner diameter at the right- and left-hand sides. The magnitude of each force was (200+200j)kN. The results of this analysis are of little interest, except to show that this particular problem is completely acceptable to the processor, and that the results appear sensible in relation to the load conditions. This latter point was demonstrated by the fact that the highest vibration amplitudes on the outside occurred at left- and right-hand sides, decreasing to zero at top and bottom. The print-out gave all phase angles as 45° or -135°. The exciting forces had been defined with real and imaginary parts of equal magnitude in order to ensure output was generated in complex form. They were thus at 45° to the datum of the complex plane. Although they may be considered to be in phase when the annulus is drawn central on the

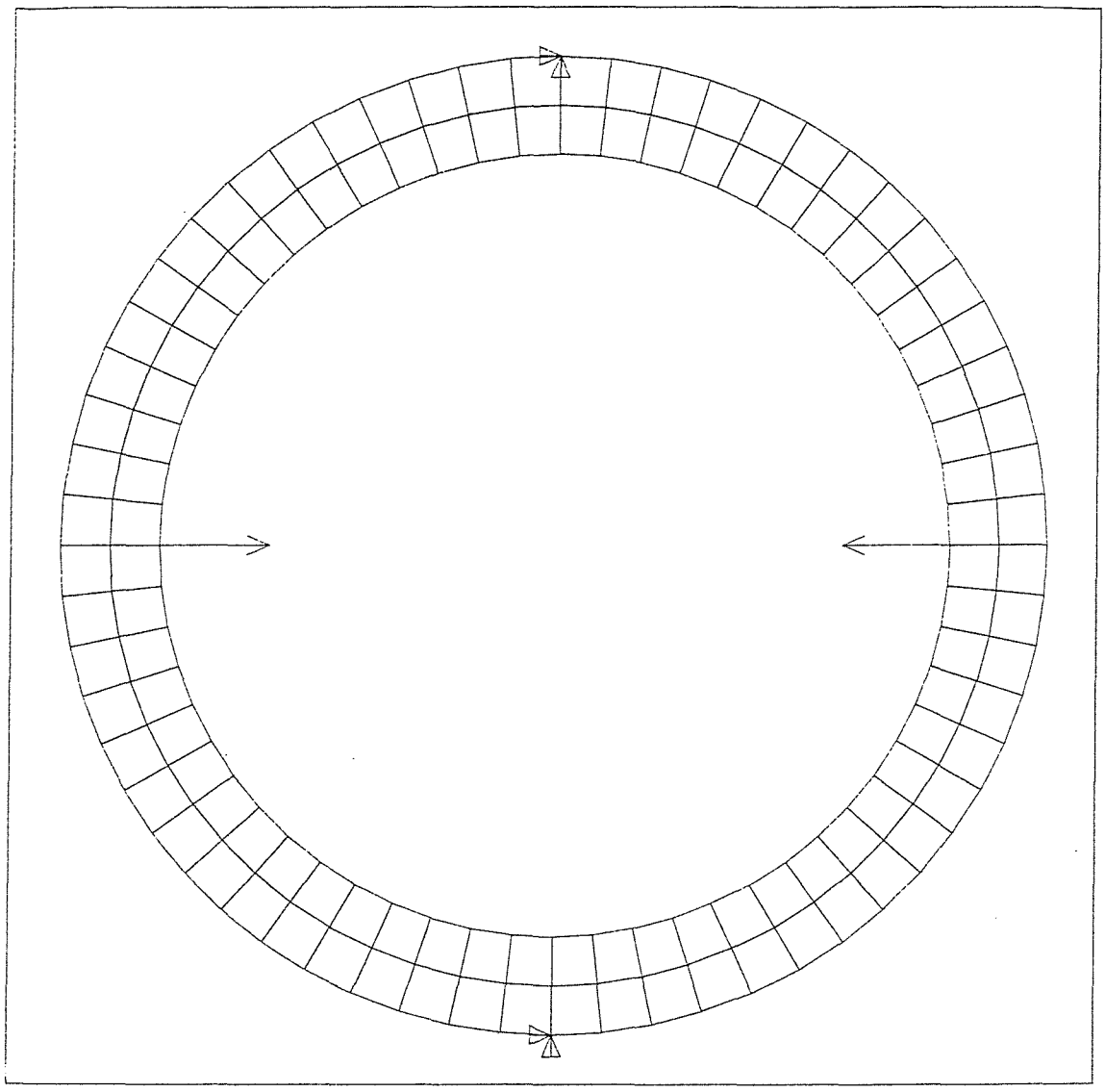

Figure 5.1 Simple annulus for initial tests (opposing applied forces and fixing points are shown)

origin of a polar plane, the output is in x-y form, and the forces appear to be in anti-phase when the annulus is drawn symmetrical about the y axis of a Cartesian plane. This explains the mix of in-phase and anti-phase angles obtained. The analysis was repeated with the forces in quadrature, with respect to the polar plane, and the results were again sensible.

As an important aim of these tests was to examine how far boundary conditions could be reduced, the next stage was to remove the fixing point at the top of the annulus. Then only one force was applied, at the right-hand side. The processor handled this situation without trouble, but the results were difficult to visualise in this distorted situation. The test was then repeated with two opposite forces as before. The results of this, even in numerical form, were very visual. For a section of about a quarter of the annulus on the extreme right-hand side all x-displacements were positive; on the left-hand side they were correspondingly negative, to demonstrate elongation of the shape along its horizontal axis. In the middle, the x-displacements had the opposite sign. All y-displacements were negative, due to the fixing point at the bottom.

Now it was time for a bold step. What would happen if all constraints were removed, leaving the ring completely free? Such a situation was defined, retaining the two opposing harmonic forces of the previous test. A warning message was issued on the screen whilst the data input was being written to th analysis file. However, the analysis processor experienced no problems in solving the equations for an unrestrained structure in this instance, and the results were beautiful in their symmetry.

In the ANSYS Examples Manual, the definition of structural problems characteristically includes the acceleration due to gravity. The effect of including and

excluding gravity was investigated in the situations described above. Its effect was simply to depress the annulus in the y direction. Its absence did not upset the processor. Even the case in which gravity was present without constraints proceded without difficulty; the annulus did not drift indefinitely in the negative y direction. Clearly ANSYS inhibits whole body movement.

The conclusion of these tests is that the ideal may be achieved: a completely isolated and unrestrained stator core.

An assessment of the complexity of problems which may be solved can be made by investigating the wavefront of various test analyses. The wavefront of the annulus used for the tests described above was 16. To determine how the wavefront is affected by resolution of the mesh, another simple annulus was analysed. This annulus had a coarser mesh: it was of identical dimensions but had one radial element and 30 circumferential elements; a total of one quarter the number of elements in the other annulus. Its wavefront was found to be 12. This showed that wavefront is not directly related to mesh resolution, and that it is in theory possible to increase the mesh resolution by a considerable amount before exceeding the maximum wavefront of the processor.

The next annulus examined represented a more serious attempt to model the stator of the Ferrybridge machine. The outer diameter was specified to be that of the stator. The material properties of the core iron were retained. Thus, to retain the true mass of the core, it was necessary to define a fictitious inner diameter. The contents of the slots were ignored at this stage. From knowledge of the slot width and slot depth, the tooth area was determined. The area filled by all 54 teeth was assigned to an annulus whose outer diameter was the same as the diameter described

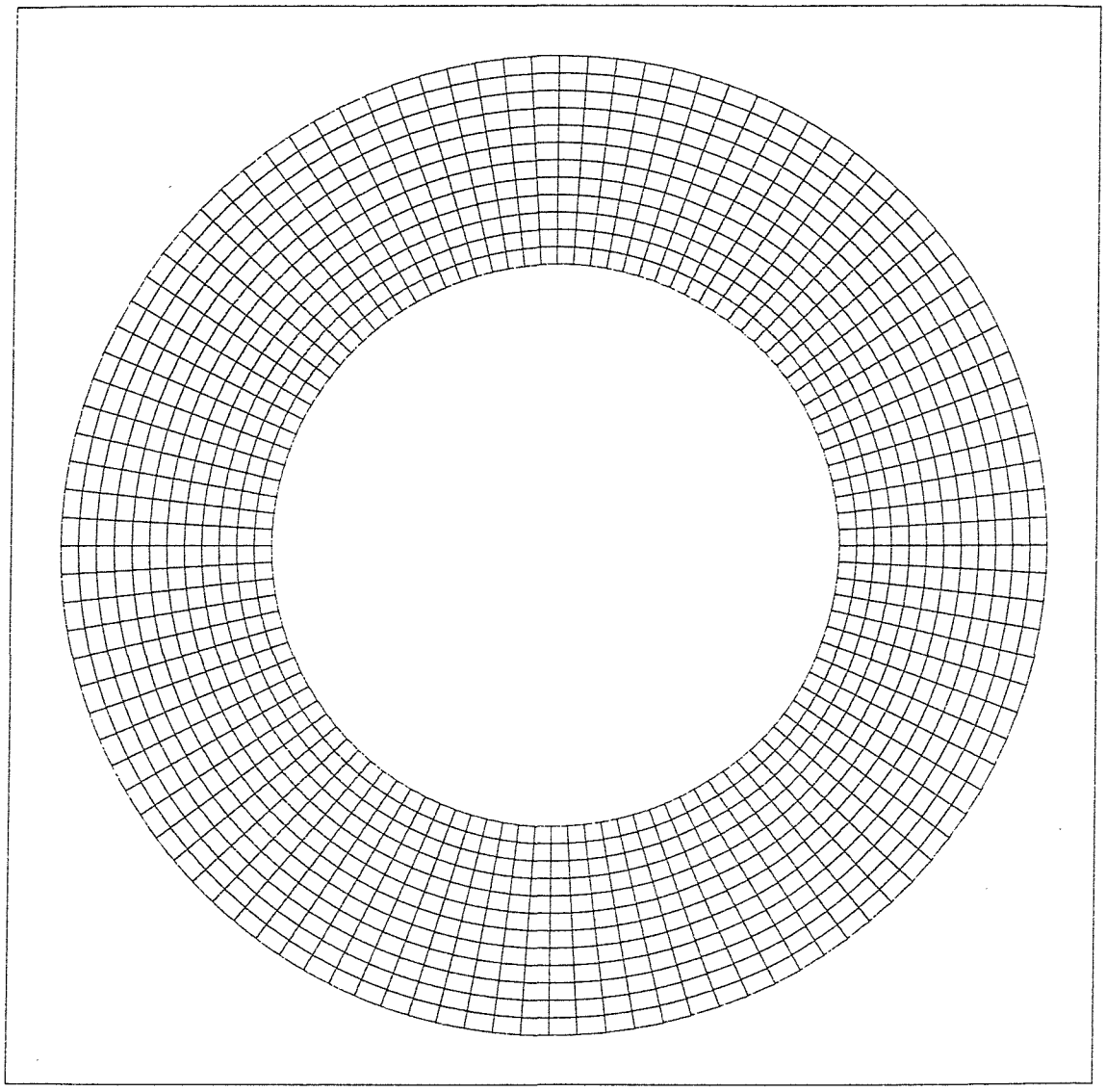

Figure 5.2 Simple annulus representation of the Ferrybridge stator

by the slot bottoms of the stator. Its inner diameter was therefore a dependent variable, and worked out at 1.4871m. This annulus was nested inside that of the stator core body to form a single annulus. It was meshed with 12 radial and 108 circumferential elements (Figure 5.2). It ran with two test forces, the print-out revealing its wavefront to be 56.

Mesh definition of simple annuli is a very straightforward matter. For those described above, node 1 is always defined as the extreme right-hand node on the inner diameter. Then a series of consecutively numbered nodes is generated along a radius. This radial sequence of nodes is repeated at circumferential intervals around the annulus.

Later stator models had teeth. This extra complexity suggests a number of different methods of geometry generation. For instance, a section of core back may first be defined, then its tooth. In early toothed cores, a section of core back corresponding to three slot pitches was defined, then three teeth were added, and the section repeated to form an entire core. The reasons for using three teeth were partly historical, partly a desire for optimal accuracy. If a machine has fifty-four stator teeth, then it is only every three slot pitches that one can define the angle in degrees with non-recurring decimals. Three-toothed sections were also used in some very early tests on boundary conditions. However, this is an inefficient method of meshing, proven by the fact that the whole toothed core constructed using this method exceeded the maximum wavefront of the processor at some point, causing the analysis to crash.

Later toothed geometries obtained optimal efficiency by defining first a set of radial nodes, then, an increment around the circumference, another set of radial nodes of which some describe the tooth outline. A section of one

slot pitch is generated, which is then repeated the necessary number of times for completion of the structure. Inaccuracies which creep in as a result of truncated decimal numbers are not really significant. Sections of core thus generated all run with a wavefront of 48; when joined up to form a complete core the wavefront is 72. This is very comfortably below the maximum of 250 for a harmonic analysis.

5.3 Combined Radial and Circumferential Forcing of an Annulus

The tooth force results of Section 4.5 show an increase in radial force between open circuit and full rated load, although this is considered due to the fact that use of load data from the real machine is not strictly appropriate in an idealised model, confirmed by the observation that the terminal voltage is not satisfied. If a constant B_r is considered over all load conditions, the radial tooth force would decrease with increased load due to the effect of B_θ. This approach was investigated in the work discussed in Section 2.4.3, and found to predict a vibration reduction far less than that observed.

The other difference between the two tooth force plots is the appearance of a circumferential tooth force in the full load case, which is not present on open circuit. The amplitude of this force is more than one third the amplitude of the radial force, and the two are phase displaced in time.

The work described in this Section is an investigation of the way a double-angle (four-pole) circumferential force distribution at the bore of an annulus may affect the distortion caused by a separate radial force distribution, when the two are of the same wavelength but at various phase

displacements. Its purpose is to verify that certain combinations of such force patterns may produce substantial reductions in ovalising distortion over other combinations, without any reduction in the amplitudes of the forces. Once this has been verified it is then necessary to determine whether such conditions exist within a large turbogenerator on load. This latter question is pursued in Chapters Six and Seven.

The annulus used for the tests was the Ferrybridge stator representation described in Section 5.2.2, in which the teeth had effectively been sawn off half-way down, the upper portions being used to fill up the slots. The tooth tips were defined, for the purpose of application of tooth forces, as those points around the inner diameter corresponding to the circumferential locations of the actual tooth tips around the stator bore. As the model has 108 circumferential nodes and the stator 54 teeth, a force was applied to every alternate node. The test forces were 100Hz oscillating forces of amplitude 100kN; the forces on successive teeth phase displaced in time to produce a rotating ovalising force distribution. Two sets of forces were defined: one radial, one circumferential. These forces were applied first separately, then together at a variety of phase displacements. A simple computer program converted each situation into data acceptable to ANSYS: x- and y-directed forces in real and imaginary parts.

The results took the form of 100Hz x and y displacements at the outer diameter of the annulus. Only the results from the four points where x and y displacement corresponds directly to radial and circumferential displacement were examined, to avoid the need for lengthy conversion calculations. The maximum variation in outer diameter displacement would have been shown up from these results, as the top and bottom points on the outer diameter are opposite a force application point on the inner

diameter, whilst at the left- and right-hand sides the displacement output points lie circumferentially intermediate between two adjacent points of force application. The radial and circumferential displacements obtained from these four outer points were equal to the nearest whole number of micrometres, i.e. two significant figure accuracy. As the force data was only input to the nearest whole number of kN, this was the greatest accuracy that could be meaningfully assumed anyway.

Test Case	$\hat{d}_r$ (μm)	$\hat{d}_\theta$ (μm)
1. F_r only	60	10
2. F_θ only	50	10
3. F_r and F_θ in phase	78	14
4. F_θ lags F_r by 45°	43	8
5. F_θ lags F_r by 90°	10	0
6. F_θ leads F_r by 45°	102	19
7. F_θ leads F_r by 90°	110	20
8. F_θ leads F_r by 135°	102	18

Table 5.1 Displacements of the test annulus due to combinations of radial and circumferential force

The results for radial and circumferential displacements, d_r and d_θ, are given in Table 5.1. These results show two important things: first, that the circumferential forces produce substantial radial displacement at the outer diameter of the annulus; secondly, that the combination of the two forcing systems is capable of producing large reductions in displacement below the displacement due to one system alone. The extreme cases occur when the circumferential tooth forces are time-phase

displaced from the radial tooth forces by 90°, which is equivalent to a geometrical displacement of 45°. When this is a lag angle, there results a reduction in displacement of 83% below that due to the radial tooth forces alone. A lead angle produces an increase of 83%. The reason for this is illustrated in Figure 5.3 which shows the elliptical distortions of a circular ring subjected to double-angle sinusoidal radial and circumferential force distributions. Figure 5.3(a) shows that a purely radial force distribution produces a displacement distribution in phase with the force distribution. Figure 5.3(b) shows that a purely circumferential force distribution produces a displacement distribution with its peak displaced by 45° in the positive Θ direction from that of the force distribution. In the expressions accompanying the Figure, $d_{r,r}$ represents a radial displacement due to a radial force; $d_{r,\theta}$ a radial distribution due to a circumferential force.

Figure 5.3(c) shows that application of a circumferential force distribution with its peak at 45° to the reference angle Θ=0 produces a displacement distribution in direct opposition to that of Figure 5.3(a). Thus simultaneous application of these two force distributions would result in a much lower displacement amplitude than that of Figure 5.3(a). Indeed, if the displacements were of identical amplitude, the ovalising would be suppressed entirely. It is important to note that all forces and displacements here are double-angle effects; thus 45° in space corresponds to 90° within the period of the force or displacement. This is the origin of the results in Table 5.1.

Under normal operating conditions, the stator core of a large turbogenerator behaves as a linear elastic structure. Thus it is valid to calculate the combined effects of the two force distributions by phasor arithmetic. In general, a radial force distribution of:

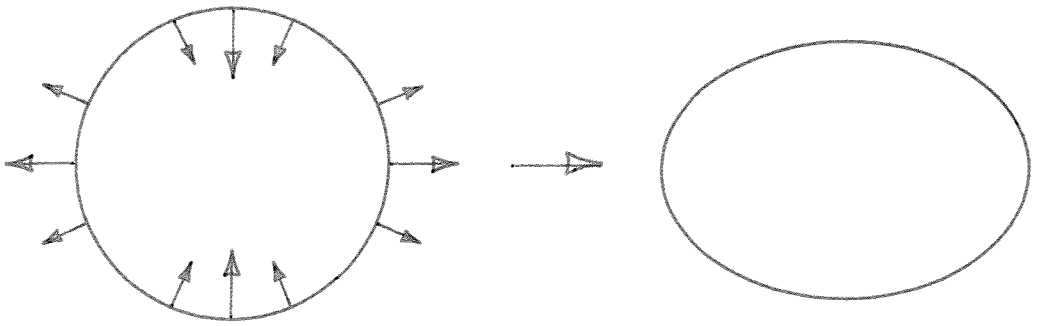

(a) $F_r = \hat{F}_r \cos 2\theta$ $d_{r,r} = \hat{d}_{r,r} \cos 2\theta$

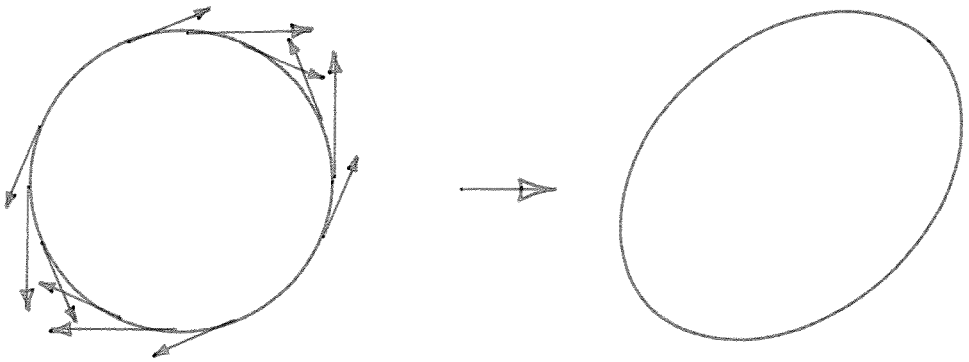

(b) $F_\theta = \hat{F}_\theta \cos 2\theta$ $d_{r,\theta} = \hat{d}_{r,\theta} \cos 2(\theta - 45°)$

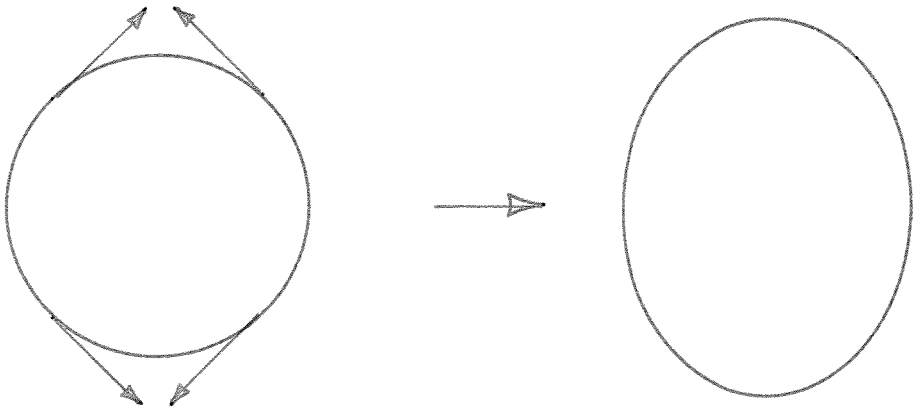

(c) $F_\theta = \hat{F}_\theta \cos 2(\theta - 45°)$ $d_{r,\theta} = -\hat{d}_{r,\theta} \cos 2\theta$

Figure 5.3 Displacements due to radial and circumferential four-pole force distributions

$$F_r = \hat{F}_r \cos 2\Theta \tag{5.1}$$

produces a radial core-back displacement distribution of:

$$d_{r,r} = \hat{d}_{r,r} \cos 2\Theta \tag{5.2}$$

If this is combined with a circumferential force distribution of:

$$F_\theta = \hat{F}_\theta \cos (2\Theta - \Psi) \tag{5.3}$$

which alone would produce a radial core-back displacement distribution of:

$$d_{r,\theta} = \hat{d}_{r,\theta} \cos (2\Theta - \Psi - 90°) \tag{5.4}$$

the total radial displacement d_r would be given, with reference to the phasor diagram of Figure 5.4, by

$$\hat{d}_r^2 = \hat{d}_{r,r}^2 + \hat{d}_{r,\theta}^2 - 2\hat{d}_{r,r}\hat{d}_{r,\theta} \cos (90° - \Psi) \tag{5.5}$$

There will be a range of Ψ over which $\hat{d}_r$ is reduced below the value of $\hat{d}_{r,r}$. The exact range and the proportional reduction depend on the value of $\hat{d}_{r,\theta}$. Minimum and maximum values of Ψ for this range can be obtained from equation (5.5) by setting $\hat{d}_r^2 = \hat{d}_{r,r}^2$ and subtracting this quantity from both sides of the equation. The condition for minimum Ψ is then given by:

$$\hat{d}_{r,\theta} / \hat{d}_{r,r} = 2 \sin \Psi_{min} \tag{5.6}$$

whilst Ψ_{max} may be found by symmetry:

$$\Psi_{max} = 180° - \Psi_{min} \tag{5.7}$$

The circumferential displacement, d_θ, composed of the displacement due to radial force, $d_{\theta,r}$, and that due to circumferential force, $d_{\theta,\theta}$, may be obtained from a similar phasor diagram. Circumferential displacement due to circumferential force is in phase with that force, whilst that due to radial force leads the force by 45° in space. This can be deduced by inspection of Figure 5.3. The circumferential displacements are considered to be of lesser importance than the radial displacements. Their magnitude

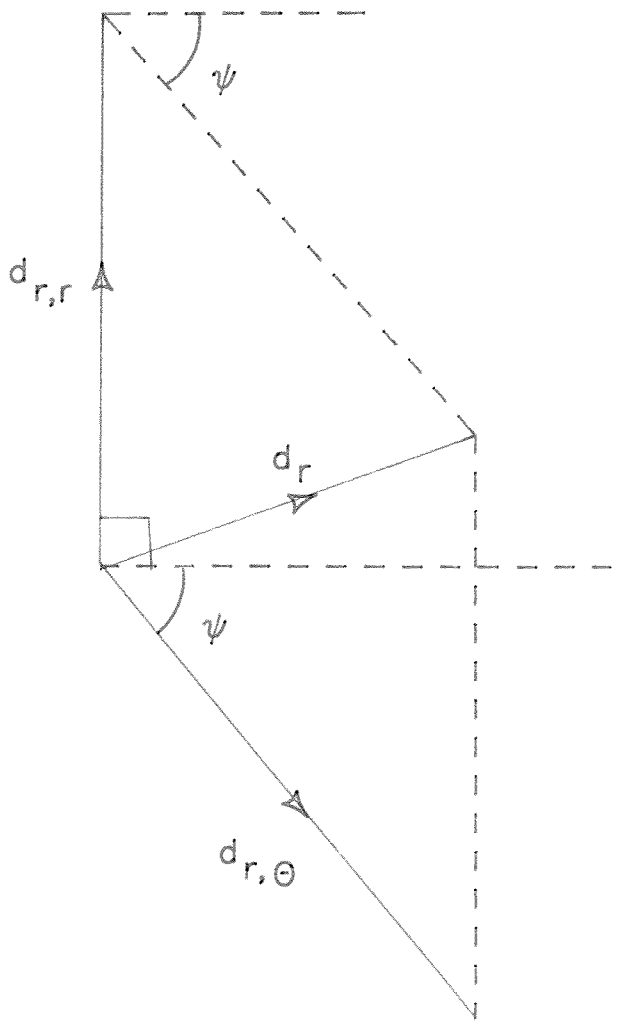

Figure 5.4 Phasor combination of radial deflections due to radial and circumferential four-pole force distributions on an annulus

at the core back is only a fraction of the magnitude of the radial displacements. Early impressions of test measurements suggested that they were more difficult to measure consistently than the associated radial displacements, as they varied more widely with measurement point. Later understanding suggested that their level may be more affected by surrounding structure, especially as the inner to outer frame mounting arrangements are designed with intent to resist the torque force and thereby to suppress circumferential motion. In any event, they provide no new information about the variation of double-frequency stator core vibration with machine load and excitation, and as such do not merit extensive special study.

The practical manifestation of the linear elastic behaviour of the stator core is an immense simplification of the mechanical part of the vibration model. For each machine, only two mechanical analyses need by done: one to determine the response to a set of radial test forces; the other to a set of circumferential test forces. The results of these two analyses are a quartet of transfer coefficients:

(i) $k_{r,r}$: radial force to radial displacement
(ii) $k_{r,\theta}$: circumferential force to radial displacement
(iii) $k_{\theta,r}$: radial force to circumferential displacement
(iv) $k_{\theta,\theta}$: circumferential force to circumferential displacement

From these coefficients and the tooth forces calculated by the electromagnetic model, the separate displacements due to the components of tooth force may be calculated.

$$\hat{d}_{r,r} = k_{r,r}\hat{F}_r \tag{5.8a}$$

$$\hat{d}_{r,\theta} = k_{r,\theta}\hat{F}_\theta \tag{5.8b}$$

$$\hat{d}_{\theta,r} = k_{\theta,r}\hat{F}_r \tag{5.8c}$$

$$\hat{d}_{\theta,\theta} = k_{\theta,\theta}\hat{F}_\theta \tag{5.8d}$$

The results may then be combined to give the predicted core-back vibration level.

5.4 Mechanical Representations of a Stator Core

5.4.1 Further Simple Annuli

The stator core representation used for the tests in Section 5.3 is sufficiently simple for further tests on its validity to be a necessity. In a dynamic situation, it is important to maintain the true mass of the structure in a simple model. However, retaining the true density and defining an artificial inner diameter effectively alters the radius of application of the forces, already shown to act on the tooth tips, and may significantly alter the result.

To gauge the scale of this effect, two extreme cases were examined. The first annulus had an inner diameter equal to that of the stator bore, and a lower density than that of the core steel. The second had an inner diameter equal to that described by the stator slot bottoms, and possessed a higher density than that of the core steel. They are shown in Figure 5.5.

Annulus (O.D.=1.2954m)	I.D. (m)	Transfer coefficients (μm/kN)			
		$k_{r,r}$	$k_{r,\theta}$	$k_{\theta,r}$	$k_{\theta,\theta}$
Thick	0.654	0.34	0.30	0.04	0.05
Intermediate	0.74356	0.60	0.50	0.10	0.10
Thin	0.84133	1.35	1.06	0.30	0.26

Table 5.2 Transfer coefficients of the three simple annuli

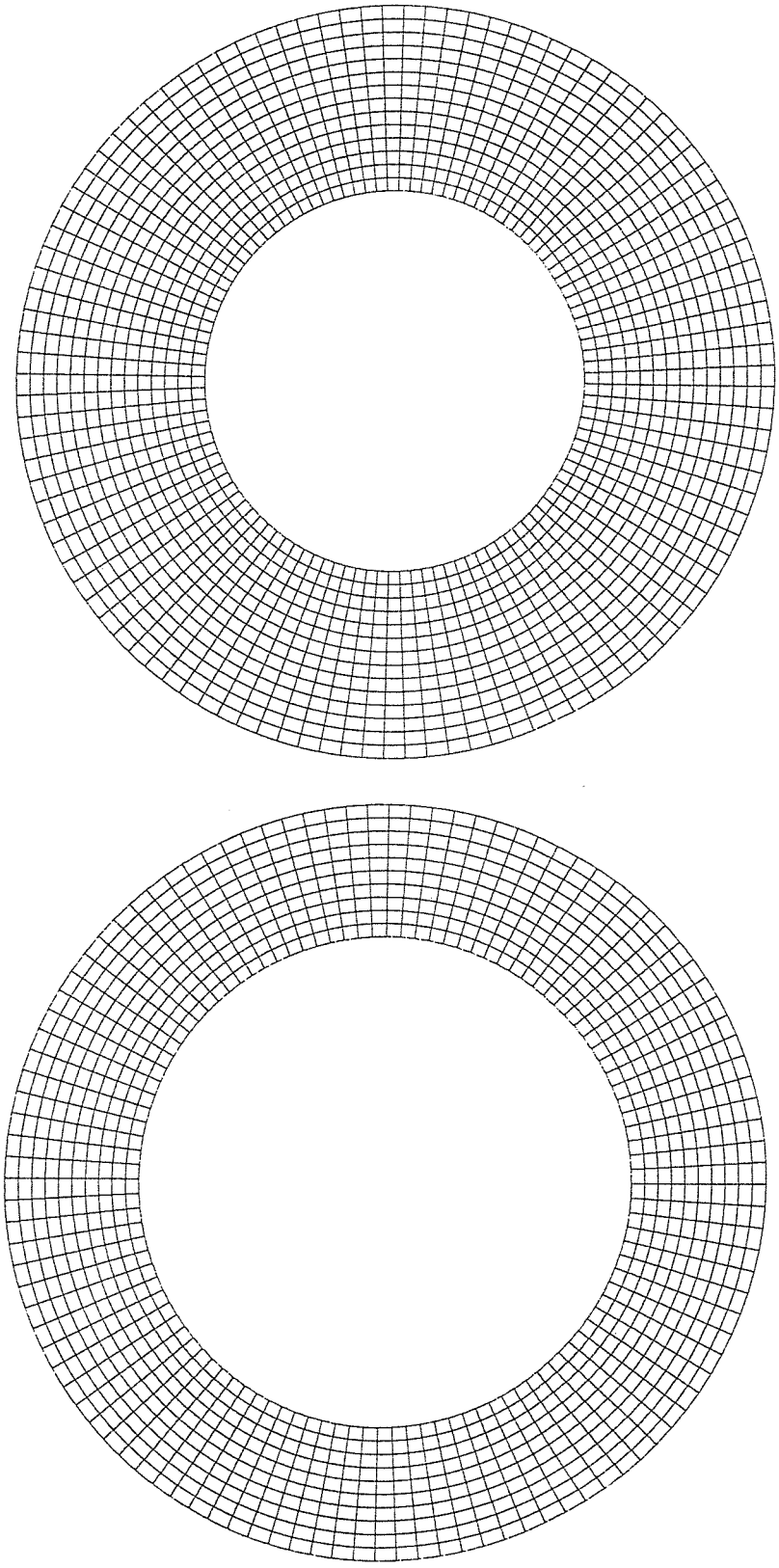

Figure 5.5 The thick and thin annuli of equal mass

These two annuli were subjected to the same sets of forces as the first had been. The resulting transfer coefficients for all three annuli are given in Table 5.2. All coefficients for the thin annulus are several times greater than those for the thick annulus, whilst the original annulus shows intermediate values.

These results are due to the difference in stiffness between the annuli. The thinner the annulus, the less stiff it is. The natural frequencies of such bodies depend upon both stiffness and mass. All the annuli have the same mass, so only the stiffness is of comparative importance. Their natural ovalising frequencies are all close to the exciting frequency of 100Hz. In such a situation the dynamic displacements at this frequency are higher than the respective displacements produced by a static force of identical magnitude. The ratio of dynamic displacement to static displacement is known as the dynamic magnifier. The less stiff the annulus, the lower its natural ovalising frequency, hence the higher its dynamic magnifier.

The consequence of these results is that if a simple annulus is to be used to obtain quantitative predictions of stator core vibration level, it must be selected with extreme care. In particular, its natural ovalising frequency should be close to that of the stator to be represented.

5.4.2 Stator Core Models Incorporating Greater Detail

In Section 5.4.1 it was found that the transfer coefficients of a simple annulus are highly dependent on the dimensions of that annulus, and the forcing frequency is close to the natural frequency of the annulus. In Section 5.3 it was shown that any possible reduction in ovalising amplitude is dependent on the relative magnitudes of the superposed displacements and the angle between them. From

this it is obvious that the ratio of one transfer coefficient to the other is of prime importance, for it determines the relative influence of the two force systems in determining eventual ovalising amplitude. There is no reason to believe that any particular simple annulus will give an appropriate ratio. Because of these two sources of uncertainty, a series of more sophisticated mechanical models of the stator core was developed, incorporating more features.

The first more detailed model was one in which the teeth were defined, but the slots were left empty. It is shown in Figure 5.6. This gave a structure of the same mass as the three simple annuli, but did not represent the true mass of the stator, which would include the mass of the windings. The same test forces were applied, this time to well-defined tooth tips. The transfer coefficients are given in Table 5.3.

$k_{r,r}$	$k_{r,\theta}$	$k_{\theta,r}$	$k_{\theta,\theta}$
1.32	1.41	0.29	0.33

Table 5.3 Transfer coefficients of the toothed core (all in μm/kN)

The radial force transfer coefficients are very close to those obtained for the thin annulus, whilst the circumferential force transfer coefficients are significantly higher than those obtained for any of the simple annuli. It is not surprising that the behaviour of the toothed core most resembles that of the thin annulus, for its stiffness depends on the depth of solid material, that is, from the slot bottoms to the core back, whilst the teeth contribute to its mass. The difference in the

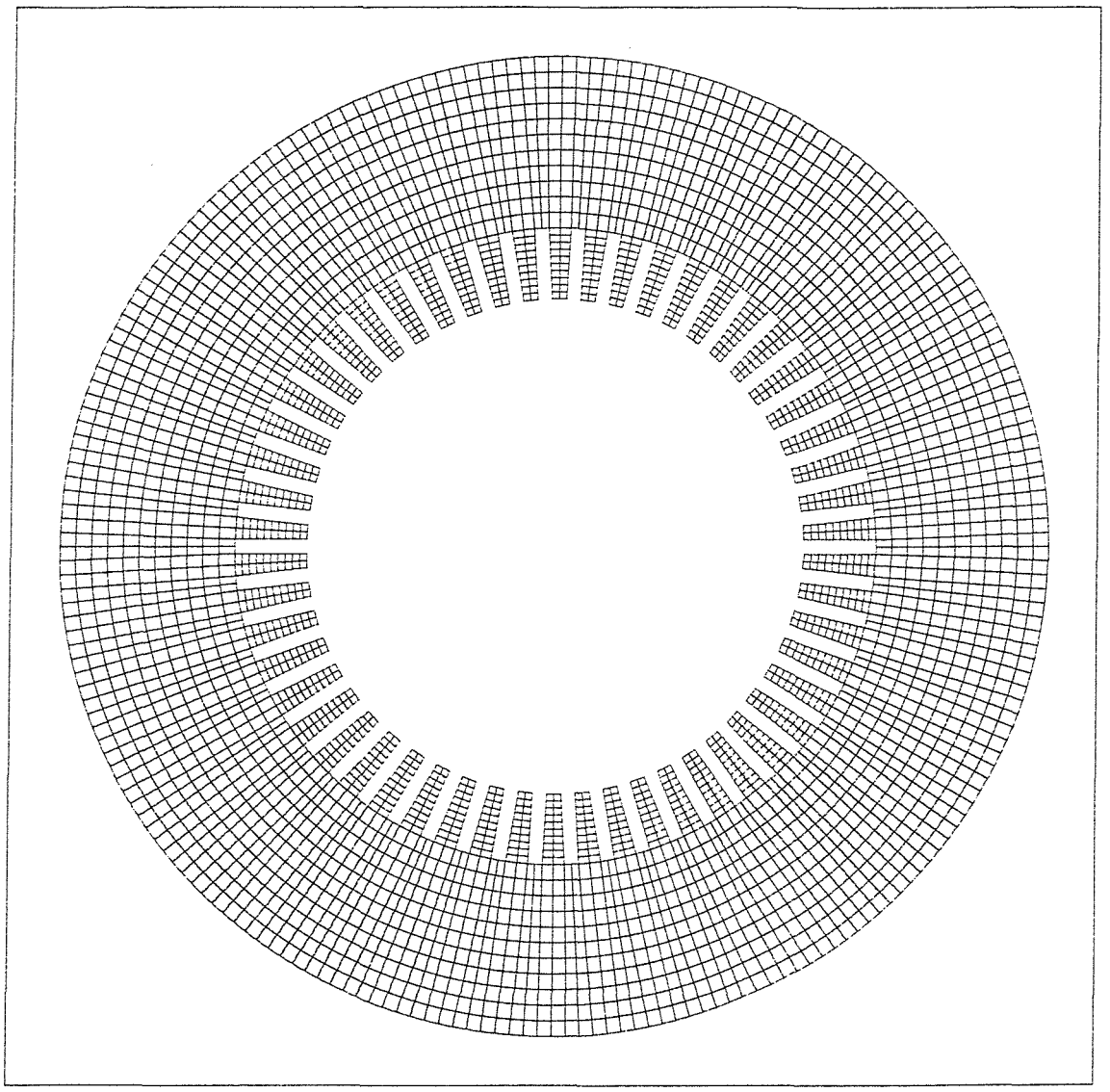

Figure 5.6 Ferrybridge stator core representation with empty slots

circumferential force transfer coefficients is likely to be mainly due to the fact that they are applied at a smaller radius than they are in the thin annulus, resulting in a greater moment at the core back.

The next stage would be to model slot wedges and conductors. However, data was not available for the Ferrybridge stator which had been used as a basis for all the representations so far. Slot wedge and conductor data was, however, available for two other machines, the West Burton generator and the 350MW generator. The West Burton stator was selected for the continuation of these more sophisticated mechanical representations.

Model	$k_{r,r}$ (μm/kN)	$k_{r,\theta}$ (μm/kN)
Empty slots	2.14	2.28
Slot wedges only	1.84	1.70
Full slot contents	1.46	1.36

Table 5.4 Radial displacement transfer coefficients for the West Burton stator core section

The West Burton stator differs from the Ferrybridge stator in two major facets. First, it has forty-eight teeth as opposed to fifty-four. Thus the total loading due to the test tooth-forces is lower because they are applied at fewer points. Secondly, it is made of a grain-oriented steel which has a particularly low Young's modulus, $1.0026 \times 10^{11} Nm^{-2}$ compared to $1.52 \times 10^{11} Nm^{-2}$ for the Ferrybridge stator core. The first factor would tend to decrease the transfer coefficients; the second to increase them. The main core dimensions are very similar. The second factor turned out to be dominant, and the transfer coefficients are

more than 60% higher, as can be seen in Table 5.4, when the core is modelled with empty slots.

The next stage was to include the slot wedges, which perform an important rôle in stiffening the core. The slot wedges are made of epoxy glass, and may be modelled fairly faithfully by defining two elements of appropriate depth which straddle the opening of each slot (Figure 5.7). These elements need to be assigned a different material number from the rest of the core, and so may be assigned different material properties.

The transfer coefficients for the wedged core are given in Table 5.4. The extra mass of the wedges is barely significant, so almost all the difference between these coefficients and the previous ones can be considered due to the stiffening effect of the wedges. The circumferential transfer coefficient has been reduced by 25%, whilst the radial transfer coefficient has been reduced by only 14%, proving that the stiffening effect is greater for one component of tooth force than for the other.

The final step in the development of these more sophisticated core representations was the inclusion of the slot contents. A stator slot of a large turbogenerator contains a complex assortment of materials, and it is necessary to simplify the situation considerably in order to model it as a small part of a core structure. There are two coil sides in each slot, as the winding is a double-layer one, each surrounded by coil insulation, and separated in the middle by a separator. Each coil side consists of a large number of sub-conductors in an array of rows and columns, each one surrounded by its own thin insulation layer and with its own central coolant channel. The columns of sub-conductors are separated by vertical separators.

For the purpose of this model, the entire contents of

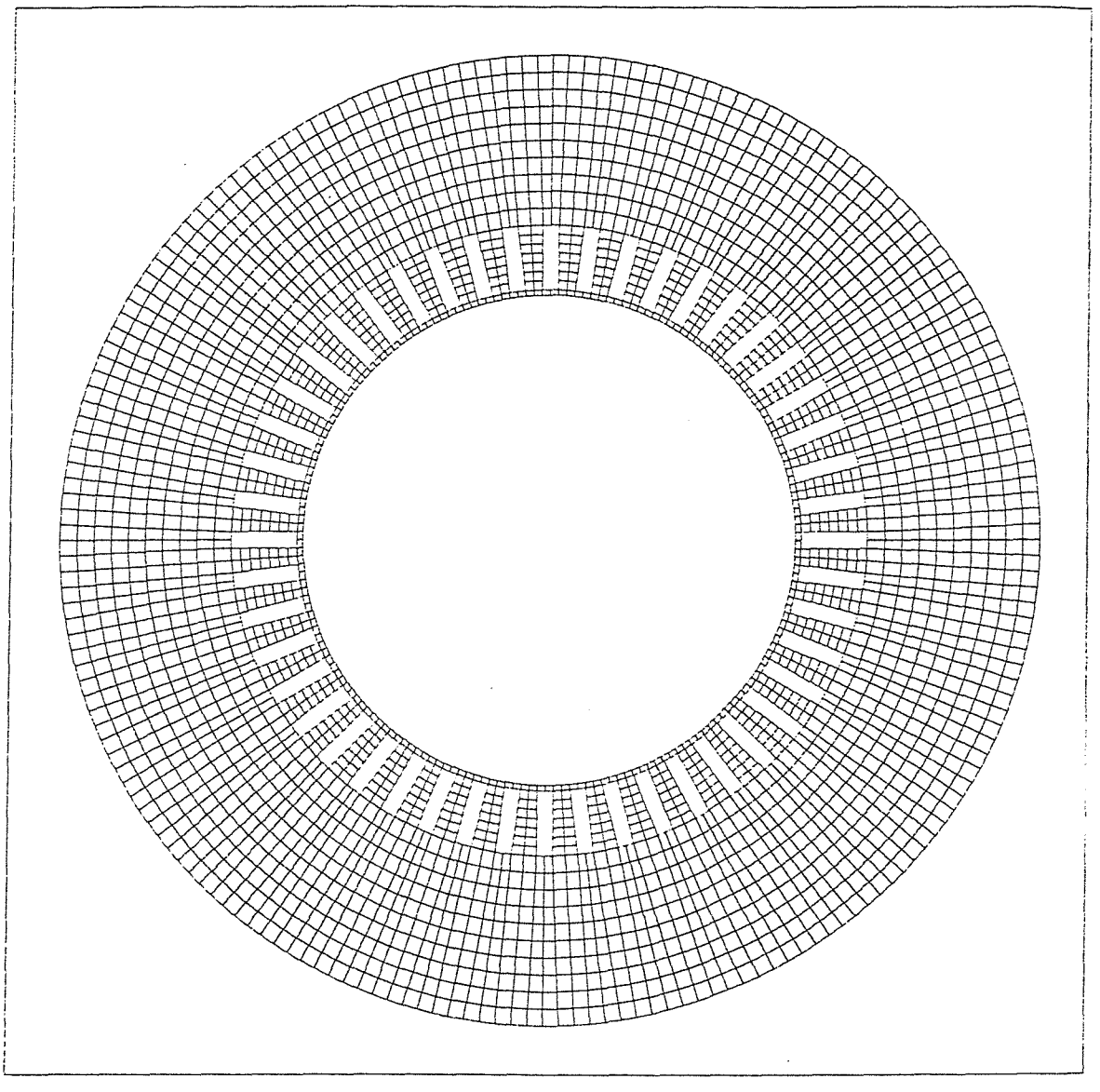

Figure 5.7 West Burton stator core representation with wedged slots

the slot were considered to be a homogenous medium. The homogenisation process operated as follows. The sub-conductor insulation and separators were ignored. The copper sub-conductors tubes which in reality have radiused corners were squared off, and the necessary packing ignored. The free sub-conductor spaces necessary to allow Roebelling of the bars were ignored. The entire coil-side region was assigned a density obtained by considering the respective densities of the copper and the coolant water. Next, the respective densities of the coil insulation, the coil separator and the already homogenised coil side were similarly conbined to give an overall effective density. The Poisson's ratios of all components exccept the copper were the same, so the homogenised mass was assigned that value.

The final material property necessary to define the slot contents is the Young's modulus, which is critical in determining the overall stiffness of the slot contents. Due to the complex nature of the actual structure, an empirical value would be easier to determine than a theoretical value. This value would of necessity be artificial, for it would have to take into account the relative movement between the slot contents and the slot wall, which is not modelled in the finite-element analysis, in which elements are considered to be rigidly linked. As a start, the value selected was that given in the data as the Young's modulus of the coil insulation.

The radial displacement transfer coefficients thus obtained are the final pair in Table 5.4. The slot contents add both mass and stiffness to the core section. The extra mass would tend to raise the values of the transfer coefficients; the extra stiffness would reduce them. The coefficients are about 20% lower than those obtained in the instance of slot wedges only, indicating that the extra stiffness is dominant over the extra mass. The ratio

between radial and circumferential force transfer coefficients differs by less than 1% in these two cases, indicating that the stiffening effect of the slot contents is almost equal in both directions.

5.5 Validation of the Core Representations by Modal Analysis

The purpose of the modal analyses of the various core representations is, as stated in Section 5.2.2, to assess the dynamic equivalence of these highly simplified structures to the actual stator core. A quarter core was used for the analyses. This enabled greater accuracy to be obtained, and caused no problems regarding the specification of boundary conditions, because the standard system of symmetric and antisymmetric boundary conditions was used. Whereas the precise response to a general forcing system may actually need the finite-element analysis to predict it, the mode-shapes of a ring section are well defined and only need their natural frequencies determined by analysis.

The standard boundary conditions forbid movement in the direction of one or other of the axes. The symmetric boundary condition allows radial movement only; the antisymmetric condition allows circumferential movement only. The complete mode shape may be easily reconstructed given a quarter mode shape and known boundary condititions. The symmetric boundary condition acts as a plane of symmetry. To each side of an antisymmetric boundary, pairs of points within the original undistorted shape lying in mirror-image positions with respect to the boundary exhibit equal radial movement, but in opposite directions.

When a quarter annulus is used, modes of even order may be extracted when the two boundary conditions are the same, be they symmetric or antisymmetric. Modes of odd order may

be extracted when the two boundaries are assigned different conditions. This is demonstrated for the 2nd and 3rd order radial modes in Figure 5.8.

For a simple annulus, analytical formulae exist which give the natural frequencies of various types of vibration. The validity of these formulae is dependent on the thickness of the ring being small in proportion to the mean radius[37]. This is not strictly true for the turbo-generator stator, but insight may be gained from the results of such a calculation, especially if these are compared with the results of the finite-element analysis.

The formula for the natural frequency of a flexural mode n when the flexural vibration occurs solely in the plane of the ring is:

$$f_n = \frac{1}{2\pi}\sqrt{\left(\frac{EI}{\rho A r^4} \cdot \frac{n^2(1-n^2)^2}{1+n^2}\right)} \qquad (5.9)$$

where E is the Young's modulus, ρ the density, I the moment of inertia of the cross-section with respect to a principal axis at right angles to the plane of the ring, A the cross-sectional area of the section, r the mean radius and n the order of the mode, which must be greater than or equal to 2.

If b is the thickness of the annulus, and L the length of the stator core represented, the area referred to is bL, and the moment of inertia is $b^3L/12$. Hence the length is cancelled out of the equation as might be expected.

The stator used to investigate modal behaviour was that of the West Burton (500MW) machine. For this first test, a thin annulus similar to that used to represent the Ferrybridge stator in Section 5.4.1 was defined. Its density was calculated to be 8884kgm^{-3}. An outer radius of 1.27m and a slot bottom radius of 0.8255m gave it a thickness of 0.4445m and a mean radius of 1.04775m. Thus

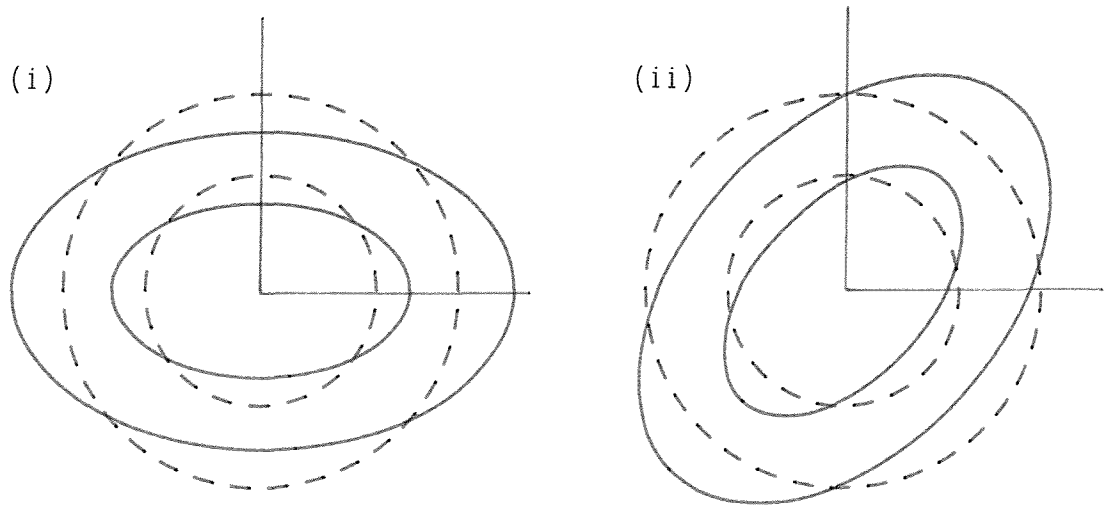

(a) Extraction of radial mode n=2 with (i) symmetric and (ii) antisymmetric boundary conditions

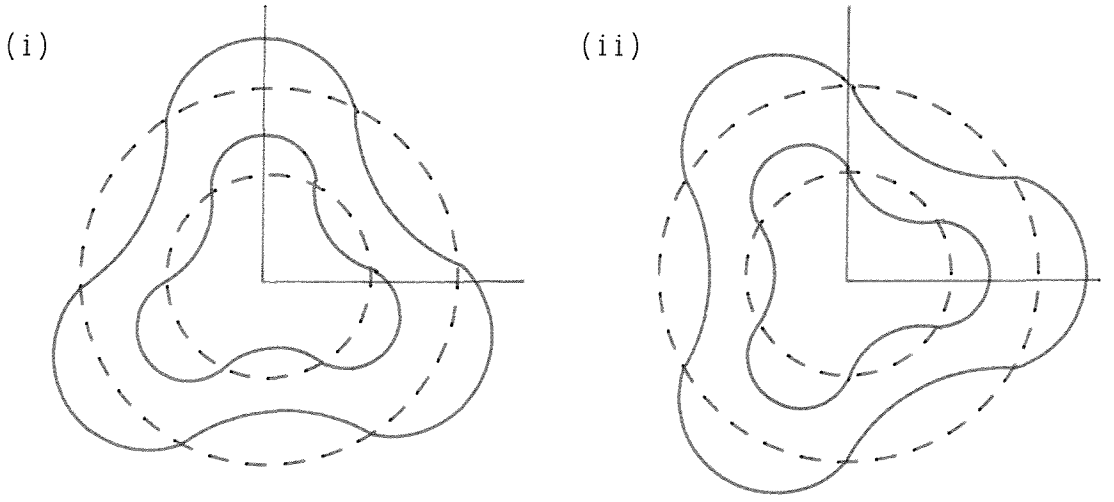

(b) Extraction of radial mode n=3 with (i) symmetric boundary condition on the y axis and antisymmetric on the x axis and (ii) symmetric boundary condition on the x axis and antisymmetric on the y axis

Figure 5.8 Extraction of mode shapes

for the mode n=2, the frequency produced by the equation is 168Hz. This is certainly within the expected range for large turbogenerator stators.

The finite-element calculation produces a mode frequency of 163Hz. Figure 5.9 shows the modal displacement plot for the annulus. Table 5.5 provides a comparison between the results of the formula and the results from finite elements for this and higher modes. It shows that the validity of the equation when applied to relatively thick annuli decreases sharply for higher modes, although it is a reasonable approximation for n=2.

Order of Mode	Natural Mode Frequency (Hz)	
	Equation	Finite elements
2	168	163
3	474	416
4	909	715
5	1471	1040
6	2158	1379
7	2970	1738
8	3907	2082

Table 5.5 Comparison of algebraic and numerical predictions of radial mode frequencies for the simple West Burton stator core representation

The finite-element calculation was repeated, in this first instance, for a core with empty slots, and then for a core with slot wedges and filled slots. The Young's modulus was taken to be first that of the copper and secondly that of the coil insulation in two separate such analyses. The mode frequencies obtained are listed in Table 5.6.

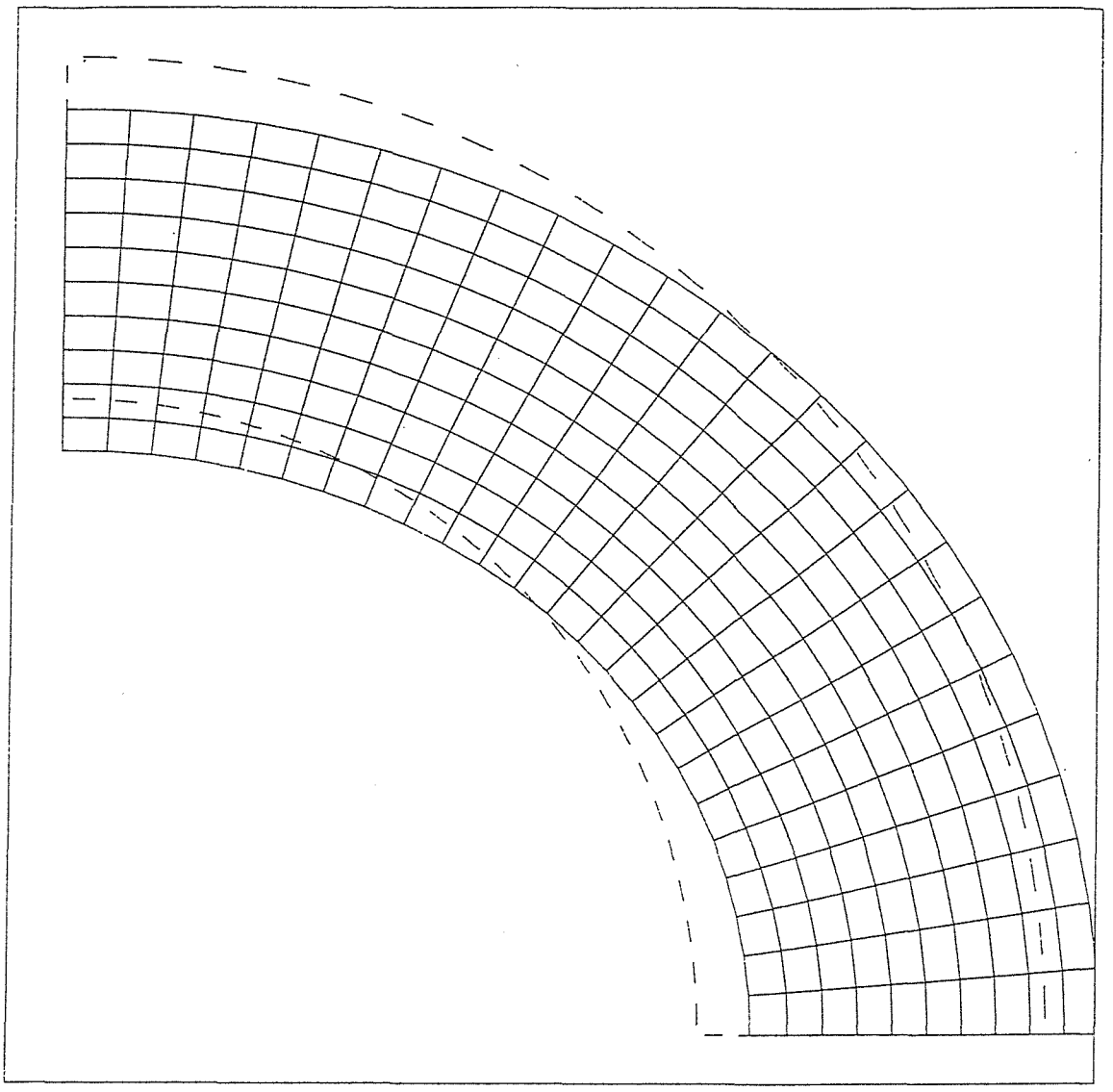

Figure 5.9 Modal displacement plot for second order radial mode of thin annulus representation of West Burton stator

Order of Mode	Core Representation			
	Simple ring	Toothed ring	High modulus slot contents	Low modulus slot contents
Radial				
0	548	548	700	550
1	-	-	-	-
2	163	161	282	179
3	416	403	677	449
4	715	666	1098	768
5	1040	868	1548	1146
6	1379	950	1939	1538
7	1738	977	2355	1875
8	2082	988	-	-
Circ'l Modes				
Core				
1	741	774	865	778
2	1150	-	1302	1348
3	1613	-	1778	-
4	-	-	2362	-
Teeth		987		
1			-	1549
2			-	1689

Table 5.6 Natural mode frequency results (all in Hz)

The package proved unable to extract non-zero frequencies for the first order radial mode, which is a simple lateral translation with no distortion. Of the radial mode frequencies which were extracted, those of the toothed annulus were the lowest; those of the core representation with the high Young's modulus slot contents the highest by far. The latter are quite evidently too high for this representation to be pursued seriously any further. Even the representation with the low Young's modulus, which would under-represent the stiffness of the slot contents if taken in isolation, gives a value of ovalising resonant frequency higher than might be expected given a 500MW core of grain-oriented steel. This is likely to be because this representation does not model the relative movement between slot contents and slot wall mentioned in Section 5.4.2.

The analysis extracted circumferential modes as well as radial ones. Their frequencies are too high to be excited significantly in an operational stator, but they are of interest in a comparative study of the core representations. The one circumferential mode frequency extracted for the toothed annulus is higher than the corresponding mode frequency of the simple annulus, although all the radial mode frequencies of this representation are lower. The toothed annulus also produces a definite resonance of the teeth at 987Hz. The representations with filled slots have two separate sets of circumferential mode frequencies. The core exhibits resonance at one particular frequency, then the inner annulus formed by the teeth and slot contents exhibits resonance in the same mode at a different frequency. At this stage, slotted region resonances were observed only for the case with lower Young's modulus, as in the other case this region was simply too stiff for its natural frequencies to appear within the first twelve modes extracted.

It was evident that if the slot contents were to be

represented as a homogenised mass inseparably connected to the slot wall, then they would have to be assigned a low Young's modulus which does not relate to any true property.

Initially, in an attempt to find limits on the mode frequencies which could be obtained from such a structure, the slot contents Young's modulus was set to $1Nm^{-2}$. The ANSYS processor, however, proved unable to handle a problem in which the ratio of stresses in two adjacent regions is more than 10^8. This is certainly the case for a Young's modulus ratio of 10^{11}. A second attempt was made, setting the Young's modulus to 10^5Nm^{-2}. The first six modes extracted with symmetric conditions on both boundaries were all around 40Hz, and the mode shapes were not identifiable. It was likely that such results showed various resonances of the slot contents alone, and as such were not in the least helpful.

A third attempt was made with the slot contents Young's modulus set to 10^8Nm^{-2}. This time distinct mode shapes were extracted. The radial and (core) circumferential mode frequencies are given in Table 5.7. There were also five unidentifiable circumferential modes of the slotted region at around 1250 Hz.

n	0	1	2	3	4	5
Radial	640	-	166	481	923	1192
Circ'l	-	990	-	-	-	-

Table 5.7 Mode frequencies of the core representation with slot contents Young's modulus of 10^8Nm^{-2}

Examination of these results reveals the mode frequencies to be higher than those obtained for the core

representation with the slot contents Young's modulus equal to that of the coil insulation ($3.2 \times 10^9 Nm^{-2}$). The only exception is the ovalising mode frequency. It seemed unlikely that the stress ratio should be a problem in this case, as the Young's moduli differ by a factor of only 10^3. However, a further analysis was performed with slot contents Young's modulus of $10^9 Nm^{-2}$. The mode frequencies extracted were intermediate between the other two sets, which still meant that the trend was not as expected. The mode shapes were mostly identifiable, but somehow messy, with ragged edges, as indeed the previous set had been.

The problem now seemed quite unlikely to be caused by the stress ratio between regions. It seemed more likely to be a case of insufficient numbers of master degrees of freedom. The usual rule is that the number of master degrees of freedom should be at least twice the number of modes to be extracted[38]. In the analyses described, 100 master degrees of freedom had been specified, and twelve modes extracted, which is well within these guidelines. However, it seemed possible that when a structure is composed of regions with different properties, more master degrees of freedom are necessary. Increasing the number of master degrees of freedom would in any case increase the accuracy of the results, but it would also increase the wavefront of the problem. A series of tests was performed with various numbers of master degrees of freedom to assess the balance between these two factors. The results are summarised in Table 5.8.

The change in frequencies calculated is relatively small between 250 and 350 master degrees of freedom, but still significant for higher modes. However, no further increase in master degrees of freedom was considered necessary as the higher modes are not of immense interest in this work, and the computing time had already increased from about 20 minutes c.p.u. time using 100 masters to about two

and a half hours using 350 masters. Assessment of the wavefront figures indicated that an analysis of 450 masters would run, but this was not considered worth the extra time.

Order of mode	Number of master degrees of freedom			
	100	150	250	350
Radial				
0	567	550	535	532
2	169	169	169	169
4	778	738	717	711
6	1710	1480	1364	1334
Circumferential				
Core 2	1419	1326	1223	1182
Slotted region 2	1570	1445	1343	1330
Wavefront	142	192	292	392

Table 5.8 Variation of mode frequency (Hz) and wavefront with number of master degrees of freedom for core representation with $E=10^9 Nm^{-2}$ for slot contents

A complete set of mode frequencies was produced using 350 masters for core representations with slot contents Young's moduli of $3.2\times10^8 Nm^{-2}$, $1.0\times10^9 Nm^{-2}$ and $3.2\times10^9 Nm^{-2}$ (coil insulation). Analyses were also performed for the cases with empty slots, and slot wedges only. Repetition of the thin annulus was considered unnecessary, as such a simple structure ought to obey the standard guidelines for recommended numbers of master degrees of freedom. Repetition of the core representation with the slot contents assigned a Young's modulus equal to that of copper was not

repeated either, as it had already been dismissed as a useful model. The results are given in Table 5.9. They show that a second order radial mode frequency may be selected at will by tuning the Young's modulus of the slot contents. The attainable minimum is probably somewhere slightly below the 161Hz calculated for the empty slotted core, due to the extra mass of the slot contents.

Order of Mode	Core representation (contents of slots)				
	Empty slots	Wedges only	Modulus 3.2×10^9	Modulus 1.0×10^9	Modulus 3.2×10^8
Radial					
0	524	546	541	532	529
1	-	-	-	-	-
2	161	170	179	169	165
3	401	425	444	421	412
4	658	718	748	711	696
5	858	1029	1076	1021	995
6	944	1343	1412	1334	1286
Circ'l					
Core					
1	753	756	753	746	744
2	-	1184	1193	1182	1155
3	-	-	1682	-	-
Teeth	986				
1		1194	1476	1209	1084
2		1318	1622	1330	1223
3		1482	-	1480	1336

Table 5.9 Mode frequencies (Hz) obtained using 350 master degrees of freedom

Unfortunately the exact resonant frequencies of the West Burton core are not known. The vibration data available give only 100Hz levels at various loads. The best strategy, therefore, for selecting a core representation, is to match the 100Hz transfer coefficients with those exhibited by the structure being modelled. If, as already discussed, it proves not possible to reproduce with an isolated core model the vibrations measured on the machine in operation, the correct trend in vibration with load and excitation may be reproduced by employing a core representation with radial and circumferential transfer coefficients in an appropriate ratio. This selection process cannot be carried out until the 100Hz transfer coefficients have been determined.

The West Burton core is made of grain oriented steel, which typically has a low Young's modulus, in this case $1.0026 \times 10^{11} Nm^{-2}$. By contrast, the 350MW generator stator is made of non-oriented steel, and consequently has a Young's modulus of $2.06 \times 10^{11} Nm^{-2}$. To assess the effect this higher core modulus has on the natural frequencies of the core, this stator was represented in a similar way to the West Burton one, with slot wedges and homogenised slot contents of Young's modulus $1.0 \times 10^{9} Nm^{-2}$. The even frequencies only were extracted as only the second order radial mode is of real interest. In Table 5.10 the results are compared with those of the appropriate West Burton representation.

The radial mode frequencies are all higher by factors close enough to the square root of two to indicate that this is the dominant relationship when the Young's modulus is doubled, as predicted by equation (5.9). It is also interesting to note that the second order circumferential mode frequencies of the two nested annuli of each representation have swapped over. For the less stiff core, the mass of the core back is sufficient to ensure it has a lower resonant frequency than the slotted region. However,

the extra stiffness of the stiffer core is sufficient to ensure that it has a higher resonant frequency than the slotted region, despite its greater mass.

Mode	West Burton	350 MW
Radial		
0	532	774
2	169	234
4	711	981
6	1334	1796
Circumferential		
Core 2	1182	1714
Teeth 2	1330	1601

Table 5.10 Comparison of the natural frequencies of the two stator cores

The second order radial mode frequency is considerably above the top of the range usually quoted for turbogenerator stators. However, in the absence of a measurement there is no reason to believe this is not the case. It is really not sensible to suppose that a much stiffer object of similar size to a less stiff object would have the same resonant frequencies.

5.6 Sub-resonant Dynamic Behaviour of the Core Representations

The ovalising forces on the stator bore of a large two-pole turbogenerator are at either 100Hz or 120Hz, depending on whether a 50Hz or 60Hz power supply is being produced.

This is far enough below the core resonant frequency to avoid excessive and damaging vibration levels, but close enough for the dynamic magnifier to be significant.

To assess the significance of the dynamic magnifier at 100Hz, the frequency responses of two of the West Burton core representations were determined. The representations used were the core with empty slots and the core with wedges and slots filled with material of Young's modulus $3.2 \times 10^{9} Nm^{-2}$. Radial forcing only was used in each case, as it was assumed that the response to circumferential forcing would be similar. Transfer coefficients were then derived from harmonic analyses at a range of frequencies from 40Hz to 200Hz.

It is important to consider damping in such an investigation, because the level of damping determines the sharpness of the resonant peak. Representation of damping forces in any system is a difficult matter, because, unlike mass and stiffness, they are not an inherent characteristic of the system. They may also depend on exterior conditions[39]. Damping in any system ensures that natural vibrations excited by a force which is then removed eventually decay away. It is a concept which encompasses a wide range of energy dissipation mechanisms. However, damping effects are customarily categorised as structural, viscous or Coulomb damping.

Structural damping is due to internal friction within the material. The damping forces are proportional to the strain experienced and act to oppose the local velocity at points within the body. Viscous damping occurs when a system vibrates in fluid, including air, and the forces are proportional to, and in opposition to, the velocity. Coulomb damping occurs when a body slides along a dry surface. The damping force is almost constant. The first two forms of damping are most relevant to the turbogenerator

stator.

When modelling damping effects as part of a wider analysis, considerable simplification may be obtained by representing the total damping as an equivalent viscous damping, such that the energy dissipation of the system is the same as if this viscous damping alone had existed in reality[40]. This representation is especially useful because it makes the concept of critical damping meaningful. When a system is vibrating freely, the frequency of the oscillations depends on the level of damping. The higher the damping, the lower the frequency, until a point where the oscillations stop altogether. This is critical damping[41]. Experimental data on damping properties is usually in the form of ratios of actual damping to critical damping.

The damping ratio is dependent on frequency. ANSYS recognises both structural and viscous damping in a steady-state harmonic analysis, and allows input of separate coefficients for each. Structural damping is proportional to frequency; viscous damping inversely proportional. The damping ratio calculated is the sum of the two terms. It can be shown[42] that over a limited range of frequencies the damping ratio thus obtained is approximately constant. The package therefore also allows direct input of a damping ratio value.

Damping ratios for stator cores are difficult to obtain. A common practice is to assume a consistent value of 5%, whilst levels of damping deduced from the results of vibration tests on actual stator structures are in the range of 1% to 3% of critical damping[43]. In the light of this information, a constant damping ratio of 3% of critical damping was selected for the initial frequency response analyses. The effect of varying it was investigated at a later stage.

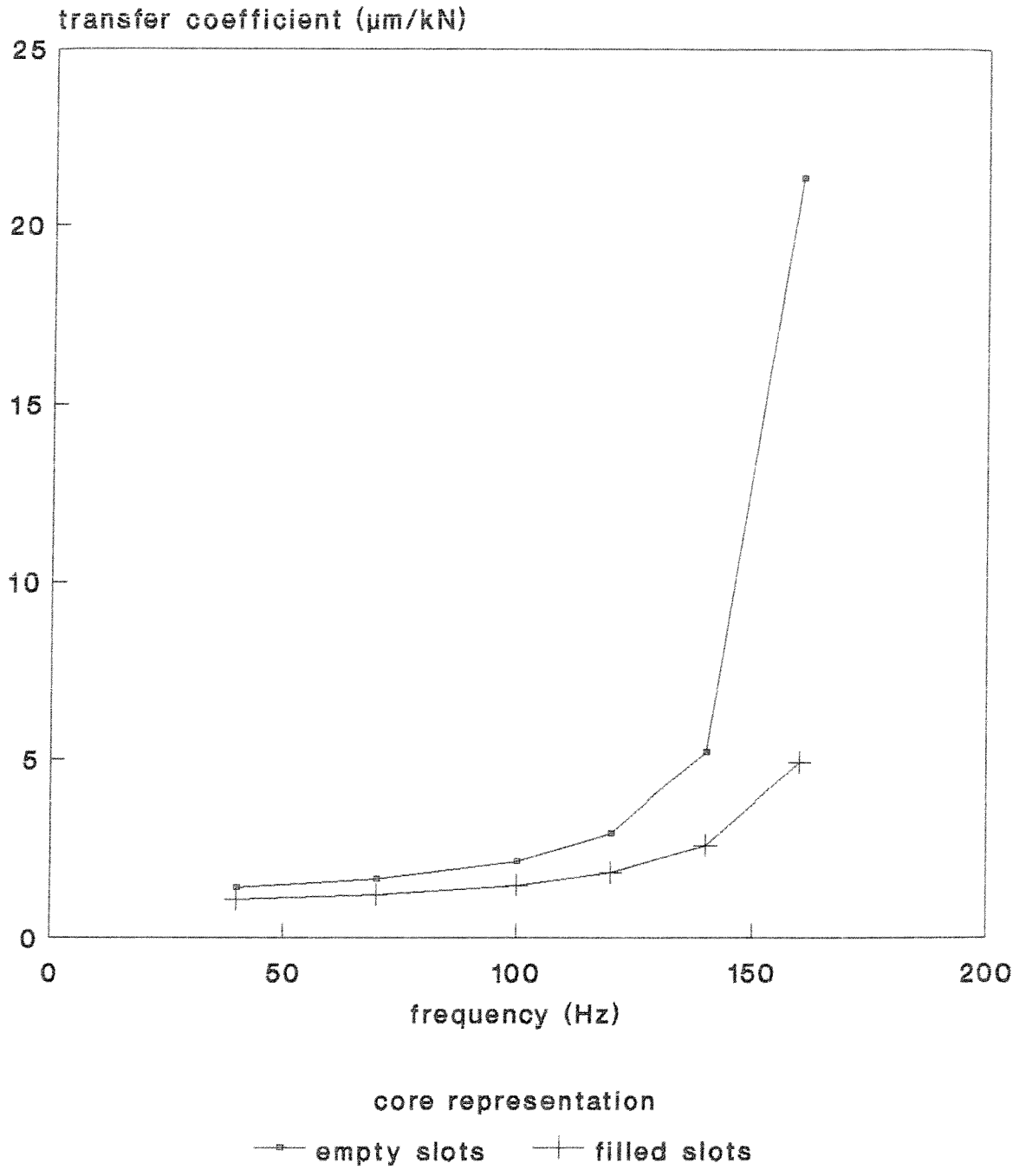

Figure 5.10 Sub-resonant frequency responses of two West Burton stator core representations

The sub-resonant frequency responses of the two core representations are shown in Figure 5.10. It can be seen that for the core with empty slots, vibration levels are higher at all frequencies; also that the dynamic magnifiers at 100Hz and 120Hz are higher due to their greater proximity to the natural mode frequency.

Natural frequencies and frequency response are important in a general assessment of a mechanical model of a stator core. However, the level of double-frequency core ovalising vibration depends on the amplitude of radial and circumferential force transfer coefficients at that frequency, and the trend with varying combinations of tooth forces depends on their ratio. To investigate the variation of the 100Hz transfer coefficients among the various core representations, these were calculated for five cases: the empty slotted core; the core with slot wedges only; the cores with slot contents assigned Young's moduli of $3.2\times10^{8}Nm^{-2}$, $1.0\times10^{9}Nm^{-2}$ and $3.2\times10^{9}Nm^{-2}$. The results are shown in Table 5.11.

Core representation	$k_{r,r}$ (μm/kN)	$k_{r,\theta}$ (μm/kN)	$k_{r,r}/k_{r,\theta}$
Empty slots	2.14	2.28	0.939
Slot wedges only	1.84	1.70	1.082
Slot contents $E=3.2\times10^{8}Nm^{-2}$	1.85	1.72	1.074
Slot contents $E=1.0\times10^{9}Nm^{-2}$	1.73	1.61	1.075
Slot contents $E=3.2\times10_{9}Nm^{-2}$	1.46	1.36	1.076

Table 5.11 Comparison of 100Hz transfer coefficients for various West Burton core representations

The empty slotted core is the only one for which the

ratio $k_{r,r}/k_{r,\theta}$ is less than unity. When the slot contents are modelled with differing Young's moduli, the variation in the ratio is less than 0.2% whilst the modulus varies by a factor of ten. This shows that the ratio between transfer coefficients, which is vital in determining the vibration trend with tooth forces, is highly insensitive to the Young's modulus of the slot contents when it is modelled in this way.

For all further analyses, the value of $1.0 \times 10^{9} Nm^{-2}$ was taken as the standard. It is low enough to give a plausible natural ovalising mode frequency for the West Burton stator core, but sufficiently high to provide confidence in the results, as the stress ratio between teeth and slots is not excessive.

The purpose of the remaining analyses was to investigate the effect of various other parameters on the 100Hz transfer coefficients of the core representations. These parameters are damping ratio, core density and core Young's modulus.

The Ferrybridge core was used to investigate the effect of varying the damping ratio. Although specific data was not available regarding slot contents for this machine, this had become unimportant in the wake of the decision to standardise the slot contents into a homogenous mass of prescribed Young's modulus. It only remained to guess a sensible thickness for the slot wedge.

The circumferential force transfer coefficient was employed to assess the sensitivity of the coefficients to damping ratio at 100Hz. The results at 1%, 3% and 5% of critical damping are shown in Table 5.12. The values of $k_{r,\theta}$ are much lower than those obtained for the West Burton core as the Young's modulus of the Ferrybridge core steel is $1.52 \times 10^{11} Nm^{-2}$ compared with $1.0026 \times 10^{11} Nm^{-2}$, resulting in a

significantly less flexible structure. It can be seen that they vary by less than 1%. It is thus of little importance which value of damping ratio is used in the analysis.

Damping ratio (% of critical damping)	$k_{r,\theta}$ (μm/kN)
1	1.11
3	1.11
5	1.10

Table 5.12 Sensitivity of 100Hz behaviour to damping ratio

The West Burton core was used to investigate the influence of core density. The representation employed was again with filled slots and the now standard Young's modulus for the contents. This particular core was selected for this test because specific data for its density became available at a fairly late stage in this work, when many modal and harmonic analyses had been performed on representations of it under the assumption that its density equalled that of the Ferrybridge core. The values taken by the radial force transfer coefficient at these two densities are shown in Table 5.13.

Density		$k_{r,r}$ (μm/kN)
Origin	Value (kgm^{-3})	
Ferrybridge	7650	1.73
West Burton	7710	1.74

Table 5.13 Sensitivity of 100Hz behaviour to core density

It can be seen that this small increase in density (less than 1%) results in an even smaller increase in radial force transfer coefficient (the order of half a percent). Thus the use of incorrect density in previous analyses cannot be considered to invalidate the results of what are in any case rather crude models of the stator.

The 350MW core was used to investigate the effect of varying core Young's modulus on the transfer coefficients. The empty slotted core representation was used, as this was in fact an early test, but such a situation is useful as it provides greater isolation of the effect than one in which slot contents are additionally defined. The three values of Young's modulus used were the true value for the core; the value for the West Burton core, which is appproximiately half the first value; and a mean value which by coincidence is similar to that of the Ferrybridge core. All four transfer coefficients were extracted in each of the three cases, and the results are shown graphically in Figure 5.11.

From the graph, it appears that an inverse proportionality is the dominant relationship. This is sensible on consideration of the fact that for zero Young's modulus the transfer coefficients will be infinite, whilst for infinite Young's modulus the coefficients will be zero. However, multiplication of the Young's modulus and corresponding transfer coefficient for each point does not give a constant product for any of the four curves, indicating that although inverse proportionality is dominant, it is not the only factor in the relationship.

The radial and circumferential force to radial displacement transfer coefficients are also given in Table 5.14, together with the ratios between them. Although the transfer coefficients themselves vary a great deal with Young's modulus of the core, the ratios vary by very little. Hence if only the trend at 100Hz is required, it is not of

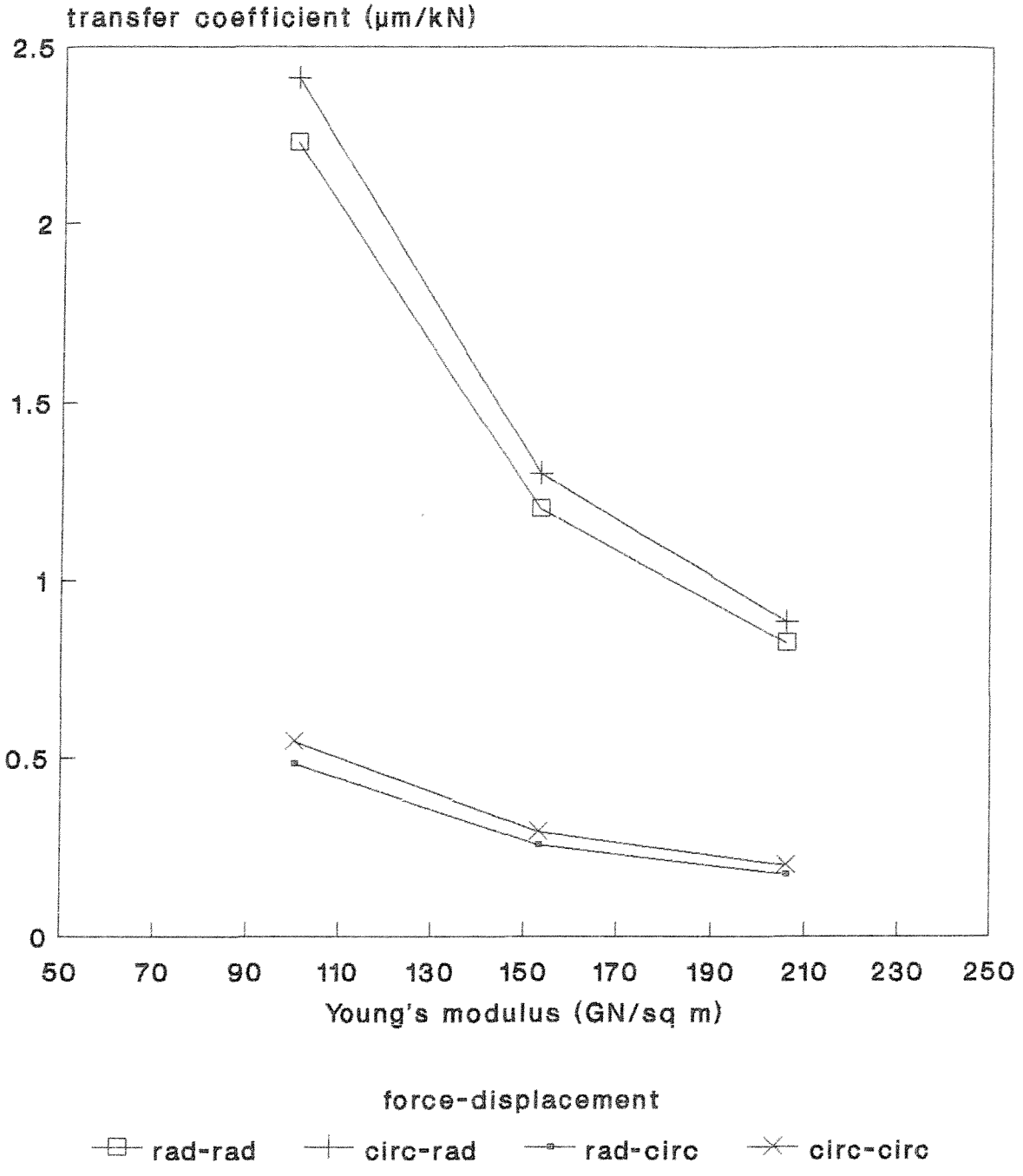

Figure 5.11 Variation of force-displacement transfer coefficients with Young's modulus for the GEC 350MW stator core representation with empty slots

great importance what value of Young's modulus is used for the core. However if, as demonstrated in Section 5.5, the natural frequencies are required, it is of considerable importance.

Core Young's modulus (GNm^{-2})	$k_{r,r}$ ($\mu m/kN$)	$k_{r,\theta}$ ($\mu m/kN$)	$k_{r,r}/k_{r,\theta}$
100	2.23	2.41	0.925
153	1.20	1.30	0.923
206	0.83	0.89	0.933

Table 5.14 Sensitivity of transfer coefficients and their ratio to core Young's modulus

The tests described in this Section have shown that the individual transfer coefficients are highly sensitive to the Young's modulus of both the core and the slot contents. They have also shown that the coefficients are highly insensitive to variations in damping ratio, as might be expected for an off-resonance response. Small variations in density have little effect either. However, the ratio between the two radial displacement transfer coefficients remains approximiately constant over a wide range of Young's modulus. This implies that a similar vibration with load trend would be shown whichever values were used. The ratios do differ, however, between different representations of the cores. From Table 5.11 it can be seen that the ratio varies by about 15% between the empty slotted core (lowest) and the core with wedges only (highest). A final selection would best be made on comparison with the trends produced by test results.

CHAPTER SIX
DEVELOPMENT OF A SELF-CONSISTENT ELECTROMAGNETIC FORCE MODEL OF A CYLINDRICAL ELECTRICAL MACHINE

6.1 A Linear Model with Two Degrees of Freedom

6.1.1 Development

In Section 4.5 it was shown that use of measured rotor and stator currents of the Ferrybridge machine on full load in a simple model produced unrealistically high levels of air-gap flux density. This is because in the real machine these currents have to provide sufficient m.m.f. to overcome leakage and magnetic saturation, so are of necessity significantly higher than those required to produce the same flux density in an ideal, infinitely permeable machine. The conclusion reached in that Section was that if such an idealised representation is to be used, it must be with restricted degrees of freedom. Some of the quantities must be assigned fictitious values in order that the global system may be self-consistent.

The quantity in the model which must be kept true to its physical counterpart is the machine load, in MW and MVAR. This is absolutely necessary as the purpose of the present study is to investigate the variation of double frequency stator core vibration with load.

The important quantities in determining the vibration level are the radial and circumferential Maxwell stresses. The circumferential stress is closely related to the machine torque, and therefore to the power output, which is part of the load condition specified. The radial stress is most heavily dependent on the resultant radial air-gap flux density. If stator leakage is ignored, terminal voltage is directly dependent on this flux density. Thus terminal voltage was selected to be the second independent variable

in the model.

An expression for the r.m.s. generated e.m.f. was derived in Section 3.2, and given as equation (3.5). It was also used in Section 4.5 to demonstrate the inconsistency of using measured rotor current in a simple model. Rearranged, it gives the peak fundamental radial flux density necessary to generate rated terminal voltage on open circuit.

$$\hat{B}_{roc} = \frac{V_T}{\sqrt{2}\sqrt{3}\pi f z L R_s K_w} \qquad (6.1)$$

In Section 4.1, expressions for flux density were derived from vector potential expressions, and as such were in terms of peak fundamental current density of both rotor and stator current sheets. On open circuit there is no stator current, so the second term in equation (4.12) is zero, leaving:

$$B_{roc} = \hat{B}_{roc} \cos(\Theta - \omega t) \qquad (6.2)$$

The magnitude of this sinusoidal distribution may usefully be expressed as:

$$\hat{B}_{roc} = \mu_o T_R C_R I_{Roc} \qquad (6.3)$$

where:

$$T_R = 2[(R_S/R_R)^2 - 1] \qquad (6.4)$$

and C_R is defined such that:

$$C_R I_R = \hat{K}_{R1} \qquad (6.5)$$

It is a condition of this model that the value of $\hat{B}_r$ be kept at $\hat{B}_{roc}$ through all load conditions. On load, the stator term from equation (4.12) reappears, and the complete expression may be rewritten using similar terms for the stator as given for the rotor in (6.4) and (6.5).

$$B_r = \mu_o [T_R C_R I_R \cos(\Theta - \omega t) + T_S C_S I_S \cos(\Theta - \omega t + \lambda)] \qquad (6.6)$$

where: $$T_S = \frac{1+(R_R/R_S)^2}{1-(R_R/R_R)^2} \tag{6.7}$$

and: $$C_S I_S = \hat{K}_{S1} \tag{6.8}$$

To determine the magnitude of B_r, it is necessary to express the latter in terms of components in cos $(\Theta-\omega t)$ and sin $(\Theta-\omega t)$.

$$B_r = \mu_o [\{T_S C_S I_S \cos \lambda + T_R C_R I_R\} \cos (\Theta-\omega t) - T_S C_S I_S \sin \lambda \sin (\Theta-\omega t)] \tag{6.9}$$

whence:

$$\hat{B}_r^2 = \mu_o^2 [(T_S C_S I_S)^2 + (T_R C_R I_R)^2 + 2 T_S T_R C_S C_R I_S I_R \cos \lambda] \tag{6.10}$$

If equation (6.3) is now squared, the two right hand sides can be equated to produce an expression which may be rearranged into the following convenient form:

$$I_R^2 + \frac{2 T_S C_S I_S I_R}{T_R C_R} \cos \lambda + \frac{T_S^2 C_S^2 I_S^2}{T_R^2 C_R^2} - I_{Roc}^2 = 0 \tag{6.11}$$

If U is defined as:

$$U = \frac{T_S C_S I_S}{T_R C_R} \tag{6.12}$$

the equation may be written:

$$I_R^2 + 2 U I_R \cos \lambda + (U^2 - I_{Roc}^2) = 0 \tag{6.13}$$

T_S, C_S, T_R and C_R are all dependent only on machine geometry and so are constant for any given machine. The only quantity in U which may vary is I_S. It is for this reason that U is named the "Current Function". I_S is an independent variable in the model, being obtained from the load and the terminal voltage. Thus (6.13) is an equation in two unknowns, I_R and λ, which must assume unique fictitious values at every load condition for the model to be self-consistent. In order to solve for I_R and λ a second expression is needed. The first was obtained from the

terminal voltage condition; the second comes from the load condition.

The output power of the machine is given by:

$$P = \sqrt{3} V_T I_S \cos \phi \qquad (6.14)$$

which can be related to the electrical torque as follows:

$$P = 2\pi f T_e \qquad (6.15)$$

An expression for T_e was derived in Section 3.6 and is givien in equation (3.33) as:

$$T_e = \pi \hat{B}_{rR} \hat{K}_{s1} R_s^2 L \sin \lambda \qquad (3.33)$$

In the new terminology this becomes:

$$T_e = \pi \mu_o T_R C_R I_R C_S I_S R_s^2 L \sin \lambda \qquad (6.16)$$

Hence T_e may be eliminated from equations (6.15) and (6.16) to give a second expression in I_R and λ:

$$I_R \sin \lambda = \frac{\sqrt{3} V_T \cos \Phi}{2\pi^2 \mu_o f T_R C_R C_S R_s^2 L} = W \qquad (6.17)$$

The quantity W is independent of stator current. Besides geometry, it depends only on the terminal voltage and power factor. It is named the "Power Function" from its origin.

It is now possible to substitute for I_R into (6.13), producing an equation in λ only which may be solved algebraically.

$$W^2/\sin^2\lambda + 2UW \cos \lambda/\sin \lambda + (U^2 - I_{Roc}^2) = 0 \qquad (6.18)$$

Equation (6.18) is not readily soluble in its present form. The method of solution developed expresses it as a quadratic in $\sin^2\lambda$ and thereby uses the standard solution for a quadratic equation[44]. The procedure is first to multiply through by $\sin^2\lambda$, replace $\cos \lambda$ by $\sqrt{(1-\sin^2\lambda)}$, and square the whole equation to give:

$$[(U^2 - I_{Roc}^2)^2 + 4U^2W^2]\sin^4\lambda - 2W^2(I_{Roc}^2 + U^2)\sin^2\lambda + W^4 = 0 \qquad (6.19)$$

Equation (6.19) has four roots. The two negative roots are of no interest. The two positive roots may be substituted back into equation (6.17) to produce two values of I_R. It is evident that one such value applies if the machine is underexcited; the other if it is overexcited. The overexcited value is of course the larger in magnitude. At unity power factor the two will be equal.

Extraction of λ is not as simple. The inverse sine is a multi-valued function, and squaring the equation causes the quadrant locations of the original angles to be lost. They can, however, be recovered by considering a graphical solution to equation (6.18). This is simplest if the equation is again multiplied by $\sin^2\lambda$, and the term $\sin\lambda \cos\lambda$ replaced by $\frac{1}{2} \sin 2\lambda$, as in equation (4.19). This gives:

$$W^2 + UW \sin 2\lambda + (U^2 - I_{Roc}^2) \sin^2\lambda = 0 \qquad (6.20)$$

Equation (6.20) may be rearranged into:

$$W^2 + UW \sin 2\lambda = - (U^2 - I_{Roc}^2) \sin^2\lambda \qquad (6.21)$$

If the two sides of this equation are plotted as separate functions on the same set of axes, the solutions occur at the intersection of the two curves. Figure 6.1 shows the three possible situations pertaining in this graphical solution.

Figure 6.1(a) shows the situation in which $U^2 > I_{Roc}^2$. As U^2 is dependent only on stator current for a given machine, this will occur at higher loads. Both values of λ lie in the second quadrant.

There are two possible situations for $I_{Roc}^2 > U^2$. Over a range of loads U and I_{Roc} will be very close in magnitude, and the difference of their squares will be less than the square of the power function. This is shown in Figure 6.1(b). Again, both solutions lie in the second quadrant. At the lowest loads, U is so much smaller than I_{Roc} that the

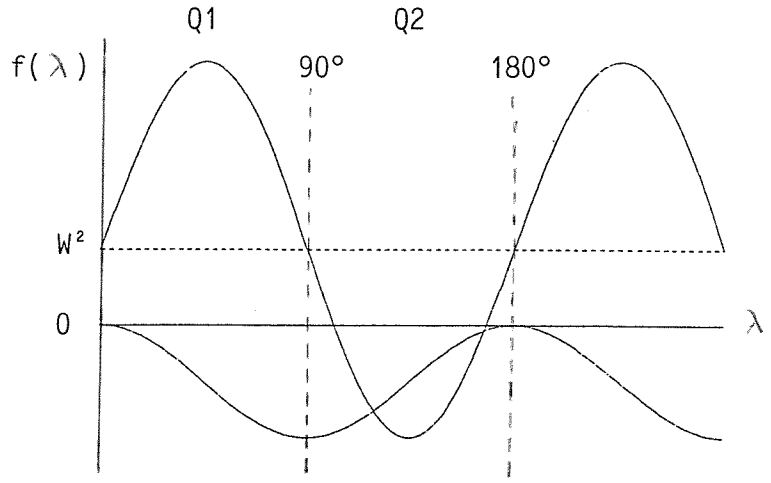

(a) $U^2 > I_{Roc}^2$

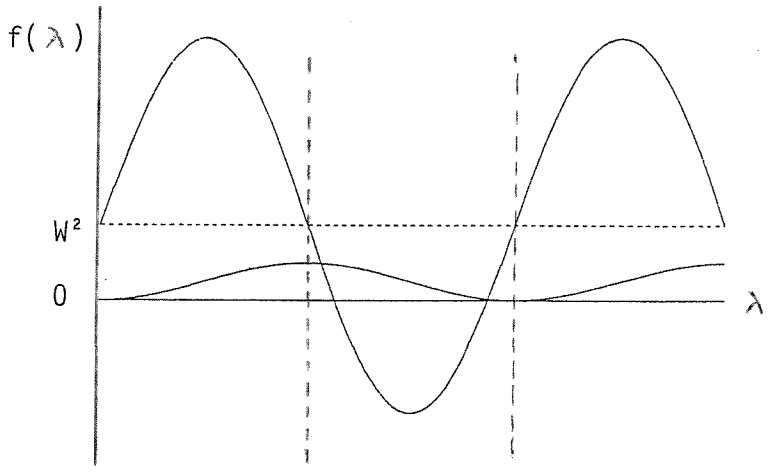

(b) $U^2 < I_{Roc}^2$ and $I_{Roc}^2 - U^2 \leq W^2$

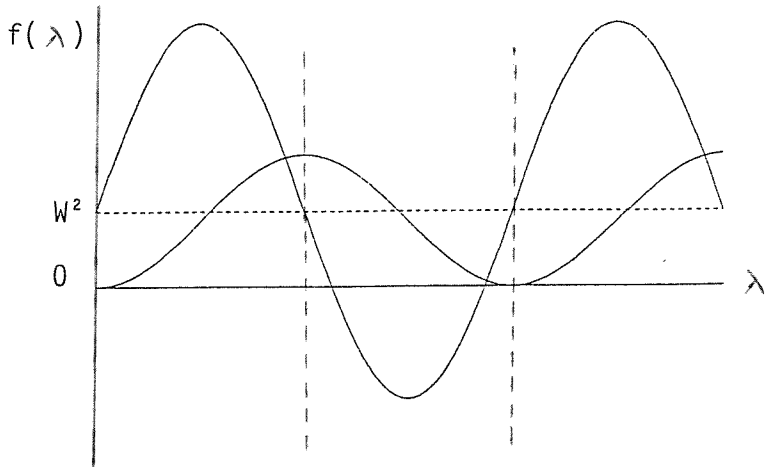

(c) $U^2 < I_{Roc}^2$ and $I_{Roc}^2 - U^2 > W^2$

Figure 6.1 Graphical solutions for torque angle

difference in their squares exceeds the square of the power function. Now one of the solutions lies in the first quadrant, as shown in Figure 6.1(c).

The power function is dependent, for a given terminal voltage, on power factor. Thus the range of loads for which the second situation applies is largest at unity power factor and collapses to zero at zero power factor.

A computer solution to equation (6.19) would, on completing the solution of the quadratic, test the relative magnitudes of the relevant quantities and thereby assign suitable quadrant locations to λ.

As previously stated, the two values of I_R converge in the unity power factor case. Further insight into the model may be obtained by consideration of the relevant algebraic relationships. With reference to equation (6.19) and the standard quadratic solution, the following is true:

$$4W^4(I_{Roc}^2+U^2)^2 = 4W^4[(U^2-I_{Roc}^2)^2+4U^2W^2] \qquad (6.22)$$

After dividing through by $4W^4$ and multiplying out, this becomes:

$$I_{Roc}^4+2U^2I_{Roc}^2+U^4 = U^4-2U^2I_{Roc}^2+I_{Roc}^4+4U^2W^2 \qquad (6.23)$$

Elimination of terms which appear on both sides and collecting other like terms gives:

$$4U^2I_{Roc}^2 = 4U^2W^2 \qquad (6.24)$$

whence:

$$I_{Roc} = W \qquad (6.25)$$

Thus it appears that the unity power factor condition is characterised by the fact that the power function is equal to the open circuit rotor current consistent with the infinitely permeable model.

Further light can be shed upon this equality by defining W' such that:

$$W = W' \cos \phi \tag{6.26}$$

which enables equation (6.17) to be written:

$$I_R \sin \lambda = W' \cos \phi \tag{6.27}$$

This relationship applies at all conditions of the model, which must therefore include open circuit. Figure 6.2 shows the e.m.f. phasor diagrams for open circuit, and for a very low load approaching open circuit.

On open circuit, the generated e.m.f. and the terminal voltage are the same, as shown in Figure 6.2(a). It can be seen from Figure 6.2(b) that as the load approaches open circuit, i.e. the stator current tends to zero, the angles λ and Φ tend to limits of 90° and 0° respectively. Hence

$$I_{Roc} = W' \tag{6.28}$$

The power function can therefore be defined as the open circuit rotor current consistent with the infinitely permeable model multiplied by the power factor. This may also be proved by manipulation of the terminal voltage equation.

6.1.2 Implementation

The computer program to implement the model starts by reading in the terminal voltage from the computer terminal. It then calculates the open circuit air-gap flux density using equation (6.1), and the constants C_R, T_R and T_S; finally concluding this preliminary section by calculating the open circuit rotor current consistent with the infinitely permeable model.

The next section handles the load condition input. The user is offered a choice of input format: either in terms of power and power factor or active and reactive power. The

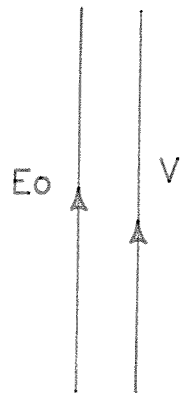

(a) Open circuit

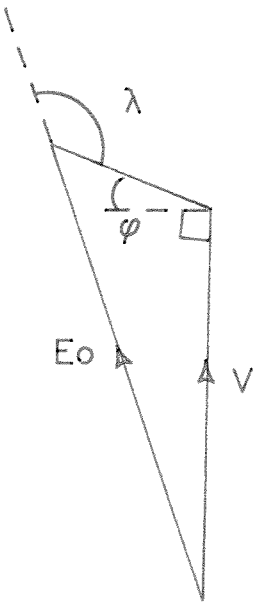

(b) Very low load

Figure 6.2 E.m.f. phasor diagrams

nature of the power factor is also requested, with the options given as 'lead' and 'lag'. This is necessary to ensure selection of the correct value of I_R. From this information the peak stator current and the power factor angle are calculated. To avoid the possibility of accumulated rounding errors producing imaginary roots to equation (6.19), an input of unity power factor is reset to 0.999999999. There is also a routine which ensures the main calculation is bypassed when an open circuit condition is requested. This is to avoid the situation of dividing by zero. Finally the fundamental peak stator current density $\hat{K}_{S1}$ is calculated.

The section which follows these preliminaries actually implements the model developed, producing I_R and λ as output. First, the power function, W, is evaluated from the consistent open circuit rotor current and the power factor. Secondly, the current function, U, is evaluated. Then the coefficients of the quadratic equation (6.19) are defined as single variables A1, A2 and A3, after which this equation is solved to give two values of sin λ. Tests are then performed in accordance with the conditions identified in Figure 6.1 to determine the quadrant locations of the two values of λ, hence the actual values. Which value is relevant to the input load condition is determined subsequent to the calculation of the two corresponding values of I_R. If a lagging power factor load has been specified, the larger I_R is selected and the corresponding λ becomes that to be used. If a leading power factor load has been specified the smaller I_R is selected.

All that remains is for the peak fundamental rotor current density to be calculated from the rotor current, before the analysis can procede as described in Sections 4.1 and 4.4 to produce the radial and circumferential tooth forces.

Following the work of Chapter Five, output can be produced in the useful form of core-back radial vibration levels. The tooth forces are multiplied by the relevant transfer coefficients, which are read in as part of the data for a given machine. Then, with reference to the phasor diagram of Figure 5.4, a little simple trigonometry produces a net core-back radial vibration level.

6.1.3 Results

P (MW)	cos ϕ	F_r (kN)	F_0 (kN)	ψ (°)	d_r (μm)	Red'n below o/c (%)
0	1.0	11.98	0.00	0.00	14.01	-
125	.85 lag	11.93	2.22	147.77	12.82	8.49
250	.85 lag	11.80	4.44	146.42	11.82	15.63
375	.85 lag	11.60	6.66	144.12	11.01	21.41
500	.85 lag	11.34	8.88	140.75	10.38	25.91
625	.85 lag	11.08	11.09	136.22	9.94	25.09
500	.75 lead	11.90	10.06	231.55	23.71	-69.24
500	.85 lead	11.34	8.88	219.25	20.94	-49.46
500	.95 lead	10.95	7.94	202.29	18.09	-29.12
500	1.0	10.79	7.54	180.00	15.15	-8.14
500	.95 lag	10.95	7.94	157.71	12.49	10.85
500	.85 lag	11.34	8.88	140.75	10.38	25.91
500	.75 lag	11.90	10.06	128.45	8.66	38.19
588 MVAR	0 lead	13.62	8.88	270.00	25.79	-84.08
588 MVAR	0 lag	13.62	8.88	90.00	6.09	56.53

Table 6.1 Results of the two-degree-of-freedom model

Table 6.1 gives the vibration levels for various loads at the rated power factor of 0.85 lag and various power factors at the rated load of 500MW for the Ferrybridge generator. The transfer coefficients used are those obtained with the standardised slot contents of Young's modulus equal to $1.0 \times 10^9 Nm^{-2}$. The Table also gives the tooth forces and phase angles between them from which the vibration amplitudes are obtained.

The first section of the table shows the result of increasing power from zero to 25% overload whilst retaining the rated power factor of 0.85 lag. The radial tooth force decreases by a small amount over the range, due to the increase in B_θ. The circumferential tooth force increases in proportion to stator current; to be expected, as constant B_r is a defined condition of the model. The angle ψ between the forces decreases with increased load. Thus there are two effects which tend to decrease the overall vibration level. As the angles in question are greater than 90°, a decrease brings the forces more directly into opposition, whilst the equalising of the forces facilitates a greater level of cancellation.

The second section shows the effect of varying the power factor, between 0.75 lead and 0.75 lag through unity, whilst retaining the rated active load of 500MW. The circumferential force once again shows its direct dependence on stator current. The radial force shows its greatest decrease where the stator current is lowest, at unity power factor, indicating that the change in internal angle of the machine is of greater importance here than the magnitude of the flux density. It is interesting to note that the sum of the phase difference between the forces for any given leading power factor and the corresponding quantity for the same lag angle is equal to 360°. At unity power factor this phase difference is unsurprisingly 180°. The third section of Table 6.1 shows the machine on rated stator current but

at zero power factor, lead and lag. It can be seen that for zero leading power factor the angle between tooth forces is 270°, leading to direct mutual reinforcement of the ovalising distortions; whilst for zero lag the angle is 90°, leading to direct cancellation.

The vibration results therefore show a decrease with increased power for constant power factor, and a decrease from low leading to low lagging power factor for constant power. The highest and lowest vibration levels for any load current may be expected at zero leading and zero lagging power factor respectively.

The decrease in vibration between open circuit and full rated load is 25.91%. This is lower than the observed decrease of 30-40%. Therefore this simple model cannot be considered adequate for the modelling of stator core vibration of a large turbogenerator on load. However, it has shown that the trend with load and power factor is in the same direction as that observed on real machines, and given insight as to why this is so by demonstrating that the phase difference between the radial and circumferential tooth forces is linked to the power factor angle.

It is now possible to conclude that the primary mechanism behind the observed variation in double-frequency stator core vibration with load is the variation in magnitude and phase difference of the radial and circumferential components of double-frequency electromagnetic force on the stator bore. In order to model the variation with acceptable accuracy, however, it is necessary to extend the model to incorporate secondary mechanisms. The two most important secondary mechanisms are likely to be the combination of higher m.m.f. harmonics to produce a double-frequency force component, and magnetic saturation.

The behaviour of the higher harmonics was discussed at length in Section 4.2, when it was concluded that their effect would be highly machine geometry dependent and that a general analysis would therefore be of little use. The analysis performed in this Section used the minimum model of Section 4.1, but the two-degree-of-freedom equations could equally be programmed in a numerical analysis of the type described in Section 4.3, which could include the higher harmonics if required.

Inclusion of magnetic saturation is not as straightforward. Such a scheme would first require that the rotor and stator be assigned finite permeability, which would complicate the vector potential boundary condition equations considerably. Then it would be necessary to devise a method of adjusting permeability with load, to simulate different degrees of saturation. However, it is likely that such a step is necessary, as the internal angles of the machine have been shown to be crucial in determining vibration level. Recent work involving finite element magnetic field analyses of turbogenerators[45] has shown that the presence of saturation has a significant effect on load angles.

In the next Section, the philosophy of the two-degree-of-freedom model is applied to a broadened electromagnetic scenario by the development of a model which can incorporate both saturation and harmonics.

6.2 Development of a Model to Include Harmonics and Magnetic Saturation

6.2.1 Introduction: Philosophy of the Model

The model developed in this Section has two important purposes. The first is to provide a better model than that of Section 6.1 of the variation of double-frequency stator

core vibration of a large turbogenerator on load. The second is to provide a framework for investigating the effects of various parameters on the calculated vibration levels. Thus those found to be of greatest importance may be modelled with greatest care, and those found to be of least importance may be discarded in order to keep the model as simple as practicable. Simplicity is important if the model is to provide the basis for an on-line monitoring scheme.

To satisfy the second purpose, the model needs to be very flexible, with scope for varying many parameters easily. Figure 6.3 shows a section of the multi-region model devised according to this criterion. The machine cross-section is modelled in seven regions, numbered outwards one to seven. Region 1 is the rotor body. Regions 2 and 3 cover the cross-section occupied by the rotor teeth and slots. They are separated by the rotor current sheet. Region 4 is the air gap. Regions 5 and 6 represent the stator slotted region, being separated, in a similar manner to regions 2 and 3, by the stator current sheet. Region 7 is the stator core.

All regions possess finite relative permeability, which may be defined separately for each region. This is important, because saturation is not uniform throughout the machine. It tends to be higher in the rotor body than in the stator core, and highest of all in the teeth. Furthermore, whilst the two bodies may reasonably be considered homogenous, and therefore be presenting the same reluctance to flux in any direction, the same does not apply to the slotted regions. Here, radial flux passes through an array of teeth and slots in parallel whilst circumferential flux must pass through each tooth and slot in turn: obviously a path of far higher reluctance. A scheme is developed in Section 6.2.2 for modelling this anisotropy by the use of directional permeabilities.

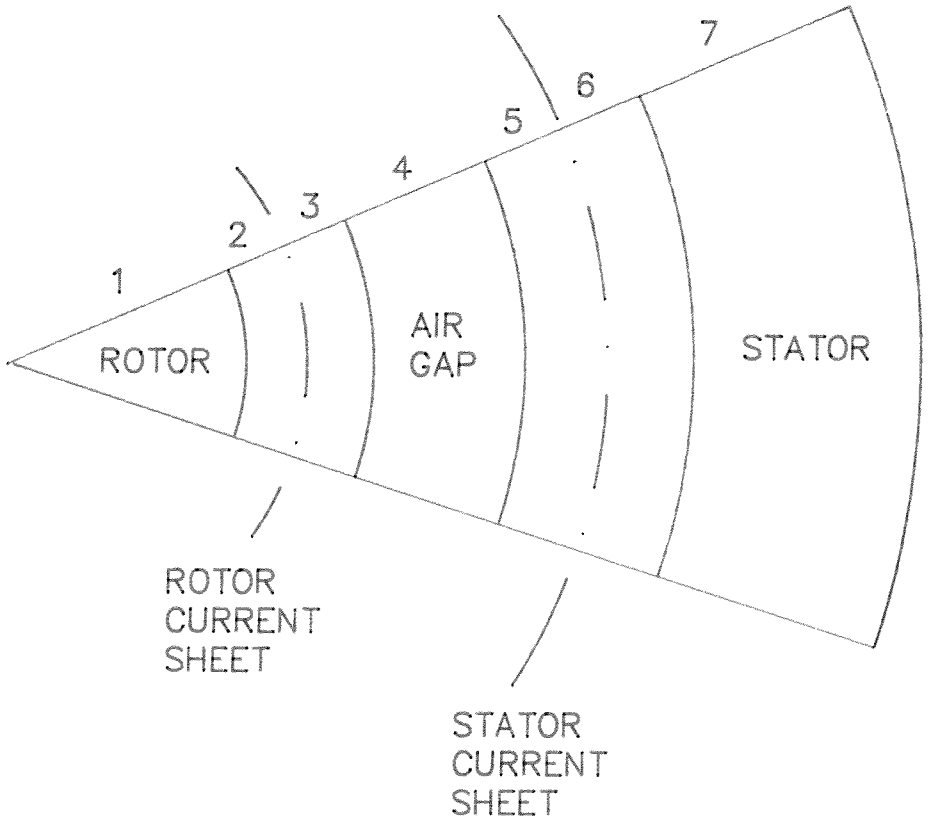

Figure 6.3 A section of the multi-region model

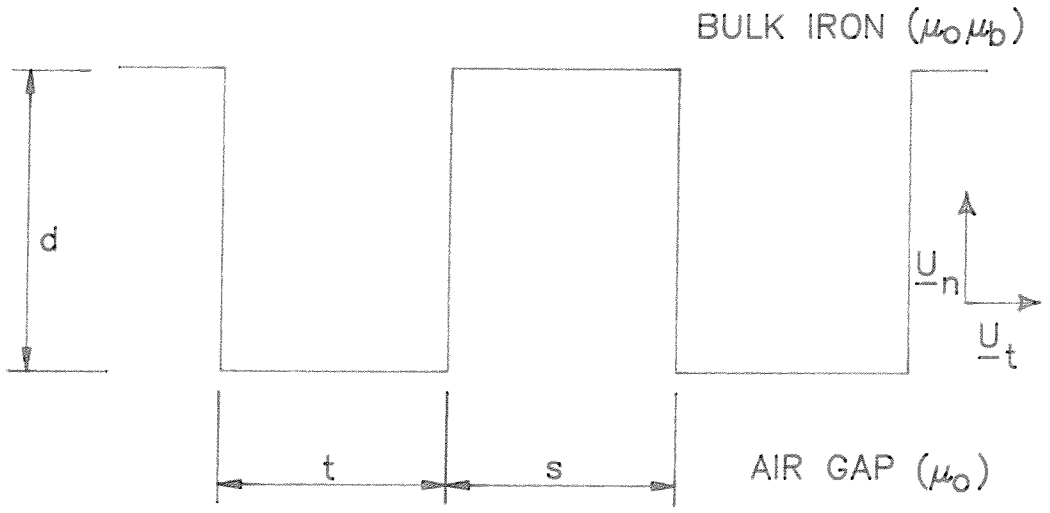

Figure 6.4 Geometry of the slotted regions

The positions of the current sheets may be varied within the slotted regions, by adjusting the radii of the cylindrical sheets. The purpose of this is to investigate the validity of placing them on the rotor surface and stator bore as hitherto, and, if necessary, to determine suitable alternative positions.

The end result has the initial appearance of being excessively complex. However, the available modes of simplification are many and straightforward. To return to the old infinite permeability model, the relative permeabilities of the iron regions may be set to a very high value, e.g. ten thousand. To make them all homogenous the slotted regions may be shrunk to a nominal thickness below the error margin of the dimensional data: effectively zero. Similarly, the current sheets may be shrunk onto the surfaces of the air gap by assigning minimal dimensions to regions 3 and 5. It is simpler to shrink regions to nominal dimensions than to remove them altogether. To do the latter would demand a new system of equations, because it amounts to altering the boundary conditions.

6.2.2 Modelling the Slotted Regions

Figure 6.4 shows the geometry of a generalised case of a slotted region, similar to that of either the stator or the rotor. By inspection, it is evident that the normal permeability, if t and s are approximately equal, will be about half the bulk permeability μ_b; also that the tangential permeability will be approximately two.

A more exact formula for the normal permeability, μ_n, may be derived by considering an equivalent reluctance of one slot pitch, R', such that :

$$R' = \frac{d}{(t+s)\mu_o \mu_n} \qquad (6.29)$$

This is obtained from the respective reluctances of the tooth and the slot:

$$R_t = \frac{d}{t\mu_o\mu_b} \qquad \text{and} \qquad R_s = \frac{d}{s\mu_o} \tag{6.30}$$

combined in parallel:

$$R' = \frac{R_s R_t}{R_s + R_t} \tag{6.31}$$

The normal permeability emerges as:

$$\mu_n = \frac{s+t\mu_b}{s+t} \tag{6.32}$$

The following formula may be applied to obtain the tangential permeability, μ_t:

$$\mu_t = \frac{1}{1-\delta+\delta/\mu_b} \tag{6.33}$$

where δ is the iron-space factor defined as:

$$\delta = \frac{t}{t+s} \tag{6.34}$$

Equation (6.33) was derived in work of which the purpose was to study magnetic fields in the end region of a turbogenerator with the aim of calculating eddy current losses[46]. Thus the "tangential" direction corresponded to the axial direction in the machine, whereas in the present work it corresponds to the circumferential direction. The constant δ was the packing factor for the laminations. The two situations are similar in that they comprise an alternation of layers of magnetic and non-magnetic material.

Calculation of μ_n and μ_t for the stator is straightforward, because the bore is uniformly slotted. The rotor, however, has solid pole faces, so to use physical dimensions for t and s would not be strictly valid. The approach adopted here is to consider a dummy slot pitch equivalent to that which would be in evidence if the rotor possessed the

same number of slots as it does in reality, but evenly spaced around its surface. Thus s takes its true dimension, but t adopts a larger value.

6.2.3 Implementation of the Multi-region Model

As in previous electromagnetic models, the result required is the air-gap flux density at the stator bore, from the components of which the Maxwell stresses may be calculated. Expressions for flux density are obtained from expressions for magnetic vector potential through the relationship B = curl A.

For the rotor body, stator core and air gap, the expressions for vector potential are those given in equations (3.27). However, in the regions of anisotropic permeability, Laplace's equation does not apply, and it is necessary to return to the original definition curl A = B, and also to consider the fact that there are no volume currents: i.e. curl H = 0.

The full vector expression for flux density in this case is:

$$B = \mu_o \mu_n H_r \mathbf{u}_r + \mu_o \mu_t H_\theta \mathbf{u}_\theta \qquad (6.35)$$

where $\mathbf{u}_r$ and $\mathbf{u}_\theta$ are unit vectors in radial and circumferential directions. A has an axial component only, as before, so application of the curl equations gives:

$$\frac{1}{r}\frac{\partial A}{\partial \Theta} = \mu_o \mu_n H_r \qquad (6.36a)$$

and

$$-\frac{\partial A}{\partial r} = \mu_o \mu_t H_\theta \qquad (6.36b)$$

Expanding curl H = 0, with $H_z = 0$ and $\partial/\partial z = 0$ gives:

$$\frac{\partial H_\theta}{\partial r} + \frac{H_\theta}{r} - \frac{1}{r}\frac{\partial H_r}{\partial \Theta} = 0 \qquad (6.37)$$

If equations (6.36) are then substituted into equation

(6.37) such that H_r and H_θ are eliminated, the result is a differential equation in A.

$$\mu' \frac{\partial^2 A}{\partial r^2} + \frac{\mu'}{r} \frac{\partial A}{\partial r} + \frac{1}{r^2} \frac{\partial^2 A}{\partial \Theta^2} = 0 \qquad (6.38)$$

where $\mu' = \mu_n / \mu_t$.

If it is assumed that, as in the Laplacian case, A is the product of functions in r and Θ, i.e.:

$$A = R(r)\ T(\Theta) \qquad (6.40)$$

then equation (6.38) may be written, after rearrangement:

$$\frac{\mu' r^2}{R} \frac{d^2 R}{dr^2} + \frac{\mu' r}{R} \frac{dR}{dr} + \frac{1}{T} \frac{d^2 T}{d\Theta^2} = 0 \qquad (6.41)$$

The function T will be a sinusoid, so it is possible to substitute:

$$\frac{1}{T} \frac{d^2 T}{d\Theta^2} = - p^2 \qquad (6.42)$$

If q is defined such that:

$$q = p/\sqrt{\mu'} \qquad (6.43)$$

the solution for R is of the form $R \propto r^{\pm q}$. Therefore, in the region of anisotropic permeability, the vector potential takes the form:

$$A = (Lr^q + Mr^{-q}) \sin p\Theta \qquad (6.44)$$

where p is now obviously the order of the harmonic component of A when the vector potential is expressed as a Fourier series, in line with a Fourier series representation of the windings.

If the simplifying assumption is made that no flux leaks from the core back, expressions for the vector potential in each of the seven regions may be written. Each expression represents the case for any harmonic, p, of the Fourier series. As the directional permeabilities of rotor and stator slotted regions are not the same, it is necessary

to define separate indices for the relevant expressions in place of q used in the derivation.

For the rotor: $g = p\sqrt{(\mu_{tR}/\mu_{nR})}$ (6.45)

For the stator: $h = p\sqrt{(\mu_{ts}/\mu_{ns})}$ (6.46)

in which μ_{tR}, μ_{nR}, μ_{ts} and μ_{ns} are the directional permeabilities of the rotor and stator slotted regions as defined by equations (6.32) and (6.33). The radii R_1 to R_7 are defined as the outer radii of the region with the same number. R_7 is the core-back radius, and here A=0. Within Region 1 there is no dependence on r^{-p}. The complete set of expressions is:

$$A_1 = L_1 r^p \sin p\Theta \quad (6.47a)$$

$$A_2 = (L_2 r^g + M_2 r^{-g}) \sin p\Theta \quad (6.47b)$$

$$A_3 = (L_3 r^g + M_3 r^{-g}) \sin p\Theta \quad (6.47c)$$

$$A_4 = (L_4 r^p + M_4 r^{-p}) \sin p\Theta \quad (6.47d)$$

$$A_5 = (L_5 r^h + M_5 r^{-h}) \sin p\Theta \quad (6.47e)$$

$$A_6 = (L_6 r^h + M_6 r^{-h}) \sin p\Theta \quad (6.47f)$$

$$A_7 = L_7 (r^p - R_7^{2p} r^{-p}) \sin p\Theta \quad (6.47g)$$

There are twelve unknowns in total of which only two, L_4 and M_4, need to be found explicitly. However, this still requires that twelve equations be found to provide the explicit solutions. The conditions at the six inter-region boundaries described in Section 3.3 provide the necessary equations. These are that A is continuous across a boundary and the difference in circumferential magnetic field intensity between one side of the boundary and the other is equal to the surface current density on that boundary.

The following conditions ensue:

1) at $r=R_1$

$$A_1 = A_2 \quad \text{and} \quad \frac{1}{\mu_R}\frac{\partial A_1}{\partial r} - \frac{1}{\mu_{tR}}\frac{\partial A_2}{\partial r} = 0 \quad (6.48a)$$

2) at $r=R_2$

$$A_2 = A_3 \quad \text{and} \quad \frac{\partial A_2}{\partial r} - \frac{\partial A_3}{\partial r} = \mu_o \mu_{tR} \hat{K}_R \sin p(\Theta-\delta) \qquad (6.48b)$$

3) at $r=R_3$

$$A_3 = A_4 \quad \text{and} \quad \frac{1}{\mu_{tR}} \frac{\partial A_3}{\partial r} - \frac{\partial A_4}{\partial r} = 0 \qquad (6.48c)$$

4) at $r=R_4$

$$A_4 = A_5 \quad \text{and} \quad \frac{\partial A_4}{\partial r} - \frac{1}{\mu_{ts}} \frac{\partial A_5}{\partial r} = 0 \qquad (6.48d)$$

5) at $r=R_5$

$$A_5 = A_6 \quad \text{and} \quad \frac{\partial A_5}{\partial r} - \frac{\partial A_6}{\partial r} = \mu_o \mu_{ts} \hat{K}_S \sin p(\Theta+\alpha) \qquad (6.48e)$$

6) at $r=R_6$

$$A_6 = A_7 \quad \text{and} \quad \frac{1}{\mu_{ts}} \frac{\partial A_6}{\partial r} - \frac{1}{\mu_s} \frac{\partial A_7}{\partial r} = 0 \qquad (6.48f)$$

where μ_S and μ_R are body permeabilities and α and δ are the stator and rotor load angles.

Solution of the equations is simplified considerably if, as before, the rotor and stator are considered to be excited separately and alone. This way, instead of using the resultant field axis as reference, the rotor field axis can be used, so that rotor quantities vary as Θ whilst stator quantities vary as $\Theta+\lambda$. Then the Θ-dependent parts of the A expressions are completely cancelled from each set of equations. There is also the inherent increase in simplicity of going from twelve equations in twelve unknowns to ten.

When the stator is excited, equation (6.48b) may be discarded, and A_3 replaced by A_2 in equation (6.48c).

At R_1, the rotor slot bottom radius (equations 6.48a), the first boundary condition gives the following expression

for L_1:

$$L_1 = L_2 R_1^{g-p} + M_2 R_1^{-g-p} \tag{6.49}$$

The second boundary condition gives:

$$L_1 = \frac{g\mu_R}{p\mu_{tR}} \left(L_2 R_1^{g-p} - M_2 R_1^{-g-p}\right) \tag{6.50}$$

Elimination of L_1 between the equations gives M_2 in terms of L_2:

$$M_2 = L_2 R_1^{2g} X_2 \tag{6.51}$$

where:
$$X_2 = \frac{\frac{g\mu_R}{p\mu_{tR}} - 1}{\frac{g\mu_R}{p\mu_{tR}} + 1} \tag{6.52}$$

At R_3, the rotor surface (equations 6.48c), the first boundary conditon gives:

$$L_2 = \frac{L_4 R_3^{g+p} + M_4 R_3^{g-p}}{R_3^{2g} + X_2 R_1^{2g}} \tag{6.53}$$

and the second gives:

$$L_2 = \frac{p\mu_{tR}}{g} \frac{(L_4 R_3^{p+g} - M_4 R_3^{g-p})}{(R_2^{2g} - X_2 R_1^{2g})} \tag{6.54}$$

From which:

$$M_4 = L_4 R_3^{2p} X_3 \tag{6.55}$$

where:
$$X_3 = \frac{1 - \frac{g \quad (R_3^{2g} - X_2 R_1^{2g})}{p\mu_{tR} (R_3^{2g} + X_2 R_1^{2g})}}{1 + \frac{g \quad (R_3^{2g} - X_2 R_1^{2g})}{p\mu_{tR} (R_3^{2g} + X_2 R_1^{2g})}} \tag{6.56}$$

At R_4, the stator bore radius (equations 6.48d), the first boundary condition gives:

$$L_4 = \frac{L_5 R_4^{p+h} + M_5 R_4^{p-h}}{R_4^{2p} + X_3 R_3^{2p}} \tag{6.57}$$

whilst the second gives:

$$L_4 = \frac{h}{p\mu_{ts}} \frac{(L_5 R_4^{p+h} - M_5 R_4^{p-h})}{(R_4^{2p} - X_3 R_3^{2p})} \tag{6.58}$$

From which:

$$M_5 = L_5 R_4^{2h} X_4 \tag{6.59}$$

where: $$X_4 = \frac{1 - \frac{p\mu_{ts}(R_4^{2p} - X_3 R_3^{2p})}{h (R_4^{2p} + X_3 R_3^{2p})}}{1 + \frac{p\mu_{ts}(R_4^{2p} - X_3 R_3^{2p})}{h (R_4^{2p} + X_3 R_3^{2p})}} \tag{6.60}$$

The next boundary, R_5 (equations 6.48e), is the position of the stator current sheet. The first boundary conditions give a similar expression to that at previous boundaries:

$$L_5 = \frac{L_6 R_5^{2h} + M_6}{R_5^{2h} + X_4 R_4^{2h}} \tag{6.61}$$

However, the current sheet appears in the second boundary condition, producing an expression for L_5 in L_6, M_6 and $\hat{K}_s$.

$$L_5 = \frac{L_6 R_5^{2h} - M_6 + \frac{\mu_o \mu_{ts}}{h} \hat{K}_s R_5^{h+1}}{R_5^{2h} - X_4 R_4^{2h}} \tag{6.62}$$

Combining the two gives a rather more involved relationship between M_6 and L_6 than between previous pairs of coefficients.

$$M_6 = L_6 R_5^{2h} \frac{(1-X_5)}{(1+X_5)} + \frac{\mu_o \mu_{ts} \hat{K}_s R_5^{h+1}}{h(1+X_5)} \tag{6.63}$$

where: $$X_5 = \frac{R_5^{2h} - X_4 R_4^{2h}}{R_5^{2h} + X_4 R_4^{2h}} \tag{6.64}$$

The stator slot bottom radius is the final boundary to be considered (equations 6.48f), and the result is an explicit expression for L_7, the coefficient for the stator core.

$$L_7 = \frac{\frac{\mu_o \mu_{ts}}{h} \hat{K}_S R_5^{h+1} \frac{(1+X_6)}{(1+X_5)}}{X_6 (R_6^{h+p} - R_7^{2p} R_6^{h-p}) - \frac{p\mu_{ts}}{h\mu_s} (R_6^{h+p} - R_7^{2p} R_6^{h-p})} \qquad (6.65)$$

where: $$X_6 = \frac{R_6^{2h} - R_5^{2h} \frac{(1-X_5)}{(1+X_5)}}{R_6^{2h} - R_5^{2h} \frac{(1-X_5)}{(1+X_5)}} \qquad (6.66)$$

All that remains to be done now is to substitute backwards through equations (6.61) and (6.57) until an explicit expression for L_4 is obtained:

$$L_6 = \frac{L_7 (R_6^{h+p} - R_7^{2p} R_6^{h-p}) - \frac{\mu_o \mu_{ts}}{h} \frac{\hat{K}_S R_5^{h+1}}{(1+X_5)}}{R_6^{2h} + R_5^{2h} \frac{(1-X_5)}{(1+X_5)}} \qquad (6.67)$$

$$L_5 = L_6 + \frac{\mu_o \mu_{ts}}{2h} \hat{K}_S R_5^{1-h} \qquad (6.68)$$

$$L_4 = \frac{L_5 R_4^{p+h} (1+X_4)}{R_4^{2p} + X_3 R_3^{2p}} \qquad (6.69)$$

Now let $L_4 = L_S$ and $M_4 = M_S$, where M_4 is defined by equation (6.55). The pth harmonic of vector potential at the stator bore due to the stator current sheet is given by:

$$A_{sp} = (L_{sp} R_S^p + M_{sp} R_S^{-p}) \sin(p\Theta \pm \omega t + \lambda) \qquad (6.70)$$

where R_S is used as before to denote the stator bore radius, and is equivalent to R_4 in this new model.

When the rotor is excited equation (6.48e) may be discarded, and A_6 replaced by A_5 in equation (6.48f). It is evident from the stator analysis that the algebra increases considerably in complexity on passage through the boundary on which the current sheet is situated. Maximum simplicity is always something to aim for in work like this, as it minimises the risk of human errors occurring and saves

computer time when the model is programmed. Thus for the rotor analysis it is sensible to start eliminating from the equations at the stator core back.

At R_6, the stator slot bottom radius, the two boundary conditions (equations 6.48f) give the following expressions for L_7:

$$L_7 = \frac{L_5 R_6^{h} + M_5 R_6^{-h}}{R_6^{p} - R_7^{2p} R_6^{-p}} \tag{6.71}$$

$$L_7 = \frac{h\mu_s \left(L_5 R_6^{h-1} - M_5 R_6^{-h-1}\right)}{p\mu_{ts}\left(R_6^{p-1} + R_7^{2p} R_6^{-p-1}\right)} \tag{6.72}$$

From which:

$$M_5 = L_5 R_6^{2h} Y_6 \tag{6.73}$$

where:
$$Y_6 = \frac{(1-X_6)}{(1+X_6)} \tag{6.74}$$

and:
$$X_6 = \frac{\left(R_6^{h+p} + R_7^{2p} R_6^{h-p}\right)}{\left(R_6^{h+p} - R_7^{2p} R_6^{h-p}\right)} \frac{p\mu_{ts}}{h\mu} \tag{6.75}$$

At R4, the stator bore radius, the two boundary conditions (equations 6.48d) give the following expressions for L_5:

$$L_5 = \frac{L_4 R_4^{2p} + M_4}{R_4^{p+h} + R_4^{p-h} R_6^{2h} Y_6} \tag{6.76}$$

$$L_5 = \frac{p\mu_{ts}}{h} \frac{\left(L_4 R_4^{2p} - M_4\right)}{\left(R_4^{p+h} - R_4^{p-h} R_6^{2h} Y_6\right)} \tag{6.77}$$

From which:

$$M_4 = L_4 R_4^{2p} Y_4 \tag{6.78}$$

where:
$$Y_4 = \frac{(1-X_4)}{(1+X_4)} \tag{6.79}$$

and:
$$X_4 = \frac{h}{p\mu_{ts}} \frac{\left(R_4^{p+h} - R_4^{p-h} R_6^{2h} Y_6\right)}{\left(R_4^{p+h} + R_4^{p-h} R_6^{2h} Y_6\right)} \tag{6.80}$$

At R_3, the rotor surface (equations 6.48c), the expressions obtained for L_4 are:

$$L_4 = \frac{L_3 R_3^{2g} + M_3}{R_3^{g+p} + R_3^{g-p} R_4^{2p} Y_4} \tag{6.81}$$

$$L_4 = \frac{g}{p\mu_{tR}} \frac{(L_3 R_3^{2g} - M_3)}{(R_3^{g+p} - R_3^{g-p} R_4^{2p} Y_4} \tag{6.82}$$

From which:

$$M_3 = L_3 R_3^{2g} Y_3 \tag{6.83}$$

with $$Y_3 = \frac{(1+X_3)}{(1-X_3)} \tag{6.84}$$

and $$X_3 = \frac{p\mu_{tR}}{g} \frac{(R_3^{g+p} - R_3^{g-p} R_4^{2p} Y_4)}{(R_3^{g+p} + R_3^{g-p} R_4^{2p} Y_4)} \tag{6.85}$$

At the next boundary (equations 6.48b), the rotor current sheet enters the argument. The resulting expressions for L_3 are:

$$L_3 = \frac{L_2 R_2^{2g} + M_2}{R_2 + R_3^{2g} Y_3} \tag{6.86}$$

$$L_3 = \frac{L_2 R_2^{2g} - M_2 - \dfrac{\mu_{tR} \mu_o \hat{K}_R R_2^{g+1}}{g}}{R_2 - R_3^{2g} Y_3} \tag{6.87}$$

From which:

$$M_2 = L_2 R_2^{2g} \frac{(1-X_2)}{(1+X_2)} - \frac{\mu_o \mu_{tR} \hat{K}_R R_2^{g+1}}{g(1+X_2)} \tag{6.88}$$

where: $$X_2 = \frac{R_2^{2g} - R_3^{2g} Y_3}{R_2^{2g} + R_3^{2g} Y_3} \tag{6.89}$$

Finally, the rotor slot bottom radius, R_1, is considered (equations 6.48a). The result is an explicit expression in L_2:

$$L_2 = \frac{\mu_o \hat{K}_R R_2^{g+1} (\mu_R/p + \mu_{tR}/g)}{R_1^{2g}(1+X_2)\left(1-\dfrac{g\mu_R}{p\mu_{tR}}\right) + R_2^{2g}(1-X_2)\left(1+\dfrac{g\mu_R}{p\mu_{tR}}\right)} \tag{6.90}$$

An explicit expression for L_4, hence also M_4, may be obtained by substituting back through equations (6.86) and (6.81). Now the pth harmonic of vector potential at the stator bore due to the rotor current sheet may be written as:

$$A_{Rp} = (L_{Rp}R_S^{p} + M_{Rp}R_S^{-p}) \sin p(\Theta-\omega t) \qquad (6.91)$$

The computational procedure differs little from that described in Sections 4.3 and 4.4. Extra data is necessary in the form of the four permeabilities: body permeabilities for rotor and stator; also bulk slotted region permeabilities from which the directional values are calculated. This calculation of directional permeabilities is performed immediately subsequent to the reading of the data file.

In early test versions of the program, the two-degree-of-freedom model calculations of I_R amd λ were not used; there was simply a user input facility for I_R, I_S and λ. Then, as described in Section 4.3, arrays are filled with the peak values of the individual harmonics of flux density; only in this case the expressions developed from the seven regions and their boundary conditions are used, instead of the simple ones given in that Section.

The remainder of the program is mainly as before, producing the radial and circumferential forces on each tooth with their phase difference. But, in the light of the work of Chapter Five, an extra calculation based on the phasor diagram of Figure 5.4 produces the predicted radial core-back vibration amplitude. A suitable pair of transfer coefficients is read in as part of the machine data file.

6.3 Sensitivity Studies on the Multi-region Model

This Section describes a series of tests performed on the multi-region model to determine its sensitivity to various parameters, in accordance with the philosophy outlined in Section 6.2.1. The parameters examined were the depth of the slotted region, the position of the current sheets within the slotted regions, and the permeability of the teeth.

As the tests were intended for comparative purposes, both current sheets were assumed to be of fundamental distribution only, thus avoiding irrelevant complexity. The Ferrybridge machine on full load was used, with transfer coefficients obtained from the empty-slot core representation. The rotor current and torque angle used were obtained from an early experimental version of the two-degree-of-freedom model in which active length was adjusted so that the open circuit rotor current kept its measured value. Thus it is not strictly a true full-load condition in terms of the eventual consistent model. As with the current sheet harmonics, this fact is unimportant in a comparative study. The input data were: I_S=15437A; I_R=3716A; λ=163.52°.

In the first set of tests, the effect of including a slotted region when all bulk permeabilities assume a very high value was investigated. The value of permeability chosen was 10,000 in all cases. Four tests were performed: one in which both the rotor and the stator possessed a slotted region, one in which neither did, and two in which only one did. As mentioned earlier, a slotted region is in fact suppressed by reducing it to a nominal depth; 0.02mm in this case with the current sheet central. Where the slotted region was of significant depth, the current sheet position was retained as 0.01mm from the air gap. The results are given in Table 6.2.

Slotted member(s)	Neither	Rotor	Stator	Both
B_{rR} (T)	3.1372	3.1342	3.1366	3.1336
B_{rs} (T)	2.4568	2.4544	2.4563	2.4539
B_r (T)	1.0470	1.0460	1.0468	1.0458
F_r (kN)	15.896	15.865	15.889	15.859
F_θ (kN)	10.439	10.431	10.437	10.429
ψ (°)	142.9	142.8	142.9	142.8
d_r (μm)	16.85	16.81	16.85	16.81

Table 6.2 Effect of the presence of a slotted region when all relative permeabilities are set at 10,000

It can be seen from Table 6.2 that the variation in flux and force quantities is very small. Slotting of the rotor appears to have slightly more effect than slotting of the stator, but the variation in all quantities is of the order of 0.1%.

In the second set of tests, both regions were considered slotted, but the positions of the current sheets were taken to be either the top or the bottom of the slotted regions; the top being defined as 0.01mm from the air gap and the bottom 0.01mm from the slot bottoms. The results are summaried in Table 6.3.

It can be seen that, with this very high permeability, all flux and force quantities again vary by about 0.1%. Movement of the rotor current sheet appears to have slightly more effect than movement of the stator current sheet.

Rotor Stator	Current sheet positions Top Top	 Top Bottom	 Bottom Top	 Bottom Bottom
B_{rR} (T)	3.1336	3.1336	3.1333	3.1333
B_{rs} (T)	2.4539	2.4536	2.4539	2.4536
B_r (T)	1.0458	1.0460	1.0456	1.0458
F_r (kN)	15.859	15.865	15.853	15.859
F_θ (kN)	10.429	10.429	10.427	10.428
ψ (°)	142.8	142.8	142.8	142.8
d_r (μm)	16.81	16.81	16.80	16.81

Table 6.3 Effect of current sheet position when all relative permeabilities are set at 10,000

B_{rR} (T)	3.1434
B_{rs} (T)	2.4617
B_r (T)	1.0490
F_r (kN)	15.96
F_θ (kN)	10.46
ψ (°)	142.9
d_r (μm)	16.93

Table 6.4 Infinite permeability case

A result for the same condition was also produced by the algebraic model which deals only with an infinitely

permeable slotless condition. The result is given in Table 6.4. It is unsurprisingly very similar to all the results in Tables 6.2 and 6.3, although all quantities are the order of 0.3% higher than for a finite permeability of 10,000.

The obvious next stage was to decrease the permeabilities of the slotted regions further, and to assess the effect of current sheet position under these conditions. However, before proceeding, further tests were done to compare the results of the last set with those obtained by the well-known Carter method of accounting for slotting whilst ignoring saturation, based on the conformal transformation technique. Thus if slotting were found to be of greater importance than saturation, this would provide a much simpler mechanism for incorporating it into the model.

In the Carter method[47] the air-gap length, l_g, is considered to be expanded by a factor, k_g, to an effective air-gap length, l_g':

$$l_g' = k_g l_g \tag{6.92}$$

The constant factor k_g is derived by considering the fact that the permeance of the air gap is lower than if the slots were ignored and the surface considered to be solid iron; but higher than if the flux were assumed to pass through the teeth only, with the slots as dead space. Using the same symbols as in the derivation of the current density magnitudes, the effective slot pitch Δ' is given by:

$$\Delta' = \Delta - 2k_o \tau \tag{6.93}$$

where k_o is a function of the ratio of slot opening to air-gap length. The relationship is shown graphically by M.G. Say[48]. As both the rotor and the stator are slotted, the Carter coefficient k_g is a combination of separate coefficients obtained by considering the effective slot pitch of each. Thus:

$$k_g = k_{gR} . k_{gS} = \frac{\Delta_R}{\Delta_R - 2k_{oR}\tau_R} . \frac{\Delta_S}{\Delta_S - 2k_{oS}\tau_S} \tag{6.94}$$

The rotor of a large turbogenerator is not fully slotted, so the formula given here is not strictly correct if the true slot pitch is used. A dummy slot pitch was therefore used, as discussed in Section 6.2.2 in connection with the derivation of directional permeabilities.

Specification of an effective air-gap length then raises the question of how much of each of the rotor and stator should be sacrificed to provide this extra gap space. In this work it was decided to reduce the rotor radius only, leaving the stator bore intact, thereby maintaining the correct radius of application of the stator bore stresses. Using the Ferrybridge machine, the Carter procedure increased the air gap from 82.55mm to 87.40mm. This results in a rotor radius of 566.6mm.

Three tests were performed using Carter coefficients. In the first two, the load data specified for the last set of tests were used: (1) for a Carter model using the limiting case of the multi-region model with high relative permeability and vanishingly small slotted zones and (2) for a Carter model using the algebraic (infinite permeability) model. The third test was an open circuit condition, again using the multi-region model. The results are given in Table 6.5, with the first column showing the full multi-region result from Table 6.3 for comparison.

There is little difference between the Carter representations of the two different models. However, there is a considerable difference between these results and those of the multi-region model, producing a predicted vibration level 12% lower for the Carter cases.

The Carter open circuit case was included to obtain an estimate of the vibration reduction between open circuit and full load. If this turned out to be close to the measured value of 30-40%, the Carter model would be worth pursuing.

From Table 6.5 it can be seen to be 24%. This is a similar result to that obtained from the model of Section 6.1. It was therefore concluded that this line of investigation was not worth pursuing further.

Case	Full load		Open cct	
	Multi-region	Carter (1)	Carter (2)	Carter (1)
B_{rR} (T)	3.1336	2.9481	2.9536	0.9837
B_{rs} (T)	2.4539	2.3114	2.3157	0.0000
B_r (T)	1.0458	0.9824	0.9843	0.9837
F_r (kN)	15.859	13.919	13.970	14.618
F_θ (kN)	10.429	9.795	9.810	0.005
ψ (°)	142.8	142.3	142.3	90.0
d_r (μm)	16.81	14.75	14.82	19.29

Table 6.5 Comparison of multi-region and Carter models

In the final set of tests, the permeabilities of the slotted regions were varied, whilst the body permeabilities were kept at 10,000. To obtain an overall assessment of whether positions of the current sheets were important at lower permeabilities, two extreme situations were used for each test: one with both current sheets at the slot tops and one with both at the slot bottoms. Permeability values used for the slotted regions were 10^4, 100, 50 and 10. The results are given in Table 6.6.

It can be seen that the positions of the current sheets become more important as the permeability of the teeth decreases, but that even at the low value of μ_{teeth}=10, the difference in vibration between the two extreme cases is

little more than 1%.

μ_{teeth}	10^4		100		50		10	
current pos'n	Top	Bottom	Top	Bottom	Top	Bottom	Top	Bottom
B_{rR} (T)	3.134	3.133	2.964	2.961	2.812	2.807	2.038	2.034
B_{rs} (T)	2.454	2.454	2.322	2.319	2.204	2.198	1.601	1.585
B_r (T)	1.046	1.046	0.989	0.988	0.938	0.937	0.677	0.676
F_r (kN)	15.86	15.86	14.14	14.13	12.69	12.68	6.58	6.58
F_θ (kN)	10.43	10.43	9.94	9.92	9.49	9.46	7.11	7.02
ψ (°)	142.8	142.8	141.3	141.3	139.9	139.8	128.9	128.7
d_r (µm)	16.81	16.81	14.76	14.74	13.07	13.03	6.36	6.27

Table 6.6 Effect of variation of tooth permeability and current sheet position

The vibration levels at the different tooth permeabilities show a marked change. For μ_{teeth}=50 there is a decrease of 22% below that for μ_{teeth}=10^4, whilst for μ_{teeth}=10 there is a decrease of 63%. The vibration obtained for the multi-region model with all permeabilities high on open circuit was 21.9µm, thus it appears that using a tooth permeability of 50 on full load would give a reduction in vibration of 40% between open circuit and full load. This would be if the iron were considered to be unsaturated on open circuit; allowing for open circuit saturation might give a figure of about 35%.

These results are in fact not as encouraging as they first appear. Besides reductions in force and vibration, there are also substantial reductions in the flux quantities, including resultant radial air-gap flux density. In the self-consistent two-degree-of-freedom model it is a

condition that the resultant radial air-gap flux density be kept constant. If the ultimate aim is to graft the calculation of I_R and λ incorporated in this model onto the front end of the multi-region model, the eventual results must be self-consistent. Steps will have to be taken to ensure that, despite modelling of saturation by reduced tooth permeability, the air-gap flux density maintains a value which satisfies terminal voltage.

The approach adopted was simply to mimic nature. Flux levels are maintained in the presence of saturation in a real machine by raising excitation current. In the next Section an iterative scheme is developed to tune the rotor current used by the model to a value which satisfies the flux requirement.

The current sheets were kept at the tops of the slotted regions for all future analyses, their positions having been shown to be relatively unimportant.

6.4 Automation of Flux Density Requirement and Tooth Permeability Selection

Prior to further development of the self-consistent electromagnetic force model, the calculations of I_R and λ developed in Section 6.1 had to be grafted onto the front end of the multi-region model computer program. Also, the input of I_S had to be altered to the more convenient load input format. These adaptations were straightforward, as in essence both were concerned with replacement of a user input by a calculation from other data.

Once the hybrid program described was running satisfactorily, the question of maintaining flux density levels at lowered tooth permeabilities could be addressed. The philosophy applied, as stated at the end of Section 6.3,

is to mimic nature by increasing excitation current. The method employed is essentially a proportional control algorithm. First, an error is formed from the calculated resultant flux density and the open circuit value.

$$e_b = (B_{roc} - B_r)/B_{roc} \qquad (6.95)$$

Next, the size of the error is examined to discover whether it is within a tolerance level defined by the program. The level used is 10^{-5}. If the error is greater than 10^{-5}. the rotor current is adjusted using the formula:

$$I_{R[k+1]} = I_{R[k]}(1 + k_b e_b) \qquad (6.96)$$

The constant k_b was determined empirically, eventually assuming a value of 0.4 which gives stability in all the large selection of conditions programmed for three different machines. Whilst values were being investigated, many unstable ones came to light, so a loop counter had to be included to terminate operation in such cases. This counter is incremented on every pass, causing termination whenever its value exceeds one thousand. It was considered prudent to retain this facility once a working value of k_b had been selected.

In previous versions of the model, in which a numerical scheme was used to calculate flux, stress and force at the stator bore, the peak value of the resultant fundamental radial flux density was not actually necessary for the main calculation; hence it was calculated at the end immediately prior to output as a data item. In the present scheme it is needed in order to form a flux error, e_b. Thus it is calculated immediately following the individual rotor and stator flux density calculations. This involves in essence only simple trigonometry, as can be seen by reference to the flux density phasor diagram of Figure 6.5.

An extremely simple expression for B_r can be given in terms of B_{rS}, B_{rR} and λ. However, this would result in λ being kept invariant throughout the iterative scheme,

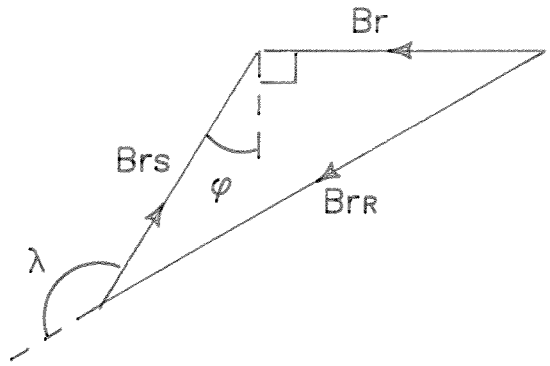

Figure 6.5 Air-gap flux density phasor diagram

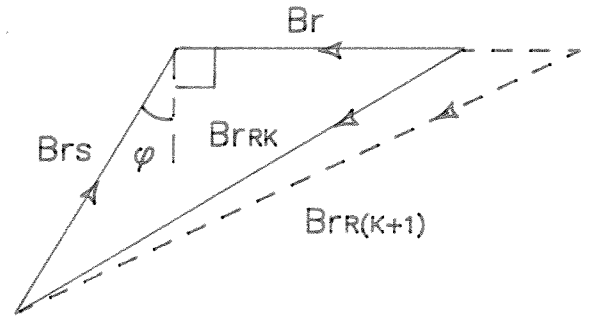

(a) lagging power factor

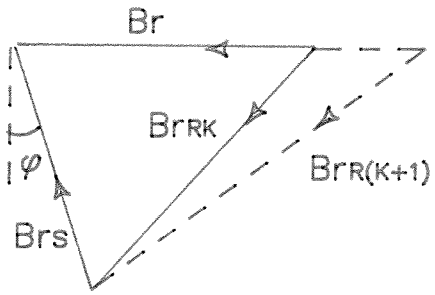

(b) leading power factor

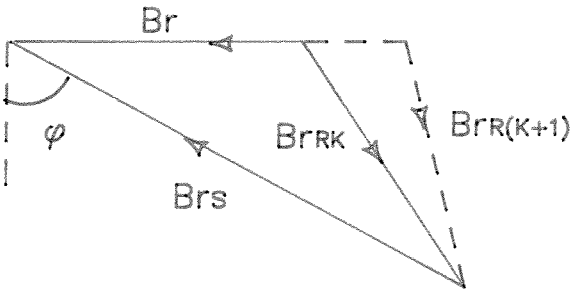

(c) leading power factor (unstable situation)

Figure 6.6 Operation of the algorithm for adjusting I_R

resulting in a change in power factor angle. The power factor is part of the load condition, which must be honoured as a condition of the model. Thus a quadratic must be solved in B_r in order that ϕ be a constant rather than λ.

For the lagging power factor case shown in the Figure, the cosine rule gives:

$$B_{rR}^2 = B_r^2 + B_{rs}^2 - 2B_rB_{rs} \cos (90+\phi) \qquad (6.97)$$

If a leading power factor example were taken, the argument of the cosine would be $(90-\phi)$. Both may be converted to sine functions, and the expression written in the form of a standard quadratic, as in equations (6.98a) and (6.98b), for lagging and leading power factors respectively.

$$B_r^2 + 2B_{rs} \sin \phi \; . \; B_r + (B_{rs}^2 - B_{rR}^2) = 0 \qquad (6.98a)$$

$$B_r^2 - 2B_{rs} \sin \phi \; . \; B_r + (B_{rs}^2 - B_{rR}^2) = 0 \qquad (6.98b)$$

Instead of the program containing both equations, selection depending on the nature of the power factor, a sign variable ± 1 was defined from this condition. The solution then took the form of the standard quadratic solution, with program termination and error message generation should the case arise in which it has imaginary roots. Of the two solutions, only one is meaningful. The solution closest to the open circuit flux density is selected by comparison with B_{roc}.

It is also necessary to calculate the value of torque angle λ consistent with the solution. The sine rule may be used in this case:

$$\sin (180-\lambda) = \frac{B_r}{B_{rR}} \sin (90+\phi) = \frac{B_r}{B_{rR}} \cos \phi \qquad (6.99)$$

In most cases, λ is in the second quadrant, so the Fortran ASIN function returns $180-\lambda$. However, for low loads on high leading power factors, λ will drift into the first quadrant. The condition for this is evidently:

$$B_{rs}^2 + B_{rR}^2 < B_r^2 \qquad (6.100)$$

resulting in the true value of λ being returned by ASIN in the first instance.

During the operation of the algorithm, B_{rs} and ϕ are kept constant as part of the load condition of the machine. B_{rR} and λ are adjusted until B_r attains its prescribed value. The operation of the algorithm is shown for three separate cases in Figure 6.6. Figure 6.6(a) represents a lagging power factor case. The dotted outline shows the position of the B_{rR} phasor after the application of equation (6.96) with e_b positive. It can be seen that increase of I_R, hence B_{rR}, produces an increase in B_r, as required. Figure 6.6(b) shows the case for leading power factor. The same applies. Figure 6.6(c) shows the case for a high load on high leading power factor. Such a case would not occur in reality because it is unstable (the load angle δ being greater than 90°), but can and does occur within the model, which must therefore be able to handle it. It is arguable that a model devised to represent a true situation should not include impossible cases. However, in this model it is helpful to do so for two reasons. First, when investigating thoroughly the effect of various parameters on the model it is more informative to enter an identifiably unstable state than to observe a simple program crash. The second reason becomes more apparent when tooth permeability is also adjusted by an algorithm. Many leading power factor cases are unstable in the early iterations but transform into stable situations as the end point is approached.

It can be seen from Figure 6.6(c) that a decrease in B_{rR}, hence in I_R, is necessary to obtain an increase in B_r and occurs when the load angle δ between B_r and B_{rR} is greater then 90°. This is equivalent to $\lambda+\phi$ being greater than 180°, which is the condition used in the program. Equation (6.96) now becomes:

$$I_{R[k+1]} = I_{R[k]} (1 - k_b e_b) \qquad (6.101)$$

Once the scheme described above was fully operational, a series of tests at various tooth permeabilities was performed for the Ferrybridge machine at full rated load (500MW 0.85 lag). Body permeabilities were kept at 10,000 throughout. The transfer coefficients used were those obtained for the core representation with empty slots. The results given in Table 6.7 show the values of I_R and λ produced by the iterations to maintain the open circuit level of flux density, as well as the vibration levels obtained as the end result. The values in the top row of the Table are those produced by the calculations of Section 6.1 and are the same for all values of permeability specified in the multi-region part of the model. An open circuit condition is included for comparison, in which the teeth are assumed to maintain the same high permeability as the bodies.

μ_{teeth}	I_R (A)	λ (°)	d_r (μm)	Red'n below o/c (%)
∞	3578	165.52	11.99	24.1
10,000	3581	165.48	11.98	24.2
200	3603	165.15	11.91	24.6
100	3626	164.83	11.85	25.0
50	3671	164.19	11.72	25.8
10	4020	159.92	10.81	31.6
8	4124	158.83	10.56	33.2
6	4293	157.20	10.18	35.6
5	4423	156.05	9.90	37.3
Open cct	1056	90.00	15.80	-

Table 6.7 Variation of vibration, rotor current and torque angle with tooth permeability for the Ferrybridge machine on full rated load

From these results it can be seen that the lower the tooth permeability, the lower the vibration. Therefore the reductions shown in Section 6.3 were not solely a result of reduced resultant flux density in the air gap, but were partly due to the reduced permeability of the slotted region. A particularly interesting result may be noted at $\mu_{teeth}=5$. Here the rotor current is 4423A and the vibration is reduced by 37.3% below the open circuit level. This rotor current is very close to the quoted full rated load rotor current for the machine (4420A). Also, the vibration reduction is of the order sought. This suggests a way of determining the value assigned to tooth permeability at any load: specifying that it produce the correct value of rotor current for the given condition on the real machine. Of course the reduction of 37.3% is not strictly valid here, as the rotor current calculated for open circuit is not the same as the value quoted in the machine data, which is 1240A. To investigate the significance of this, a search through various tooth permeabilities was performed for the open circuit condition to find one which would give the correct rotor current. The closest attained with an integral value of tooth permeability was for $\mu_{teeth}=33$. This gave $I_R=1238A$ and $d_r=15.30\mu m$; making the reduction at full load now equal to 35.3%. This result confirmed the feasibility of using actual rotor current to select the value of tooth permeability used in the model.

It is notable that the actual values of tooth permeability produced by the rotor current condition appear excessively low in comparison to what one might expect in reality. It is also true that the body permeabilities of 10,000 are considerably higher than true values for electrical steels. Some tests were performed to investigate the effect of reducing the permeability of the bodies from its previous value of 10,000 to a more realistic 1,000. First, the tooth force and vibration quantities for open circuit and full rated load were compared in the cases where

all permeabilities are either 10,000 or 1,000. The results are given in Table 6.8.

Condition	μ_b	F_r (kN)	F_θ (kN)	ψ (°)	d_r (μm)
open cct	10,000	11.976	0.007	90.0	15.80
	1,000	11.976	0.071	90.0	15.71
full load	10,000	11.342	8.879	140.7	11.98
	1,000	11.358	8.913	140.3	11.91

Table 6.8 Effect of variation of bulk permeabilities

It can be seen that the differences in the results for these two permeabilities are significant but small: fractions of one per cent. Comparison with Table 6.7 shows that the full load case with all permeabilities equal to 1,000 gives the same vibration result as the full load case with body permeabilities of 10,000 and tooth permeabilities of 200.

In the second test, rotor currents and tooth permeabilities for open circuit and full load were compared, given that body permeabilities are now set to 1,000. Table 6.9 shows some results for open circuit and full load. Now for open circuit the tooth permeability required to obtain 1238A has been increased from 33 to 38. But to obtain rated rotor current on full rated load the tooth permeability still needs to be around 5. It is evident that this method of modelling the teeth is taking account of saturation in the machine, but not in the simple manner of representing the true permeability of the steel. Further investigations into its validity are performed in Section 6.5. For future analyses the stator body permeability was set at 1,000, and the rotor body permeability at 100.

(a) open circuit		(b) full load	
μ_{teeth}	I_R (A)	μ_{teeth}	I_R (A)
200	1110	100	3644
100	1141	50	3689
50	1201	30	3749
40	1231	20	3823
38	1238	10	4039
37	1243	8	4144
		6	4313
		5	4443

Table 6.9 Variation of rotor current with tooth permeability given body permeabilities of 1,000

Implementation of this empirically satisfactory scheme for selecting slotted region permeability in the model was by means of a similar algorithm to equation (6.96). First the current error is obtained from the desired value of I_R, $I_{R,des}$, and the most recently calculated value from the flux algorithm.

$$e_i = (I_{R,des} - I_R)/I_{R,des} \tag{6.102}$$

Then both values of tooth permeability, μ_{satR} and μ_{satS}, are updated together:

$$\mu_{satR[k+1]} = \mu_{satR[k]}(1 - k_i e_i) \tag{6.103a}$$

$$\mu_{satS[k+1]} = \mu_{satS[k]}(1 - k_i e_i) \tag{6.103b}$$

Operation is concluded when e_i becomes less than 10^{-5}, and there is also a loop counter to terminate the program if more than 1,000 iterations are performed. The constant k_i eventually assumed an empirically determined value of 1.0.

This complete scheme is far simpler than the one necessary to deal with flux density adjustments as flux density is a vector quantity and rotor current a scalar. No problems were experienced producing results for open circuit and full rated load on the Ferrybridge machine, which were entirely as expected from previous tests.

Complications with the scheme did arise, however, on loads with high leading MVAR. These were met when performing a series of program runs to model a large number of test measurements taken on a machine of the same design as the Ferrybridge generator, which is installed at Fawley power station. These results will be described in more detail in the next Section.

The first complication would always cause a crash on the first pass through the loop. Figure 6.7 depicts the situation in phasor diagram form. The unsaturated rotor current calculated by the two-degree-of-freedom model is so small that the corresponding flux density phasor is too short to complete the triangle where B_{rs} and ϕ are defined. This problem was cured by insertion of a short routine to give an initial boost to the rotor current. This routine is activated by the combination of two conditions: the roots of equation (6.98) being imaginary and the flux density loop counter being zero. The rotor current is then increased by a factor of 1.01, and operation returned to the start of the calculation of rotor flux density magnitudes. Thus it may be repeated on several passes until the rotor flux density is of sufficient magnitude to complete the triangle before control is returned to the flux density iteration loop. A loop counter of maximum value 100 is included to terminate operation in error situations.

The other complication arose from an effect referred to earlier in the Section. The phasor diagram to represent some high loads on leading power factor looks like Figure

6.6(c) when the unsaturated values of B_{rs} and B_{rR} are calculated. However, the end point of the algorithms is a situation like Figure 6.6(b). Thus the algorithm operational during early passes is equation (6.101). The rotor current is steadily reduced, resulting in a reduction of the load angle, δ, which is the angle between B_r and B_{rR}, towards 90°. Eventually it is reduced to a point where the situation of Figure 6.7 ensues. However, giving a simple boost to the rotor current at this point does not work, because it merely effects a return to Figure 6.6(c), and the program oscillates between these two states until the loop counter reaches 1,000 and it crashes.

The remedy devised for such cases is a straight jump to the outer loop in which slotted region permeability is adjusted according to rotor current error. This jump occurs whenever the flux density triangle has imaginary roots and the loop counter is non-zero. The effect of such a step is to shorten the B_{rs} phasor. Several iterations may be necessary to reach a state in which the very first pass through the flux density loop produces the situation of Figure 6.6(b), but once this is achieved there are no further problems.

A regime such as the one described, with two nested control loops, uses a lot of computer power. It was not easy to determine exactly how much processor time was involved on a multi-user mainframe computer, but the mere fact that individual load analyses took perceptible amounts of time, i.e. substantial fractions of one minute, suggested this sort of solution to be inappropriate for use on a micro-computer as a minor part of a broader monitoring program. A neater solution would be an explicit equation in both MW and MVAR to approximate the value of the slot region permeability which would be generated eventually by the control algorithm. The nature of suitable such equations is discussed in Section 6.5.4. However, for continued

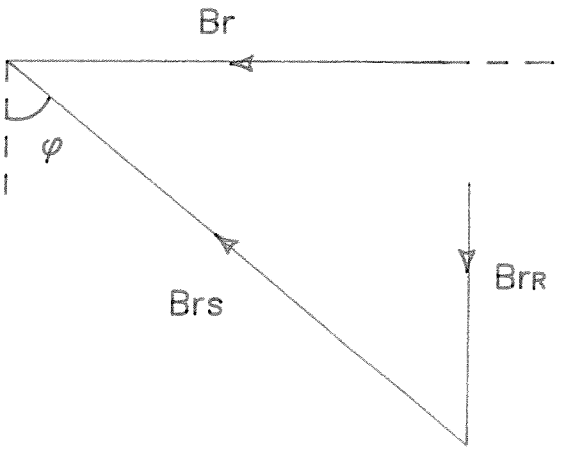

Figure 6.7 A problem with some high loads on leading power factor

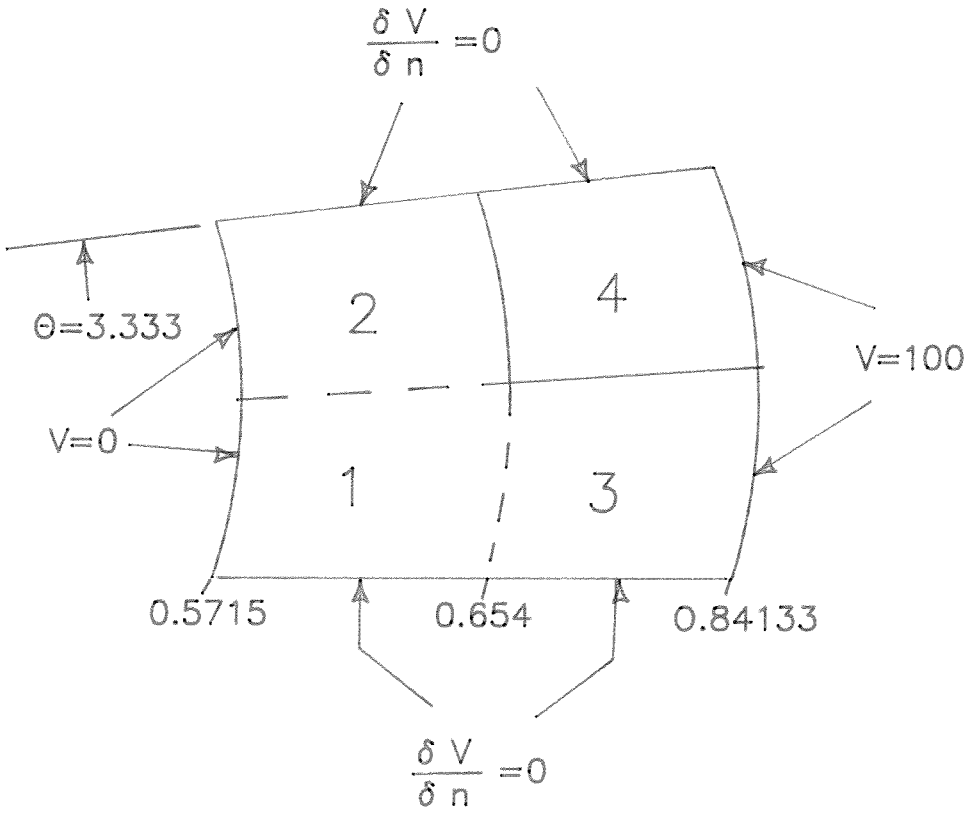

Figure 6.8 Half stator slot pitch geometry and boundary conditions for finite-element flux study

investigation of the model, in particular for comparison of its results with test measurements, the control algorithm was used. During this development work neither time nor computer power were significant limitations, whilst validation of the principles behind the model were of prime importance. It did not make sense at this stage to risk losing clues to factors of significance in the origin of stator core vibration in the midst of extensive approximations.

6.5 Validation of the Saturated Model

6.5.1 Application of the Flux Density Algorithm to an Open Circuit Carter Model

In Section 6.3 a "Carter model" with an enlarged air gap but no saturation was investigated as a possible alternative to a multi-region model. The conclusion drawn was that this is not a promising approach, and that it is really necessary to take account of saturation in the model.

In this Section, a similar model is used, but with a different purpose: to provide some validation for the algorithm which maintains air-gap flux density by adjustment of rotor current. The method of Carter coefficients is a well-established technique used to account for the effect of slotting on the permeability of the complete magnetic circuit. It does not, however, account for magnetic saturation. Thus if the algorithm were applied to a Carter model like the one investigated in Section 6.3, the resulting rotor current ought to correspond to that obtained from the air line at rated open circuit voltage, rather than that obtained from the measured open circuit saturation characteristic.

Open circuit analyses of all three machines, the

Ferrybridge, West Burton and 350MW generators, were performed along these lines using Carter models like the one described in Section 6.3. The bulk permeabilities were retained at 1,000. The computer program was adapted to bypass the iterations of slotted region permeability. The output of interest is the rotor current calculated to maintain the required air-gap flux density. The results for all three machines are given in Table 6.10, together with the air line and saturation curve rotor currents corresponding to rated terminal voltage (22kV for Ferrybridge and West Burton; 18kV for the 350MW generator).

Current (A)	Ferrybridge	West Burton	350MW
1) Carter	1141	1322	1039
2) Air line	1120	1310	1120
3) Saturated	1240	1508	1340
Diff. btwn 1 & 2 (%)	1.9	0.9	-7.2

Table 6.10 Comparison of open circuit rotor currents

It can be seen that the correlation between calculated and air line currents for the two 500MW generators is excellent, whilst for the 350MW generator it is moderate. These results provide confidence in the scheme employed by the model to maintain the necessary air-gap flux density to induce the rated terminal voltage on open circuit.

6.5.2 Saturated Teeth: A Finite-Element Flux Study

The purpose of the study described in this Section is to obtain some physical understanding, and hence assess the validity, of the values of saturated tooth permeability

generated by the outer algorithm of the automated multi-region model. The principle behind the method employed is that of the magnetic circuit: in any magnetic circuit the magnetomotive force is equal to the flux times the reluctance. A condition of the two-degree-of-freedom model is that the radial air-gap flux density be constant. Thus any change of reluctance between the unsaturated and saturated state will be proportional to the change in excitation current.

In the study, a small section of the magnetic circuit of the Ferrybridge machine is modelled: half a slot pitch comprising half a tooth and half a slot, extending radially from the rotor surface to the stator slot bottom. The electromagnetic finite-element package PE2D is used for the analysis. Meshing is semi-automatic in PE2D, unlike ANSYS, where nodes are defined by the operator. In PE2D, the problem geometry is defined by the operator as a mosaic of regions, within each of which the mesh is generated automatically by the pre-processor, given the number of element-edges required along each boundary. On external boundaries a fixed value of magnetic potential may be defined; alternatively a differential condition $\partial V/\partial n=0$ equivalent to containment of the flux within the boundary. Regions may be assigned any value of relative permeability.

The geometry devised is shown in Figure 6.8. Regions 1, 2 and 3 are air regions (the slot conductors are ignored as they are not relevant to this magnetic study) and Region 4 is the half-tooth. Whilst the dimensions are true to the geometry of the machine, the magnetic potential values are arbitrary. They do not have to mean anything: it is enough that they are unequal so that flux is driven radially through the section in this comparative study. If the same values are used whilst the permeability of Region 4 is varied, the flux passing between the two radial boundaries varies. This is the converse of the situation in the two-

degree-of-freedom model where the flux is constant but the excitation varies. In the finite-element flux study the excitation is constant, so the flux varies in inverse proportion to the reluctance of the magnetic circuit. If the two situations are equivalent, the ratio of the two fluxes obtained (using a high permeability for Region 4 and a permeability equivalent to the saturated value generated by the automated multi-region model) should be the reciprocal of the ratio between the Carter current calculated in Section 6.5.1 and the measured saturated current. It is valid to equate values of permeability directly between the two models as they are relative, and therefore dimensionless, values. The finite-element analysis produces flux density values at all points within the problem boundary. To obtain the total radial flux it is necessary to integrate the normal component of flux density along a circumferential line. PE2D possesses a post-processor command to facilitate this integration, which was performed at a radius of 0.6m.

The permeability values used for Region 4 included a very high value, 10^4, for reference, then 1,000 and 100 followed by a closer range of smaller values which specifically included 32 and 5, the permeabilities obtained by the automated multi-region model at open circuit and full rated load. The results are shown in Table 6.11. For comparison, the ratios between saturated and Carter currents on open circuit and full rated load were required. The former could be calculated directly from the results of Section 6.5.1 for a Carter current of 1141A and a measured current of 1240A. The ratio is thus 1.0868. This compared very well with the value of flux ratio corresponding to the permeability of 32 in Table 6.11. In fact, the two ratios differ by only about 1%. This is a very encouraging result, tending to suggest that on open circuit the means of modelling permeability in the multi-region model has some basis in physical reality.

μ_r	Φ	$\Phi_{10,000}/\Phi$
10,000	42.256	1.0000
1,000	42.132	1.0029
100	40.936	1.0322
32	38.425	1.0997
20	36.512	1.1573
10	32.432	1.3029
7	29.775	1.4192
5	27.031	1.5632
3	22.738	1.8584
2	19.531	2.1635

Table 6.11 Variation of flux with tooth permeability in the finite-element flux study

To provide a comparison for the full load case, it was necessary to repeat the Carter analysis of Section 6.5.1 with the appropriate input data. The resulting rotor current was 3647A. The ratio of the saturated rotor current (4420A) to this is therefore 1.2120. With reference to Table 6.11 this calculation would tend to suggest 15 as an appropriate value for saturated tooth permeability on full load. As the value produced by the automated multi-region model is only 5, it appears that this model is not as well validated on a high load condition as it is on open circuit.

However, it must be remembered that an electrical machine on high load is a complex system with many non-linear variables. Saturation is present to a greater or lesser extent in most parts of the magnetic circuit, whereas in the model the only part allowed to saturate is the

slotted region. Field leakage also increases in a non-linear fashion on high loads, especially those with a lagging power factor. This matter will be considered further in Section 6.5.4, but here it is enough to note that its effect, too, is included in the modelling of the saturated teeth. In the light of the fact that body saturation and field leakage are taken into account by the model in the form of tooth saturation, it is hardly surprising that the calculated permeability of the teeth is far lower than one might expect when considering them in isolation.

Another important factor is that in the flux study described here, only radial flux has been investigated. This is quite valid for the open circuit situation, but on load there is also circumferential flux present, which is furthermore phase displaced from the radial flux, hence cannot be represented in a static analysis. As the system is non-linear, neither is it possible to justify superposition of results.

It is best to conclude that the method of the automated multi-region model may be considered an adequate predictor of global quantities, despite the fact that its smaller-scale representation of the system diverts significantly from physical reality. This is a similar philosophy to that embodied in the concept of Maxwell stress.

6.5.3 Validation of Saturation Modelling: Load Angle Prediction

The results so far have shown that in the prediction of turbogenerator vibration, as in the prediction of other aspects of synchronous machine behaviour, accounting for iron saturation is of great importance. The non-linearity of the saturation process makes this an inherently difficult piece of modelling. De Mello and Hannett have this to say

on the matter:

> "It is recognised that any practical method of saturation representation must be based on semi-heuristic reasoning and empirical approximations."[49]

In the relevant paper, these authors go on to advise that the model structure should be simple, based on principles approximating the physics of the process, and require if possible no more than historically available data on machine characteristics.

The model developed here achieves relative simplicity by its reliance on an analytical representation of the field distribution within the machine. Adjustment of relative magnetic permeability mirrors what is happening during saturation in reality. Adjustment of permeability in the teeth only is justified as a simplifying step on the grounds that teeth saturate far more than bodies on load. If all load quantities and excitation current are measured at the terminals, only data regarding the geometry of the machine is further required.

Most work on modelling saturation concerns the prediction of the saturated values of the equivalent circuit parameters, in particular the direct and quadrature axis values of synchronous reactance. Early work had to be performed without the help of powerful digital computers, and relied mainly on open circuit characteristics, whereas the advent of finite-element modelling enabled a complete field picture of the machine to be obtained at any given load. A pioneering paper on the subject describes work in which the open circuit and zero power factor characteristics were used[50]. The authors recognised the distinction between the effects of d- and q-axis saturation, and that both are important: d-axis saturation affects the m.m.f. necessary to drive flux around the field leakage path; q-axis saturation affects the rotor load angle, δ, reducing it in all cases below what it would be in an unsaturated machine under the same load condition. Indeed, other work

has shown[51] that to take into account only direct axis saturation, when the aim is to predict steady-state load angles and the swing curves resulting from a subsequent fault, is not worth the trouble. Saturation on the q-axis is further of greater importance because it tends to be significantly heavier than d-axis saturation, due to the presence of teeth in the rotor portion of the magnetic circuit[52].

Finite-element methods have been used both as a primary means of predicting saturated behaviour[53] and as an intermediate tool for the derivation of saturated equivalent circuit parameters[54][45]. An interesting hybrid has also appeared, in which magnetic saturation in the iron is modelled with finite elements whilst the air-gap flux solution is analytical[55]. De Mello and Hannett, however, feel that the long-established philosophy of representing a machine by d- and q-axis windings is inappropriate and can be a hindrance when saturation effects are to be seriously modelled[49]. This view is supported by recent work on cross-axis reactances[45][56] which shows that under saturated conditions, current on one axis gives rise to flux on the other. In Reference 56, a special experimental machine is constructed to investigate the effect, whilst in Reference 45 an overall finte-element model of the saturated machine is excited on each axis independently, allowing a form of non-linear superposition. This technique is also used by Minnich et al[54], who also identify the cross-axis reactances. Their main aim is to construct functions to describe the variation of the main reactances with saturation, so they attempt to incorporate the cross-axis effects into "total" reactances.

The model developed in the present work appears, in the light of this discussion, to be at an advantage in its global approach, as it bypasses the use of axis reactances altogether. However, the proof of a model is in the results

it gives. Such models are usually assessed on the accuracy of their predictions of rotor current and load angle. The automated multi-region model takes rotor current as part of the input data, so assessment must rely on its ability to predict the load angle, δ, for a number of test conditions.

A large number of measurements of all terminal quantities at five separate loads and a wide range of power factors exists for a 500MW generator of Ferrybridge design in operation at Fawley Power Station. Tables 6.12 to 6.16 give the results for test and model for each load condition. The values of slotted region permeability generated in each case are also noted. Table 6.17 gives the average error for each load, and the overall average. The sign of the error is ignored for the purpose of calculating the average error.

It can be seen that except for the lowest load, the model generally underpredicts load angle. The accuracy of most of the results is good, however; within two or three degrees. The accuracy decreases sharply for loads with high leading MVAR, errors of more than 10° being evident in a few cases. These occasional high errors tend to bring the average up. Both Reference 54 and Reference 49 contain extensively tabulated comparisons between these authors' calculated load angles and measured values. The results of de Mello and Hannett are excellent. Their saturated models predict within average errors of less than 2°. It is interesting to note that they tend to underpredict for leading power factor and overpredict for lagging. Minnich et al obtain very good accuracy (fractions of a degree) for lagging power factor, and errors of two or three degrees for leading power factor. They tend to underpredict in general. Reference 49 also compares unsaturated versions of the models developed with test, obtaining errors of 4.4° and 7°. Reference 54 selects a "Conventional Saturation Algorithm" to show off the authors' model favourably. This gives overpredictions in the region of 10° for leading power

factors; overpredictions of around 4° for lagging power factors. Unsaturated models tend consistantly to overpredict load angle.

It is not surprising that the automated multi-region model performs less well in the prediction of load angle than other saturated machine models, for this is not the purpose for which it was developed. There are, however, two encouraging aspects to the results. The first is that it performs significantly better than both the unsaturated models of de Mello and Hannett and the "conventional" saturation algorithm of Minnich et al. The second is its tendency to underpredict load angles. Saturation decreases the load angle, so a model which similarly tightens load angle can be said in some way to be mimicking the effect of saturation.

MW	MVAR lag	I_R (A)	V_T (kV)	μ_{teeth}	δ (°) test	δ (°) model	δ (°) error
42.0	54.8	1610	22.6	40.95	7.5	7.23	-0.27
37.3	-34.6	1110	22.5	71.77	8.5	9.37	0.87
38.7	-110	700	22.5	201.44	14.5	15.53	1.03
40.3	-175	420	22.6	179.85	25.0	27.57	2.57
38.1	-207	308	22.6	97.46	34.0	36.64	2.64
44.8	-230	260	22.6	86.13	44.5	56.23	11.73

Table 6.12 Fawley generator, test at 10% of rated load

MW	MVAR lag	I_R (A)	V_T (kV)	μ_{teeth}	δ (°) test	δ (°) model	δ (°) error
98.6	257	2840	22.0	15.72	10.0	9.93	-0.07
100	182	2400	22.1	20.17	12.5	11.88	-0.62
98.2	109	1960	22.2	29.69	15.0	14.26	-0.74
96.0	38.8	1590	22.3	37.31	17.5	17.18	-0.32
103	-31	1230	22.3	56.92	23.5	24.17	0.67
103	-88	1000	22.5	53.04	30.5	29.95	-0.55
111	-100	1020	23.1	45.43	30.5	30.92	0.42

Table 6.13 Fawley generator, test at 20% of rated load

MW	MVAR lag	I_R (A)	V_T (kV)	μ_{teeth}	δ (°) test	model	error
256	66.5	2210	22.7	18.48	36.0	33.86	-2.14
253	335	3640	22.3	9.43	22.0	19.93	-2.07
252	246	3070	22.3	13.35	26.0	23.72	-2.28
252	164	2640	22.4	16.27	29.5	27.74	-1.76
252	80	2240	22.4	19.22	34.5	33.25	-1.25
252	-4.4	1880	22.4	22.03	42.5	40.78	-1.72
248	-77.6	1620	22.4	21.07	50.5	48.25	-2.25
250	-144	1450	22.5	19.03	59.0	56.79	-2.21
257	-174	1420	22.5	17.30	65.0	61.45	-3.35
246	-205	1300	22.6	17.99	68.0	66.11	-1.89
244	-235	1260	22.6	15.04	74.0	69.39	-4.61
258	-265	1325	22.6	10.75	80.5	70.39	-10.11

Table 6.14 Fawley generator, test at 50% of rated load

MW	MVAR lag	I_R (A)	V_T (kV)	μ_{teeth}	δ (°) test	δ (°) model	δ (°) error
384	89	2760	22.2	14.19	46	43.21	-2.79
392	-181	2100	22.4	10.01	73	65.69	-7.31
394	50	2680	22.1	13.27	50	46.63	-3.37
390	131	2980	22.2	12.27	44	40.11	-3.89
387	212	3310	22.2	11.53	38	35.15	-2.85
386	300	3770	22.2	9.24	33	30.30	-2.70
380	-219	1980	22.4	9.78	76	69.56	-6.44
379	-160	2060	22.4	11.28	69	63.88	-5.12
380	-100	2160	22.4	13.87	62	59.10	-2.90
380	-37	2330	22.4	14.02	55	52.70	-2.30
362	69	2615	22.2	14.15	45	42.94	-2.06
358	-263	1860	22.4	7.57	82	70.16	-11.8

Table 6.15 Fawley generator, test at 75% of rated load

MW	MVAR lag	I_R (A)	V_T (kV)	μ_{teeth}	δ (°) test	model	error
506	90	3320	22.2	9.70	51	48.66	-2.34
506	-212	2680	22.2	6.39	79	68.71	-10.29
506	49	3170	22.2	10.31	55	51.83	-3.17
508	127	3450	22.2	9.71	49	46.50	-2.50
506	207	3750	22.1	9.27	44	41.90	-2.10
507	293	4150	22.1	8.02	39	37.23	-1.77
508	-245	2660	22.2	5.81	83	70.55	-12.45
509	-189	2700	22.2	7.27	77	68.40	-8.60
507	-129	2780	22.2	8.13	71	64.04	-6.96
508	-66	2900	22.2	9.04	65	59.68	-5.32

Table 6.16 Fawley generator, test at 100% of rated load

Load condition	Average error (°)
10% load	3.185
20% load	0.484
50% load	2.970
75% load	4.461
100% load	5.550
all	3.557

Table 6.17 Average load angle errors

6.5.4 Incidental Modelling of Field Leakage: An Investigation of the Variation of Tooth Permeabilities with Load

The automated multi-region model does not explicitly take account of leakage, but, by adjusting itself to satisfy global parameters, performs this task in an incidental manner. Account of armature leakage and saturation of the armature leakage path is taken by stealth; the leakage reactance being but a few per cent of the synchronous reactance and its variation with saturation smaller still. That field leakage and saturation of the field leakage path are being accounted for is clearly shown when the variation of calculated slotted region permeability with MVAR for each of the nominal MW loads of the Fawley machine is plotted, as in Figure 6.9.

In their classic paper on the saturated synchronous machine, Robertson, Rogers and Dalziel explain the consequences of saturation of the field leakage path for the relationship between excitation current and induced e.m.f. in the machine on load[50]. On open circuit, the field current can be regarded as consisting of two components. The first drives the flux necessary to induce rated terminal voltage across the air gap. This is the air-line field current. The second drives this flux through the partially saturated iron of the magnetic circuit. On load, the excitation-voltage curve is displaced from the voltage axis at the zero voltage point (i.e. short circuit) by the amount of field current necessary to overcome armature reaction and armature leakage reactance. This on-load saturation curve, however, is not parallel to the open circuit curve, as at higher levels of air-gap voltage extra excitation is needed to drive leakage flux through the saturated pole face and stator teeth. Also, the proportion of rotor m.m.f. driving leakage flux increases. This is because the reluctance of the leakage flux path, passing mainly through air, increases

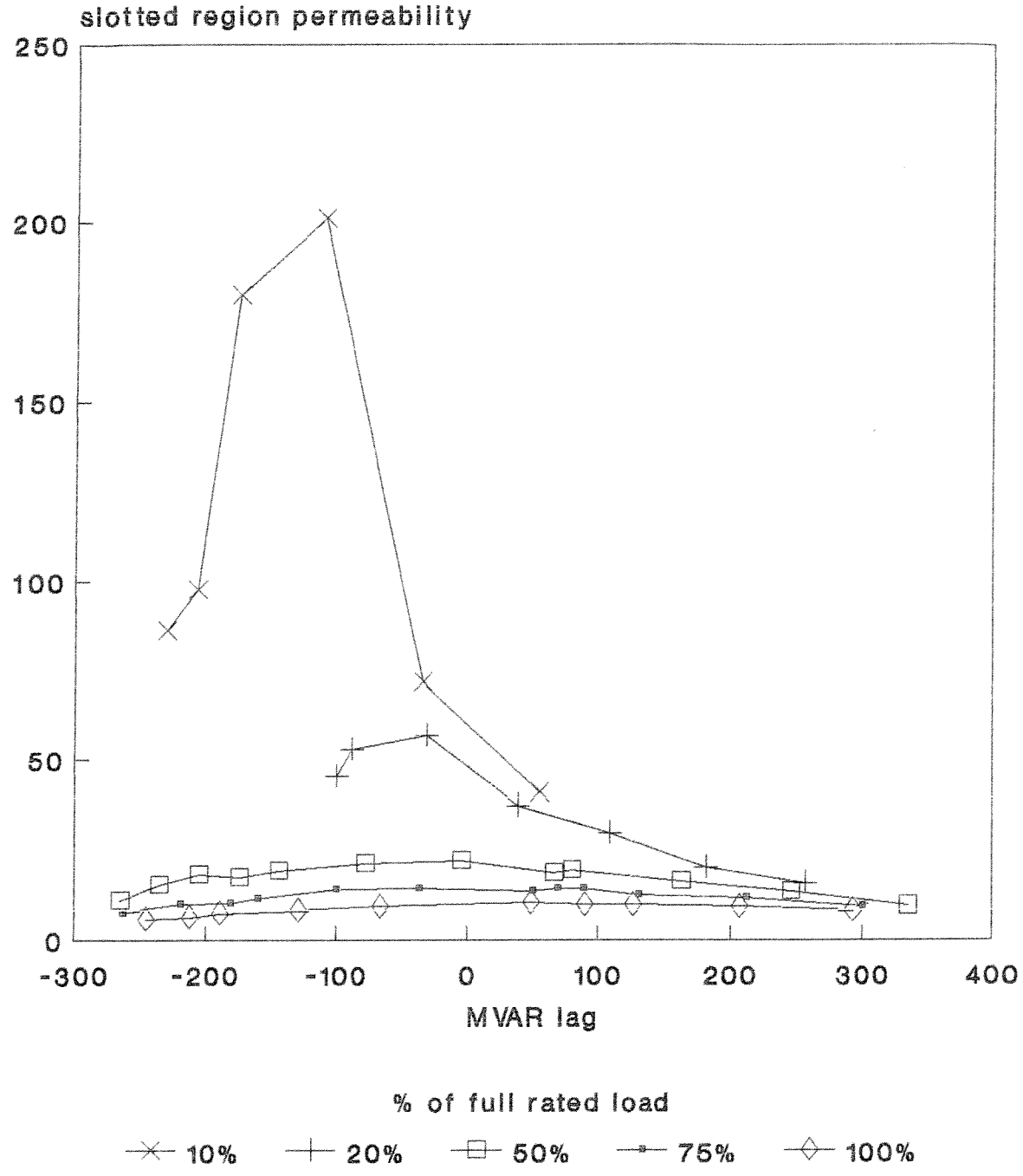

Figure 6.9 Variation of slotted region permeability with MVAR for the model of the Fawley generator (Ferrybridge design)

by a lower proportion than that of the mutual flux path, which passes mainly through saturable iron. Thus the ratio between the reluctances of the two paths changes.

The amount of flux in the field leakage path depends on the excitation current. Thus there will be more field leakage, and more saturation of the field leakage path, in the presence of a demagnetising armature reaction (lagging power factor) than for a magnetising armature reaction (leading power factor). This is why simple methods for obtaining excitation current from the open circuit characteristic tend to produce underestimates for lagging power factor cases and overestimates for leading power factors.

Examination of Figure 6.9 reveals the two distinct effects bearing on the value calculated for slotted region permeability. The load effect produces lower values of permeability due to higher saturation caused by higher stator current. The excitation effect produces lower values of permeability due to higher saturation caused by higher rotor current. At 500MW the load effect is almost completely dominant, whereas at 50MW very high values of permeability are generated at lower leading MVAR. At higher leading MVAR the increased stator current once again becomes the dominant source of saturation.

A set of curves such as those in Figure 6.9, originating from easily identifiable physical principles, immediately suggest the possibility of algebraic description. Such an approach is particularly attractive from the point of view of the multi-region model, as the control algorithm is extremely wasteful of computer time. If a suitable value of slotted region permeability could be selected directly from knowledge of generated MW and MVAR, none of the iterations would be necessary. As with all saturation modelling, the expression to be used would have

to originate from empirical approximations.

Inspection of Figure 6.9 hints at a normal distribution, indicating that the curves might be adequately represented by an expression of the form:

$$\mu_{teeth} = \frac{A(P,Q)}{\sqrt{(2\pi)}} \exp\left[-\frac{B(P)}{2}\left(Q - Q_o(P)\right)^2\right] \qquad (6.104)$$

where the amplitude A is a function of both P (active power in MW) and Q (reactive power in MVAR); the offset Q_o and the lateral expansion B are both functions of P. Clearly, a set of curves derived from Figure 6.9 but displaying the relationship between MW and tooth permeability for a selection of MVAR values is a necessary pre-requisite to attempted identification of A, Q_o and B. It is also clear that this method requires a large amount of test data (or alternatively a large number of finite element analyses) prior to completion of the model. It therefore fails miserably with respect to one criterion of de Mello[49], although other authors[45][54] appear unperturbed at the prospect of finite-element analyses at very many load points. The fact still remains that these analyses need only be performed once, in a batch, the results being then condensed into an algebraic approximation. Such methods seem very much the modern trend in matters of electrical machine modelling.

CHAPTER SEVEN
COMPARISON OF MODEL AND TEST RESULTS

7.1 Test Measurements on Generators

Although reports of vibration reductions between open circuit and full rated load for various machines of "about 30% to 40%" were legion, the availability of meaningful numerical data was poor. For the purposes of assessing the model developed in this work, vibration measurements on two different machines were used which had been supplied early on by GEC Alsthom of Stafford. These machines, the 500MW West Burton generator and the 350MW generator, were described in Section 1.5.

Measurements of radial vibration amplitude and phase were taken on the 350MW generator for a range of MW loads at 0MVAR and a range of MVAR loads at 355MW. Four separate accelerometers were used, at angular positions of 10°, 40°, 100° and 170° clockwise from the horizontal centre line on the left hand side, when viewed from the front (turbine) end. Their axial position was well removed from the core end. The phase measurements are relative to a phase marker on the shaft. The resulting variation in core-back vibration at each individual measurement position for each of the sets of measurements is shown in Figures 7.1 to 7.4. The nature of these measurements is such that together they may be relied upon to represent the trend in vibration, although any individual measurement must be treated with caution.

From the graphs it can be seen that the position of the accelerometer has a very large effect on the vibration measured. The variation is between 15% and 30% of the average amplitude. This result demonstrates that attempted prediction of absolute core-back vibration levels from an isolated core model is not worthwhile. Instead, it is

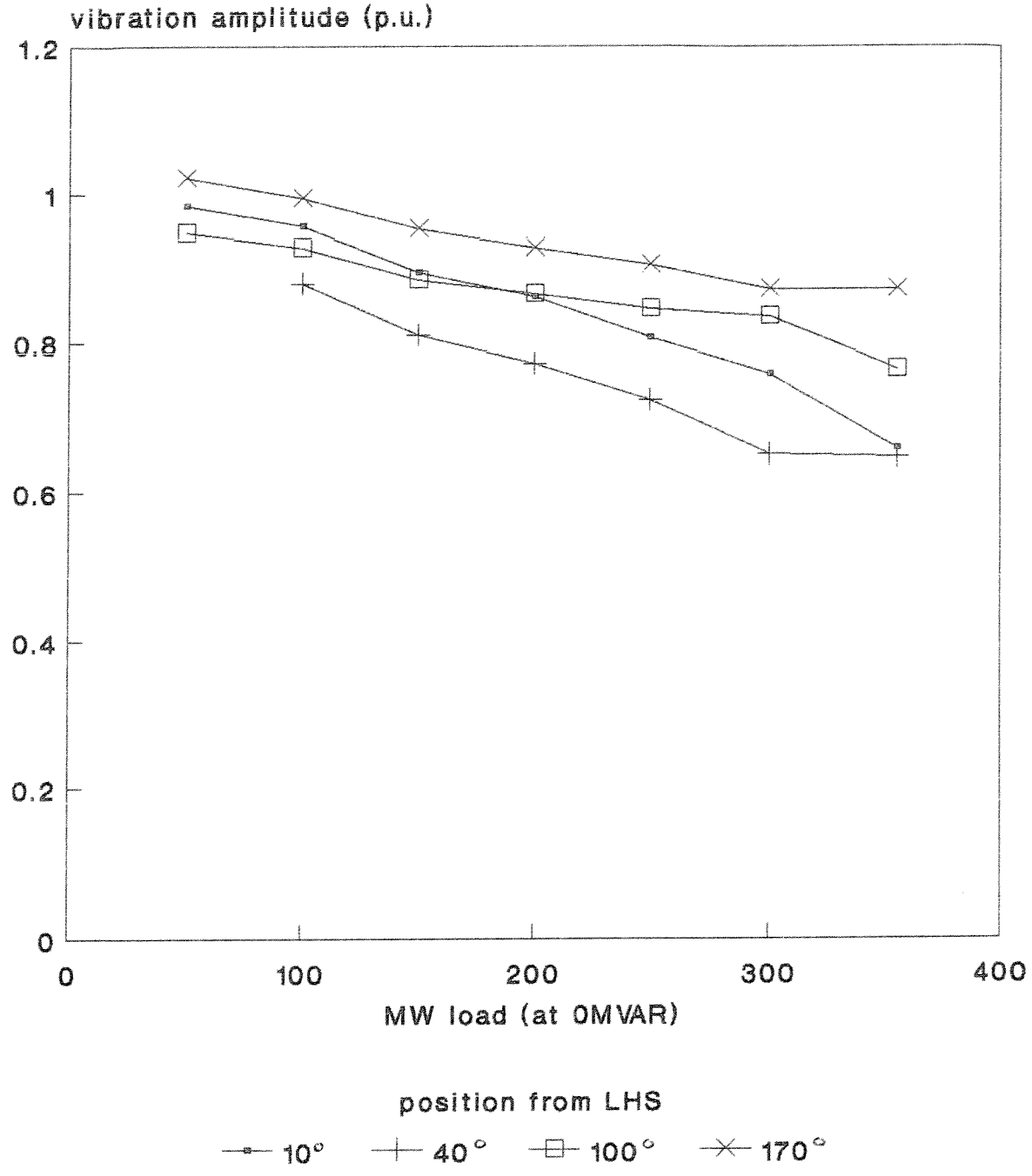

Figure 7.1 GEC 350MW generator - measured vibration amplitude variation with MW

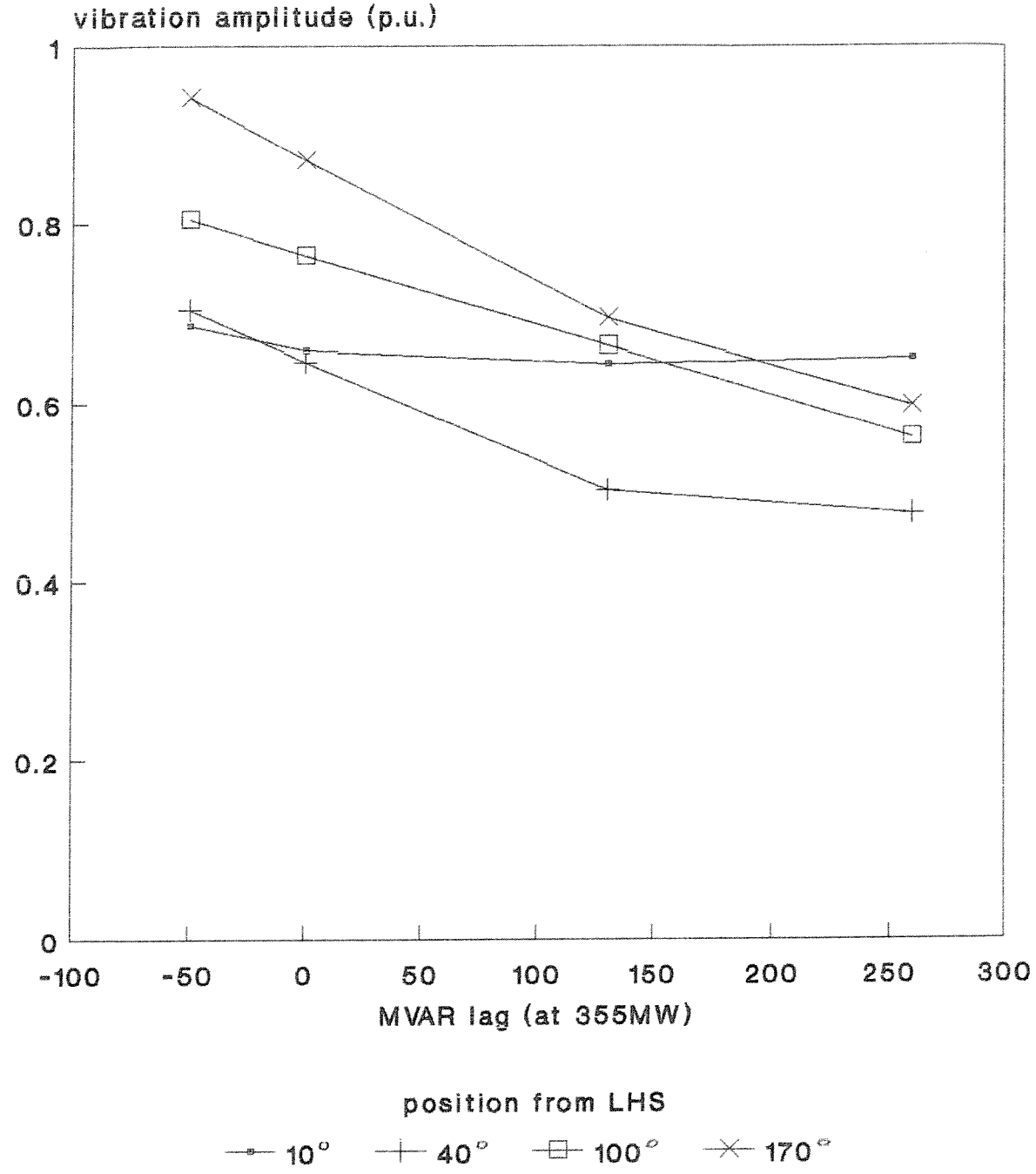

Figure 7.2 GEC 350MW generator - measured vibration amplitude variation with MVAR

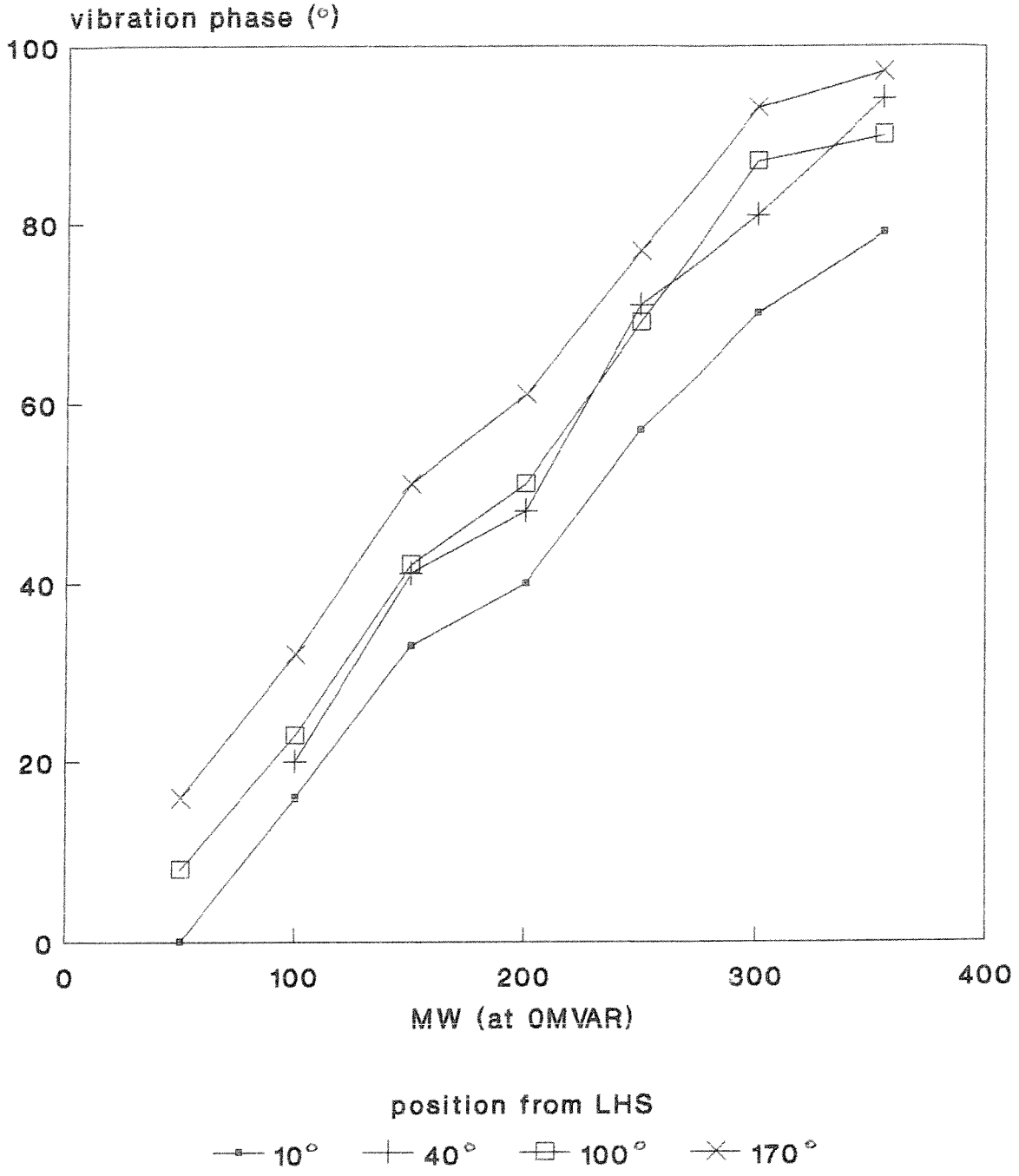

Figure 7.3 GEC 350MW generator - measured vibration phase variation with MW

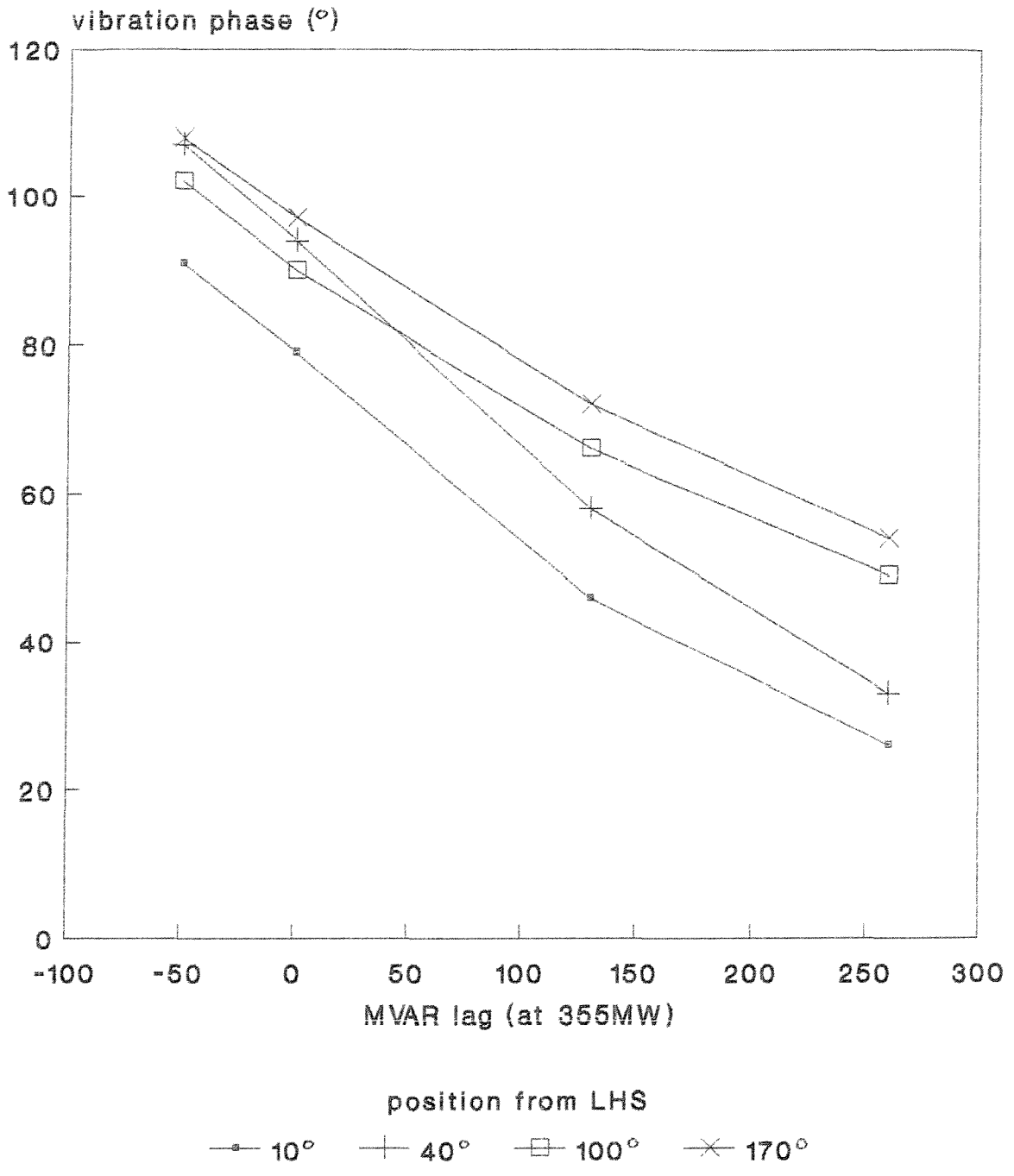

Figure 7.4 GEC 350MW generator - measured vibration phase variation with MVAR

better to predict the trend, and callibrate at a known load for each measurement position. A similar principle applies to phase prediction. As the measurements were taken with respect to an arbitrary shaft marker, it is unlikely the model could reproduce absolute values. Again, prediction of the trend is a more sensible strategy.

An open circuit vibration measurement is not included in the data. If each of the curves in Figure 7.1 is extrapolated to the 0MW axis, the reductions in vibration between open circuit and full rated load (350MW, 262.5MVAR lag) are 33% for the 10° point, 49% for the 40° point, 42% for the 100° point and 43% for the 170° point. The average is 42%.

Figure 7.5 shows the variation of radial vibration amplitude with MVAR load at 500MW for the West Burton generator. As for the 350MW machine, individual measurement points are shown separately. These points are described as: right-hand side, left-hand side, bottom, and 45° from the top on the left-hand side. An accelerometer had also been positioned at the top of the core, but this failed between installation and reading, so no results are available for this point.

These results still show distinct differentiation of vibration levels at the various measurement points. However, the trend does not conform to a smooth decrease in vibration amplitude between high leading MVAR and high lagging MVAR. Light is shed on this matter by consideration of the fact that the measurements at 175MVAR lag were taken immediately following an overhaul of the machine, and a year before the other measurements. The vibration of such machines is known to be higher immediately after an overhaul, as the reassembled structure takes time to settle down. Furthermore, the measurements at 245MVAR lag were taken three months prior to the remaining three, which were

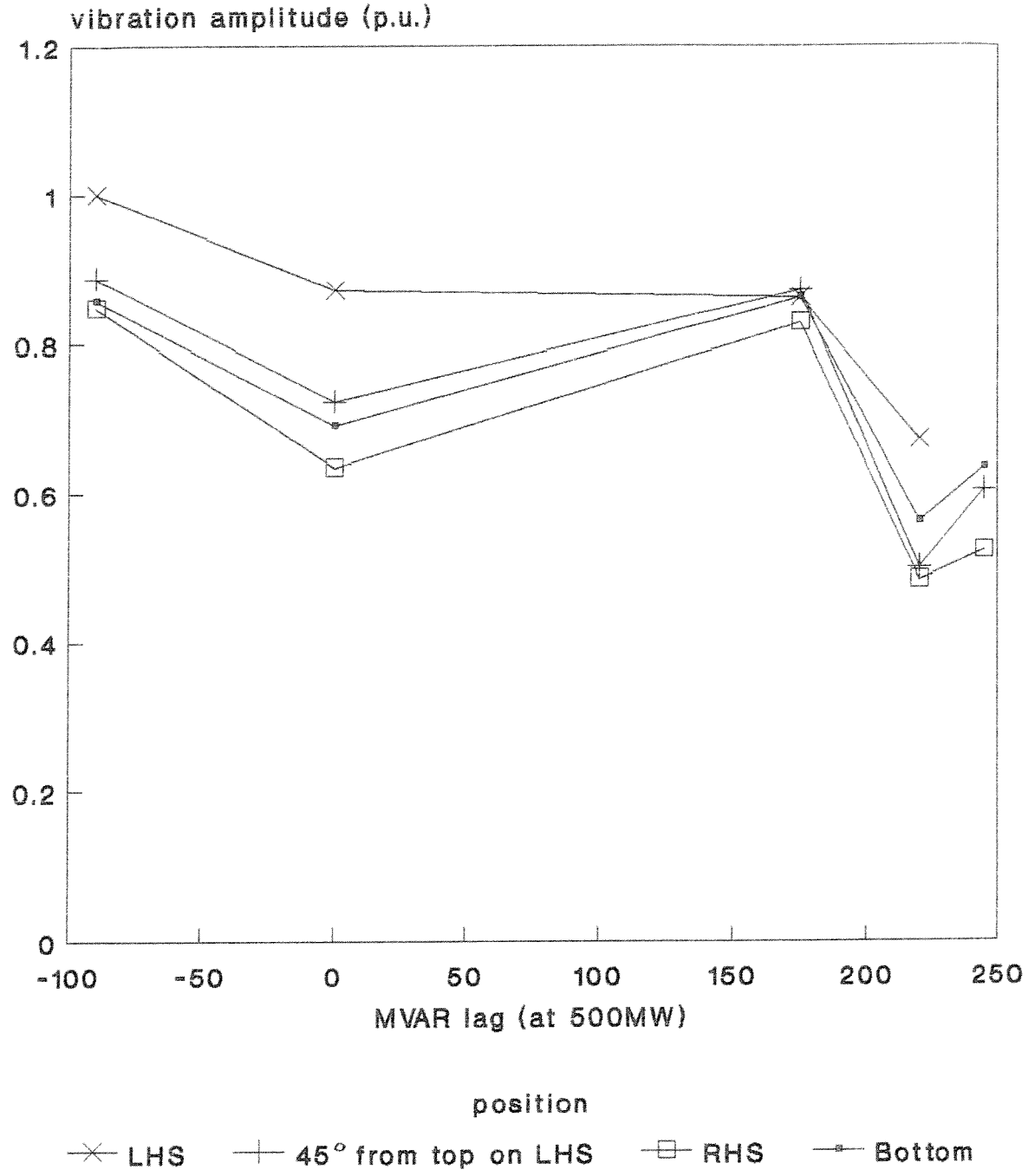

Figure 7.5 West Burton generator - measured vibration amplitude variation with MVAR

all taken on the same day. If only these measurements (at 90MVAR lead, 0MVAR and 220MVAR lag) are retained, the behaviour demonstrated becomes very similar to that observed on the 350MW generator.

The conclusion to be drawn from these results is that not only does the measured vibration level vary with transducer position; it also varies with time. Thus attempted prediction of absolute core-back vibration amplitude by an isolated model is doubly impractical. In a real situation it would be necessary not only to callibrate at each measurement point for a known load, but to recallibrate regularly to allow for variation of vibration level with time. It is also for this reason that the absolute levels of the measurements have not been given, the ordinate axes being instead scaled in a per unit fashion. The per unit base of the 350MW amplitude measurements is an extrapolated open circuit point at the left-hand side of the machine. The phase measurements are given relative to 50MW 0MVAR, again at the left hand side. In the case of West Burton, the per unit base is taken at 500MW 90MVAR lead for the left-hand side of the machine.

Results regarding the variation of vibration of the West Burton generator with MW load for steady MVAR were inconclusive. There existed two results at 0MVAR (500MW and a low load of between 55MW and 80MW) and two results at 175MVAR lag (500MW and 305MW). HOwever, both the low load point and the 500MW 175MVAR lag point were obtained immediately following overhaul, so comparison with the other points at similar MVAR is not valid.

7.2 Mechanical Influences on Core-back Vibration Levels

In Section 7.1 it was shown that vibration amplitude at the core back is very dependent on measurement position.

This is most likely to be due to differences in mechanical coupling between the core and the support structure at these different points. Variations in the stator bore stress distribution due to chording and phase-banding are likely to be mainly smoothed out by the time they are converted to core-back displacement, a supposition which is shown to be correct in Section 7.5.

It is the purpose of this Section to identify some of the effects involved. Comparison of Figures 7.1 and 7.5 shows that measurements taken at corresponding points on the two machines do not bear similar relationships to measurements at the other pairs of points. It can therefore be concluded that the magnitude of each effect is machine-dependent.

Turbogenerator frames are built in two parts: an inner frame and an outer frame or casing. The core is attached quite firmly to the inner frame by a number of key bars, whilst the outer frame is set in massive concrete supports on each side. In the GEC design, the coupling between inner and outer frames occurs at four circumferential points by means of spring plates, which are attached so as to be tangential to the outer surface of the inner frame and the inner surface of the outer frame. The idea is to allow radial deflection but restrain circumferential movement. At each circumferential position there are several plates along the length of the machine. Two sets of plates are located at the sides of the frame, to support the weight of the core; the others are located at the top and bottom to resist the machine torque. The general arrangement for the West Burton generator is shown in Figure 7.6.

All the spring plates are in compression in operation. The direction of rotation of the West Burton generator is anticlockwise, when viewed from the turbine end. Thus the left-hand spring plate, already in compression due to the

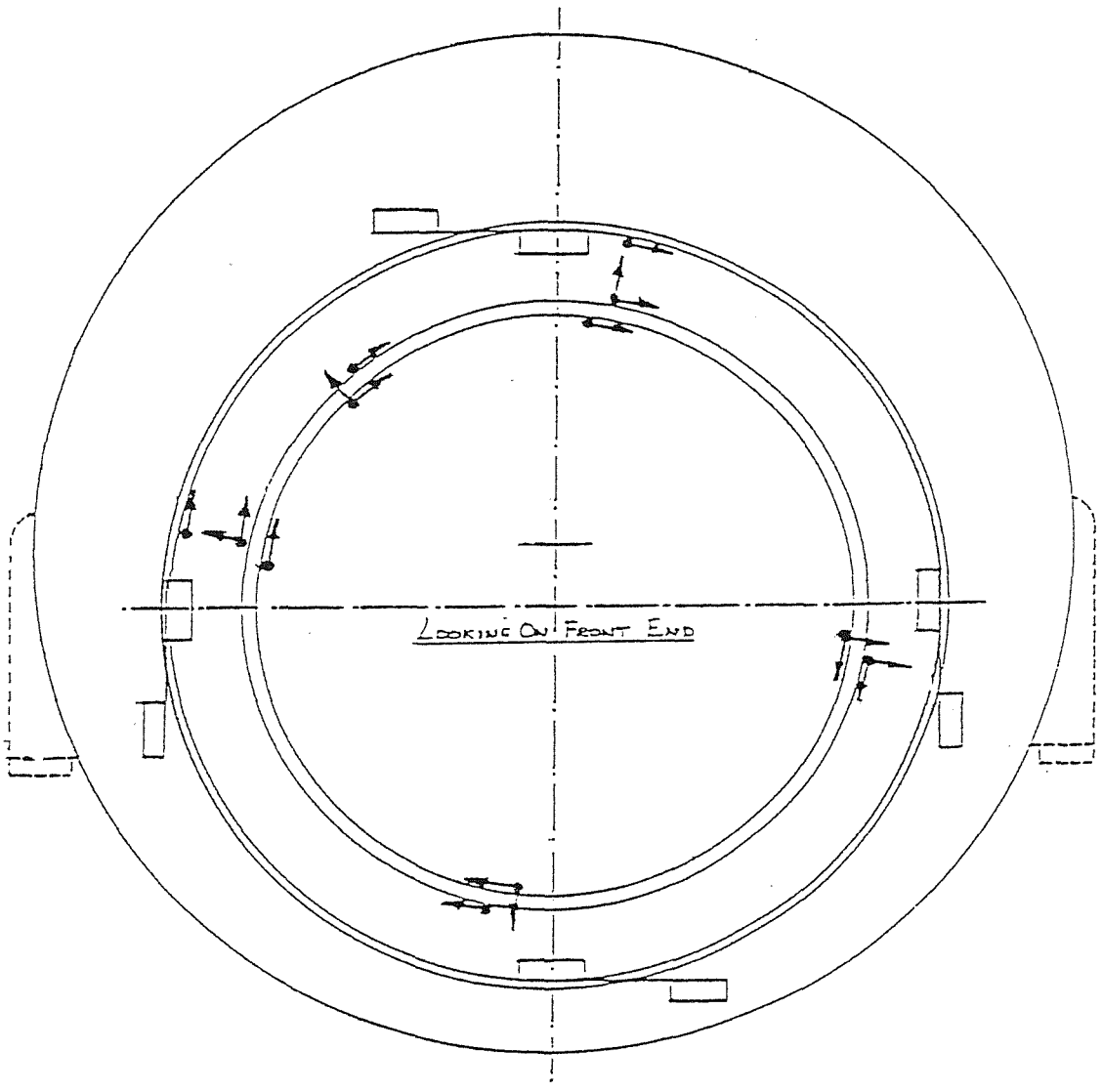

Figure 7.6 Support structure of the West Burton generator, reproduced with permission from GEC Alsthom Turbine Generators Ltd (the arrows show the positions of the accelerometers; some on the frame as well as on the stator core back)

weight of the core, will be compressed further, whilst the compressive force on the right-hand spring plate will be reduced by the opposing torque. That the force remains compressive and does not become tensile under these conditions may be shown by a simple comparison of the two opposing forces: the core weight and the torque. An approximation to the core weight may be obtained by considering it to be a hollow cylinder with a smooth bore. Thus the mass of the windings in the slots is replaced by extra mass of iron, but the end windings are not represented, so the weight thus obtained is likely to be an underestimate. It is given by the following equation:

$$W = \pi(R_B^2 - R_S^2)L\rho g \qquad (7.1)$$

where W is the weight of the core, R_B the core-back radius, R_S the stator bore radius, L the actual length of the core, ρ the density and g the acceleration due to gravity. For the West Burton generator this works out at 1.886MN. The force on one set of spring plates is half this, or 943kN. The force, F_T, due to the torque on each set of spring plates is given by:

$$F_T = \frac{P}{4R_S\omega} \qquad (7.2)$$

where P is the shaft power and $\omega=2\pi f$. The factor of 4 appears because all four sets of spring plates act to resist the torque. On full rated load of 500MW, this force is 620kN. Thus it is seen to be smaller than the force due to the weight of the core. The forces on the top and bottom spring plates will be due to the torque only, so will be equal. The 350MW generator, however, rotates in the opposite direction. In its case, the right-hand spring plate will be in greater compression due to the torque whilst the compression in the left-hand spring plate will be reduced.

The behaviour of structural elements in compression has been extensively studied, due to the importance of

understanding the factors involved in buckling. Timoshenko[57] presents a treatment of a problem which crudely represents the situation of the spring plate: a compressed bar with a lateral load applied in the middle. The lateral load of interest here is the stator core-back vibration, which is in fact applied at the end, so the spring plate actually represents half of Timoshenko's bar.

The formula obtained for the maximum static lateral deflection, d_l, for a bar of length l, Young's modulus E and second moment of area I, due to a lateral load Q, is:

$$d_l = \frac{Ql^3}{48EI} \cdot \frac{3(\tan u - u)}{u^3} \qquad (7.3)$$

The first factor on the right hand side of the equation is the lateral deflection which would result from application of the lateral force Q alone. The second factor represents an adjustment due to the compression of the bar by an axial force P, more explicitly:

$$u = \tfrac{1}{2}l.\sqrt{(P/EI)} \qquad (7.4)$$

When P is small, u is also small, and its tangent may be approximated by the first two terms of the Taylor series:

$$\tan u = u + u^3/3 \qquad (7.5)$$

which makes this second factor approximately unity. However, when u is large, tan u dominates the expression, and the deflection becomes indefinitely large as P tends towards the critical load such that $u=\tfrac{1}{2}\pi$. Such behaviour is not evident in the turbogenerator frame spring plates under normal operation, as they are stressed to loads well below buckling levels. However, the loads may be such as to provide an appreciable difference in radial stiffness at points adjacent to the four spring plate fixings.

Evidence that this is in fact the case is provided by Figures 7.1, 7.2 and 7.5. It can be seen from Figure 7.5 (West Burton) that on the side of the most compressed left-

hand spring plate the radial core-back vibration is highest whilst on the side of the least compressed right-hand spring plate it is lowest. The other two measurement points give intermediate values. Figures 7.1 and 7.2 (350MW machine) do not give such clear support to the theory. Whilst the most compressed right-hand spring plate appears again to have allowed a higher radial core-back vibration level than that measured at other points, the left-hand side measurements are not clearly distinct from those taken at the top of the core. Measurements at the point intermediate between top and left-hand side spring plates show the minimum vibration amplitudes.

A crude attempt was made to model the spring plates on ANSYS. The purpose was not to model the effect of their being in varying degrees of compression, but to investigate their effect when considered as a means of four-point tangential restraint. The standard core representation of the 350MW stator was used: slotted with wedges and homogenised slot contents of Young's modulus $1.0 \times 10^{9} Nm^{-2}$. An analysis was performed with the automated multi-region program at the load condition 350MW 0MVAR, using current sheet fundamentals only. Besides the usual radial and circumferential tooth force output, the real and imaginary components of x and y force were generated for each tooth to provide suitable input data for ANSYS. The core representation on ANSYS was restrained such that y movement was prohibited at the extreme right- and left-hand side nodes; x movement at the top and bottom.

Output from ANSYS could only be in terms of x and y displacements, although an option is available which allows these to be expressed in amplitude and phase angle form. Radial displacements were required, so a simple computer program had to be written to provide the conversion. Unfortunately, data transfer between the VAX computer and the IBM was not possible, so all the x and y output had to

be typed in by hand as data for the conversion program. Displacement results were obtained at 54 core-back positions, each one opposite a tooth tip at the stator bore.

The resulting variation of radial vibration amplitude at 100Hz is shown in Figure 7.7, normalised to the level obtained with an unrestrained core. It clearly takes the form of an eight-pole wave. The peak radial vibration amplitudes are found at the points of tangential restraint; the minimum radial vibration amplitudes at points mid-way between these restraints.

The origin of this result becomes clear on consideration of the mode shape, which was shown in Figure 5.8. Displacement of points on the axes of the ellipse is in the radial direction only. Thus when these axes fall in line with the axes of the tangential restraints, the behaviour of the structure is identical to its unrestrained behaviour. However, at the mid-points between the axes of the ellipse, tangential displacement is greatest. When these axes lie at 45° to the axes of the restraints, this movement is suppressed, with the result that the overall distortion is much reduced.

Application of this result to stator core vibration would tend to suggest that amplitudes would be lowest at core-back positions mid-way between the spring plates. Inspection of Figures 7.1 and 7.2 shows clearly that for the 350MW machine this is indeed so.

It is now possible to conclude that both the level of compression in the spring plates and the effect on the ovalising mode shape of the tangential restraint they provide affect the levels of core-back vibration observed. The dominance of one effect over the other is machine-dependent. Of the two machines examined with this type of support, the first effect dominates in the West Burton core;

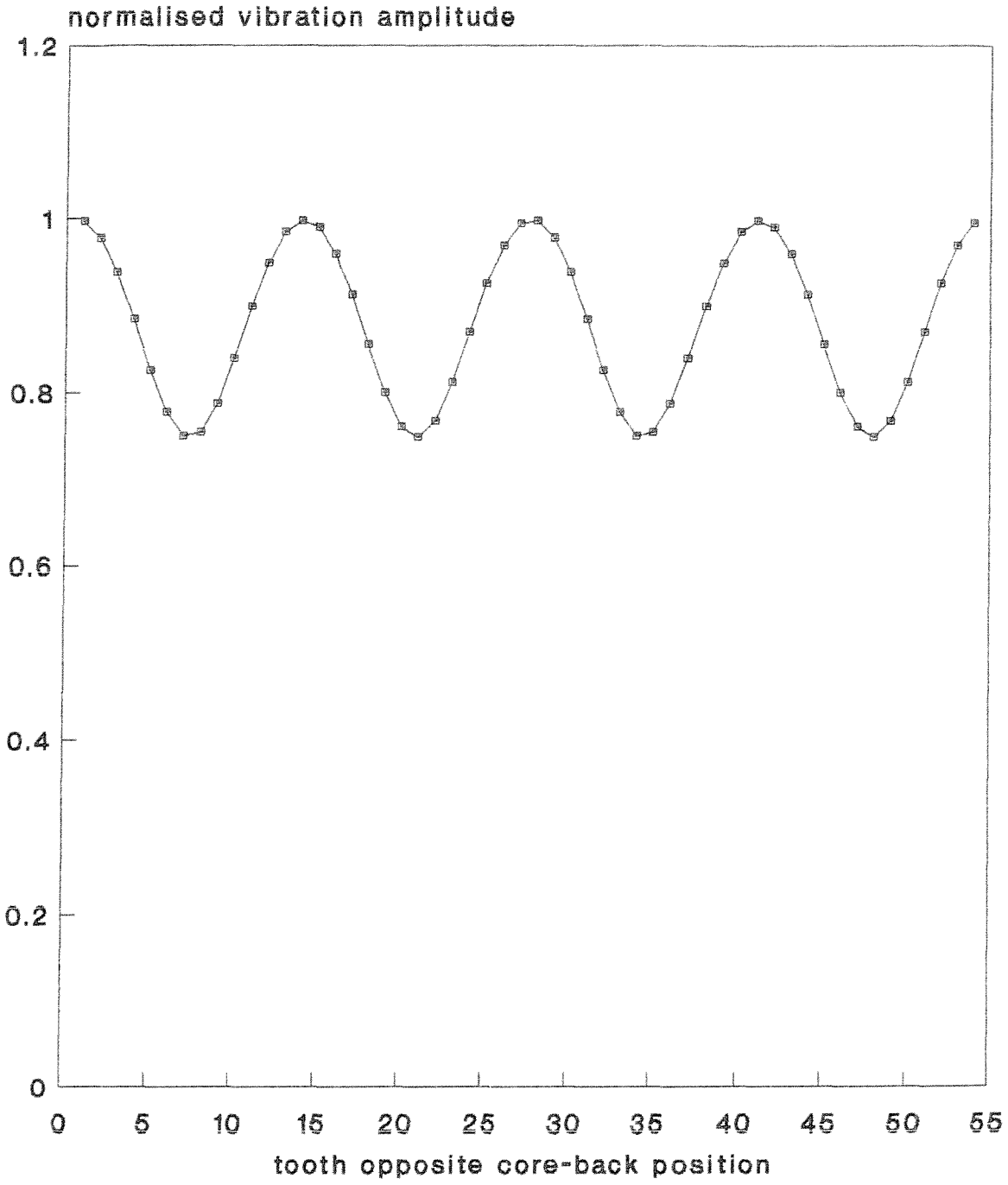

Figure 7.7 Variation of vibration amplitude around the back of an ANSYS core representation fixed tangentially at four equi-spaced core-back positions to model the spring plates

the second in the 350MW core.

7.3 Selection of a Mechanical Stator Core Representation

Sections 7.1 and 7.2 have shown that it is not reasonable to expect to predict absolute core-back vibration levels using transfer coefficients obtained from an isolated core representation. The best that can be hoped for is to predict the trends, and rely on callibration to generate absolute values.

It therefore follows that the mechanical core representation selected should be the one which most accurately predicts the trend in vibration level with load. This conclusion was hinted at in Section 5.6. There were three distinct versions of the core representation developed: one with completely empty slots; one with empty slots which were wedged at the openings; one with wedged slots filled with a homogenised conductor-insulation mass. Variations of the third version in which the slot filling assumed different values of Young's modulus were shown to yield radial and circumferential force transfer coefficients in very similar ratios, and therefore may be expected to predict similar vibration trends.

In Figure 7.8 the vibration trends predicted by the three representations of the West Burton core are shown for a load of 500MW at between 90MVAR lead and 245MVAR lag. It can be seen that the predicted amplitudes vary greatly amongst the models. However the decrease between 90MVAR lead and 245MVAR lag is 34.6% in the case of the empty slotted core, 32.5% in the case of the core with wedged empty slots, and 32.6% in the case of the core with wedged filled slots. Thus it can be concluded that once slot wedges are modelled, it makes little difference to the trend whether the slots are filled or not. The advantage of

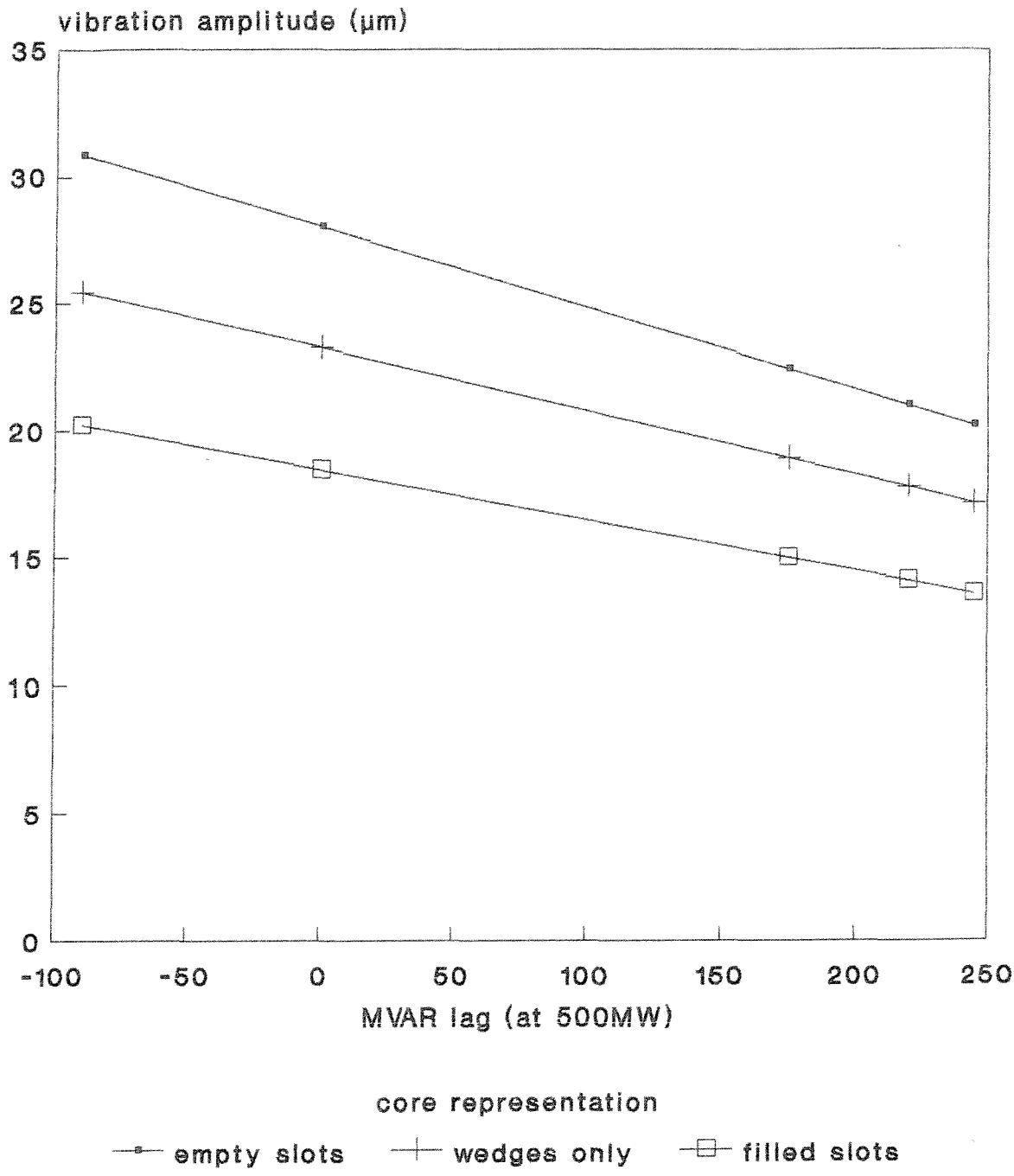

Figure 7.8 Vibration amplitudes predicted by three different representations of the West Burton stator

selecting the model with filled slots is that it is possible to tune the ovalising resonant frequency to a value approximately that of the core being modelled, by altering the Young's modulus of the slot filling.

The empty slotted core gives a higher percentage reduction that the other two between the extreme load conditions examined. However, inspection of Figure 7.5 shows that the variations in trend obtained from different transducers show a significantly wider spread than that obtained from the different models. In the light of this information, it is not important which representation is selected, although it may still be prudent to choose the one which shows the most suitable dynamic response.

7.4 Extension of the Model to Facilitate Analysis of a Comprehensive Set of Load Conditions

7.4.1 Introduction: Necessary Extensions and Final Goal

The automated multi-region model as described so far takes terminal voltage, MW and MVAR load, and excitation current as input, and produces core-back vibration amplitude as output, together with intermediate quantities such as tooth force and components of flux density at the stator bore. Extension of both input and output capabilities is necessary if it is to be assessed on its ability to reproduce the trends shown by test results. The 350MW generator is especially important, for the test data is usefully systematic, comprising, as it does, variations with MVAR at one steady MW load and with MW at one steady MVAR load. Furthermore, the data points are more or less equally spaced, and were all taken at around the same time. It is far more difficult to deduce meaningful relationships from the West Burton results due to the long timescale over which they were collected.

The results for the 350MW generator are in terms of amplitude and phase. The model program has not, so far, incorporated a vibration phase calculation, although the phase of each tooth force relative to the axis of the rotor m.m.f. is produced in the course of the calculation of the phase difference between the two components of force on each tooth. Thus to investigate whether the model satisfactorily reproduces the vibration phase change with load, it is necessary to incorporate such a calculation.

Values of rotor current at each of the load points are not available; they were not measured at the time. Thus an estimation of rotor current from the open and short circuit characteristics of the machine needs to be included. Such a routine should only be used if experimental values are unavailable as it cannot hope to be as accurate as a measurement.

It was considered also useful to incorporate a torque calculation, based on the z.f. Fourier coefficient of the circumferential tooth force. As MW load is part of the required data input, this calculation should yield very accurate results if the program is functioning correctly.

Once these three modifications are incorporated into the program, it will be possible to attempt to simulate the results shown in Figures 7.1 to 7.4. If the outcome is satisfactory, the model may be considered to give an adequate representation of the variation of double-frequency stator core vibration with load. The final stage will be to generate a comprehensive set of results at many loads and power factors, to give an overall picture of the nature of this variation.

7.4.2 Vibration Phase Calculation

This Section comprises a description of the vibration

phase calculation inserted into the automated multi-region model program with the purpose of assessing its ability to predict the variation of phase with load observed in measurements. The phase reference in the tests on the 350MW machine was an arbitrarily placed marker on the shaft. All angles produced by the model are ultimately referenced to the original Θ=0 reference, which coincides with the axis of the rotor m.m.f. at time zero. Thus a degree-variation correlation between model and measurement is sought, rather than a reproduction of actual test values.

The Fourier analysis described in Section 4.4 to extract the magnitude of the radial and circumferential components of tooth force fundamental produces, in the first instance, coefficients a_{r1}, b_{r1}, $a_{\theta 1}$ and $b_{\theta 1}$ such that:

$$F_{r1} = a_{r1} \cos 2(\Theta-\omega t) - b_{r1} \sin 2(\Theta-\omega t) \qquad (7.6a)$$

$$F_{\theta 1} = a_{\theta 1} \cos 2(\Theta-\omega t) - b_{\theta 1} \sin 2(\Theta-\omega t) \qquad (7.6b)$$

The minus sign originates from the fact that the argument of the sine functions is $\Theta-\omega t$ and the integration is over ωt.

Previously, the magnitudes and angles of F_{r1} and $F_{\theta 1}$ have been found, then the equivalent vibrations of each and the phase difference between them. This process was described in Section 5.3. If extraction of vibration phase is required, it is necessary to convert the force expressions of equation (7.6) directly to vibration expressions whilst still in Fourier series form. In the case of the component of radial vibration due to radial force, it is necessary only to multiply the entire right-hand side of equation (7.6a) by the relevant transfer coefficient, $k_{r,r}$:

$$d_{r,r} = a_{r1}k_{r,r} \cos 2(\Theta-\omega t) - b_{r1}k_{r,r} \sin 2(\Theta-\omega t) \qquad (7.7)$$

In the case of the component due to circumferential force, it is necessary not only to multiply by the transfer coefficient $k_{r,\theta}$ but to allow the vibration to lag the force

by 90°. Thus the cosine component becomes a sine, and the minus sine a cosine:

$$d_{r,\theta} = a_{\theta 1} k_{r,\theta} \sin 2(\Theta-\omega t) + b_{\theta 1} k_{r,\theta} \cos 2(\Theta-\omega t) \qquad (7.8)$$

An expression for the total vibration d_r may be obtained by summing sine and cosine components of both expressions:

$$d_r = (a_{r1} k_{r,r} + b_{\theta 1} k_{r,\theta}) \cos 2(\Theta-\omega t) + (a_{\theta 1} k_{r,\theta} - b_{r1} k_{r,r}) \sin 2(\Theta-\omega t) \qquad (7.9)$$

In the program, variable names are assigned to the expressions $a_{r1}k_{r,r}+b_{\theta 1}k_{r,\theta}$ and $a_{\theta 1}k_{r,\theta}-b_{r1}k_{r,r}$. These variables are used as arguments of the four quadrant inverse tangent subroutine described in Section 4.1. The angle returned by the routine is the phase of the vibration with respect to the axis of the rotor m.m.f. at time t=0. It is a time-phase angle on a 100Hz wave.

7.4.3 Torque Calculation

As the output power in MW is specified as part of the input data for any load condition, and the angular speed of the machine is fixed, calculation of torque from the multi-region model should be very accurate. Thus to include the calculation of torque directly from circumferential Maxwell stress can provide a check on correct operation of the program.

If the zero frequency Fourier coefficient is extracted concurrently with the fundamental sine and cosine coefficients, the result is an average circumferential tooth force over one vibration cycle. The average circumferential forces on all the teeth need to be summed to give the total average circumferential force, which must then be multiplied by the stator bore radius to give the torque per unit axial length of the machine, and finally by the active length to give the total torque.

This calculation is straightforward, except for the need to allow for different numbers of teeth being analysed. If the first tooth operated upon is always tooth number one, the value of the tooth loop variable subsequent to the calculations will be the number of teeth considered plus one. Therefore the total torque can be obtained from the number of stator teeth in the machine, the number of teeth covered in the calculation, and the sum of the tooth torques calculated on each pass. Thus if n is the total number of stator teeth, i the eventual value of the loop variable, L the active length of the machine, R_s the stator bore radius and a_{o1}, a_{o2} etc the zero frequency Fourier coefficients of force on successive teeth, the torque may be obtained from the expression:

$$T = \frac{n}{i-1} (a_{o1}+a_{o2}+\ldots+a_{oi}) L R_s \qquad (7.10)$$

7.4.4 Estimation of Rotor Current Where Measured Value is Unavailable

The vibration measurements on the 350MW machine at specified loads were not accompanied by rotor current measurements. As the automated multi-region model relies on rotor current to set a suitable level of slotted region permeability, it is important to provide an estimate if a measurement is not available. Furthermore, to carry out a comprehensive set of analyses with the model at many loads and power factors also requires that a value of rotor current be provided.

Thus a routine was added to the program which uses the Potier method to estimate rotor current. This method relies only on open- and short-circuit characteristics for the machine, and a value of stator leakage reactance. The open circuit characteristic is approximated by the computer program as a Frohlich curve, the coefficients of which are appended to the other data in the data file.

The short-circuit characteristic gives the field current necessary to produce a given stator current when the machine is on short circuit. The resistance of the stator winding of a large turbogenerator is small compared with its inductance, so the short-circuit stator current may reasonably be considered to be at zero power factor lag. The stator field, or armature reaction, is thus directly demagnetising. The rotor m.m.f. must oppose the armature reaction and also circulate flux through the stator leakage reactance. If a load is connected to the generator terminals such that the same stator current is circulated, still at zero power factor lag, extra excitation is required to maintain a voltage across that load. The total excitation is the sum of these three components. The Potier triangle is shown on Figure 7.9. Its base is the field current necessary to oppose the armature reaction on short circuit. Its height is the voltage across the stator leakage reactance. If the triangle is then displaced vertically and horizontally such that the locus of its vertex follows the open-circuit characteristic, its far right-hand point will correspond to the necessary field current to excite the terminal voltage required to circulate the stator current at zero power factor.

When a non-zero power factor load is considered, it is not possible simply to sum the currents or e.m.f.'s involved; vector addition must be used. The complete phasor diagram is shown in Figure 7.10. Thus for any load, E_g is found from V_T, I_s and X_l, for which the line value must of course be used. Then the open-circuit characteristic is used to read off a value of field current corresponding to that necessary to excite the air-gap e.m.f. E_g. The phasor calculation corresponding to the remainder of the diagram in Figure 7.10 is performed in terms of rotor current. In place of I_sX_a the field current corresponding to the base of the Potier triangle is used, eventually yielding the field current corresponding to the total excitation e.m.f., E_f.

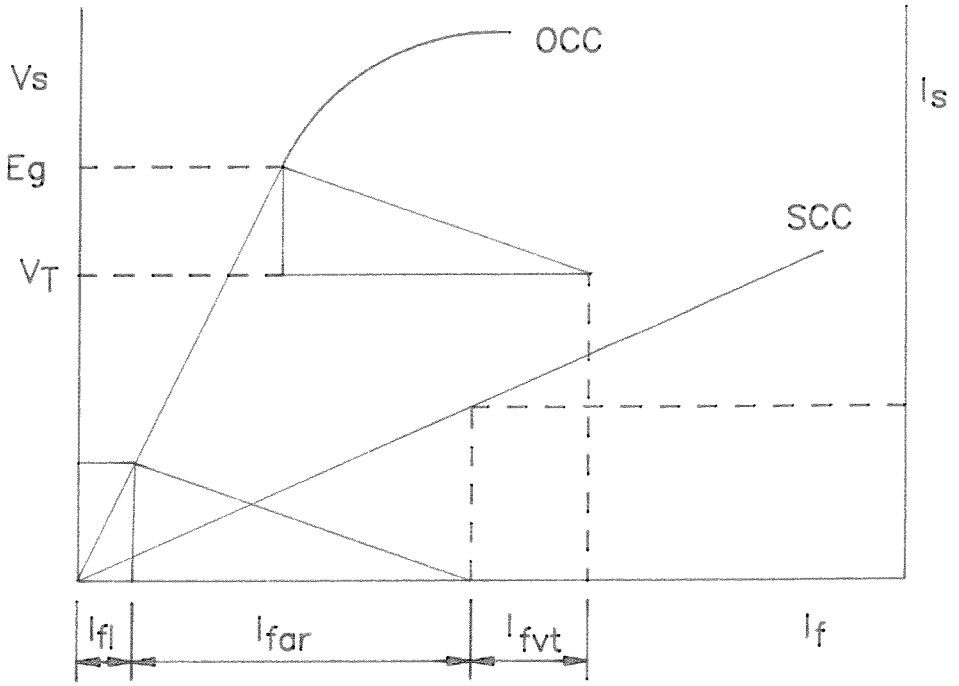

Figure 7.9 Construction of the Potier triangle

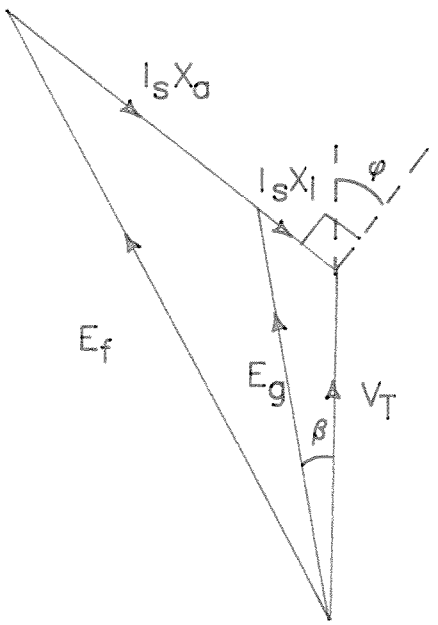

Figure 7.10 Complete phasor diagram of the synchronous generator on load

This is the required result.

The calculations performed in the program, therefore, amount to no more than simple trigonometry. However, it is also necessary to represent the open- and short-circuit characteristics in numerical form in each machine data file. The short-circuit characteristic and the air line may be represented by one value each, corresponding to their respective slopes, as both are straight lines. The saturated portion of the open-circuit characteristic requires an approximate algebraic formula. The Frohlich[58] approximation is used here, in the form:

$$E = \frac{I}{a+bI} \qquad (7.11)$$

The coefficients a and b were determined empirically for each machine by solving for them at four different pairs of E and I close to rated terminal voltage and averaging the results.

7.4.5 Model Simulation of 350MW Generator Test Results

Using the automated multi-region model equipped with the routines developed in earlier parts of Section 7.4, a set of analyses were performed for the 350MW generator at load points corresponding to the test measurements described in Section 7.1. The model cannot, of course, represent the variation amongst different measurement points. Neither do its results vary with time. It is therefore valid to label the ordinate axis in actual units (micrometres peak), provided a statement is also made about the mechanical representation of the core involved. This was the standard one with wedged slots filled with a homogenised contents of Young's modulus $1.0 \times 10^9 Nm^{-2}$.

Although slotting and saturation were taken care of by the automated multi-region model, the windings were both modelled as fundamental-only sinusoidal current sheets.

Harmonics were deliberately abandoned during the first stages of the development of the model. If it were to turn out that the model produces an adequate simulation of the vibration behaviour of a number of machines without considering harmonics, it could be concluded that such a simplified model is justified, and time could therefore be saved.

MW	MVAR	Torque (MNm)
50	0	0.159
100	0	0.318
150	0	0.477
200	0	0.637
250	0	0.796
300	0	0.955
355	50 lead	1.130
355	0	1.130
355	130 lag	1.130
355	260 lag	1.130

Table 7.1 Results of the torque calculation for the 350MW generator

The values obtained from the torque calculation are shown in Table 7.1. These should be very accurate, as power is one of the independent variables of the model. The fact that they are indeed very accurate provides confidence in the validity of the use of the tooth force to obtain electromagnetic stress at the stator bore.

The vibration phase and amplitude results for these ten

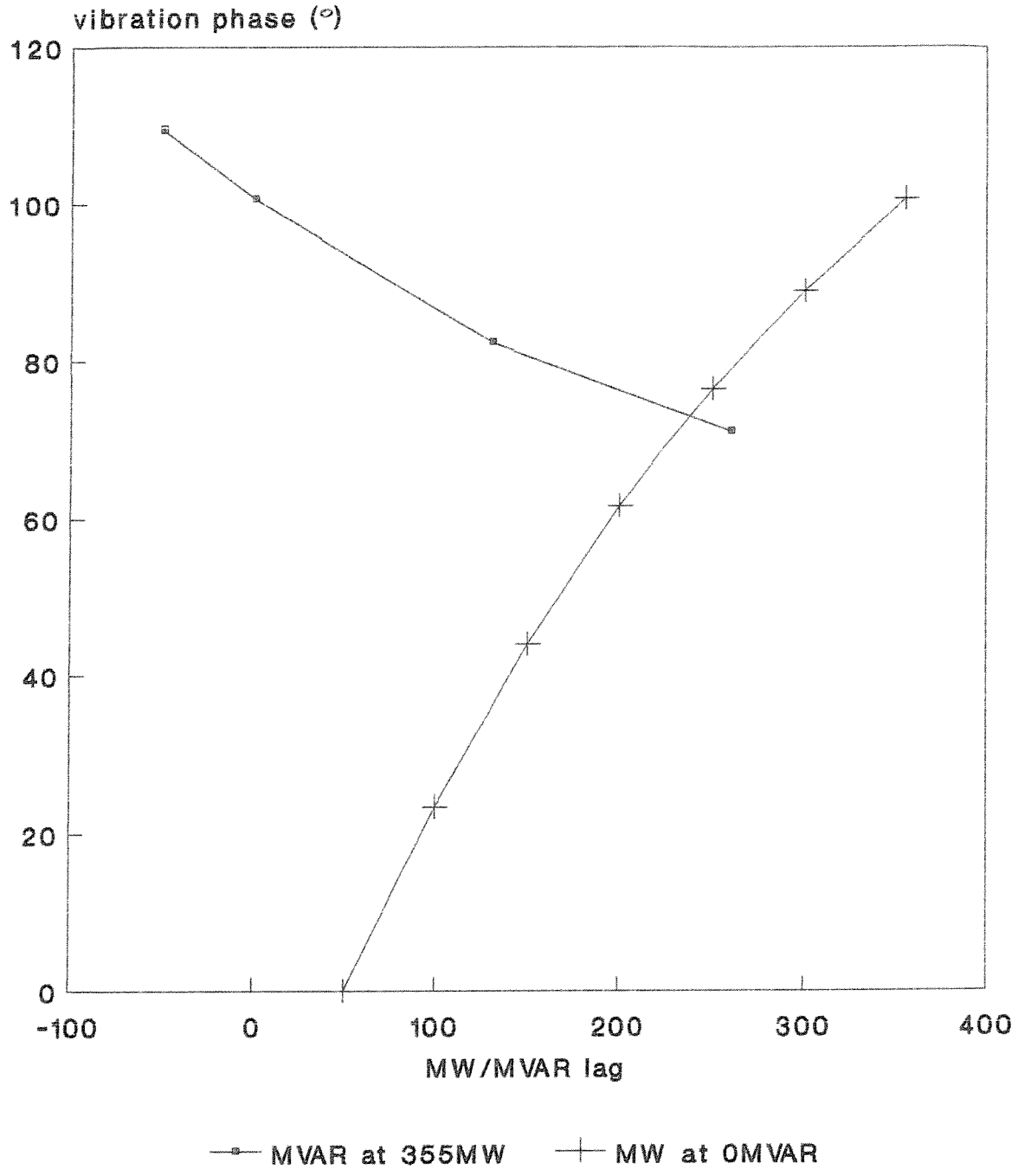

Figure 7.11 GEC 350MW generator - predicted vibration phase at points corresponding to the measurements

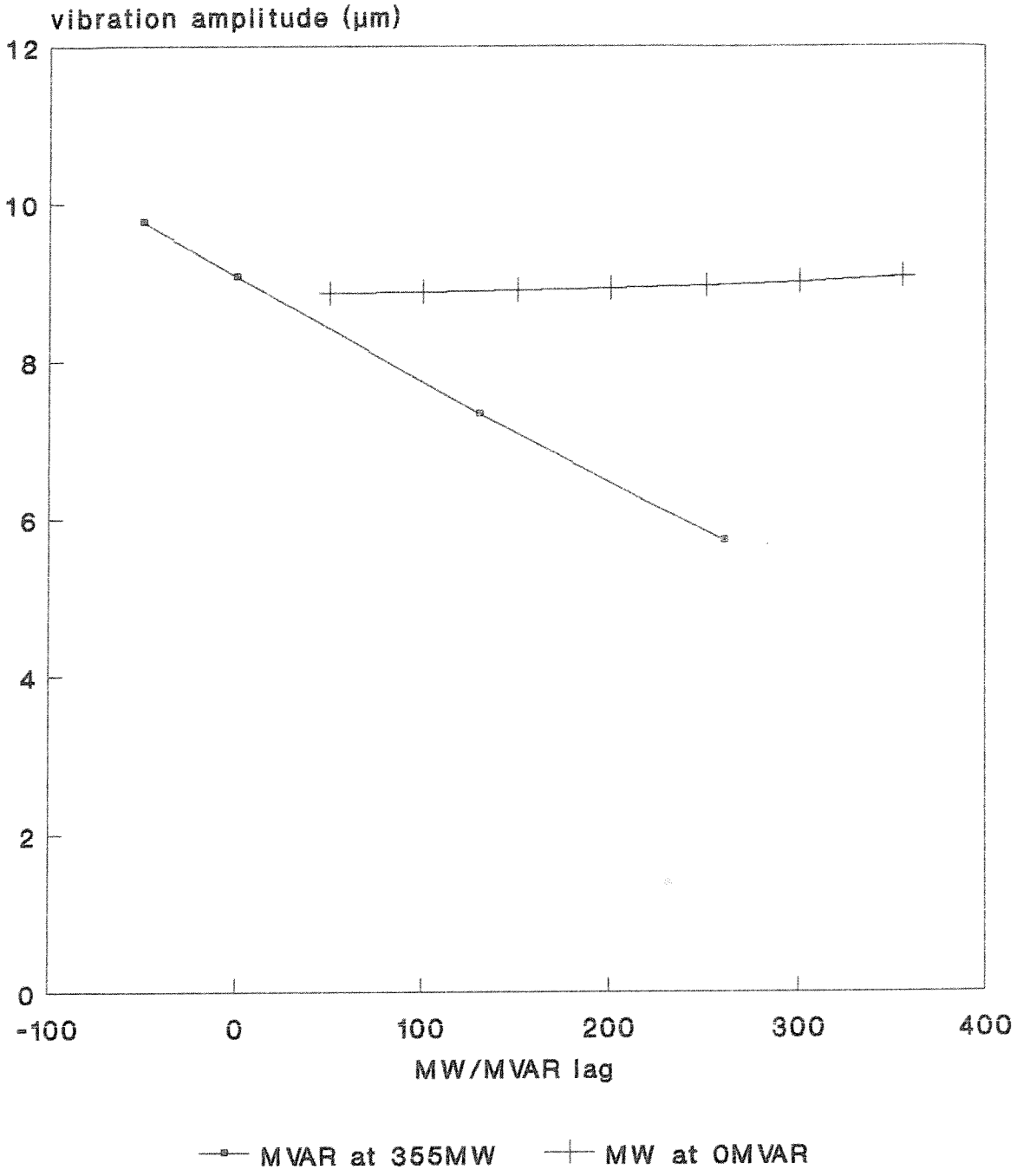

Figure 7.12 GEC 350MW generator - predicted vibration amplitude at points corresponding to the measurements

load points are shown in Figures 7.11 and 7.12 respectively. Figure 7.11 (phase) corresponds to Figures 7.3 and 7.4 of the test results. Comparison of the curves obtained shows similar trends in both cases. The model shows a slightly steeper rise in phase change for the 0MVAR curve (100° instead of 80°). This results in higher values of relative angle for the 355MW curve, exacerbated by the fact that the model also shows a less steep slope than the measurements. However, these results are close enough to be encouraging.

The amplitude results are not as favourable. Comparison of the 355MW curve in Figure 7.12 with Figure 7.2 shows a moderate agreement, although the model has a steeper slope than the average of the measured vibrations. The 0MVAR curves, however, do not correspond at all. Whilst measurement shows a decrease with increased MW at 0MVAR of the same order as that with increased lagging MVAR at 355MW, the model shows a very small increase in vibration.

Whilst the discrepancies between model and measurement in the first three cases could reasonably be attributed to general inaccuracies inherent in both, the fourth result clearly indicates some form of basic misrepresentation by the model. The most obvious possibility is the effect of current sheet harmonics. This possibility is examined in detail in Section 7.5.

7.5 The Effect of Higher Current Sheet Harmonics

The West Burton (500MW) generator was used initially to investigate the effect of including successively higher harmonics of the current sheet expressions. The analyses were performed at its full rated load condition (500MW 310MVAR lag). First, the stator current sheet was retained in a fundamental representation whilst successive rotor current sheet harmonics were included. Secondly, cases of a

fundamental-only rotor current sheet plus successive stator current sheet harmonics were investigated. Finally, a few analyses were performed in which both current sheets were represented in terms of a harmonic series.

Table 7.2 shows the results from the first set of analyses, in which the rotor current sheet harmonics only are included. From this it can be seen that harmonics higher than the 5th have very little effect, although the 3rd is highly significant, producing an increase in vibration equal to 13% of the fundamental value.

Rotor current sheet harmonics	F_r (kN)	F_θ (kN)	ψ (°)	d_r (μm)
1	12.740	9.820	131.7	14.77
1,3	12.943	10.272	137.6	16.70
1,3,5	13.010	10.285	137.0	16.60
1,3,5,7	13.032	10.287	136.8	16.57
1-13	13.031	10.287	136.8	16.57
1-29	13.031	10.287	136.8	16.57

Table 7.2 Inclusion of rotor current sheet harmonics

When stator current sheet harmonics are included, each tooth force has a different 100Hz fundamental. Thus Table 7.3, which gives the results for rotor fundamental and various stator current sheet harmonics, includes both the average and the range. The vibration results do not have any real meaning beyond their being 'equivalent' vibrations for a particular pair of tooth force components. It can be seen that the average equivalent core-back vibration is increased by less than 1% over the inclusion of stator

current sheet harmonics up to the 29th. The greatest effect of the stator harmonics is on the distribution of stress around the stator bore, mainfesting itself in a wider range of tooth force fundamentals on different teeth within a phase band. The same pattern is repeated in each phase band of eight teeth.

Stator Harms	F_r (kN) Ave	Rnge	F_θ (kN) Ave	Rnge	ψ (°) Ave	Rnge	d_r (μm) Ave	Rnge
1	12.74	0.00	9.82	0.00	131.7	0.0	14.77	0.00
1,5	12.76	1.76	9.83	1.28	131.7	4.4	14.77	0.94
1,5,7	12.76	1.29	9.83	1.74	131.8	6.8	14.79	2.52
1-13	12.78	4.04	9.88	2.47	131.7	16.1	14.85	4.27
1-29	12.79	4.07	9.76	2.65	131.7	19.6	14.87	4.82

Table 7.3 Inclusion of stator current sheet harmonics

The final investigation, in which harmonics of both current sheets were considered, showed both effects at work together: an increase in vibration amplitude due to the lower rotor harmonics coupled with an increase in range due to stator higher harmonics. The average equivalent core-back vibration level resulting from incorporation of harmonics up to the 29th in both current sheets was 16.67μm, with a range of 4.59μm.

It was suggested at the start of Section 7.2 that the effect of local variations in stress at the stator bore due to chording and phase-banding would be smoothed out by the bulk of the core, giving a uniform vibration level at the core back. In a current sheet model, chording and phase-banding are represented within the higher harmonics of the stator current sheet. To test this assertion, an analysis

was run on ANSYS in which tooth forces were applied which corresponded to the full load case with both sets of current sheet harmonics up to the 29th.

Output was obtained at core back points opposite each slot bottom, and translated into radial displacement amplitude and phase by essentially the same auxiliary program as that described in Section 7.2, where it was used to obtain the result for 4-point tangential fixing of the 350MW core. The maximum core-back vibration amplitude obtained was 16.646μm; the minimum 16.413μm. The difference between the two is just 1.4% of the mean. Vibration phase results are calculated from the magnitudes and phases of radial and circumferential tooth forces on a particular tooth, so are dependent mainly on the position of that tooth. Thus for the purposes of comparison, the differences between phase angles of successive teeth are taken. In a fundamental only case all these differences are 15%, because a slot pitch spans 7.5° and the force is a double-frequency one. In the case investigated here they range from 14.721° to 15.269°, that is, they vary by just over half a degree. From these results it can be concluded that although variations in stator bore force due to chording and phase banding (higher stator current sheet harmonics) are not so completely smoothed out by the bulk of the stator iron that the variations in core-back vibration are lower than the accuracy of the data, their effect is small compared to that of the support structure.

A similar set of tests were performed on the 350MW machine. The vibration results only are given in Table 7.4. Values obtained using stator current sheet harmonics are average values. It can be seen from these results that the only significant higher rotor harmonic is the 3rd, which reduces the calculated vibration level by 5%. Once again, the overall effect of the stator current sheet harmonics is small. However, a more important point is the fact that

addition of the rotor 3rd harmonic term produces a reduction in vibration level over that obtained using fundamentals only. In the case of the West Burton machine, an increase was produced. This raises the possibility that low rotor current sheet harmonics may influence not only the level of double-frequency vibration, but also the trend, and that the nature of their influence may be machine-dependent.

Orders of harmonics	Stator 1 with rotor harmonics	Rotor 1 with stator harmonics
1	5.61	5.61
1-3	5.34	n/a
1-5	5.34	5.61
1-7	5.34	5.63
1-13	5.34	5.65
1-29	5.34	5.65

Table 7.4 Core-back vibration levels calculated for 350MW generator using various current sheet harmonics (all results in μm peak)

Harmonics	West Burton	350MW generator
Fundamentals only	21.97	8.87
With rotor 3,5	20.60	9.32

Table 7.5 Vibration results (in μm peak) on open circuit for the two machines

To investigate this possibility further, analyses were performed for both machines on open circuit. The results are given in Table 7.5. It can be seen that the effect of the higher harmonics is to produce a decrease in vibration for West Burton and an increase for the 350MW machine, the reverse of the situation on full rated load. Thus one might expect the slope of the decrease in vibration between open circuit and full rated load to be steepened in the case of the 350MW machine but made gentler in the case of the West Burton machine.

The origin of this difference in behaviour becomes evident upon examination of the expression for the magnitudes of the higher harmonics of the rotor current sheet, $\hat{K}_{Rm}$.

$$\hat{K}_{Rm} = \frac{2n_t I_R}{m\pi\tau_R R_R} (-1)^{\frac{1}{2}(m-1)} \sin m\tau_R \frac{\sin \frac{1}{2}Q_R m\Delta_R}{\sin \frac{1}{2}m\Delta_R} \qquad (3.19)$$

The factors within this expression which affect the sign of $\hat{K}_{Rm}$ are the three sine terms and the power of minus one. The power of minus one becomes -1 for m=3,7,11 etc and +1 for m=5,9,13 etc. The angles τ_R (half slot opening) and Δ_R (slot pitch) are small, so the sines of $m\tau_R$ and $\frac{1}{2}m\Delta_R$ will be positive until m becomes quite large. The final sine factor has as its argument the much larger angle $\frac{1}{2}Q_R m\Delta_R$, where Q_R is the number of slots per pole. Its sine becomes negative at quite low values of m, the exact value dependent on Q_R and Δ_R. If this angle is less than 180° for m=3, the term is positive so $\hat{K}_{R3}$ is negative. Conversely, if it is greater than 180°, $\hat{K}_{R3}$ is positive.

Both rotors have 32 slots, so that Q_R=16. The West Burton rotor is slotted on a pitch of 52 and the 350MW rotor on a pitch of 45; thus Δ_R is $2\pi/52$ and $2\pi/45$ respectively. Hence the angle $3Q_R\Delta_R/2$ is 166° for West Burton so that its sine is positive making $\hat{K}_{R3}$ negative, and 192° for the 350MW machine so that its sine is negative making $\hat{K}_{R3}$ positive.

For both rotors $\hat{K}_{R5}$ is negative. It is interesting to note that the proximity of $5Q_R\Delta_R/2$ to 270° leads to a relatively high amplitude of the fifth harmonic in the West Burton rotor. The effect of this can be gauged by comparing the relevant entries in Tables 7.2 and 7.4.

It is also evident from the Tables that the relationship between the sign of $\hat{K}_{R3}$ and the effect of this harmonic on the vibration level is not a simple one. Indeed, this is to be expected as vibration results from the combination of radial and circumferential forces which are phase displaced in space and time. From Table 7.2 it can be seen that the negative third harmonic of rotor current results in an increase in vibration for West Burton, whilst further addition of the also negative fifth harmonic reduces the vibration. The positive third harmonic of rotor current in the 350MW machine results in a decrease in core-back vibration.

A further point to emerge from this analysis is that it is possible to suppress any harmonic of the rotor current entirely by slotting on a pitch of mQ_R. In such a case, the product $Q_R\Delta_R$, an angle indicating the extent of the slotted portion of the rotor surface, is equal to $2\pi/m$. For instance, the winding must cover two-thirds of the rotor surface and the pole faces one third, for complete suppression of the third harmonic. Furthermore, the results presented above have shown that where the pole faces cover less than one third of the surface there is a decrease in vibration level with increased MW. Conversely, an increase is shown where the pole faces cover more than one third of the surface.

To investigate the quality of the improvement obtained in the model by inclusion of 3rd and 5th rotor current sheet harmonics, the simulation of the 350MW generator test results described in Section 7.4.5 was repeated. The

results are shown in Figures 7.13 and 7.14.

Comparison of the three sets of amplitude results (Figures 7.1 and 7.2 test; Figures 7.14 and 7.12 model with and without harmonics) shows an obvious improvement resulting from the inclusion of rotor current sheet harmonics. The 0MVAR curve now shows a downward trend in vibration with increased MW. Furthermore, it has the distinctive shallow s-bend shape of the test curves, although the proportional reduction in vibration over the range is not as great as in the tests. Although the actual vibration levels are slightly reduced, the 355MW curve is of a similar gradient to that for the fundamental only case, which, as was noted in Section 7.4.5, is slightly steeper than that of the measurements. But the overall reduction between open circuit and full rated load (a combination of the changes embodied in both curves) is 42%, the same as the average decrease shown from the measurements. This is therefore a most encouraging result.

Figure 7.13 shows the phase results. The 0MVAR curve shows little perceptible change due to the inclusion of harmonics. The 355MW curve, however, is noticeably steeper in gradient, which is a change in the right direction.

It can now be concluded that the automated multi-region model with the 3rd and 5th rotor current sheet harmonics provides a reasonable working model of the vibration behaviour of the stator core of a large turbogenerator on load. Inclusion of higher stator current sheet harmonics is not necessary, as their effect is small. This is fortunate as it enables the core-back vibration level to be predicted from a calculation relating to one tooth only.

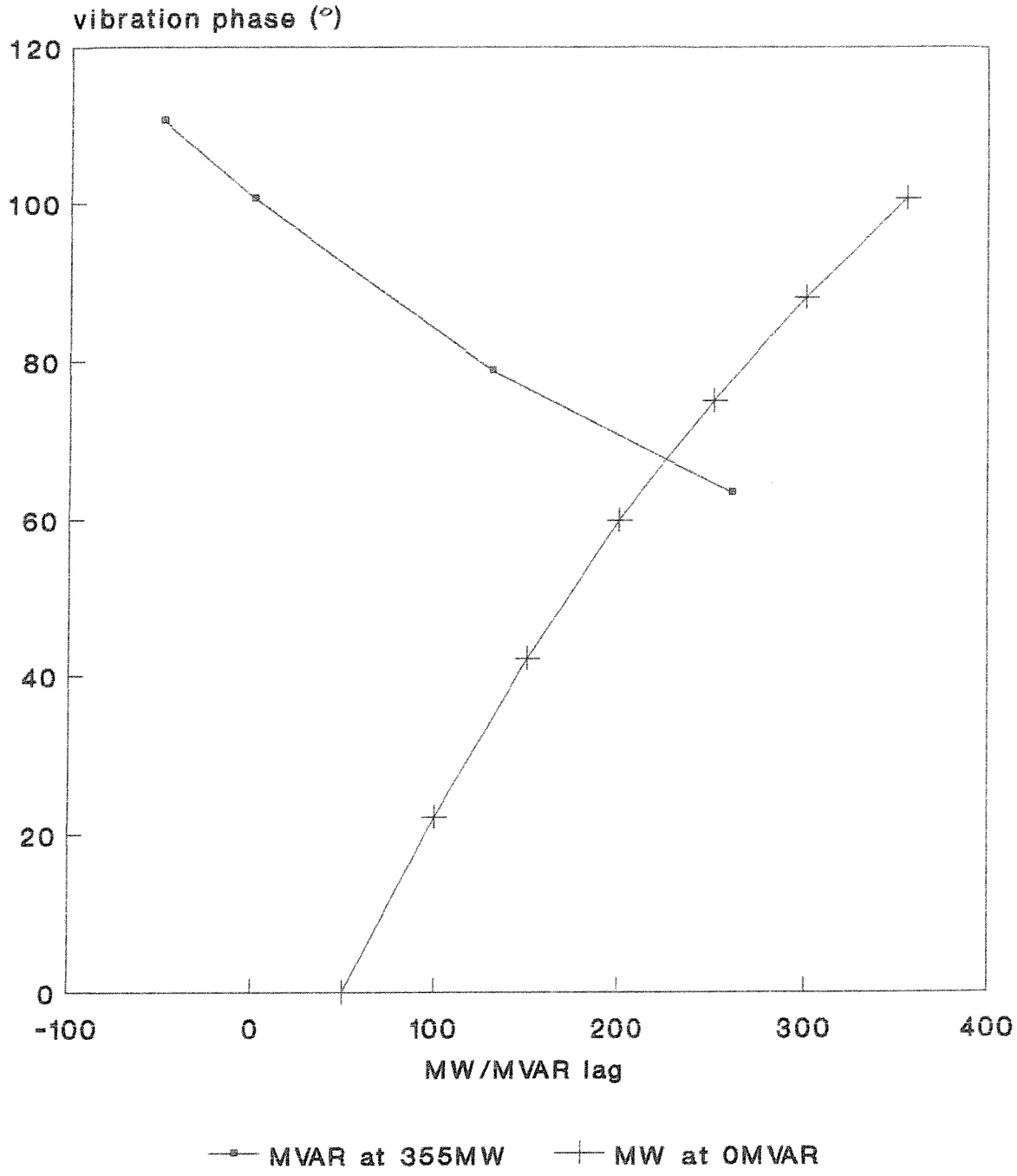

Figure 7.13 GEC 350MW generator - vibration phase at points corresponding to the measurements predicted by the model incorporating 3rd and 5th harmonics of rotor m.m.f.

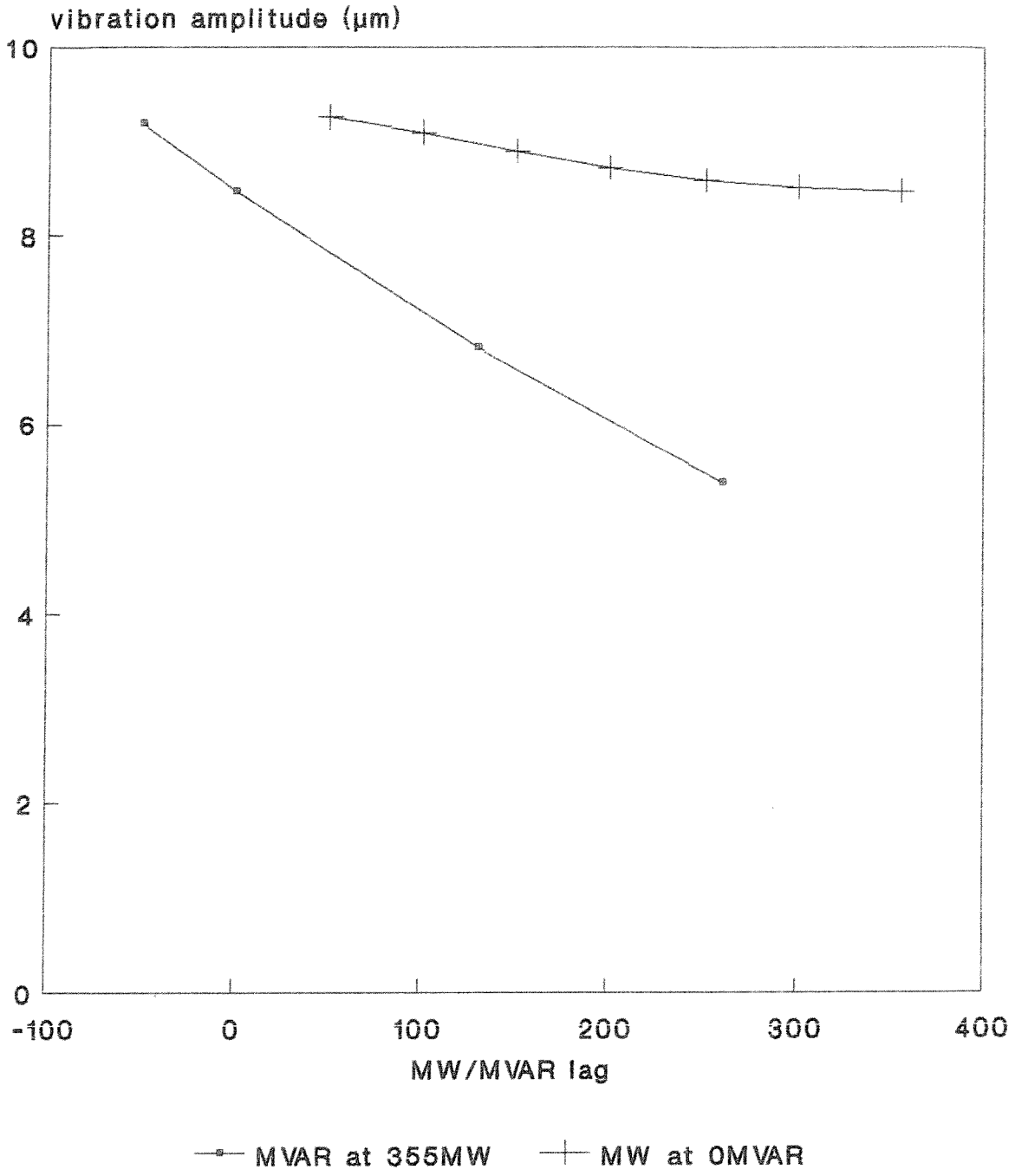

Figure 7.14 GEC 350MW generator - vibration phase at points corresponding to the measurements predicted by the model incorporating 3rd and 5th harmonics of rotor m.m.f.

7.6 Comprehensive Analyses for the Three Machines

Considerable confidence had been gained in the latest version of the model from the results of Section 7.5 in which a set of test measurements on the 350MW generator were simulated. The next stage was to use the model to obtain vibration results for a wide and systematic range of load conditions on all three machines investigated in this work. Figures 7.15 to 7.26 show these results. For each machine, load conditions were investigated at MW levels corresponding to zero, one quarter, half, three quarters and full rated load. For each MW load, values of MVAR, both lagging and leading, corresponding numerically to some of the MW values were used. For example, for one of the 500MW machines load points were selected at 0MW, 125MW, 250MW, 375MW and 500MW, paired with 250MVAR lead, 125MVAR lead, 0MVAR, 125MVAR lag, 250MVAR lag, 375MVAR lag and 500MVAR lag; a total of 35 conditions in all. The variations of vibration amplitude with MVAR at various MW are given in Figures 7.15, 7.19 and 7.23; the variations with MW at various MVAR in Figures 7.16, 7.20 and 7.24. The corresponding variations in vibration phase are shown in the other Figures in the set.

All machines show a marked decrease in vibration amplitude from high leading to high lagging MVAR at given MW. Only the 350MW machine shows a decrease in vibration amplitude with MW for given MVAR. Both the 500MW generators show an increase. This increase is considerably greater for West Burton, with a rotor slotted on a pitch 8% higher than $3Q_R$, than for Ferrybridge, which is slotted on a pitch 2% higher than $3Q_R$. The increase in vibration with MW becomes greater the higher the lagging MVAR involved.

The vibration phase results in all cases show clearly that a straight-line relationship does not generally apply. Given just the test results available, one might be tempted to draw the best straight line through the points, and

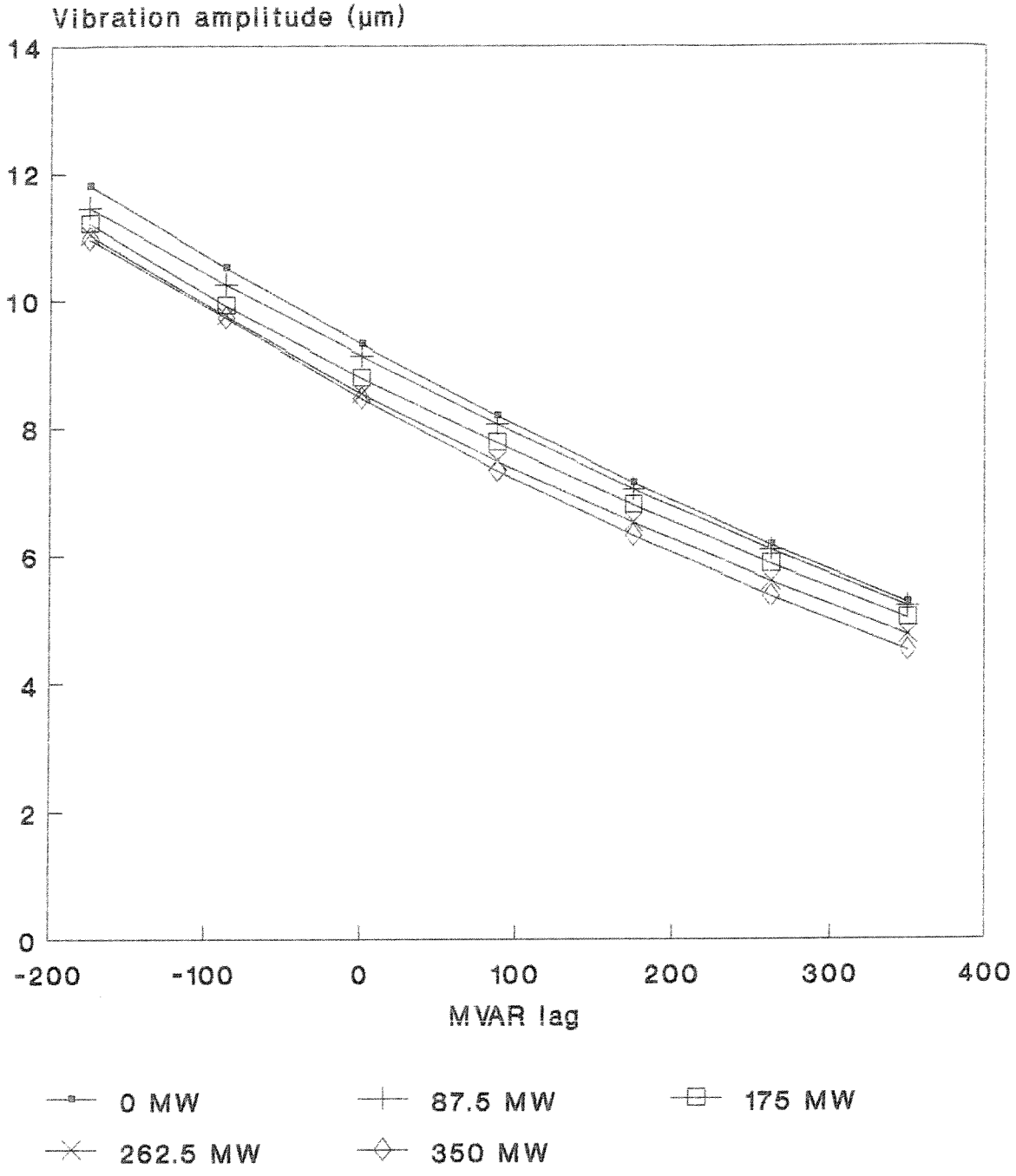

Figure 7.15 GEC 350MW generator - predicted vibration amplitude variation with MVAR at various MW

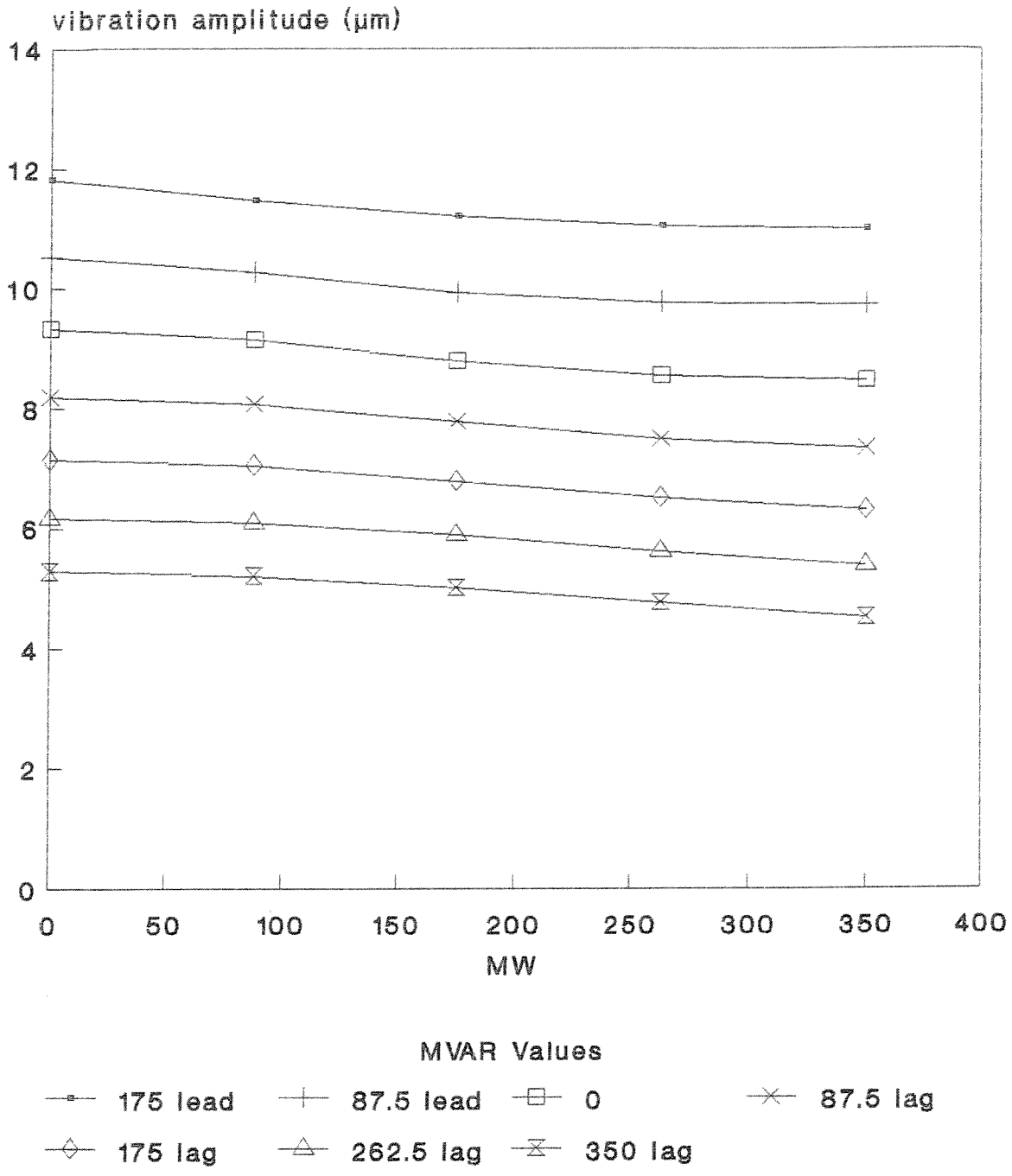

Figure 7.16 GEC 350MW generator - predicted vibration amplitude variation with MW at various MVAR

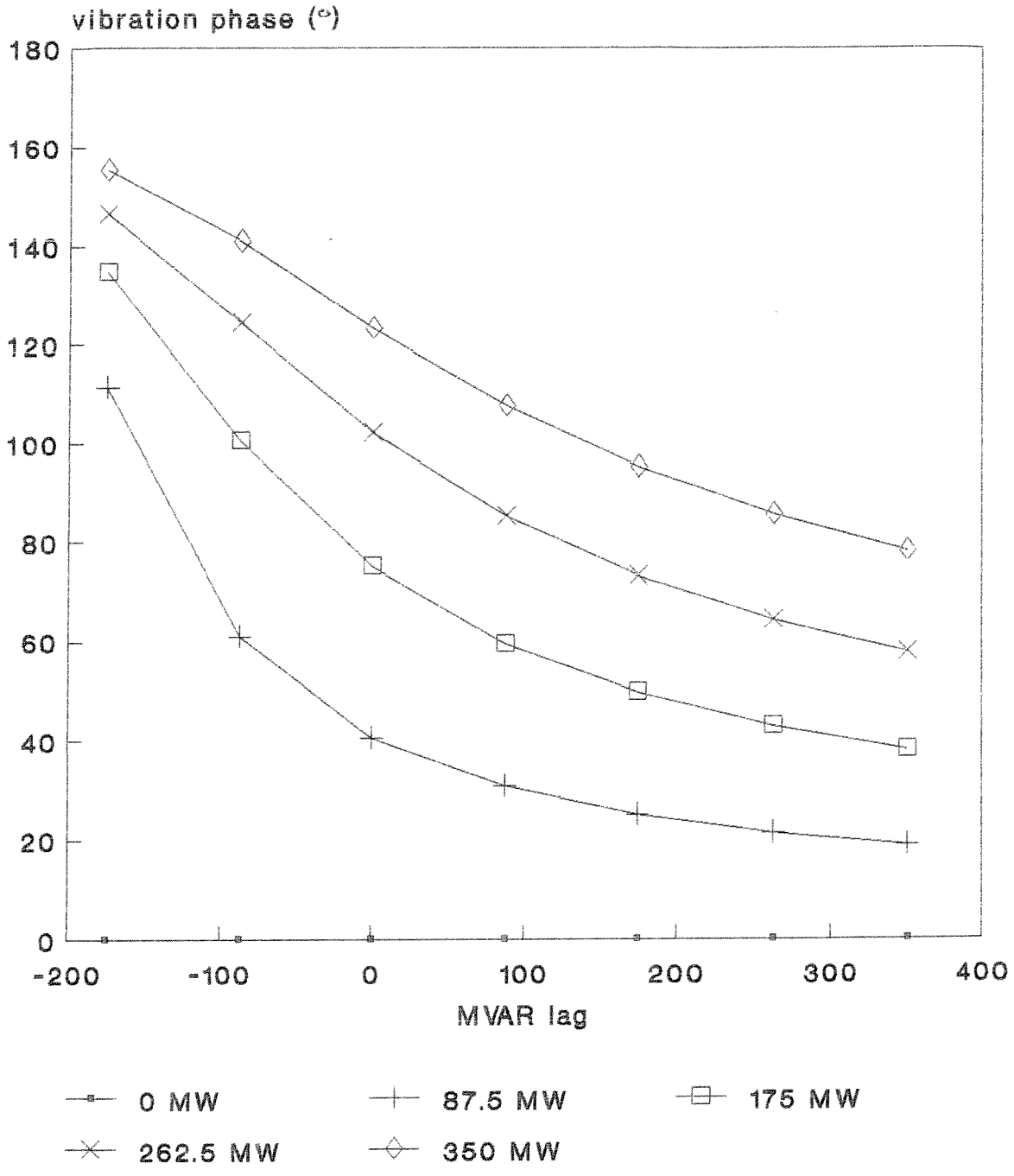

Figure 7.17 GEC 350MW generator - predicted vibration phase variation with MVAR at various MW

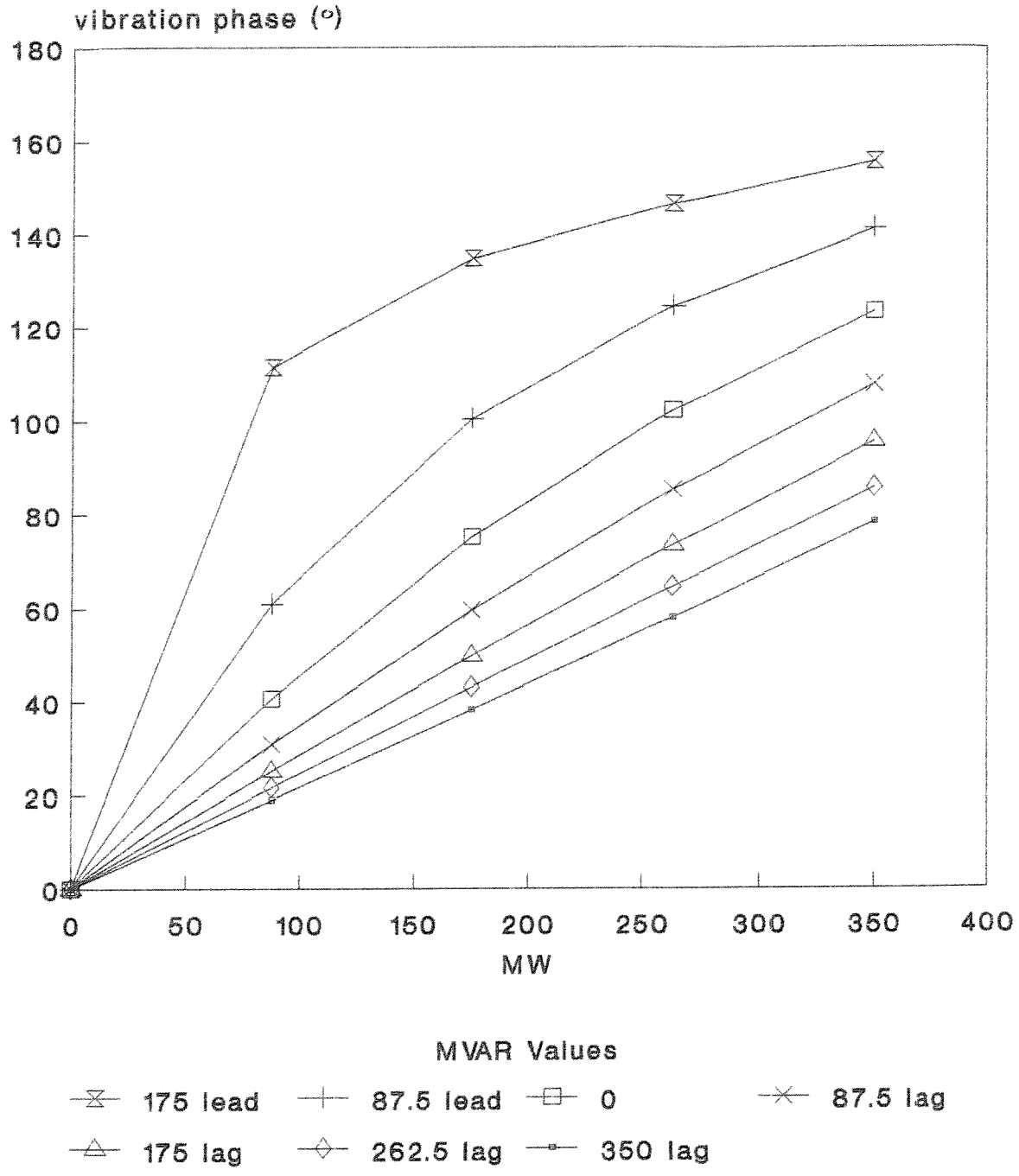

Figure 7.18 GEC 350MW generator - predicted vibration phase variation with MW at various MVAR

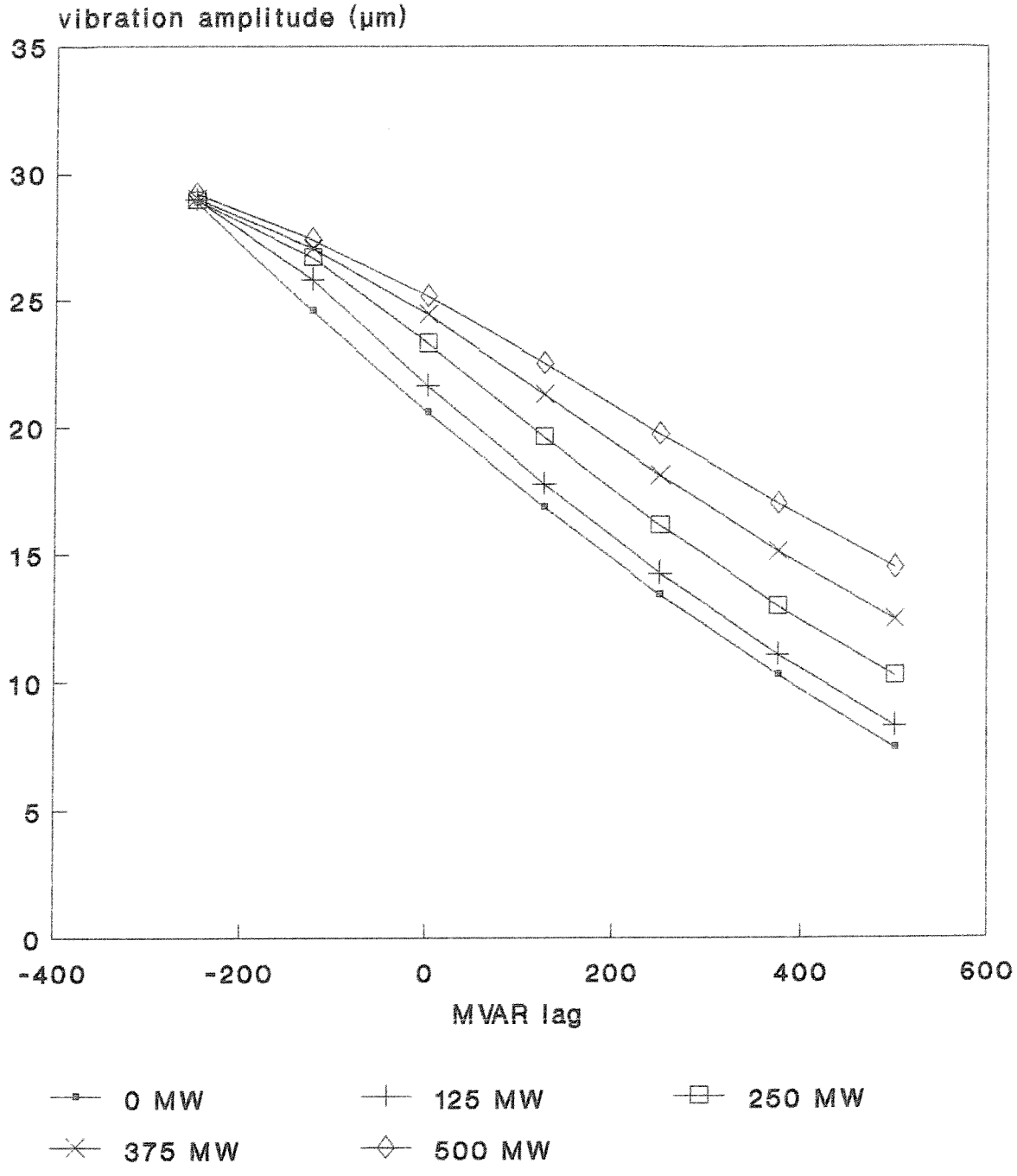

Figure 7.19 West Burton generator - predicted vibration amplitude variation with MVAR at various MW

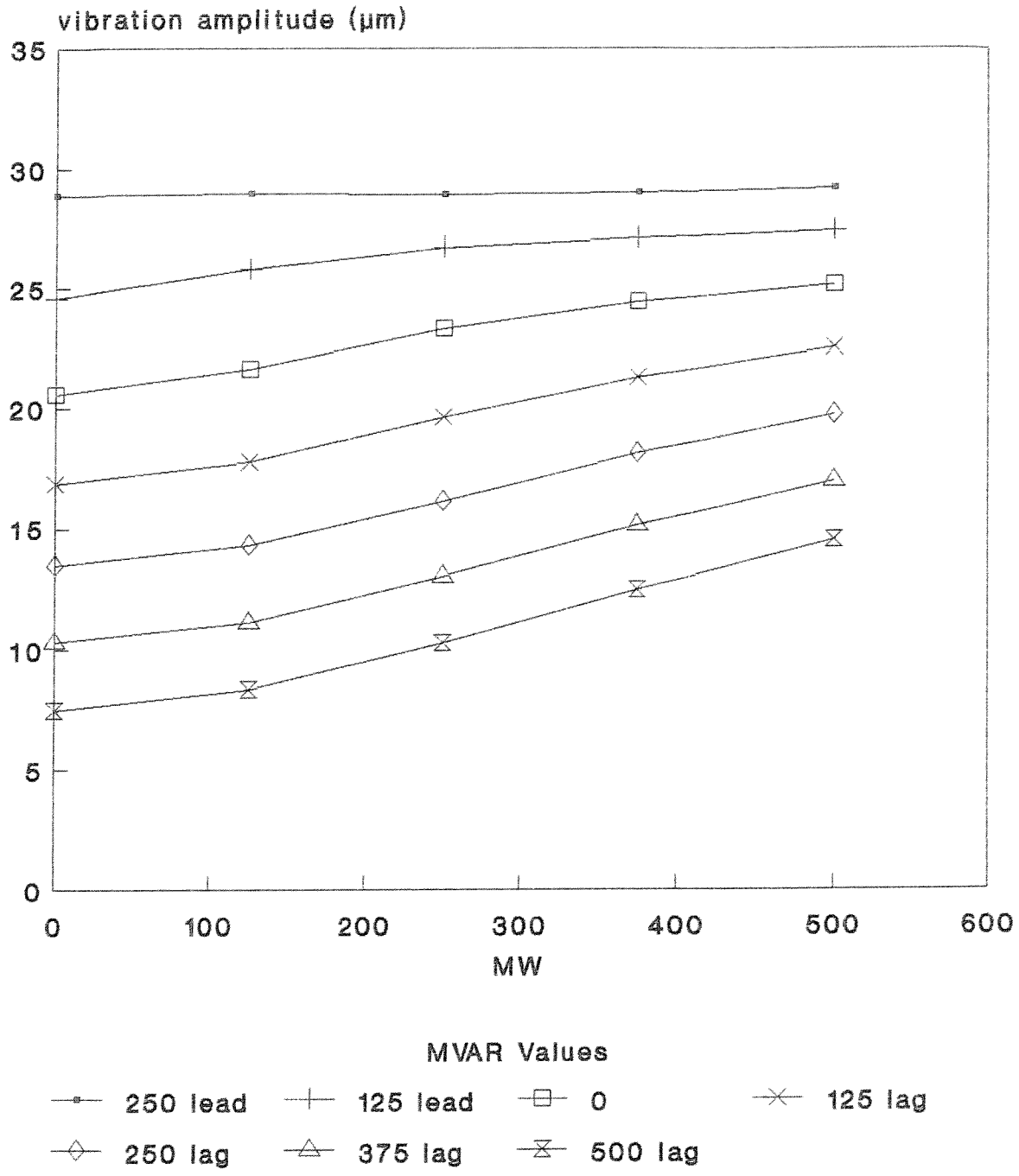

Figure 7.20 West Burton generator - predicted vibration amplitude variation with MW at various MVAR

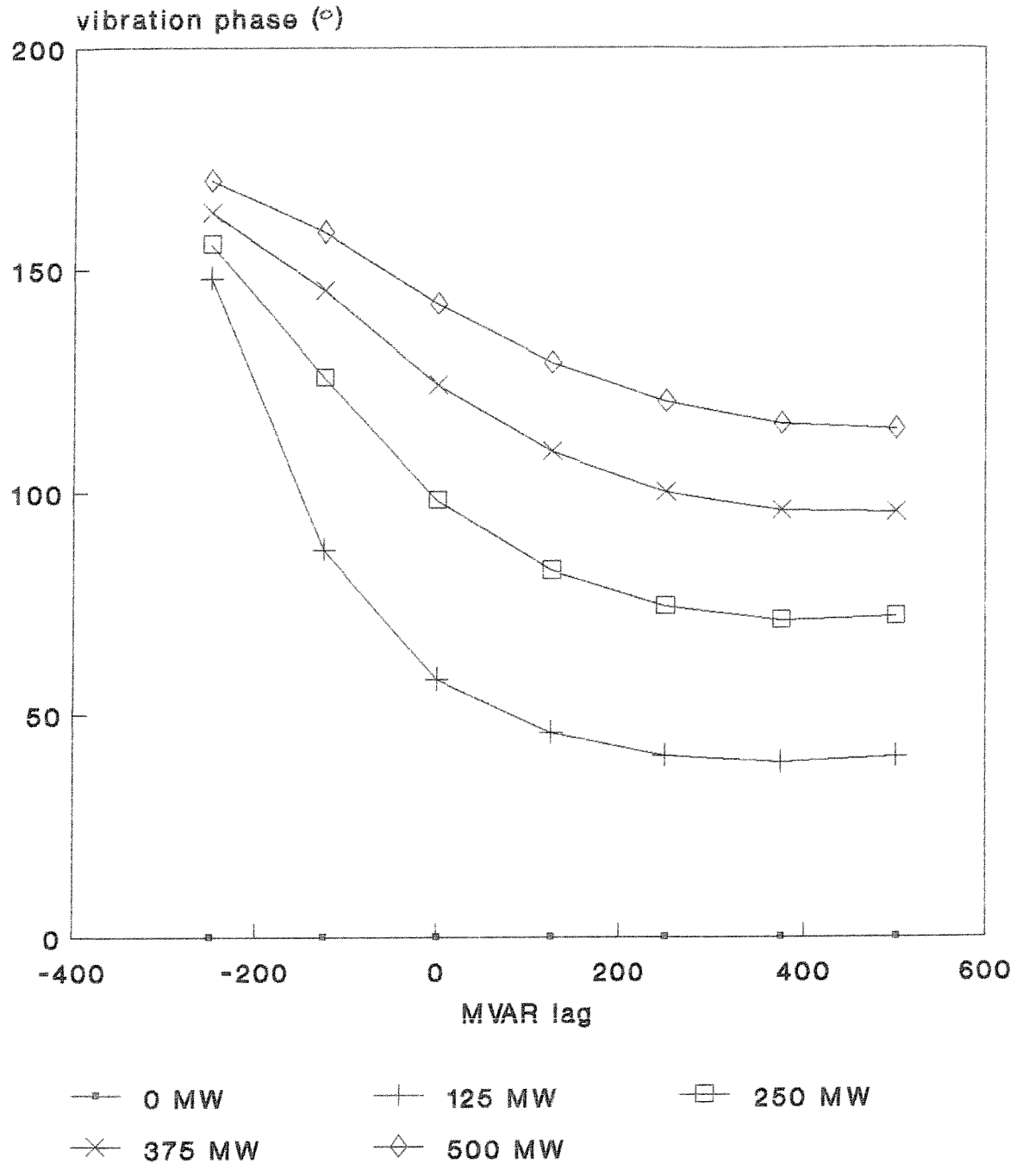

Figure 7.21 West Burton generator - predicted vibration phase variation with MVAR at various MW

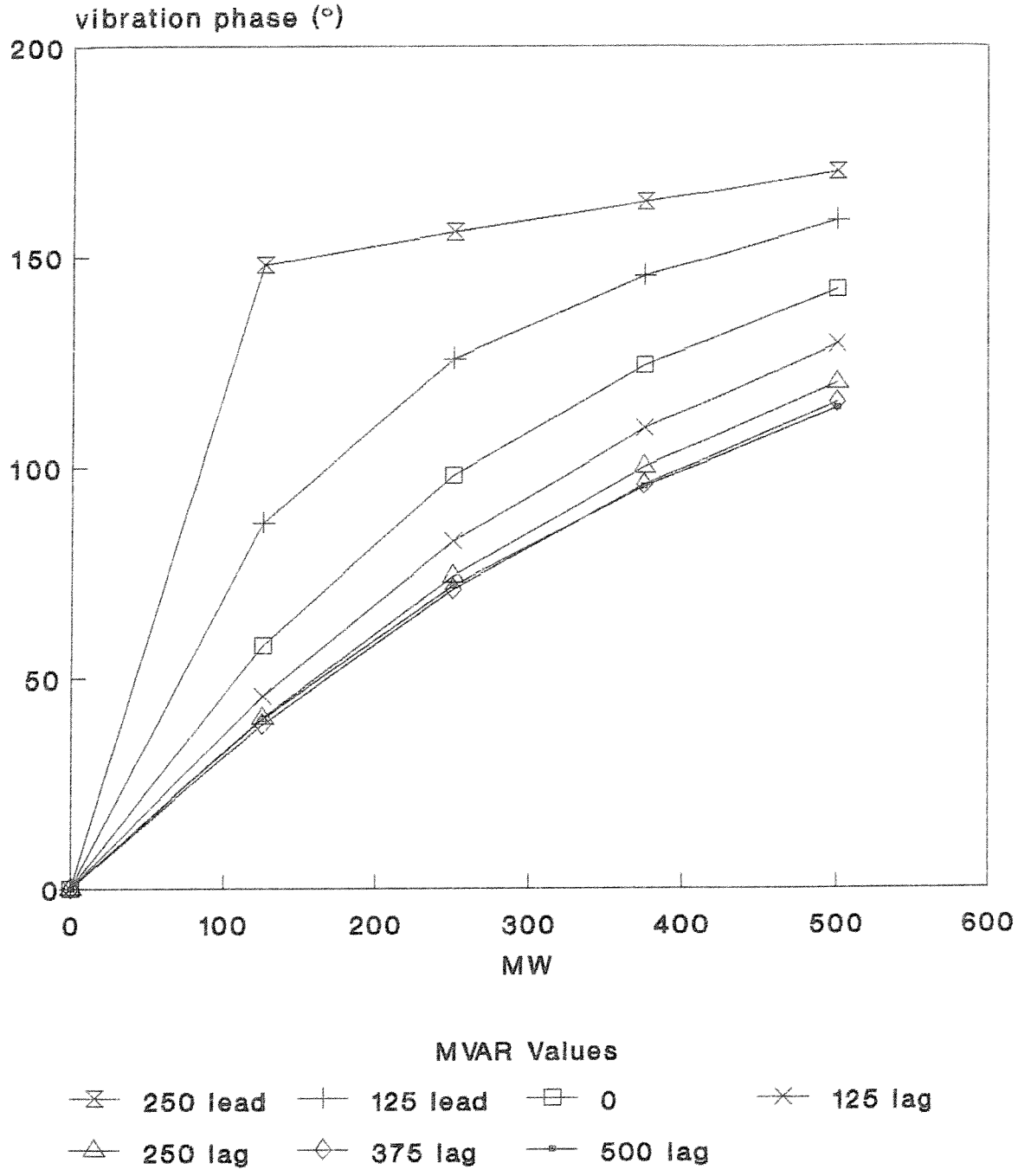

Figure 7.22 West Burton generator - predicted vibration phase variation with MW at various MVAR

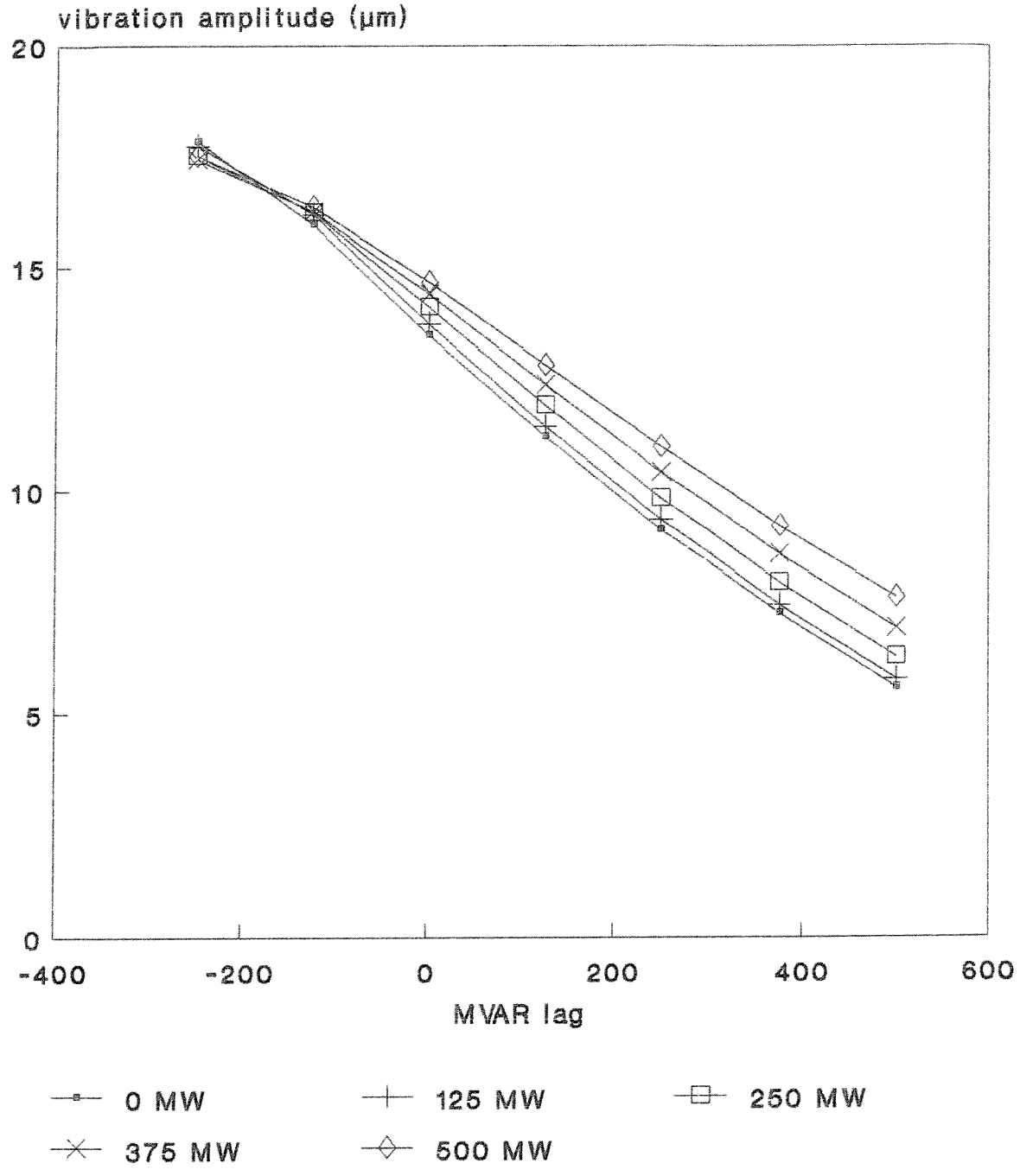

Figure 7.23 Ferrybridge generator - predicted vibration amplitude variation with MVAR at various MW

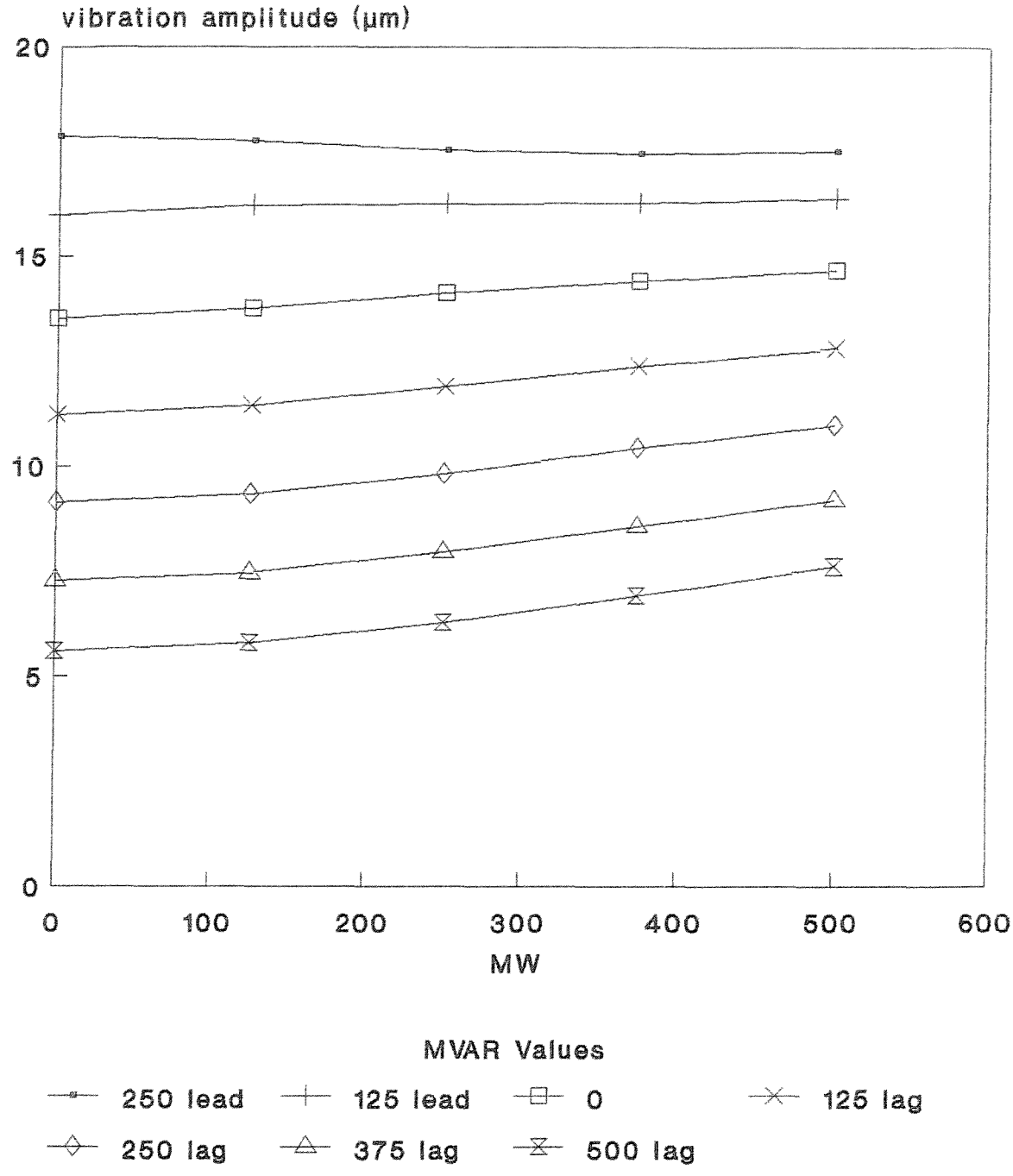

Figure 7.24 Ferrybridge generator - predicted vibration amplitude variation with MW at various MVAR

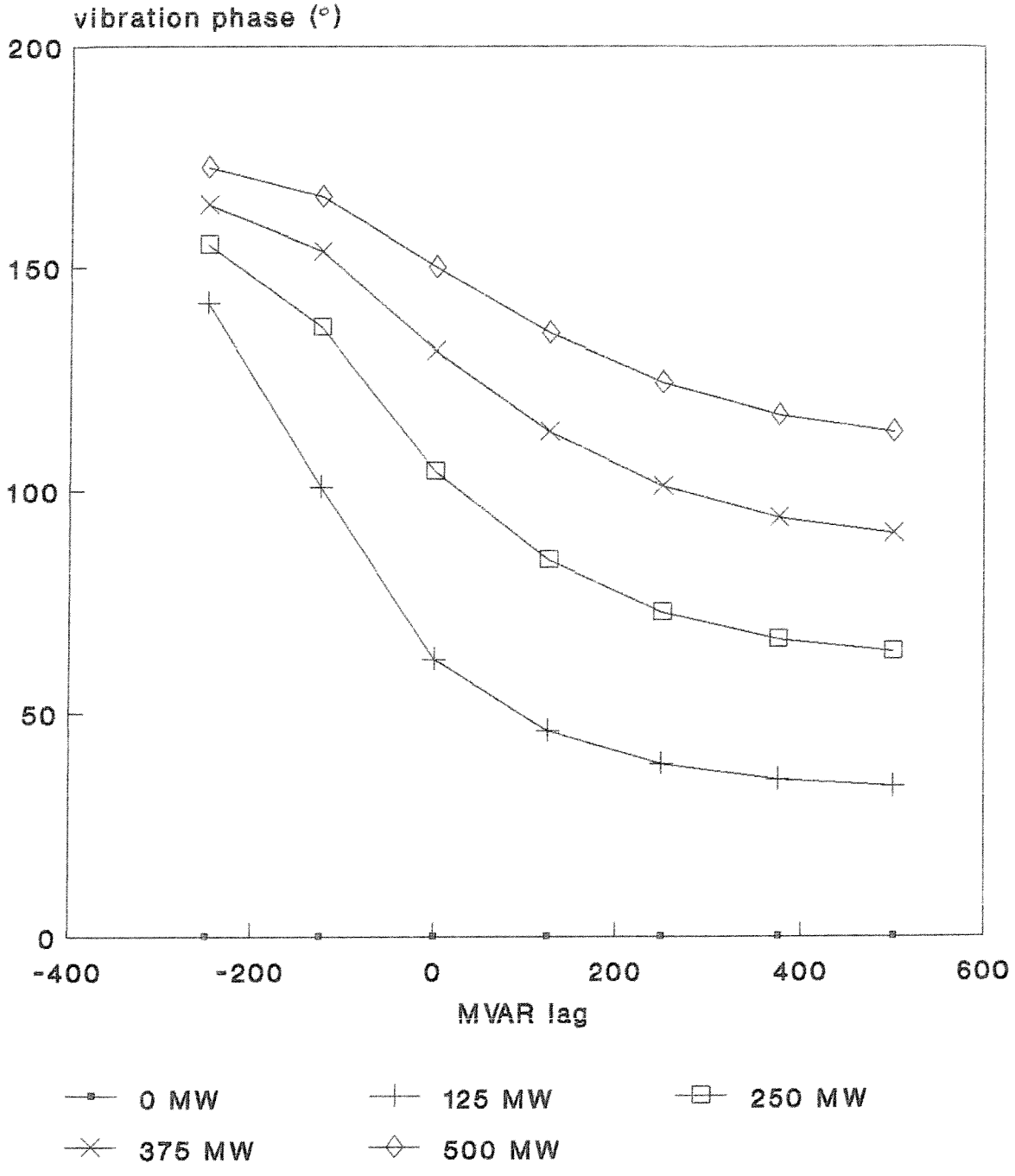

Figure 7.25 Ferrybridge generator - predicted vibration phase variation with MVAR at various MW

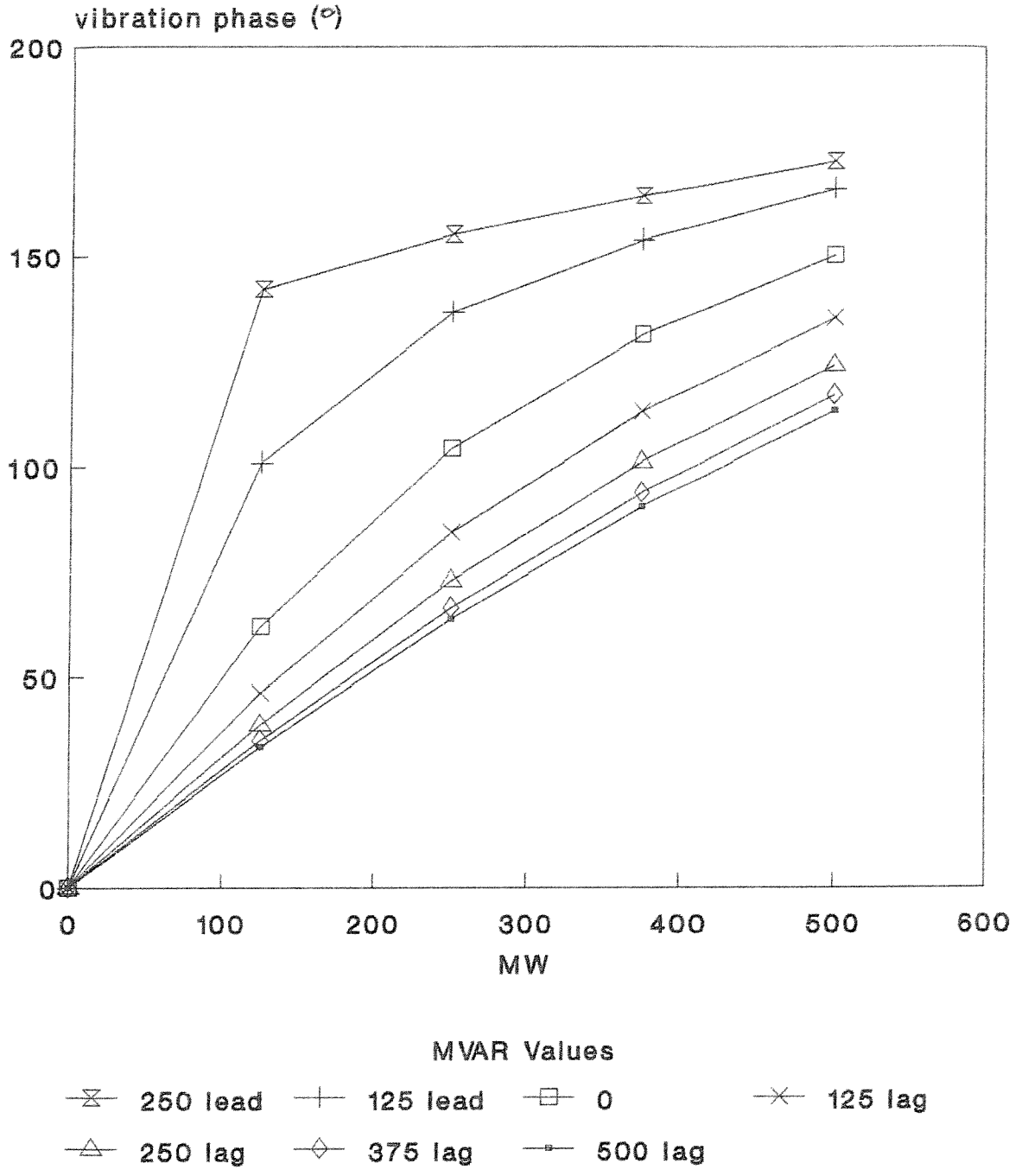

Figure 7.26 Ferrybridge generator - predicted vibration phase variation with MW at various MVAR

thereby fail to appreciate that they belong to an elegant family of curves. Sight must not be lost, however, of how small a proportion of this predicted vibration data is actually substantiated by test. It is therefore important to append a qualitative assessment of the origins and effects of possible errors in the calculations.

In Section 6.5.3 the automated multi-region model was used to predict load angle as a general test of its validity. For low loads, and for high loads with lagging power factors, the agreement between measured and calculated load angle was good, within a few degrees. However, where high leading MVAR loads were involved, some very poor agreements were noted, discrepancies of 10° or more in a few cases. The overall error on leading power factor loads was greater for higher active power loads, as can be seen from Tables 6.11 to 6.15. Thus the confidence which may be placed on the vibration predictions of the model are limited for such loads. It is possible, for instance, that the curves in Figure 7.23 (Ferrybridge, vibration amplitude with MVAR for constant MW) do not in fact cross over in real life.

The Fawley load angle predictions were made using measured excitation current as input. The model as developed does not take for granted that this value is available, and would generally produce an estimate from a Frohlich curve and a Potier calculation. To assess the nature of the errors induced by this calculation, a selection of the Fawley tests were programmed without the measured rotor currents. For each of the nominal loads three cases were chosen: one with high leading MVAR, one with high lagging MVAR and the third with a power factor close to unity. Table 7.6 shows the measured and estimated values of rotor current, with the error in the calculation; also the vibration amplitudes obtained from these respective values, and their discrepancy.

MW	MVAR (lag)	I_R (A) Test	Calc	Error (%)	d_r (μm) Test	Calc	Error (%)
44.8	-230	260	236	-9.2	18.66	18.33	0.9
37.3	-34.6	1110	1117	+0.6	14.98	14.76	-1.5
42.0	54.8	1610	1613	+0.2	13.50	13.19	-2.3
111	-100	1020	989	-3.0	16.81	16.93	+0.7
96	38.8	1590	1566	-1.5	13.38	13.25	-1.0
98.6	257	2840	2735	-3.7	9.40	9.16	-2.6
258	-265	1325	1330	+0.4	18.42	18.52	+0.5
252	-4.4	1880	1816	-3.4	14.20	14.65	+3.2
253	335	3640	3408	-6.4	8.56	8.85	+3.4
358	-263	1860	1859	-0.1	17.95	18.12	+0.9
394	50	2680	2583	-3.6	13.02	13.76	+5.7
386	300	3770	3578	-5.1	9.21	9.91	+7.6
508	-245	2660	2654	-0.2	17.56	17.77	+1.2
505	3	3050	2952	-3.2	13.93	14.75	+5.9
507	293	4150	3957	-4.7	9.49	10.48	+10.4

Table 7.6 Errors in estimated rotor current and discrepancies in vibration results produced

From Table 7.6 it is apparent that the highest discrepancies in vibration produced by errors in estimated rotor current occur at high loads on lagging power factor. These vibration discrepancies are all positive, and of the order of 5-10%. At lower loads and leading power factors agreement is excellent.

The consequence of these errors can best be appreciated with reference to Figures 7.16, 7.20 and 7.24 (vibration amplitude with MW for constant MVAR). The lowest of the curves (high MVAR lag) would be pulled down preferentially at the right hand side (i.e. at high MW). In the most extreme case the near doubling of vibration between 0MW and 500MW for West Burton on 500MVAR lag (Figure 7.20) is probably a considerable exaggeration, and, whilst an increase will be shown, it will not be of quite this order. Also, it is likely that the slope of the 0MVAR curve for the 350MW machine will be steepened a little, bringing the result closer to that of the measurements.

To provide a guide to the likely nature of adjustments necessary to take account of these errors, the analyses for the Ferrybridge machine were rerun, using rotor currents interpolated from those of the Fawley measurements. Several of the points had to be left out as the available data was inadequate for the purposes of interpolation. The result can be seen in Figure 7.27. It is notable that the 0MVAR curve has been almost flattened off, whilst the slopes of the higher lagging MVAR curves have been reduced significantly.

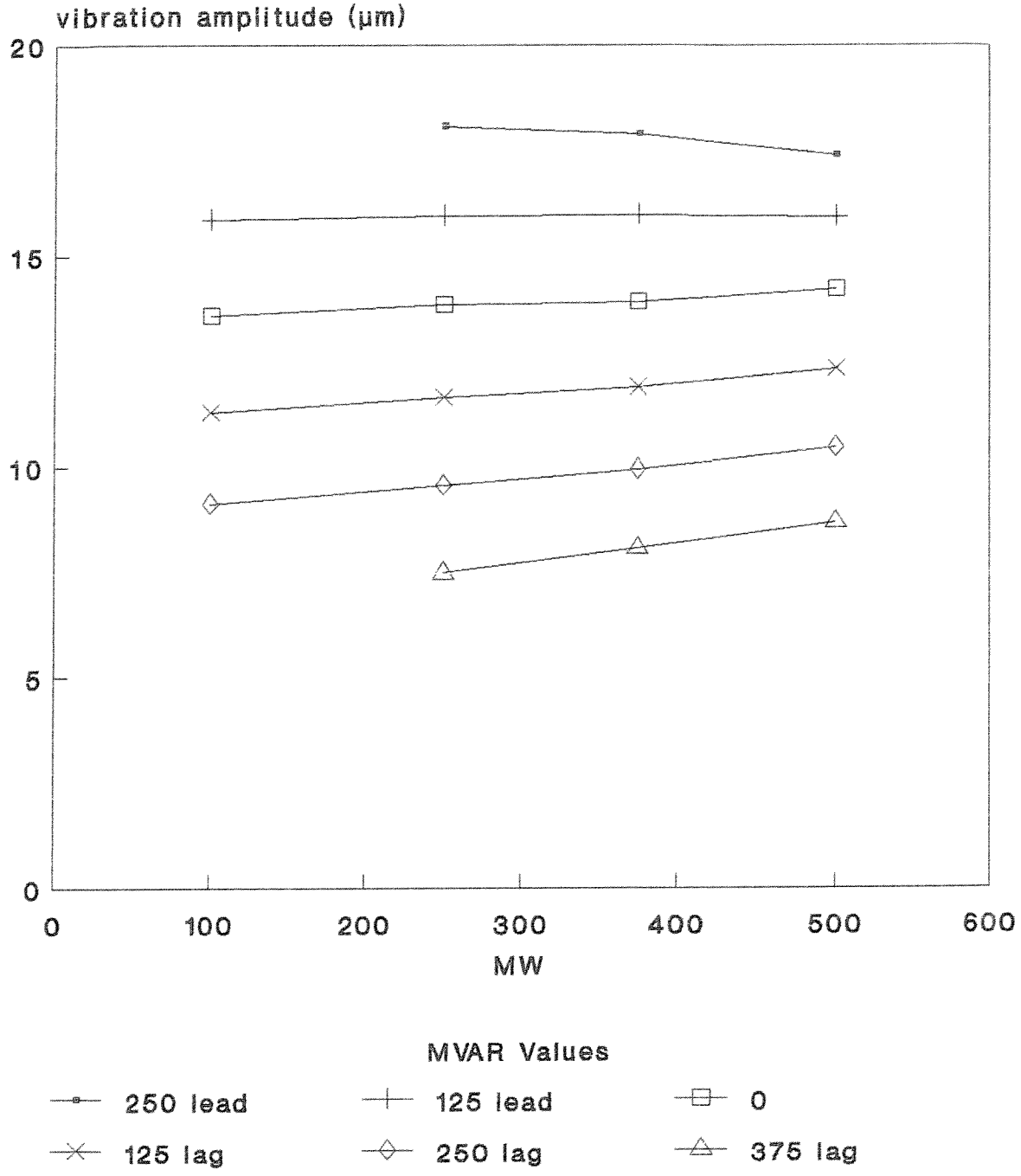

Figure 7.27 Ferrybridge generator - predicted vibration amplitude variation with MW at various MVAR using rotor currents interpolated from Fawley measurements

CHAPTER EIGHT
CONCLUSIONS

8.1 Mechanisms of Stator Core Vibration

The principal mechanism behind the observed variation in double-frequency stator core vibration with load has been identified. This vibration originates not only from double-frequency radial forces at the stator bore, but from circumferential forces also. These circumferential forces are mainly proportional to stator current, and, at rated load, are of comparable magnitude to the radial forces. They too cause core ovalising which results in double-frequency core-back vibration.

The total vibration level, therefore, depends on the combined action of the radial and circumferential forces. They are phase displaced from one another in space and time. In an idealised case of infinitely permeable iron the phase angle is directly related to power factor angle. The displacements caused by the separate force systems are in opposition when the machine is overexcited; and reinforce one another when it is underexcited. Thus vibration is higher for a generator operating on leading power factor than for one on lagging power factor at the same active load.

Whilst the circumferential forces and their phase relationship to the radial forces provide the principal mechanism, a model based purely on this effect is insufficient to represent the vibration variations for any particular machine. It is necessary also to take secondary effects into account: in particular magnetic saturation and higher m.m.f. harmonics.

Saturation is important because of its effect on internal machine angles: a saturated machine will operate

with a lower load angle than an unsaturated one on equivalent load. The angle between the radial and circumferential forces is critical in determining the vibration level, and this is in turn dependent on load angle.

Higher harmonics of m.m.f., hence of flux density, exist in the air gap due to the fact that both rotor and stator windings are made up of discrete conductors connected to create poles and phases. Certain of these higher harmonics combine to set up double-frequency (four-pole) force distributions. In particular, the rotor 3rd combines with the stator fundamental to provide a significant contribution to the total ovalising force. In some machines the rotor 5th, which combines with the rotor 3rd and 7th and the stator 7th, is also significant. Higher harmonics originating from the stator winding affect the actual tooth-to-tooth force distribution around the stator bore but have very little effect on the mean levels.

The trend in vibration with MW for constant MVAR was shown in Section 7.5 to be dependent on the slotting of the rotor, by way of the effect that this has on the 3rd harmonic of rotor m.m.f. If the rotor pole faces cover less than one third of the rotor surface, there is a decrease in vibration with increased MW. If they cover more than one third of the surface, there is an increase.

As demonstrated in Section 7.1, vibration measurements on operational turbogenerators show that the actual level of vibration at the core-back varies according to transducer position, and also changes over time. The observed overall reduction in vibration with time, most noticeable in the months following installation or overhaul, is generally accepted to be due to the machine bedding down gradually onto its supports. The variation with transducer position is due to mechanical coupling with the support structure.

Such variations are perforce dependent on the design of the support structure, which is different in machines from different manufacturers. The two machines most studied in this work were made by GEC Alsthom Turbine Generators, in which the inner and outer frames are joined by tangential spring plates. Core-back vibration levels on these machines were related, in Section 7.2, to the proximity of the transducer to the spring plates, and the level of compression in the plate to which it is closest.

It follows that it is not possible to predict absolute levels of core-back vibration unless an extremely sophisticated model taking into account all mechanical influences is employed. Such a model is beyond the scope of this work, which has therefore concentrated on representing the trend in vibration amplitude and phase with machine load.

8.2 Modelling Stator Core Vibration

An analytical approach was taken in this work for the purposes of representing fields and forces inside a machine. The main reason for this was to facilitate physical understanding of the effects involved. Such a model would also be more readily adaptable into part of a vibration monitoring scheme, for which finite-element analyses would require too much computing time.

The magnetic stress on the stator bore was represented by a series of point forces acting at the centres of the tooth tips on a cross-section of the stator. The two components of tooth force, radial and circumferential, were obtained by integrating the corresponding Maxwell stresses over a slot pitch. This method of representation can be justified theoretically and was also validated by a torque calculation based on the zero frequency component of

circumferential tooth force.

As a turbogenerator stator behaves as a linear elastic structure under the mechanical loads to which it is subjected during normal operation, stator bore force may be converted to core-back vibration by means of multiplication by a suitable transfer coefficient. The transfer coefficient relating radial force to radial displacement is generally different to that relating circumferential force to radial displacement. Structural finite-element analyses on isolated representations of the stators examined produced values for these transfer coefficients. As explained in Section 8.1, it is not possible to predict absolute core-back vibration levels from an isolated model. Therefore this was not attempted. The core representations used to obtain the transfer coefficients were developed in Section 5.5 such that their resonant frequencies were close to those of the cores represented. This was to ensure a manner of dynamic equivalence between model and structure.

When a simple analytical model is used to represent a complex non-linear system such as an electrical machine, it is necessary to restrict the degrees of freedom of the model in order to keep it self-consistent. Thus only certain variables can be allowed to assume their real values, whilst others must be assigned consistent fictitious values. Such a model was developed in Section 6.1. In a study of vibration variation with load it is important that the load, in MW and MVAR, be properly represented. The second condition selected for the initial two-degree-of-freedom model was that the resultant fundamental radial air-gap flux density should be fixed at that necessary to induce rated terminal voltage on open circuit. This was not only for purposes of convenience, but because the radial air-gap flux density is most important in determining the radial Maxwell stress. The circumferential Maxwell stress is most heavily dependent on stator current, which is a function of the

specified load condition.

A very simple analytical model, in which the iron is considered to be infinitely permeable and the windings are represented by sinusoidally distributed current sheets, is inadequate due to its inability to represent the important secondary effects of saturation and higher m.m.f. harmonics. Therefore a multi-region model was developed in Section 6.2 in which the rotor body and stator core are represented by homogenous regions of specified finite permeability, whilst the slotted portions of both are represented by regions of anisotropic permeability. The windings are represented by Fourier series. A numerical approach to the calculation of Maxwell stress enables the higher harmonic terms to be handled more easily than the corresponding algebraic approach, which would require multiplication of series. An eventual working model was found to require only the 3rd and 5th harmonics of the rotor current sheet in addition to the two fundamental components.

It was found necessary to represent saturation by the adjustment of permeability within the model. An alternative based on Carter's method, which takes account only of slotting, proved inadequate. A scheme was developed in which all the saturation in the machine is represented by reduced permeability in the slotted regions. Selection of the value of permeability at any given load was performed automatically by adjusting this value until the measured (or estimated, in the absence of a measurement) rotor current produced the required value of fundamental radial air-gap flux density. In this way the model acts in a similar manner to the real system, in which more excitation current is drawn to overcome saturation and maintain the terminal voltage demanded by the AVR. However it is wasteful of computing power to rely on an iterative scheme, so thought was given in Section 6.5.4 to the possibility of representing the variation of slotted region permeability as

an algebraic function of load.

The ability of the model to predict global effects by way of its somewhat artificial saturation modelling scheme was tested in Section 6.5.3 by comparing its calculation of load angle with values measured in tests at Fawley power station. The agreement between model and measurement was generally very good, although the model showed itself to be weak when handling loads with high leading MVAR.

Its ability to predict vibration trends was assessed by the simulation of some measurements taken on a 350MW generator. The trends produced by the model of vibration amplitude and phase over a series of MW loads at 0MVAR and a series of MVAR loads at 355MW were encouragingly close to the measured trends. In particular, the predicted decrease in vibration of 42% between open circuit and full rated load was the same as the average reduction from the four separate transducers.

The model was finally used to produce families of curves showing variations of vibration amplitude and phase with MW and MVAR load for three different machines. It thereby gave an insight into patterns of vibration behaviour over the complete range of a turbogenerator output capability, and how these patterns vary between different designs of machine.

8.3 Further Work

As a piece of investigative research, this work is virtually complete. However, there is still scope both for streamlining the model in its present form, and for improving predictions by extensions to it. The precise manner in which it might be applied within a monitoring system is still unclear.

Computing time can be saved by algebraic modelling of slotted region permeability as described in Section 6.5.4. A set of initial load conditions from which to determine the arbitrary functions of equation (6.104) may be obtained off-line from the present iterative program. Within this, there is scope for improving estimation of rotor current. Whilst a simple Potier method is used at present, machine manufacturers use adaptations of this method developed over years of experience which give more accurate figures.

The iterative program itself may be streamlined by replacing the two separate iterative routines with one. The rotor current, once estimated, can be set at that value, whilst the slotted region permeability is adjusted to give the correct peak fundamental radial air-gap flux density. This adaptation has not been performed here as it is purely a software exercise and gives no new insight into the phenomenon under study. Output from such a program would necessarily be identical to output from the present one. Such a step would furthermore remove the need for an interim calculation of fictitious rotor current, so the two-degree-of-freedom model would become redundant. This is unsurprising, as the need for it arose out of the problems of representing a non-linear system by a linear model. Once the non-linearity is incorporated directly into the model, such an approach becomes unnecessary. However, construction of this model formed an important stage of the work.

It is clear that the accuracy of predictions possible depends on two things. The first is the accuracy with which conditions within a saturated synchronous machine may be modelled. In particular, the variation of load angle due to saturation is very important, as this affects the angle between radial and circumferential stator bore ovalising forces, shown to be of key importance in the vibration trends. The second is the accuracy with which the dynamic behaviour of the support structure can be modelled. It can

be seen from Figures 7.1 to 7.5 that not only do the absolute vibration levels vary with transducer position, but the trends vary too. This is likely to be partially due to the limitations of the measuring instruments, but may also indicate that parts of the structural surroundings display a non-linear response. Highly accurate vibration predictions are likely to need such a sophisticated level of mechanical modelling that they are not worthwhile.

The factor most important in determining the required level of accuracy is the nature of the monitoring scheme into which the predictions are to be incorporated. When this project was instigated, the CEGB were showing considerable interest in the widespread installation of extensive on-line condition monitoring equipment on their generating plant. Since that time, reorganisation and privatisation have brought about a review of priorities, and on-line condition monitoring appears to have become a temporary casualty. A resurgence of interest is almost certain, although a tendency to go towards smaller units in the future may reduce the importance of stator core vibration and its effects.

REFERENCES

1. TAVNER P J, PENMAN J. Condition Monitoring of Electrical Machines, p 5. Research Studies Press Ltd. 1987.
2. HAM P A L. Trends and future scope in the monitoring of large steam turbine generators. IEE Proceedings Vol 133, Pt B, No 3, May 1986, pp 164-168.
3. TAVNER P J. Condition monitoring - the way ahead for large electrical machines. Proc. International Conference on Electrical Machines and Drives, IEE London, 1989, pp 159-162.
4. TAVNER P J, GAYDON B G, WARD D M. Monitoring generators and large motors. IEE Proceedings Vol 133, Pt B, No 3, May 1986, pp169-180.
5. INGLEBY M, RONVAL G P L. Classification of vibration signatures of turbo-generators. Proc. International Conference on Electrical Machines and Drives, IEE London, 1989, pp 172-176.
6. THOMAS D L. Vibration monitoring strategy for large turbogenerators. IMechE, 1984, pp91-99.
7. LAFFOON C M, ROSE B A. Special problems of two-pole turbine generators. IEEE Transactions, Vol 59, January 1940, pp 30-34.
8. PENNIMAN A L, TAYLOR H D. Suppression of magnetic vibration and noise of two-pole turbine generators. IEEE Transactions, Vol 60, June 1941, pp 283-288.
9. BAUDRY R A, HELLER P R, CURTIS L P. Magnetic vibrations in a-c generator stators. IEEE Transactions: Power Apparatus and Systems, Vol 73, No 12, June 1954, pp508-516.
10. BARTON R A, MASSINGILL J A, TAYLOR H D. Design features and characteristics of large steam turbine generators. IEEE Transactions: Power Apparatus and Systems, Vol 77, February 1959, pp 1335-1348.
11. RICHARDSON P. Stator vibration in large two-pole generators. IEEE Winter Power Meeting, February 1966.

12. RICHARDSON P, HAWLEY R. Generator stator vibration. IEEE Winter Power Meeting, January 1970.
13. RICHARDSON P, HAWLEY R. Quadrature axis force and generator core vibration. IEEE Transactions: Power Apparatus and Systems, Vol 92, No 4, July/August 1973, pp 1260-1265.
14. HAWLEY R, HINDMARSH R, CRAWFORD A J. Generator core load vibration: some preliminary observations. IEEE Winter Power Meeting, January 1974.
15. MARLOW B A. The mechanical design of large turbogenerators. Proc. IMechE, Vol 201, No A2, 1987, pp 91-103.
16. VERMA S P. Vibration behaviour of laminated stators of electrical machines. Proc. International Conference on Electrical Machines and Drives, IEE London, 1987, pp113-117.
17. MATSUDA T, ITOH H, YAMAMOTO Y, TACHIBANA I, MURAKAMI T. Dynamic characteristics and recent design technology of stator structures of turbine-driven generators. Toshiba Corporation. Japan.
18. BENHAM P P, WARNOCK F V. Mechanics of solids and structures, pp 100-101. Pitman. 1976.
19. Ibid. p 621.
20. GARVEY S D. The vibrational behaviour of laminated components in electrical machines. Proc. International Conference on Electrical Machines and Drives, IEE London, 1989, pp 226-231.
21. KUCERA J. Les vibrations du noyau du stator dans les turbo-alternateurs de grand puissance. Revue Generale de l'Electricité, Vol 73, April 1964, pp 227-231.
22. SAY M G. Alternating Current Machines, Fifth Edition, pp 17-18. Pitman. 1983.
23. SPIEGEL M R. Mathematical Handbook, p 17. McGraw Hill. 1968.
24. FRENCH A P. Special Relativity, Chapter 7. W W Norton. 1968.
25. HAMMOND P. Applied Electromagnetism, pp 79-80.

Pergamon Press. 1971.
26. Ibid. p 25.
27. Ibid. p 151.
28. Ibid. p 15.
29. HAMMOND P. Forces in electric and magnetic fields. Bulletin of Electrical Engineering Education, No 25, December 1960.
30. MAXWELL J C. Treatise on Electricity and Magnetism, Third Edition, Vol II Chapter 11. Clarendon Press. 1891.
31. CARPENTER C J. Surface-integral methods of calculating forces on magnetised iron parts. IEE Monograph No 342, August 1959, pp 19-28.
32. BOSE B K. Power Electronics and AC Drives, pp 44-45. Prentice-Hall. 1986.
33. HAMMOND P. Applied Electromagnetism, pp 175-176. Pergamon Press. 1971.
34. LEFEVRE Y, LAJOIE-MAZENC M, DAVAT B. Force calculation in electromagnetic devices. Proc. International Symposium on Electromagnetic Fields, Pavia, Italy, 1987, pp 227-230.
35. LENNOX S C, CHADWICK M. Mathematics for Engineers and Applied Scientists, Second Edition, p 385. Heinemann. 1977.
36. SAY M G. Alternating Current Machines, Fifth Edition, p 31. Pitman. 1983.
37. TIMOSHENKO S. Vibration Problems in Engineering, Third Edition, pp 425-430. Macmillan and Co Ltd. 1955.
38. DE SALVO G J, GORMAN R W. ANSYS Engineering Analysis System. User's Manual for Revision 4.3, Section 2.8. Swanson Analysis Systems, 1st June 1987.
39. HURTY W C, RUBINSTEIN M F. Dynamics of Structures, p 257. Prentice-Hall. 1964.
40. Ibid. p 259.
41. Ibid. p 272.
42. DE SALVO G J, GORMAN R W. ANSYS Engineering Analysis System. User's Manual for Revision 4.3, Section 2.31.

Swanson Analysis Systems, 1st June 1987.
43. WHITELAW R D M. Private Correspondence. 1989.
44. SPIEGEL M R. Mathematical Handbook, p 32. McGraw Hill. 1968.
45. MACDONALD D C, REECE A B J, TURNER P J. Turbine-generator steady-state reactances. IEE Proceedings, Vol 132, Pt C, No 3, May 1986, pp 101-108.
46. JACOBS D A H, MINORS R H, MYERSCOUGH C J, ROLLASON M L J, STEEL J G. Calculation of losses in the end region of turbogenerators. Proc IEE, Vol 124, No 4, April 1977, pp 356-362.
47. SAY M G. Alternating Current Machines, Fifth Edition, p 37. Pitman. 1983.
48. Ibid. p 38.
49. DE MELLO F P, HANNETT L N. Representation of saturation in synchronous machines. IEEE Trans: Power Systems, Vol PWRS-1, No 4, November 1986, pp 8-14.
50. ROBERTSON B L, ROGERS T A, DALZIEL C F. The saturated synchronous machine. Electrical Engineering (AIEE Transactions), Vol 56, July 1937, pp 858-863.
51. HARLEY R G, LIMEBEER D J N, CHIRRICOZZI E. Comparative study of saturation methods in synchronous machine models. IEE Proceedings, Vol 127, Pt B, No 1, January 1980, pp 1-7.
52. SHACKSHAFT G, NEILSON R. Results of stability tests on an underexcited 120MW generator. Proc. IEE, Vol 119, No 2, February 1972, pp 175-188.
53. CHIRRICOZZI E, DI NAPOLI A. Saturation effect on the magnetic field distribution in tooth region of electric machines. IEEE Transactions on Magnetics, Vol MAG-14, No 5, September 1978, pp 473-475.
54. MINNICH S H, SHARMA D K, FARMER R G, FISH J H. Saturation functions for synchronous generators from finite elements. IEEE Transactions on Energy Conversion, Vol EC-2, No 4, December 1987, pp 680-692.
55. ABDEL-RAZEK A A, COULOMB J L, FELIACHI M, SABONNACLIERE J C. The calculation of electromagnetic

torque in saturated electric machines within combined numerical and analytical solutions of the field equations. IEEE Transactions on Magnetics, Vol MAG-17, No 6, November 1981, pp 3250-3252.

56. EL-SERAFI A M, ABDALLAH A S, EL-SHERBINY M K, BADAWY E M. Experimental verification of the cross-magnetising phenomenon in saturated synchronous machines. IEEE Transactions on Magnetics, Vol MAG-23, No 5, September 1987, pp3029-3031.

57. TIMOSHENKO S. Theory of Elastic Stability, pp 2-4. McGraw Hill. 1936.

58. STOLL R L. The Analysis of Eddy Currents, p 3. Clarendon Press. 1974.

APPENDIX A

MACHINE DATA

Data Item	Ferrybridge	West Burton	GEC 350MW
R_1 (m)	0.471500	0.399000	0.411895
R_2 (m)	0.571490	0.558790	0.549990
R_3 (m)	0.571500	0.558800	0.550000
R_4 (m)	0.654000	0.641350	0.640000
R_5 (m)	0.654010	0.641360	0.640010
R_6 (m)	0.841325	0.825500	0.828000
R_7 (m)	1.295400	1.270000	1.287500
No. of stator teeth	54	48	54
τ_S (radians)	0.029664	0.033267	0.027656
c	0.814815	0.833333	0.814815
Q_S	9	8	9
Δ_S (radians)	0.116355	0.130900	0.116355
n_p	2	2	2
Δ_R (radians)	0.146120	0.120909	0.139636
τ_R (radians)	0.032896	0.028000	0.037818
Q_R	14	16	16
n_c (average)	8.000	5.875	8.875
Active length (m)	5.960000	6.851650	4.840000
μ_R	100	100	100
μ_S	1000	1000	1000
μ_{teeth} (rotor)	50	50	50
μ_{teeth} (stator)	50	50	50
Reference angle offset (°)	0.000000	3.750000	0.000000
$k_{r,r}$ (μm/kN)	1.170000	1.740000	0.749000
$k_{r,\theta}$ (μm/kN)	1.110000	1.620000	0.724000
X_1 (Ω) (line value)	0.285000	0.242000	0.251000
Slope of s.c.c.	5.000000	4.805600	5.854200
Slope of air line	19.444	16.667	16.000
Frohlich coefficient a	0.033700	0.036700	0.033600
Frohlich coefficient b	0.018300	0.021100	0.030500

NOTE: Data items are listed in the order and format in which they are read into the two computer programs listed in

Appendix B. The radii are classified according to the numbering system developed in Section 6.2.1, comprising slot bottom radii, current sheet radii and air-gap surface radii; also the stator core back radius. Geometric quantities are defined in the list of Symbols and Abbreviations. Slotted region permeabilities given are used for the purpose of starting the iterative routine. The need for a reference angle offset was explained in Section 4.4. Quantities used to describe the open and short circuit characteristics assume that voltage is given in volts and current in amps.

APPENDIX B : SOFTWARE

Algebraic (Fundamental only) Model

```
FILE: TOROMOD4 FORTRAN  A1              SOUTHAMPTON UNIVERSITY CMS REL 5

                                                                      TOR00010
      PROGRAM FUNDAL                                                  TOR00020
C     PRESENTATION VERSION 11TH JUNE 1990                             TOR00030
C                                                                     TOR00040
C     PROVIDES A SIMPLE TWO-POLE MACHINE VIBRATIONAL MODEL CONSISTING TOR00050
C     OF HOMOGENOUS ROTOR AND STATOR OF INFINITE PERMEABILITY WITH    TOR00060
C     SINUSOIDALLY DISTRIBUTED SHEETS OF SURFACE CURRENT              TOR00070
C                                                                     TOR00080
      REAL IS,IR,IR1,IR2,IROC,NC,NP,KR,KS,MUO                         TOR00090
      REAL LAMBDA,LMDR,LMDR1,LMDR2,KW                                 TOR00100
      CHARACTER TITLE*50,CONT,PF*4,ERMES*50                           TOR00110
      PI=3.14159265                                                   TOR00120
      MUO=PI*4.0E-7                                                   TOR00130
C                                                                     TOR00140
      PRINT *,'INPUT ANALYSIS TITLE (IN INVERTED COMMAS)'             TOR00150
      READ *,TITLE                                                    TOR00160
C                                                                     TOR00170
C     READ DATA FROM MACHINE DATA FILE                                TOR00180
      OPEN(UNIT=82,FORM='FORMATTED',STATUS='OLD')                     TOR00190
      READ(82,100)                                                    TOR00200
      READ(82,100)                                                    TOR00210
      READ(82,100)                                                    TOR00220
      READ(82,100)                                                    TOR00230
C     ROTOR RADIUS                                                    TOR00240
      READ(82,101) R1                                                 TOR00250
C     STATOR RADIUS                                                   TOR00260
      READ(82,101) R2                                                 TOR00270
      READ(82,100)                                                    TOR00280
      READ(82,100)                                                    TOR00290
      READ(82,100)                                                    TOR00300
C     NUMBER OF STATOR TEETH                                          TOR00310
      READ(82,102) TEETH                                              TOR00320
C     HALF STATOR SLOT OPENING                                        TOR00330
      READ(82,101) TAUS                                               TOR00340
C     STATOR COIL PITCH (CHORDING)                                    TOR00350
      READ(82,101) C                                                  TOR00360
C     STATOR SLOTS PER POLE PER PHASE                                 TOR00370
      READ(82,102) QS                                                 TOR00380
C     STATOR SLOT PITCH                                               TOR00390
      READ(82,101) DELS                                               TOR00400
C     NUMBER OF PARALLEL PATHS IN STATOR                              TOR00410
      READ(82,102) NP                                                 TOR00420
C     ROTOR SLOT PITCH IN RADIANS                                     TOR00430
      READ(82,101) DELR                                               TOR00440
C     HALF ROTOR SLOT OPENING IN RADIANS                              TOR00450
      READ(82,101) TAUR                                               TOR00460
C     NUMBER OF ROTOR SLOTS PER POLE                                  TOR00470
      READ(82,102) QR                                                 TOR00480
C     NUMBER OF ROTOR CONDUCTORS PER COIL                             TOR00490
      READ(82,101) NC                                                 TOR00500
C     ACTIVE LENGTH OF MACHINE                                        TOR00510
      READ(82,101) ACTLEN                                             TOR00520
      READ(82,100)                                                    TOR00530
      READ(82,100)                                                    TOR00540
      READ(82,100)                                                    TOR00550
```

```
      READ(82,100)                                                      TOR00560
      READ(82,100)                                                      TOR00570
C     RADIAL FORCE TRANSFER COEFFICIENT                                 TOR00580
      READ(82,101) TCRAD                                                TOR00590
C     TANGENTIAL FORCE TRANSFER COEFFICIENT                             TOR00600
      READ(82,101) TCTAN                                                TOR00610
C                                                                       TOR00620
C     OPEN OUTPUT FILE AND TITLE UP                                     TOR00630
      OPEN(UNIT=11,FORM='FORMATTED',STATUS='NEW')                       TOR00640
      WRITE(11,200) TITLE                                               TOR00650
      WRITE(11,100)                                                     TOR00660
C                                                                       TOR00670
 10   CONTINUE                                                          TOR00680
C     PRELIMINARY CALCULATIONS TO ESTABLISH OPEN CIRCUIT ROTOR CURRENT  TOR00690
C     NECESSARY TO GIVE REQUIRED TERMINAL VOLTAGE IN INFINITE           TOR00700
C     PREMEABILITY SITUATION                                            TOR00710
C     READ IN TERMINAL VOLTAGE                                          TOR00720
      PRINT *,'TERMINAL VOLTAGE IN KV'                                  TOR00730
      READ *,VLIN                                                       TOR00740
      VLIN=VLIN*1.0E3                                                   TOR00750
C     STATOR WINDING FACTOR                                             TOR00760
      KW=SIN(PI*C/2.)*SIN(QS*DELS/2.)/SIN(DELS/2.)/QS*TAUS/SIN(TAUS)    TOR00770
C     OPEN CIRCUIT RADIAL FLUX DENSITY                                  TOR00780
      BROC=VLIN/(SQRT(3.)*SQRT(2.)*PI*100.*QS*R2*KW*ACTLEN)             TOR00790
C     ROTOR CURRENT SHEET MULTIPLIER                                    TOR00800
      CR=2.*NC/PI*SIN(TAUR)/TAUR                                        TOR00810
      CR=CR*SIN(QR*DELR/2.)/SIN(DELR/2.)/R1                             TOR00820
C     RADIUS FUNCTIONS TO SCALE CURRENT SHEETS TO FLUX DENSITIES        TOR00830
      RADFR=2./((R2/R1)*(R2/R1)-1)                                      TOR00840
      RADFS=(1+(R1/R2)*(R1/R2))/(1-(R1/R2)*(R1/R2))                     TOR00850
C     OPEN CIRCUIT ROTOR CURRENT                                        TOR00860
      IROC=BROC/(MUO*CR*RADFR)                                          TOR00870
C                                                                       TOR00880
C     LOAD CONDITION INPUT FROM TERMINAL                                TOR00890
      PRINT *,'FORM OF INPUT FOR LOAD DATA'                             TOR00900
      PRINT *,'1   POWER AND POWER FACTOR'                              TOR00910
      PRINT *,'2   ACTIVE AND REACTIVE POWER'                           TOR00920
      PRINT *,'PLEASE GIVE NUMBER PRECEDING REQUIRED FORM'              TOR00930
      READ *,NCONT                                                      TOR00940
      PRINT *,'NATURE OF POWER FACTOR (LEAD/LAG)'                       TOR00950
      READ *, PF                                                        TOR00960
      PRINT *,'OUTPUT POWER IN MW'                                      TOR00970
      READ *,POUT                                                       TOR00980
      POUT=POUT*1.0E6                                                   TOR00990
      IF (NCONT.EQ.1) THEN                                              TOR01000
       PRINT *,'VALUE OF POWER FACTOR'                                  TOR01010
       READ *, PFVAL                                                    TOR01020
C      PEAK STATOR LINE CURRENT                                         TOR01030
       IS=POUT*SQRT(2.0)/(SQRT(3.0)*VLIN*PFVAL)                         TOR01040
      ELSE                                                              TOR01050
       PRINT *,'REACTIVE POWER IN MVAR'                                 TOR01060
       READ *,VARS                                                      TOR01070
       VARS=VARS*1.0E6                                                  TOR01080
       IS=SQRT(2.*(POUT*POUT+VARS*VARS)/(3.*VLIN*VLIN))                 TOR01090
       PFVAL=COS(ATAN(VARS/POUT))                                       TOR01100
```

```
      END IF                                                            TOR01110
C     PROTECT UNITY POWER FACTOR CASE FROM FLOATING POINT INACCURACIES  TOR01120
      IF (PFVAL.GT.0.999999999) THEN                                    TOR01130
       PFVAL=0.999999999                                                TOR01140
      END IF                                                            TOR01150
C     POWER FACTOR ANGLE (IN RADIANS)                                   TOR01160
      PHI=ACOS(PFVAL)                                                   TOR01170
C     RECOGNITION OF OPEN CIRCUIT CONDITION                             TOR01180
      IF (IS.LT.1.0E-9) THEN                                            TOR01190
       KS=0.0                                                           TOR01200
       IR=IROC                                                          TOR01210
       LMDR=0.0                                                         TOR01220
       GOTO 20                                                          TOR01230
      END IF                                                            TOR01240
C                                                                       TOR01250
C     PEAK STATOR SURFACE CURRENT DENSITY                               TOR01260
      KS=6*IS*KW*QS/(PI*NP*R2)                                          TOR01270
C                                                                       TOR01280
C     CALCULATIONS TO DETERMINE ROTOR CURRENT AND TORQUE ANGLE          TOR01290
C     POWER FUNCTION                                                    TOR01300
      PFUN=IROC*PFVAL                                                   TOR01310
C     CURRENT FUNCTION                                                  TOR01320
      CFUN=RADFS*KS/(RADFR*CR)                                          TOR01330
C     COEFFICIENTS OF THE FIRST EQUATION IN LAMBDA                      TOR01340
      A1=PFUN*PFUN*PFUN*PFUN                                            TOR01350
      A2=2.*PFUN*PFUN*(IROC*IROC+CFUN*CFUN)                             TOR01360
      A3=(CFUN*CFUN-IROC*IROC)*(CFUN*CFUN-IROC*IROC)                    TOR01370
      A3=A3+4.*CFUN*CFUN*PFUN*PFUN                                      TOR01380
C     SOLVING FOR LAMBDA                                                TOR01390
      ACOMP=A2*A2-4.*A1*A3                                              TOR01400
      IF (ACOMP.LT.0.0) THEN                                            TOR01410
       ERMES='IMAGINARY ROOTS - CHECK DATA'                             TOR01420
       PRINT *, ERMES                                                   TOR01430
       STOP                                                             TOR01440
      END IF                                                            TOR01450
      SINSQ1=(A2+SQRT(ACOMP))/(2.*A3)                                   TOR01460
      SINSQ2=(A2-SQRT(ACOMP))/(2.*A3)                                   TOR01470
      SILAM1=SQRT(SINSQ1)                                               TOR01480
      SILAM2=SQRT(SINSQ2)                                               TOR01490
C     DISENTANGLEMENT OF QUADRANT LOCATIONS OF LAMBDA                   TOR01500
      IF (CFUN*CFUN-IROC*IROC.LT.0.0) THEN                              TOR01510
       IF (PFUN*PFUN.LT.ABS(CFUN*CFUN-IROC*IROC)) THEN                  TOR01520
        IF (SILAM1.GT.SILAM2) THEN                                      TOR01530
         LMDR1=ASIN(SILAM1)                                             TOR01540
         LMDR2=PI-ASIN(SILAM2)                                          TOR01550
        ELSE                                                            TOR01560
         LMDR1=PI-ASIN(SILAM1)                                          TOR01570
         LMDR2=ASIN(SILAM2)                                             TOR01580
        END IF                                                          TOR01590
       ELSE                                                             TOR01600
        LMDR1=PI-ASIN(SILAM1)                                           TOR01610
        LMDR2=PI-ASIN(SILAM2)                                           TOR01620
       END IF                                                           TOR01630
      ELSE                                                              TOR01640
       LMDR1=PI-ASIN(SILAM1)                                            TOR01650
```

```
        LMDR2=PI-ASIN(SILAM2)                                          TOR01660
       END IF                                                          TOR01670
C      CALCULATION OF IR                                               TOR01680
       IR1=PFUN/SILAM1                                                 TOR01690
       IR2=PFUN/SILAM2                                                 TOR01700
       IF (PF.EQ.'LAG ') THEN                                          TOR01710
        IF (IR1.GT.IR2) THEN                                           TOR01720
         IR=IR1                                                        TOR01730
         LMDR=LMDR1                                                    TOR01740
        ELSE                                                           TOR01750
         IR=IR2                                                        TOR01760
         LMDR=LMDR2                                                    TOR01770
        END IF                                                         TOR01780
       ELSE                                                            TOR01790
        IF (IR1.LT.IR2) THEN                                           TOR01800
         IR=IR1                                                        TOR01810
        LMDR=LMDR1                                                     TOR01820
        ELSE                                                           TOR01830
         IR=IR2                                                        TOR01840
         LMDR=LMDR2                                                    TOR01850
        END IF                                                         TOR01860
       END IF                                                          TOR01870
C                                                                      TOR01880
 20    CONTINUE                                                        TOR01890
C      CALCULATION OF PEAK ROTOR SURFACE CURRENT DENSITY               TOR01900
       KR=CR*IR                                                        TOR01910
C      FLUX DENSITIES                                                  TOR01920
C      RADIAL DISTRIBUTIONS - MULTIPLY A COSINE FUNCTION               TOR01930
       BROT=MUO*KR*RADFR                                               TOR01940
       BSTATR=MUO*KS*RADFS                                             TOR01950
C      TANGENTIAL DISTRIBUTION - MULTIPLIES A MINUS SINE FUNCTION      TOR01960
       BSTATT=MUO*KS                                                   TOR01970
C      RESULTANT RADIAL GAP FLUX - FOR PRINTOUT ONLY                   TOR01980
       BGAP=BSTATR*BSTATR+BROT*BROT                                    TOR01990
       BGAP=SQRT(BGAP-2.*BROT*BSTATR*COS(PI-LMDR))                     TOR02000
C      EXPRESSION OF RADIAL AND TANGENTIAL FLUX DENSITIES IN THE       TOR02010
C      FORM:  BMAG COS (THETA - OMEGA T - BANG)                        TOR02020
       BRSI=(-1)*BSTATR*SIN(LMDR)                                      TOR02030
       BRCO=BROT+BSTATR*COS(LMDR)                                      TOR02040
       BRMAG=SQRT(BRSI*BRSI+BRCO*BRCO)                                 TOR02050
       CALL ANGLE(BRSI,BRCO,BRANG)                                     TOR02060
       BTSI=(-1)*BSTATT*COS(LMDR)                                      TOR02070
       BTCO=(-1)*BSTATT*SIN(LMDR)                                      TOR02080
       BTMAG=SQRT(BTSI*BTSI+BTCO*BTCO)                                 TOR02090
       CALL ANGLE(BTSI,BTCO,BTANG)                                     TOR02100
C                                                                      TOR02110
C      STRESS COEFFICIENTS - RADIAL                                    TOR02120
       SRSI=(BRMAG*BRMAG*SIN(2.*BRANG)-BTMAG*BTMAG*SIN(2.*BTANG))/2.   TOR02130
       SRCO=(BRMAG*BRMAG*COS(2.*BRANG)-BTMAG*BTMAG*COS(2.*BTANG))/2.   TOR02140
       SRMAG=SQRT(SRSI*SRSI+SRCO*SRCO)                                 TOR02150
       SRMAG=SRMAG/2./MUO                                              TOR02160
       CALL ANGLE(SRSI,SRCO,SRANG)                                     TOR02170
C      STRESS COEFFICIENTS - TANGENTIAL                                TOR02180
       STSI=BRMAG*BTMAG*SIN(BRANG+BTANG)/2.                            TOR02190
       STCO=BRMAG*BTMAG*COS(BRANG+BTANG)/2.                            TOR02200
```

```
      STMAG=SQRT(STSI*STSI+STCO*STCO)                                   TOR02210
      STMAG=STMAG/MUO                                                   TOR02220
      CALL ANGLE(STSI,STCO,STANG)                                       TOR02230
C     CALCULATION OF PHASE DIFFERENCE BETWEEN RADIAL AND TANGENTIAL     TOR02240
C     FORCE AND STRESS WAVES (BOTH ARE LAG ANGLES)                      TOR02250
      PHDIFR=STANG-SRANG                                                TOR02260
      IF (PHDIFR.LT.0.0) THEN                                           TOR02270
       PHDIFR=PHDIFR+2.*PI                                              TOR02280
      END IF                                                            TOR02290
      PHDIFD=PHDIFR*180./PI                                             TOR02300
C     CALCULATION OF MAGNITUDE OF TOOTH FORCE WAVE                      TOR02310
      FR=SRMAG*SIN(DELS)*R2/1.E3                                        TOR02320
      FT=STMAG*SIN(DELS)*R2/1.E3                                        TOR02330
C                                                                       TOR02340
C     CALCULATION OF RADIAL VIBRATIONS (VALUES IN MICROMETRES PEAK)     TOR02350
      DR=FR*TCRAD                                                       TOR02360
      DT=FT*TCTAN                                                       TOR02370
      VIB=SQRT(DR*DR+DT*DT-2*DT*DR*COS(PHDIFR-PI/2.))                   TOR02380
C     CALCULATION OF VIBRATION PHASE                                    TOR02390
      VIBSIN=(SRSI*TCRAD+STCO*TCTAN)*SIN(DELS)*R2*1.0E-3                TOR02400
      VIBCOS=(SRCO*TCRAD-STSI*TCTAN)*SIN(DELS)*R2*1.0E-3                TOR02410
      CALL ANGLE(VIBSIN,VIBCOS,VIBANG)                                  TOR02420
      IF (VIBANG.LT.0.0) THEN                                           TOR02430
       VIBANG=VIBANG+2.*PI                                              TOR02440
      END IF                                                            TOR02450
C     CONVERT TO DEGREES FOR OUTPUT                                     TOR02460
      VIBANG=VIBANG*180./PI                                             TOR02470
C                                                                       TOR02480
C     OUTPUT OF DATA                                                    TOR02490
      WRITE(11,100)                                                     TOR02500
      WRITE(11,214) POUT*1.0E-6                                         TOR02510
      IF (NCONT.EQ.2) THEN                                              TOR02520
       WRITE(11,215) VARS*1.0E-6                                        TOR02530
      END IF                                                            TOR02540
      WRITE(11,216) VLIN*1.0E-3                                         TOR02550
C     R.M.S. STATOR LINE CURRENT                                        TOR02560
      WRITE(11,201) IS/SQRT(2.0)                                        TOR02570
      WRITE(11,202) IR                                                  TOR02580
      LAMBDA=LMDR*180./PI                                               TOR02590
      WRITE(11,203) LAMBDA                                              TOR02600
      DPHI=PHI*180./PI                                                  TOR02610
      IF (PF.EQ.'LEAD') DPHI=(-1)*DPHI                                  TOR02620
      DELTA=LAMBDA-DPHI-90                                              TOR02630
      WRITE(11,217) DELTA                                               TOR02640
      IF (ABS(PFVAL-1.0).LT.1.0E-2) THEN                                TOR02650
       WRITE(11,213) PFVAL                                              TOR02660
      ELSE                                                              TOR02670
       WRITE(11,212) PFVAL,PF                                           TOR02680
      END IF                                                            TOR02690
      WRITE(11,100)                                                     TOR02700
      WRITE(11,211)                                                     TOR02710
      WRITE(11,204) BROT                                                TOR02720
      WRITE(11,205) BSTATR                                              TOR02730
      WRITE(11,206) BGAP                                                TOR02740
      WRITE(11,100)                                                     TOR02750
```

```
FILE: TORQMOD4 FORTRAN  A1              SOUTHAMPTON UNIVERSITY CMS REL 5

      WRITE(11,207) FR                                                  TOR02760
      WRITE(11,208) FT                                                  TOR02770
      WRITE(11,209) PHDIFD                                              TOR02780
      WRITE(11,100)                                                     TOR02790
      WRITE(11,210) VIB                                                 TOR02800
      WRITE(11,218) VIBANG                                              TOR02810
      PRINT *,'ANOTHER LOAD CASE (''Y''/''N'')?'                        TOR02820
      READ *,CONT                                                       TOR02830
      IF (CONT.EQ.'Y') THEN                                             TOR02840
        WRITE(11,100)                                                   TOR02850
        WRITE(11,100)                                                   TOR02860
        GOTO 10                                                         TOR02870
      END IF                                                            TOR02880
      STOP                                                              TOR02890
  100 FORMAT(1X)                                                        TOR02900
  101 FORMAT(40X,F8.6)                                                  TOR02910
  102 FORMAT(40X,F3.0)                                                  TOR02920
  103 FORMAT(40X,F8.2)                                                  TOR02930
  104 FORMAT(10X,'PFUN MULTIPLIER/IROC',5X,F8.2)                        TOR02940
  105 FORMAT(10X,'STATOR CURRENT SHEET',5X,F8.1)                        TOR02950
  200 FORMAT(10X,A50)                                                   TOR02960
  201 FORMAT(10X,'STATOR CURRENT',5X,F6.0,1X,'A')                       TOR02970
  202 FORMAT(10X,'ROTOR CURRENT',5X,F6.0,1X,'A')                        TOR02980
  203 FORMAT(10X,'TORQUE ANGLE',5X,F7.2,1X,'DEG')                       TOR02990
  204 FORMAT(10X,'ROTOR FLUX DENSITY',5X,F6.4,1X,'T')                   TOR03000
  205 FORMAT(10X,'STATOR FLUX DENSITY',5X,F6.4,1X,'T')                  TOR03010
  206 FORMAT(10X,'AIRGAP FLUX DENSITY',5X,F6.4,1X,'T')                  TOR03020
  207 FORMAT(10X,'RADIAL TOOTH FORCE',5X,F6.2,1X,'KN')                  TOR03030
  208 FORMAT(10X,'TANGENTIAL TOOTH FORCE',5X,F6.2,1X,'KN')              TOR03040
  209 FORMAT(10X,'PHASE LAG OF TANGENTIAL FORCE',5X,F6.2,1X,'DEG')      TOR03050
  210 FORMAT(10X,'PEAK RADIAL VIBRATION',5X,F5.2,1X,'MICROM')           TOR03060
  211 FORMAT(10X,'RADIAL VALUES')                                       TOR03070
  212 FORMAT(10X,'POWER FACTOR',5X,F4.2,5X,A4)                          TOR03080
  213 FORMAT(10X,'POWER FACTOR',5X,F4.2)                                TOR03090
  214 FORMAT(10X,'OUTPUT POWER',5X,F5.1,1X,'MW')                        TOR03100
  215 FORMAT(10X,'REACTIVE POWER',5X,F5.1,1X,'MVAR')                    TOR03110
  216 FORMAT(10X,'TERMINAL VOLTAGE',5X,F4.1,1X,'KV')                    TOR03120
  217 FORMAT(10X,'LOAD ANGLE',5X,F6.2,1X,'DEG')                         TOR03130
  218 FORMAT(10X,'VIBRATION PHASE',5X,F5.1,1X,'DEG')                    TOR03140
      END                                                               TOR03150
      SUBROUTINE ANGLE(SINVAL,COSVAL,RESULT)                            TOR03160
C     FOUR QUADRANT INVERSE TANGENT CALCULATION                         TOR03170
      PI=3.14159265                                                     TOR03180
      IF (COSVAL.LT.0.0) THEN                                           TOR03190
C       QUADRANTS 2 AND 3                                               TOR03200
        IF (SINVAL.LT.0.0) THEN                                         TOR03210
C         QUADRANT 3                                                    TOR03220
          RESULT=ATAN(SINVAL/COSVAL)-PI                                 TOR03230
        ELSE                                                            TOR03240
C         QUADRANT 2                                                    TOR03250
          RESULT=ATAN(SINVAL/COSVAL)+PI                                 TOR03260
        END IF                                                          TOR03270
      ELSE                                                              TOR03280
C       QUADRANTS 1 AND 4                                               TOR03290
        RESULT=ATAN(SINVAL/COSVAL)                                      TOR03300

FILE: TORQMOD4 FORTRAN  A1              SOUTHAMPTON UNIVERSITY CMS REL 5

      END IF                                                            TOR03310
      RETURN                                                            TOR03320
      END                                                               TOR03330
```

```
FILE: NEWMULTI FORTRAN  A1              SOUTHAMPTON UNIVERSITY CMS REL 5

      PROGRAM JUNE                                                        NEW00010
C     PRESENTATION VERSION 11TH JUNE 1990                                 NEW00020
C                                                                         NEW00030
C     AUTOMATED MULTI-REGION MODEL                                        NEW00040
C                                                                         NEW00050
      DIMENSION FLUX(0:6,1:2),S(0:6,1:2),RFOR(0:180),TFOR(0:180)          NEW00060
      DIMENSION BRRMAX(1:29),BTRMAX(1:29),BRSMAX(1:29),BTSMAX(1:29)       NEW00070
      REAL IS,IR,MUO,LMDR,LAMBDA,NC,NP                                    NEW00080
      REAL IRLEAK,IRSC,IAR,IREGAP,IRDES                                   NEW00090
      REAL MUR,MUS,MUSATR,MUSATS,MUNR,MUNS,MUTR,MUTS                      NEW00100
      INTEGER RH1,RH2,SH1,SH2,OMEGAT,TOOTH                                NEW00110
      REAL KRA,KRB,KMR,KSA,KSB,KNS                                        NEW00120
      REAL MR,LR,LS,MS,L5,L2,M2,L3,M3                                     NEW00130
      REAL KW,IROC,KS1,LMDR1,LMDR2,IR1,IR2                                NEW00140
      CHARACTER TITLE*50,PF*4,ERMES*50,CONT,MARK                          NEW00150
      PI=3.141592653                                                      NEW00160
      MUO=PI*4.0E-7                                                       NEW00170
C                                                                         NEW00180
      PRINT *,'INPUT ANALYSIS TITLE (IN INVERTED COMMAS)'                 NEW00190
      READ *,TITLE                                                        NEW00200
C                                                                         NEW00210
C     DATA INPUT FROM MACHINE DATA FILE                                   NEW00220
      OPEN(UNIT=82,FORM='FORMATTED',STATUS='OLD')                         NEW00230
      READ(82,103)                                                        NEW00240
      READ(82,103)                                                        NEW00250
C     GENERAL CONSTANTS                                                   NEW00260
      READ(82,150) R1                                                     NEW00270
C     ROTOR SLOT BOTTOM RADIUS                                            NEW00280
      READ(82,150) R2                                                     NEW00290
C     ROTOR CURRENT SHEET RADIUS                                          NEW00300
      READ(82,150) R3                                                     NEW00310
C     ROTOR SURFACE RADIUS                                                NEW00320
      READ(82,150) R4                                                     NEW00330
C     STATOR BORE RADIUS                                                  NEW00340
      READ(82,150) R5                                                     NEW00350
C     STATOR CURRENT SHEET RADIUS                                         NEW00360
      READ(82,150) R6                                                     NEW00370
C     STATOR SLOT BOTTOM RADIUS                                           NEW00380
      READ(82,150) R7                                                     NEW00390
C     STATOR CORE BACK RADIUS                                             NEW00400
      READ(82,152) TEETH                                                  NEW00410
C     NUMBER OF STATOR TEETH                                              NEW00420
C     WINDING GEOMETRY CONSTANTS                                          NEW00430
      READ(82,150) TAUS                                                   NEW00440
C     HALF STATOR SLOT OPENING                                            NEW00450
      READ(82,150) C                                                      NEW00460
C     COIL PITCH (CHORDING)                                               NEW00470
      READ(82,152) QS                                                     NEW00480
C     STATOR SLOTS PER POLE PER PHASE                                     NEW00490
      READ(82,150) DELS                                                   NEW00500
C     STATOR SLOT PITCH                                                   NEW00510
      READ(82,152) NP                                                     NEW00520
C     NUMBER OF PARALLEL PATHS IN STATOR                                  NEW00530
      READ(82,150) DELR                                                   NEW00540
C     ROTOR SLOT PITCH IN RADIANS                                         NEW00550
```

```
      READ(82,150) TAUR                                                  NEW00560
C     HALF ROTOR SLOT OPENING IN RADIANS                                 NEW00570
      READ(82,152) QR                                                    NEW00580
C     NUMBER OF ROTOR SLOTS PER POLE                                     NEW00590
      READ(82,152) NC                                                    NEW00600
C     NUMBER OF ROTOR CONDUCTORS PER COIL                                NEW00610
      READ(82,150) ACTLEN                                                NEW00620
C     ACTIVE LENGTH OF MACHINE                                           NEW00630
C     RELATIVE PERMEABILITIES                                            NEW00640
      READ(82,153) MUR                                                   NEW00650
C     ROTOR PERMEABILITY                                                 NEW00660
      READ(82,153) MUS                                                   NEW00670
C     STATOR PERMEABILITY                                                NEW00680
      READ(82,153) MUSATR                                                NEW00690
      FSTMTR=MUSATR                                                      NEW00700
C     ROTOR SATURATED TEETH PERMEABILITY (VALUE TO START ITERATIONS)     NEW00710
      READ(82,153) MUSATS                                                NEW00720
      FSTMTS=MUSATS                                                      NEW00730
C     STATOR SATURATED TEETH PERMEABILITY (VALUE TO START ITERATIONS)    NEW00740
      READ(82,150) HSPO                                                  NEW00750
C     HALF STATOR SLOT PITCH IN DEGREES, FOR REF. ANGLE OFFSET           NEW00760
      READ(82,150) TCRAD                                                 NEW00770
C     RADIAL FORCE TRANSFER COEFFICIENT                                  NEW00780
      READ(82,150) TCTAN                                                 NEW00790
C     TANGENTIAL FORCE TRANSFER COEFFICIENT                              NEW00800
      READ(82,150) XLEAK                                                 NEW00810
C     STATOR LEAKAGE REACTANCE (LINE VALUE)                              NEW00820
      READ(82,150) CSC                                                   NEW00830
C     SLOPE OF SHORT CIRCUIT CHARACTERISTIC                              NEW00840
      READ(82,152) CAIR                                                  NEW00850
C     SLOPE OF AIR LINE                                                  NEW00860
      READ(82,150) AFROH                                                 NEW00870
C     FROHLICH A COEFFICIENT                                             NEW00880
      READ(82,150) BFROH                                                 NEW00890
C     FROHLICH B COEFFICIENT                                             NEW00900
C                                                                        NEW00910
C     OPEN OUTPUT FILES AND TITLE UP                                     NEW00920
      OPEN(UNIT=11,FORM='FORMATTED',STATUS='NEW')                        NEW00930
      WRITE(11,300) TITLE                                                NEW00940
      WRITE(11,103)                                                      NEW00950
      WRITE(11,103)                                                      NEW00960
      WRITE(11,110)                                                      NEW00970
      WRITE(11,111)                                                      NEW00980
      WRITE(11,112)                                                      NEW00990
      WRITE(11,103)                                                      NEW01000
C     SECOND OUTPUT FILE GIVES X-Y FORCES FOR ANSYS                      NEW01010
      OPEN(UNIT=10,FORM='FORMATTED',STATUS='NEW')                        NEW01020
      WRITE(10,300) TITLE                                                NEW01030
      WRITE(10,103)                                                      NEW01040
      WRITE(10,100)                                                      NEW01050
      WRITE(10,101)                                                      NEW01060
      WRITE(10,103)                                                      NEW01070
C                                                                        NEW01080
 23   CONTINUE                                                           NEW01090
C     PRELIMINARY CALCULATIONS RELATED TO FUNDAMENTAL QUANTITIES         NEW01100
```

```
C     CONSISTENT WITH INFINITE PERMEABILITY SITUATION                    NEW01110
C     READ IN TEST VALUE OF TERMINAL VOLTAGE                             NEW01120
      PRINT *,'TERMINAL VOLTAGE IN KV'                                   NEW01130
      READ *,VLIN                                                        NEW01140
      VLIN=VLIN*1.0E3                                                    NEW01150
C     STATOR WINDING FACTOR                                              NEW01160
      KW=SIN(PI*C/2.)*SIN(QS*DELS/2.)/SIN(DELS/2.)/QS*TAUS/SIN(TAUS)     NEW01170
C     OPEN CIRCUIT RADIAL FLUX DENSITY                                   NEW01180
      BROC=VLIN/(SQRT(3.)*SQRT(2.)*PI*100.*QS*R5*KW*ACTLEN)              NEW01190
C     ROTOR CURRENT SHEET MULTIPLIER                                     NEW01200
      CR=2.*NC/PI*SIN(TAUR)/TAUR                                         NEW01210
      CR=CR*SIN(QR*DELR/2.)/SIN(DELR/2.)/R2                              NEW01220
C     RADIUS FUNCTIONS TO SCALE CURRENT SHEETS TO FLUX DENSITIES         NEW01230
      RADFR=2./((R5/R2)*(R5/R2)-1)                                       NEW01240
      RADFS=(1+(R2/R5)*(R2/R5))/(1-(R2/R5)*(R2/R5))                      NEW01250
C     OPEN CIRCUIT ROTOR CURRENT                                         NEW01260
      IROC=BROC/(MUO*CR*RADFR)                                           NEW01270
C                                                                        NEW01280
C     LOAD CONDITION INPUT FROM TERMINAL                                 NEW01290
      PRINT *,'FORM OF INPUT FOR LOAD DATA'                              NEW01300
      PRINT *,'1   POWER AND POWER FACTOR'                               NEW01310
      PRINT *,'2   ACTIVE AND REACTIVE POWER'                            NEW01320
      PRINT *,'PLEASE GIVE NUMBER PRECEDING REQUIRED FORM'               NEW01330
      READ *,NCONT                                                       NEW01340
      PRINT *,'NATURE OF POWER FACTOR (LEAD/LAG)'                        NEW01350
      READ *,PF                                                          NEW01360
      PRINT *,'OUTPUT POWER IN MW'                                       NEW01370
      READ *,POUT                                                        NEW01380
      POUT=POUT*1.0E6                                                    NEW01390
      IF (NCONT.EQ.1) THEN                                               NEW01400
       PRINT *,'VALUE OF POWER FACTOR'                                   NEW01410
       READ *,PFVAL                                                      NEW01420
C      PEAK STATOR LINE CURRENT                                          NEW01430
       IS=POUT*SQRT(2.0)/(SQRT(3.0)*VLIN*PFVAL)                          NEW01440
      ELSE                                                               NEW01450
       PRINT *,'REACTIVE POWER IN MVAR'                                  NEW01460
       READ *,VARS                                                       NEW01470
       VARS=VARS*1.0E6                                                   NEW01480
       IS=SQRT(2.*(POUT*POUT+VARS*VARS)/(3.*VLIN*VLIN))                  NEW01490
       PFVAL=COS(ATAN(VARS/POUT))                                        NEW01500
      END IF                                                             NEW01510
C     PROTECT UNITY POWER FACTOR CASE FROM FLOATING-POINT INACCURACIES   NEW01520
      IF (PFVAL.GT.0.999999999) THEN                                     NEW01530
       PFVAL=0.999999999                                                 NEW01540
      END IF                                                             NEW01550
C     POWER FACTOR ANGLE (IN RADIANS)                                    NEW01560
      PHI=ACOS(PFVAL)                                                    NEW01570
C                                                                        NEW01580
      PRINT *,'IS ROTOR CURRENT AVAILABLE? (''Y''/''N'')'                NEW01590
      READ *,CONT                                                        NEW01600
      IF (CONT.EQ.'Y') THEN                                              NEW01610
C      READ IN TEST VALUE OF ROTOR CURRENT                               NEW01620
       PRINT *,'ROTOR CURRENT IN AMPS'                                   NEW01630
       READ *,IRDES                                                      NEW01640
      ELSE                                                               NEW01650
```

```
C       CALCULATION OF ROTOR CURRENT USING FROHLICH REPRESENTATION       NEW01660
C       OF OPEN CIRCUIT CHARACTERISTIC                                   NEW01670
C       VOLTAGE DROP ACROSS LEAKAGE REACTANCE                            NEW01680
        VLEAK=XLEAK*IS*SQRT(0.5)                                         NEW01690
C       COMPONENT OF EXCITATION CURRENT TO INDUCE ABOVE                  NEW01700
        IRLEAK=VLEAK/CAIR                                                NEW01710
C       EXCITATION CURRENT TO CIRCULATE STATOR CURRENT ON SHORT CIRCUIT  NEW01720
        IRSC=IS*SQRT(0.5)/CSC                                            NEW01730
C       COMPONENT OF EXCITATION CURRENT TO OPPOSE ARMATURE REACTION      NEW01740
        IAR=IRSC-IRLEAK                                                  NEW01750
C       AIR-GAP E.M.F.                                                   NEW01760
        IF (PF.EQ.'LAG') THEN                                            NEW01770
         EGAP=VLIN*VLIN+VLEAK*VLEAK+2.*VLIN*VLEAK*SIN(PHI)               NEW01780
        ELSE                                                             NEW01790
         EGAP=VLIN*VLIN+VLEAK*VLEAK-2.*VLIN*VLEAK*SIN(PHI)               NEW01800
        END IF                                                           NEW01810
        EGAP=SQRT(EGAP)                                                  NEW01820
C       LOAD ANGLE OF LEAKAGE REACTANCE                                  NEW01830
        BETA=ASIN(VLEAK/EGAP*COS(PHI))                                   NEW01840
C       EXCITATION CURRENT TO INDUCE AIR-GAP E.M.F. ON OPEN CIRCUIT      NEW01850
        IREGAP=AFROH*EGAP/(1.-BFROH*EGAP*1.0E-3)                         NEW01860
C       CALCULATION OF ESTIMATED ROTOR CURRENT                           NEW01870
        IF (PF.EQ.'LAG') THEN                                            NEW01880
         IRDES=IREGAP*IREGAP+IAR*IAR-2.*IREGAP*IAR*COS(PI*0.5+PHI+BETA)  NEW01890
        ELSE                                                             NEW01900
         IRDES=IREGAP*IREGAP+IAR*IAR-2.*IREGAP*IAR*COS(PI*0.5-PHI+BETA)  NEW01910
        END IF                                                           NEW01920
        IRDES=SQRT(IRDES)                                                NEW01930
       END IF                                                            NEW01940
C                                                                        NEW01950
C      AVOID DIVIDING BY ZERO IN OPEN CIRCUIT CASE                       NEW01960
       IF (IS.LT.1.0E-9) THEN                                            NEW01970
        KS1=0.0                                                          NEW01980
        IR=IROC                                                          NEW01990
        LMOR=0.0                                                         NEW02000
        LAMBDA=0.0                                                       NEW02010
        ERMES='OPEN CIRCUIT'                                             NEW02020
        FSTIR=IR                                                         NEW02030
        FSTLAM=LAMBDA                                                    NEW02040
        GOTO 25                                                          NEW02050
       END IF                                                            NEW02060
C                                                                        NEW02070
C      PEAK FUNDAMENTAL STATOR SURFACE CURRENT DENSITY                   NEW02080
       KS1=6.*IS*KW*QS/(PI*NP*R5)                                        NEW02090
C                                                                        NEW02100
C      CALCULATIONS TO DETERMINE ROTOR CURRENT AND TORQUE ANGLE          NEW02110
C      POWER FUNCTION                                                    NEW02120
       PFUN=IROC*PFVAL                                                   NEW02130
C      CURRENT FUNCTION                                                  NEW02140
       CFUN=RADFS*KS1/(RADFR*CR)                                         NEW02150
C      COEFFICIENTS OF THE FIRST EQUATION IN LMOR                        NEW02160
       A1=PFUN*PFUN*PFUN*PFUN                                            NEW02170
       A2=2.*PFUN*PFUN*(IROC*IROC+CFUN*CFUN)                             NEW02180
       A3=(CFUN*CFUN-IROC*IROC)*(CFUN*CFUN-IROC*IROC)                    NEW02190
       A3=A3+4.*CFUN*CFUN*PFUN*PFUN                                      NEW02200
```

```
C     SOLVING FOR LAMBDA                                                NEW02210
      ACOMP=A2*A2-4.*A1*A3                                              NEW02220
      IF (ACOMP.LT.0.0) THEN                                            NEW02230
       PRINT *,'IMAGINARY ROOTS IN LAMBDA EQUATION'                     NEW02240
       STOP                                                             NEW02250
      END IF                                                            NEW02260
      SINSQ1=(A2+SQRT(ACOMP))/(2.*A3)                                   NEW02270
      SINSQ2=(A2-SQRT(ACOMP))/(2.*A3)                                   NEW02280
      SILAM1=SQRT(SINSQ1)                                               NEW02290
      SILAM2=SQRT(SINSQ2)                                               NEW02300
C     DISENTANGLEMENT OF QUADRANT LOCATIONS OF LAMBDA                   NEW02310
      IF (CFUN*CFUN-IROC*IROC.LT.0.0) THEN                              NEW02320
       IF (PFUN*PFUN.LT.ABS(CFUN*CFUN-IROC*IROC)) THEN                  NEW02330
        IF (SILAM1.GT.SILAM2) THEN                                      NEW02340
         LMDR1=ASIN(SILAM1)                                             NEW02350
         LMDR2=PI-ASIN(SILAM2)                                          NEW02360
         ERMES='LOW CURRENT A'                                          NEW02370
        ELSE                                                            NEW02380
         LMDR1=PI-ASIN(SILAM1)                                          NEW02390
         LMDR2=ASIN(SILAM2)                                             NEW02400
         ERMES='LOW CURRENT B'                                          NEW02410
        END IF                                                          NEW02420
       ELSE                                                             NEW02430
        LMDR1=PI-ASIN(SILAM1)                                           NEW02440
        LMDR2=PI-ASIN(SILAM2)                                           NEW02450
        ERMES='INTERMEDIATE CURRENT '                                   NEW02460
       END IF                                                           NEW02470
      ELSE                                                              NEW02480
       LMDR1=PI-ASIN(SILAM1)                                            NEW02490
       LMDR2=PI-ASIN(SILAM2)                                            NEW02500
       ERMES='HIGH CURRENT'                                             NEW02510
      END IF                                                            NEW02520
C     CALCULATION OF IR                                                 NEW02530
      IR1=PFUN/SILAM1                                                   NEW02540
      IR2=PFUN/SILAM2                                                   NEW02550
      IF (PF.EQ.'LAG ') THEN                                            NEW02560
       IF (IR1.GT.IR2) THEN                                             NEW02570
        IR=IR1                                                          NEW02580
        LMDR=LMDR1                                                      NEW02590
       ELSE                                                             NEW02600
        IR=IR2                                                          NEW02610
        LMDR=LMDR2                                                      NEW02620
       END IF                                                           NEW02630
      ELSE                                                              NEW02640
       IF (IR1.LT.IR2) THEN                                             NEW02650
        IR=IR1                                                          NEW02660
        LMDR=LMDR1                                                      NEW02670
       ELSE                                                             NEW02680
        IR=IR2                                                          NEW02690
        LMDR=LMDR2                                                      NEW02700
       END IF                                                           NEW02710
      END IF                                                            NEW02720
C     RECORD INITIAL VALUES FROM 2 D-D-F ROUTINE                        NEW02730
      FSTIR=IR                                                          NEW02740
      FSTLAM=180.*LMDR/PI                                               NEW02750
```

```
C                                                                       NEW02760
C     RESET PERMEABILITY LOOP COUNTER EVERY LOAD CONDITION              NEW02770
 25   NCERR=0                                                           NEW02780
C     RESET FLUX LOOP COUNTER EVERY PERMEABILITY ITERATION              NEW02790
 26   NBERR=0                                                           NEW02800
 24   CONTINUE                                                          NEW02810
C     HARMONICS PRESENT                                                 NEW02820
C     LOWEST AND HIGHEST ROTOR HARMONICS                                NEW02830
      RH1=1                                                             NEW02840
      RH2=5                                                             NEW02850
C     LOWEST AND HIGHEST STATOR HARMONICS                               NEW02860
      SH1=1                                                             NEW02870
      SH2=1                                                             NEW02880
C     STATOR DIRECTIONAL PERMEABILITY CALCULATIONS                      NEW02890
      MUNS=(2.*TAUS+(DELS-2.*TAUS)*MUSATS)/(DELS)                       NEW02900
C     STATOR TOOTH REGION RADIAL PERMEABILITY                           NEW02910
      GAMMA=(DELS-2.*TAUS)/(DELS)                                       NEW02920
      MUTS=1./(1.-GAMMA+GAMMA/MUSATS)                                   NEW02930
C     STATOR TOOTH REGION TANGENTIAL PERMEABILITY                       NEW02940
C     ROTOR DIRECTIONAL PERMEABILITY CALCULATIONS                       NEW02950
      MUNR=(2.*TAUR+(PI/QR-2.*TAUR)*MUSATR)/(PI/QR)                     NEW02960
      GAMMA=(1.-2.*TAUR*QR/PI)                                          NEW02970
      MUTR=1./(1.-GAMMA+GAMMA/MUSATR)                                   NEW02980
C                                                                       NEW02990
C     STATOR EXPRESSIONS INDEPENDENT OF ANGULAR POSITION                NEW03000
      DO 30,N=SH1,SH2,2                                                 NEW03010
C      SKIP OVER HARMONIC MULTIPLES OF 3                                NEW03020
       IF(ABS(N/3-N/3.0).LT.1E-3) GOTO 30                               NEW03030
C      PEAK HARMONIC STATOR SURFACE CURRENT DENSITY                     NEW03040
       KSA=6*IS/NP/PI*SIN(N*TAUS)/N/TAUS/R5                             NEW03050
       KSB=SIN(N*PI*C/2)*SIN(N*QS*DELS/2)/SIN(N*DELS/2)                 NEW03060
       KNS=KSA*KSB                                                      NEW03070
C      CALCULATION OF AIR-GAP VECTOR POTENTIAL COEFFICIENTS             NEW03080
       G=SQRT(MUTR/MUNR)                                                NEW03090
       H=SQRT(MUTS/MUNS)                                                NEW03100
       X2=(MUR/MUTR*G/N-1.)/(MUR/MUTR*G/N+1.)                           NEW03110
       X3=(R3**(2.*G)-X2*R1**(2.*G))/(R3**(2.*G)+X2*R1**(2.*G))         NEW03120
       X3=(1.-G/N/MUTR*X3)/(1.+G/N/MUTR*X3)                             NEW03130
       X4=(R4**(2*N)-X3*R3**(2*N))/(R4**(2*N)+X3*R3**(2*N))             NEW03140
       X4=(1.-N*MUTS/H*X4)/(1.+N*MUTS/H*X4)                             NEW03150
       X5=(R5**(2*H)-X4*R4**(2*H))/(R5**(2*H)+X4*R4**(2*H))             NEW03160
       X6=R5**(2*H)*(1.-X5)/(1.+X5)                                     NEW03170
       X6=(R6**(2*H)-X6)/(R6**(2*H)+X6)                                 NEW03180
       L5=X6*(R6**(H+N)-R7**(2*N)*R6**(H-N))                            NEW03190
       L5=L5-N*MUTS/H/MUS*(R6**(H+N)+R7**(2*N)*R6**(H-N))               NEW03200
       L5=(1.+X6)*(R6**(H+N)-R7**(2*N)*R6**(H-N))/L5-1.                 NEW03210
       L5=L5*MUO*MUTS/H*KNS*R5**(H+1)/(1.+X5)                           NEW03220
       L5=L5/(R6**(2.*H)+R5**(2*H)*(1.-X5)/(1.+X5))                     NEW03230
       LS=L5+MUO*MUTS/2./H*KNS*R5**(1.-H)                               NEW03240
       LS=LS*R4**(N+H)*(1.+X4)/(R4**(2*N)+X3*R3**(2*N))                 NEW03250
       MS=LS*R3**(2*N)*X3                                               NEW03260
C      PEAK HARMONIC COMPONENTS OF FLUX DENSITY ORIGINATING             NEW03270
C      FROM THE STATOR CURRENT SHEET                                    NEW03280
       BRSMAX(N)=(LS*R4**(N-1)+MS*R4**(-N-1))*N                         NEW03290
       BTSMAX(N)=(MS*R4**(-N-1)-LS*R4**(N-1))*N                         NEW03300
```

```
 30    CONTINUE                                                        NEW03310
C      RESET ROTOR CURRENT BOOST LOOP COUNTER                          NEW03320
       NIR=0                                                           NEW03330
 27    CONTINUE                                                        NEW03340
C      ROTOR EXPRESSIONS INDEPENDENT OF ANGULAR POSITION               NEW03350
       DO 20,M=RH1,RH2,2                                               NEW03360
C       PEAK HARMONIC ROTOR SURFACE CURRENT DENSITY                    NEW03370
        KRA=2.*NC*IR/PI/TAUR/M*(-1)**((M-1)/2)*SIN(M*TAUR)             NEW03380
        KRB=SIN(QR*M*DELR/2)/SIN(M*DELR/2)/R2                          NEW03390
        KMR=KRA*KRB                                                    NEW03400
C       CALCULATION OF AIR-GAP VECTOR POTENTIAL COEFFICIENTS           NEW03410
        G=M*SQRT(MUTR/MUNR)                                            NEW03420
        H=M*SQRT(MUTS/MUNS)                                            NEW03430
        X6=R6**(H+M)+R7**(2*M)*R6**(H-M)                               NEW03440
        X6=X6/(R6**(H+M)-R7**(2*M)*R6**(H-M))*M*MUTS/H/MUS             NEW03450
        Y6=(1.-X6)/(1.+X6)                                             NEW03460
        X4=(R4**(M+H)-R4**(M-H)*R6**(2.*H)*Y6)*H                       NEW03470
        X4=X4/(R4**(M+H)+R4**(M-H)*R6**(2.*H)*Y6)/M/MUTS               NEW03480
        Y4=(1.-X4)/(1.+X4)                                             NEW03490
        X3=(R3**(G+M)-R3**(G-M)*R4**(2*M)*Y4)*M*MUTR                   NEW03500
        X3=X3/(R3**(G+M)+R3**(G-M)*R4**(2*M)*Y4)/G                     NEW03510
        Y3=(1.-X3)/(1.+X3)                                             NEW03520
        X2=R2**(2.*G)-R3**(2.*G)*Y3                                    NEW03530
        X2=X2/(R2**(2.*G)+R3**(2.*G)*Y3)                               NEW03540
        L2=R1**(2.*G)*(1.+X2)*(1.-G*MUR/M/MUTR)                        NEW03550
        L2=L2+R2**(2.*G)*(1.-X2)*(1.+G*MUR/M/MUTR)                     NEW03560
        L2=MUO*KMR*R2**(G+1.)*(MUR/M+MUTR/G)/L2                        NEW03570
        M2=L2*R2**(2.*G)*(1.-X2)/(1.+X2)                               NEW03580
        M2=M2-MUO*MUTR*KMR*R2**(G+1.)/G/(1.+X2)                        NEW03590
        L3=L2*R2**(2.*G)+M2                                            NEW03600
        L3=L3/(R2**(2.*G)+R3**(2.*G)*Y3)                               NEW03610
        M3=L3*R3**(2.*G)*Y3                                            NEW03620
        LR=L3*R3**(2.*G)+M3                                            NEW03630
        LR=LR/(R3**(G+M)+R3**(G-M)*R4**(2*M)*Y4)                       NEW03640
        MR=LR*R4**(2*M)*Y4                                             NEW03650
C       PEAK HARMONIC COMPONENTS OF FLUX DENSITY ORIGINATING           NEW03660
C       FROM THE ROTOR CURRENT SHEET                                   NEW03670
        BRRMAX(M)=(LR*R4**(M-1)+MR*R4**(-M-1))*M                       NEW03680
        BTRMAX(M)=(MR*R4**(-M-1)-LR*R4**(M-1))*M                       NEW03690
 20    CONTINUE                                                        NEW03700
C      CALCUALTION OF RESULTANT FUNDAMENTAL AIR-GAP FLUX DENSITY       NEW03710
       IF (PF.EQ.'LAG') THEN                                           NEW03720
        SI=1                                                           NEW03730
       ELSE                                                            NEW03740
        SI=-1                                                          NEW03750
       END IF                                                          NEW03760
       BRSQRT=BRSMAX(1)*BRSMAX(1)*SIN(SI*PHI)*SIN(SI*PHI)              NEW03770
       BRSQRT=BRSQRT-(BRSMAX(1)*BRSMAX(1)-BRRMAX(1)*BRRMAX(1))         NEW03780
       IF (BRSQRT.LT.0.0) THEN                                         NEW03790
C      FLUX TRIANGLE DOES NOT JOIN UP                                  NEW03800
        IF (NBERR.GT.0) THEN                                           NEW03810
C        JUMP STRAIGHT TO PERMEABILITY LOOP                            NEW03820
         GOTO 42                                                       NEW03830
        ELSE                                                           NEW03840
C        THIS IS FIRST PASS SO BOOST ROTOR CURRENT                     NEW03850
```

```
          IR=IR*1.01                                                    NEW03860
          IF (NIR.LT.100) THEN                                          NEW03870
           NIR=NIR+1                                                    NEW03880
           GOTO 27                                                      NEW03890
          ELSE                                                          NEW03900
C          LOOP COUNTER REACHED MAX ALLOWABLE VALUE                     NEW03910
           PRINT *,'OVERFLOW IN CURRENT BOOST LOOP'                     NEW03920
           STOP                                                         NEW03930
          END IF                                                        NEW03940
         END IF                                                         NEW03950
        END IF                                                          NEW03960
C       SELECT REAL SOLUTION CLOSEST TO DESIRED VALUE                   NEW03970
        BR1=BRSMAX(1)*COS(PI*.5+SI*PHI)+SQRT(BRSQRT)                    NEW03980
        BR2=BRSMAX(1)*COS(PI*.5+SI*PHI)-SQRT(BRSQRT)                    NEW03990
        IF (ABS(BROC-BR1).LT.ABS(BROC-BR2)) THEN                        NEW04000
         BR=BR1                                                         NEW04010
        ELSE                                                            NEW04020
         BR=BR2                                                         NEW04030
        END IF                                                          NEW04040
C       OBTAIN TORQUE ANGLE                                             NEW04050
        LMDR=ASIN(BR*PFVAL/BRRMAX(1))                                   NEW04060
        IF (BR*BR.GT.BRSMAX(1)*BRSMAX(1)+BRRMAX(1)*BRRMAX(1)) THEN      NEW04070
         CONTINUE                                                       NEW04080
        ELSE                                                            NEW04090
         LMDR=PI-LMDR                                                   NEW04100
        END IF                                                          NEW04110
C       FORM FLUX ERROR                                                 NEW04120
        BERR=(BROC-BR)/BROC                                             NEW04130
        NBERR=NBERR+1                                                   NEW04140
        IF (NBERR.EQ.1000) THEN                                         NEW04150
C        LOOP COUNTER REACHED MAX ALLOWABLE VALUE                       NEW04160
         PRINT *,'OVERFLOW IN FLUX LOOP'                                NEW04170
         STOP                                                           NEW04180
        END IF                                                          NEW04190
        IF (ABS(BERR).GT.1.0E-5) THEN                                   NEW04200
C       ITERATE                                                         NEW04210
        BERK=.4                                                         NEW04220
         IF (PF.EQ.'LEAD'.AND.LMDR+ACOS(PFVAL).GE.PI) THEN              NEW04230
          IR=IR*(1.-BERR*BERK)                                          NEW04240
         ELSE                                                           NEW04250
          IR=IR*(1.+BERR*BERK)                                          NEW04260
         END IF                                                         NEW04270
         GOTO 24                                                        NEW04280
        END IF                                                          NEW04290
 42     CONTINUE                                                        NEW04300
C       ITERATION OF TEETH PERMEABILITIES                               NEW04310
C       FORM CURRENT ERROR                                              NEW04320
        CERR=(IRDES-IR)/IRDES                                           NEW04330
        NCERR=NCERR+1                                                   NEW04340
        IF (NCERR.EQ.1000) THEN                                         NEW04350
C        LOOP COUNTER REACHED MAX ALLOWABLE VALUE                       NEW04360
         PRINT *,'OVERFLOW IN PERMEABILITY LOOP'                        NEW04370
         STOP                                                           NEW04380
        END IF                                                          NEW04390
        IF (ABS(CERR).GT.1.0E-5) THEN                                   NEW04400
```

```
C       ITERATE                                                          NEW04410
        CERK=1.0                                                         NEW04420
        MUSATS=MUSATS*(1.-CERR*CERK)                                     NEW04430
        MUSATR=MUSATR*(1.-CERR*CERK)                                     NEW04440
        GOTO 26                                                          NEW04450
       END IF                                                            NEW04460
C      MAIN CALCULATION LOOP (PER TOOTH)                                 NEW04470
C      RESET SUM OF TOOTH TORQUES                                        NEW04480
       TOTORQ=0.0                                                        NEW04490
       DO 90,TOOTH=1,1                                                   NEW04500
        HSP=HSP0+(TOOTH-1)*360.0/TEETH                                   NEW04510
C       ONE TOOTH FORCE OVER ONE VIBRATION CYCLE (HALF POWER CYCLE)      NEW04520
        DO 80,OMEGAT=0,180                                               NEW04530
         OMTR=OMEGAT*PI/180.0                                            NEW04540
C        START OF FLUX CALCULATION                                       NEW04550
C        CLEAR FLUX ARRAY                                                NEW04560
         DO 10,I=0,6                                                     NEW04570
          DO 10,J=1,2                                                    NEW04580
 10         FLUX(I,J)=0.0                                               NEW04590
C        FILL ARRAY WITH ROTOR FLUX TERMS                                NEW04600
         DO 21,M=RH1,RH2,2                                               NEW04610
          DO 21,I=0,6                                                    NEW04620
           RADI=(I*360.0/TEETH/6.0+HSP)*PI/180.0                         NEW04630
           BRR=BRRMAX(M)*COS(M*(RADI-OMTR))                              NEW04640
           BTR=BTRMAX(M)*SIN(M*(RADI-OMTR))                              NEW04650
           FLUX(I,1)=FLUX(I,1)+BRR                                       NEW04660
 21        FLUX(I,2)=FLUX(I,2)+BTR                                       NEW04670
C        FILL ARRAY WITH STATOR FLUX TERMS                               NEW04680
         DO 40,N=SH1,SH2,2                                               NEW04690
          IF(ABS(N/3-N/3.0).LT.1E-3) GOTO 40                             NEW04700
          DO 40,I=0,6                                                    NEW04710
           RADI=(I*360.0/TEETH/6.0+HSP)*PI/180.0                         NEW04720
           IF (ABS((N-1)/3-(N-1)/3.0).LT.1E-3) THEN                      NEW04730
            BRS=BRSMAX(N)*COS(N*RADI-OMTR+LMDR)                          NEW04740
            BTS=BTSMAX(N)*SIN(N*RADI-OMTR+LMDR)                          NEW04750
           ELSE IF (ABS((N+1)/3-(N+1)/3.0).LT.1E-3) THEN                 NEW04760
            BRS=BRSMAX(N)*COS(N*RADI+OMTR+LMDR)                          NEW04770
            BTS=BTSMAX(N)*SIN(N*RADI+OMTR+LMDR)                          NEW04780
           ELSE                                                          NEW04790
             PRINT *,'ERROR IN HARMONIC SPECIFICATION'                   NEW04800
           END IF                                                        NEW04810
           FLUX(I,1)=FLUX(I,1)+BRS                                       NEW04820
           FLUX(I,2)=FLUX(I,2)+BTS                                       NEW04830
 40        CONTINUE                                                      NEW04840
C        END OF FLUX CALCULATION                                         NEW04850
C        START OF STRESS CALCULATION                                     NEW04860
C        CLEAR STRESS ARRAY                                              NEW04870
         DO 60,I=0,6                                                     NEW04880
          DO 60,J=1,2                                                    NEW04890
 60         S(I,J)=0.0                                                  NEW04900
C        CALCULATION OF STRESS VALUES                                    NEW04910
         DO 50,J=0,6                                                     NEW04920
          S(J,2)=FLUX(J,1)*FLUX(J,2)/MUO                                 NEW04930
 50       S(J,1)=(FLUX(J,1)*FLUX(J,1)-FLUX(J,2)*FLUX(J,2))/2.0/MUO       NEW04940
C        FORMATION OF TANGENTIAL AND RADIAL TOOTH FORCES                 NEW04950
```

```
C       USING SEVEN POINT SIMPSON'S RULE                                NEW04960
        HSPA=360.0/TEETH/6.0*PI/180.0*R4                                NEW04970
        TFOR(OMEGAT)=S(0,2)+4.*S(1,2)+2.*S(2,2)+4.*S(3,2)+2.*S(4,2)     NEW04980
        TFOR(OMEGAT)=HSPA*(TFOR(OMEGAT)+4.*S(5,2)+S(6,2))/3./1.E3       NEW04990
        RFOR(OMEGAT)=S(0,1)+4.*S(1,1)+2.*S(2,1)+4.*S(3,1)+2.*S(4,1)     NEW05000
        RFOR(OMEGAT)=HSPA*(RFOR(OMEGAT)+4.*S(5,1)+S(6,1))/3./1.E3       NEW05010
C       CONTINUE WITH NEXT TIME INCREMENT                               NEW05020
 80     CONTINUE                                                        NEW05030
C      CALCULATION OF ZERO FREQUENCY AND FUNDAMENTAL FOURIER            NEW05040
C      COEFFICIENTS ON THIS TOOTH USING SIMPSON'S RULE INTEGRATION      NEW05050
       RADCOS=RFOR(0)                                                   NEW05060
       RADSIN=0.0                                                       NEW05070
       TANCOS=TFOR(0)                                                   NEW05080
       TANSIN=0.0                                                       NEW05090
       TORQ=TFOR(0)                                                     NEW05100
       DO 70,JLOOP=1,177,2                                              NEW05110
        RADCOS=RADCOS+4.*RFOR(JLOOP)*COS(JLOOP*PI/90.)                  NEW05120
        RADSIN=RADSIN+4.*RFOR(JLOOP)*SIN(JLOOP*PI/90.)                  NEW05130
        TANCOS=TANCOS+4.*TFOR(JLOOP)*COS(JLOOP*PI/90.)                  NEW05140
        TANSIN=TANSIN+4.*TFOR(JLOOP)*SIN(JLOOP*PI/90.)                  NEW05150
        TORQ=TORQ+4.*TFOR(JLOOP)                                        NEW05160
        RADCOS=RADCOS+2.*RFOR(JLOOP+1)*COS((JLOOP+1)*PI/90.)            NEW05170
        RADSIN=RADSIN+2.*RFOR(JLOOP+1)*SIN((JLOOP+1)*PI/90.)            NEW05180
        TANCOS=TANCOS+2.*TFOR(JLOOP+1)*COS((JLOOP+1)*PI/90.)            NEW05190
        TANSIN=TANSIN+2.*TFOR(JLOOP+1)*SIN((JLOOP+1)*PI/90.)            NEW05200
 70     TORQ=TORQ+2.*TFOR(JLOOP+1)                                      NEW05210
       RADCOS=RADCOS+4.*RFOR(179)*COS(179.*PI/90.)                      NEW05220
       RADSIN=RADSIN+4.*RFOR(179)*SIN(179.*PI/90.)                      NEW05230
       TANCOS=TANCOS+4.*TFOR(179)*COS(179.*PI/90.)                      NEW05240
       TANSIN=TANSIN+4.*TFOR(179)*SIN(179.*PI/90.)                      NEW05250
       RADCOS=RADCOS+RFOR(180)                                          NEW05260
       TANCOS=TANCOS+TFOR(180)                                          NEW05270
       TORQ=TORQ+4.*TFOR(179)+TFOR(180)                                 NEW05280
C      SIMPSON INCREMENT IS PI/90 BUT DIV BY PI FOR FOURIER COEFF       NEW05290
       HTIM=1./90.                                                      NEW05300
       RADCOS=1./3.*HTIM*RADCOS                                         NEW05310
       RADSIN=1./3.*HTIM*RADSIN                                         NEW05320
       TANCOS=1./3.*HTIM*TANCOS                                         NEW05330
       TANSIN=1./3.*HTIM*TANSIN                                         NEW05340
       TORQ=1./6.*HTIM*TORQ                                             NEW05350
C      CALCULATION OF FORCE MAGNITUDE AND PHASE ANGLE                   NEW05360
       RADMAG=SQRT(RADCOS*RADCOS+RADSIN*RADSIN)                         NEW05370
       TANMAG=SQRT(TANCOS*TANCOS+TANSIN*TANSIN)                         NEW05380
C      RADIAL FORCE ANGLE                                               NEW05390
       CALL ANGLE(RADSIN,RADCOS,RADPH)                                  NEW05400
C      TANGENTIAL FORCE ANGLE                                           NEW05410
       CALL ANGLE(TANSIN,TANCOS,TANPH)                                  NEW05420
       PHDIF=RADPH-TANPH                                                NEW05430
C      CONVERT TO DEGREES FOR OUTPUT                                    NEW05440
       RADPHD=RADPH*180./PI                                             NEW05450
       TANPHD=TANPH*180./PI                                             NEW05460
       IF (PHDIF.LT.0.0) THEN                                           NEW05470
        PHDIF=PHDIF+2.*PI                                               NEW05480
       END IF                                                           NEW05490
       PHDIFD=PHDIF*180./PI                                             NEW05500
```

```
C       CALCULATION OF RADIAL VIBRATION IN MICROMETRES                    NEW05510
        RVIB=RADMAG*TCRAD                                                 NEW05520
        TVIB=TANMAG*TCTAN                                                 NEW05530
        VIB=SQRT(RVIB*RVIB+TVIB*TVIB-2.*RVIB*TVIB*COS(PHDIF-PI/2.))       NEW05540
C       CALCULATION OF VIBRATION PHASE                                    NEW05550
        VIBSIN=(TANCOS*TCTAN)-(RADSIN*TCRAD)                              NEW05560
        VIBCOS=(RADCOS*TCRAD)+(TANSIN*TCTAN)                              NEW05570
        CALL ANGLE(VIBSIN,VIBCOS,VIBANG)                                  NEW05580
        IF (VIBANG.LT.0.0) THEN                                           NEW05590
         VIBANG=VIBANG+2.*PI                                              NEW05600
        END IF                                                            NEW05610
        VIBANG=VIBANG*180./PI                                             NEW05620
        WRITE(11,114) TOOTH,RADMAG,TANMAG,PHDIFD,VIB,VIBANG               NEW05630
        PRINT *,TOOTH,RADMAG,TANMAG,PHDIFD,VIB,VIBANG                     NEW05640
C                                                                         NEW05650
C     CONVERSION TO CARTESIAN COORDINATES FOR ANSYS DATA FILE             NEW05660
      ALPHA=PI/TEETH*(TOOTH*2.-1.)                                        NEW05670
      AX=RADMAG*COS(ALPHA)*SIN(RADPH)-TANMAG*SIN(ALPHA)*SIN(TANPH)        NEW05680
      BX=RADMAG*COS(ALPHA)*COS(RADPH)-TANMAG*SIN(ALPHA)*COS(TANPH)        NEW05690
      AY=RADMAG*SIN(ALPHA)*SIN(RADPH)+TANMAG*COS(ALPHA)*SIN(TANPH)        NEW05700
      BY=RADMAG*SIN(ALPHA)*COS(RADPH)+TANMAG*COS(ALPHA)*COS(TANPH)        NEW05710
      WRITE(10,104) TOOTH,BX,AX,BY,AY                                     NEW05720
C                                                                         NEW05730
C      UPDATA CUMULATIVE SUM OF TOOTH TORQUES                             NEW05740
       TOTORQ=TOTORQ+TORQ                                                 NEW05750
C      PROCEDE TO NEXT TOOTH                                              NEW05760
 90    CONTINUE                                                           NEW05770
C     CONVERT SUM OF TOOTH TORQUES TO MACHINE TORQUE                      NEW05780
      TOTORQ=TOTORQ*TEETH/(TOOTH-1.)*R5*ACTLEN                            NEW05790
C     OUTPUT OF TERMINAL INPUT DATA FOR CONFIRMATION                      NEW05800
      WRITE(11,103)                                                       NEW05810
      WRITE(11,215) POUT*1.0E-6                                           NEW05820
      IF (NCONT.EQ.2) THEN                                                NEW05830
       WRITE(11,219) VARS*1.0E-6                                          NEW05840
      END IF                                                              NEW05850
      WRITE(11,216) PFVAL,PF                                              NEW05860
      WRITE(11,223) VLIN*1.0E-3                                           NEW05870
C     OUTPUT OF CURRENT DATA                                              NEW05880
      WRITE(11,103)                                                       NEW05890
      WRITE(11,200) IS/SQRT(2.0)                                          NEW05900
      WRITE(11,201) IR                                                    NEW05910
C     OUTPUT OF ANGLES                                                    NEW05920
      LAMBDA=LMDR*180./PI                                                 NEW05930
      WRITE(11,202) LAMBDA                                                NEW05940
      DPHI=PHI*180./PI                                                    NEW05950
      IF (PF.EQ.'LEAD') DPHI=(-1)*DPHI                                    NEW05960
      DELTA=LAMBDA-DPHI-90.                                               NEW05970
      WRITE(11,222) DELTA                                                 NEW05980
C     OUTPUT OF TORQUE                                                    NEW05990
      WRITE(11,226) TOTORQ/1.0E3                                          NEW06000
C     OUTPUT OF INITIAL RESULTS OF 2 D-D-F CALCULATION                    NEW06010
      WRITE(11,103)                                                       NEW06020
      WRITE(11,220) FSTIR                                                 NEW06030
      WRITE(11,221) FSTLAM                                                NEW06040
C     OUTPUT OF FLUX QUANTITIES                                           NEW06050
```

```
      WRITE(11,103)                                                    NEW06060
      WRITE(11,203) BRSMAX(1)                                          NEW06070
      WRITE(11,204) BRRMAX(1)                                          NEW06080
      WRITE(11,205) BR                                                 NEW06090
      BT=BTSMAX(1)*BTSMAX(1)+BTRMAX(1)*BTRMAX(1)                       NEW06100
      BT=SQRT(BT-2.*BTSMAX(1)*BTRMAX(1)*COS(PI-LMOR))                  NEW06110
      WRITE(11,217) BT                                                 NEW06120
      WRITE(11,218) BROC                                               NEW06130
C     OUTPUT OF RADIUS DATA                                            NEW06140
      WRITE(11,103)                                                    NEW06150
      WRITE(11,214) R3                                                 NEW06160
      WRITE(11,206) R1                                                 NEW06170
      WRITE(11,207) R2                                                 NEW06180
      WRITE(11,208) R5                                                 NEW06190
      WRITE(11,209) R6                                                 NEW06200
C     OUTPUT OF PERMEABILITIES                                         NEW06210
      WRITE(11,103)                                                    NEW06220
      WRITE(11,210) MUS                                                NEW06230
      WRITE(11,211) MUSATS                                             NEW06240
      WRITE(11,212) MUR                                                NEW06250
      WRITE(11,213) MUSATR                                             NEW06260
C     OUTPUT OF TRANSFER COEFFICIENTS                                  NEW06270
      WRITE(11,103)                                                    NEW06280
      WRITE(11,224) TCRAD                                              NEW06290
      WRITE(11,225) TCTAN                                              NEW06300
C     RECORD OF CALCULATION BRANCH IMPLEMENTED                         NEW06310
      WRITE(11,103)                                                    NEW06320
      WRITE(11,300) ERMES                                              NEW06330
      PRINT *,'ANOTHER LOAD CASE (''Y''/''N'')?'                       NEW06340
      READ *,CONT                                                      NEW06350
      IF (CONT.EQ.'Y') THEN                                            NEW06360
       MUSATR=FSTMTR                                                   NEW06370
       MUSATS=FSTMTS                                                   NEW06380
       WRITE(11,103)                                                   NEW06390
       WRITE(11,103)                                                   NEW06400
       GOTO 23                                                         NEW06410
      END IF                                                           NEW06420
      STOP                                                             NEW06430
 100  FORMAT(9X,'TOOTH',7X,'X FORCE (KN)',7X,'Y FORCE (KN)')           NEW06440
 101  FORMAT(22X,'REAL',3X,'IMAG',8X,'REAL',3X,'IMAG')                 NEW06450
 103  FORMAT(1X)                                                       NEW06460
 104  FORMAT(11X,I2,6X,2F7.1,5X,2F7.1)                                 NEW06470
 110  FORMAT(8X,'TOOTH',3X,'RADIAL',3X,'TANG''L',3X,'PHASE',3X,'RADIAL',NEW06480
     *5X,'VIB''N')                                                    NEW06490
 111  FORMAT(16X,'FORCE',4X,'FORCE',4X,'DIFF.',3X,'VIB''N',6X,'PHASE') NEW06500
 112  FORMAT(17X,'(KN)',5X,'(KN)',4X,'(DEG)',3X,'(MICROM)',3X,'(DEG)') NEW06510
 114  FORMAT(10X,I2,3X,F7.3,2X,F7.3,3X,F5.1,3X,F5.2,6X,F5.1)           NEW06520
 150  FORMAT(40X,F8.6)                                                 NEW06530
 152  FORMAT(40X,F6.3)                                                 NEW06540
 153  FORMAT(40X,F8.2)                                                 NEW06550
 200  FORMAT(8X,'STATOR CURRENT',5X,F6.0,1X,'A')                       NEW06560
 201  FORMAT(8X,'ROTOR CURRENT',5X,F6.0,1X,'A')                        NEW06570
 202  FORMAT(8X,'TORQUE ANGLE',5X,F6.2,1X,'DEG')                       NEW06580
 203  FORMAT(8X,'FUNDAMENTAL RADIAL STATOR FLUX DENSITY',5X,F6.4,1X,'T')NEW06590
 204  FORMAT(8X,'FUNDAMENTAL RADIAL ROTOR FLUX DENSITY',5X,F6.4,1X,'T') NEW06600
```

```
 205  FORMAT(8X,'RESULTANT FUND''L RADIAL FLUX DENSITY',5X,F6.4,1X,'T') NEW06610
 206  FORMAT(8X,'ROTOR SLOT BOTTOM RADIUS',5X,F8.6,1X,'M')              NEW06620
 207  FORMAT(8X,'ROTOR CURRENT SHEET RADIUS',5X,F8.6,1X,'M')            NEW06630
 208  FORMAT(8X,'STATOR CURRENT SHEET RADIUS',5X,F8.6,1X,'M')           NEW06640
 209  FORMAT(8X,'STATOR SLOT BOTTOM RADIUS',5X,F8.6,1X,'M')             NEW06650
 210  FORMAT(8X,'STATOR BODY PERMEABILITY',5X,F6.0)                     NEW06660
 211  FORMAT(8X,'STATOR TOOTH PERMEABILITY',5X,F8.2)                    NEW06670
 212  FORMAT(8X,'ROTOR BODY PERMEABILITY',5X,F6.0)                      NEW06680
 213  FORMAT(8X,'ROTOR TOOTH PERMEABILITY',5X,F8.2)                     NEW06690
 214  FORMAT(8X,'ROTOR RADIUS',5X,F8.6)                                 NEW06700
 215  FORMAT(8X,'OUTPUT POWER',5X,F5.1,1X,'MW')                         NEW06710
 216  FORMAT(8X,'POWER FACTOR',5X,F4.2,1X,A4)                           NEW06720
 217  FORMAT(8X,'RESULTANT FUND. CIRC. FLUX DENSITY',5X,F6.4,1X,'T')    NEW06730
 218  FORMAT(8X,'OPEN CIRCUIT RADIAL FLUX DENSITY',5X,F6.4,1X,'T')      NEW06740
 219  FORMAT(8X,'REACTIVE POWER',5X,F5.1,1X,'MVAR')                     NEW06750
 220  FORMAT(8X,'INITIAL ROTOR CURRENT',5X,F6.0,1X,'A')                 NEW06760
 221  FORMAT(8X,'INITIAL TORQUE ANGLE',5X,F6.2,1X,'DEG')                NEW06770
 222  FORMAT(8X,'LOAD ANGLE',5X,F6.2,1X,'DEG')                          NEW06780
 223  FORMAT(8X,'TERMINAL VOLTAGE',5X,F4.1,1X,'KV')                     NEW06790
 224  FORMAT(8X,'RADIAL FORCE TRANSFER COEFFICIENT',5X,F4.2)            NEW06800
 225  FORMAT(8X,'TANGENTIAL FORCE TRANSFER COEFFICIENT',5X,F4.2)        NEW06810
 226  FORMAT(8X,'MACHINE TORQUE',5X,F6.3,1X,'MNM')                      NEW06820
 227  FORMAT(8X,I2,3X,F8.5,3X,F8.5)                                     NEW06830
 300  FORMAT(8X,A50)                                                    NEW06840
 400  FORMAT(F30.15)                                                    NEW06850
 401  FORMAT(14X,A1)                                                    NEW06860
      END                                                               NEW06870
      SUBROUTINE ANGLE(SINVAL,COSVAL,RESULT)                            NEW06880
C     FOUR QUADRANT INVERSE TANGENT CALCULATION                         NEW06890
      PI=3.14159265                                                     NEW06900
      IF (COSVAL.LT.0.0) THEN                                           NEW06910
C      QUADRANTS 2 AND 3                                                NEW06920
       IF (SINVAL.LT.0.0) THEN                                          NEW06930
C       QUADRANT 3                                                      NEW06940
        RESULT=ATAN(SINVAL/COSVAL)-PI                                   NEW06950
       ELSE                                                             NEW06960
C       QUADRANT 2                                                      NEW06970
        RESULT=ATAN(SINVAL/COSVAL)+PI                                   NEW06980
       END IF                                                           NEW06990
      ELSE                                                              NEW07000
C      QUADRANTS 1 AND 4                                                NEW07010
       RESULT=ATAN(SINVAL/COSVAL)                                       NEW07020
      END IF                                                            NEW07030
      RETURN                                                            NEW07040
      END                                                               NEW07050
```